Electronic structure of sodium niobate

Fermi energy, band gap, defects, and transport properties

Zur Erlangung des Grades eines Doktors der Naturwissenschaften (Dr. rer. nat.)
Genehmigte Dissertation von Nicole Bein aus Frankfurt am Main
Tag der Einreichung: 06.12.2023, Tag der Prüfung: 22.02.2024

1. Gutachten: Prof. Dr. Andreas Klein
2. Gutachten: Dr. Till Frömling
Darmstadt, Technische Universität Darmstadt

TECHNISCHE UNIVERSITÄT DARMSTADT

Materials and Earth Sciences Department

Electronic Structure of Materials

Electronic structure of sodium niobate
Fermi energy, band gap, defects, and transport properties

Accepted doctoral thesis by Nicole Bein

Date of submission: 06.12.2023
Date of thesis defense: 22.02.2024

Darmstadt, Technische Universität Darmstadt

Erklärungen laut Promotionsordnung

§ 8 Abs. 1 lit. c PromO

Ich versichere hiermit, dass die elektronische Version meiner Dissertation mit der schriftlichen Version übereinstimmt.

§ 8 Abs. 1 lit. d PromO

Ich versichere hiermit, dass zu einem vorherigen Zeitpunkt noch keine Promotion versucht wurde. In diesem Fall sind nähere Angaben über Zeitpunkt, Hochschule, Dissertationsthema und Ergebnis dieses Versuchs mitzuteilen.

§ 9 Abs. 1 PromO

Ich versichere hiermit, dass die vorliegende Dissertation selbstständig und nur unter Verwendung der angegebenen Quellen verfasst wurde.

§ 9 Abs. 2 PromO

Die Arbeit hat bisher noch nicht zu Prüfungszwecken gedient.

Darmstadt, 06.12.2023

N. Bein

Zusammenfassung

Kondensatoren mit hoher Energiedichte sind wichtige Komponenten in Gleichrichtern, welche zur Invertierung von AC- zu DC-Signalen gebraucht werden, um z.B. Akkumulatoren elektrischer Fahrzeuge zu laden oder die Windenergie von Windturbinen in unser elektrisches Netz zu speißen. Antiferroelektrische Materialien sind aufgrund ihrer hohen Energiedichte im Vergleich zu dielektrischen oder ferroelektrischen Kondensatoren und ihrer hohen Leistungsdichte im Vergleich zu elektrochemischen Kondensatoren erfolgsversprechende Kandidaten für solche hochenergetischen Kondensatoren. Bisher sind allerdings die einzigen geeigneten antiferroelektrischen Materialien für solche Anwendungen Bleizirkonattitanat (PZT) basierende Materialien. Während der Herstellung und des Recyclings dieser Materialien entstehen giftige bleihaltige Komponenten. Im Gegensatz dazu sind die nicht giftigen Alternativen wie Silber- (AN) oder Natriumniobat (NN) sehr teuer. Dementsprechend ist die Nachfrage nach nicht giftigen kostengünstigen antiferroelektrischen Alternativen sehr hoch.

In dieser Arbeit wurde die Elektronenstruktur des antiferroelektrischen Materials Natriumniobat untersucht. Zum Vergleich wurde das ferroelektrische Material Kaliumniobat (KN) analysiert, um mögliche Unterschiede, die verantwortlich für die (anti)ferroelektrischen Eigenschaften dieser beiden Materialsysteme sind, zu identifizieren. Rasterelektronenmikroskopie (REM) und Röntgenbeugung (XRD) wurden verwendet, um die Zusammensetzung, Kristallstruktur und Mikrostruktur der hergestellten Keramiken zu verifizieren. Das Polarisationsverhalten mit sich änderten elektrischem Feld wurde untersucht, um die (anti)ferroelektrischen Eigenschaften zu qualifizieren. Die elektronische Struktur inklusive Bandlücke und energetischen Fallen, welche das Ferminiveau begrenzen können, wurden mittels Röntgenphotoelektronenspektroskopiemessungen (XPS) in Verbindung mit oxidierenden und reduzierenden Behandlungen untersucht. Die Arten und Mechanismen des Ladungstransports, die Art der Leitfähigkeit und mögliche präsente Defekte wurden mittels feld-, temperatur-, atmosphären- und zeitabhängiger Leitfähigkeitsmessungen analysiert. Diese Experimente wurden mit temperatur- und feldabhängigen Leitfähigkeitsmessung während der Aufnahme von XP-Spektren komplementiert. Mit diesen Ergebnissen wurde ein erstes Modell postuliert, das die elektronische Struktur von Natrium- und Kaliumniobat erklärt. Zudem wurden nächste Schritte zur Verifizierung des Modells aufgeführt. Dementsprechend schafft diese Arbeit die Basis für weitere Untersuchungen zur Analyse der Verbindung zwischen elektronischer Struktur und antiferroelektrischen Eigenschaften, um neue, günstige und nicht giftige antiferroelektrische Materialzusammensetzungen vorherzusagen.

Abstract

High-energy density capacitors are an important component of electrical power converters, which are required to invert AC- to DC-signals for, e.g. charging the batteries of electric vehicles or to feed the wind power of wind turbines into our electric grid. Antiferroelectric materials are promising candidates for such high-energy density capacitors because of their higher energy densities compared to dielectric or ferroelectric capacitors and their higher power densities in comparison to electrochemical capacitors. However, the only suitable antiferroelectric materials for these applications so far, are lead zirconate titanate (PZT) based materials. During production and recycling of these materials toxic lead-containing species are formed. In contrast, non-toxic alternatives such as silver (AN) or sodium niobate (NN) are very expensive. Hence, the demand of new non-toxic but cheap antiferroelectric materials is high.

In this work, the electronic structure of the antiferroelectric material sodium niobate is investigated. For comparison, the ferroelectric material potassium niobate (KN) is analyzed to identify possible differences, which are responsible for the (anti)ferroelectric properties of these two systems. Scanning electron microscopy (SEM) and x-ray diffraction (XRD) are used to verify the composition, crystal structure, and microstructure of the prepared ceramics. The polarization behavior with changing electric fields is examined to qualify the (anti)ferroelectric properties. In order to analyze the electronic structure including band gap and trapping states, which can confine the Fermi level, x-ray photoelectron spectroscopy (XPS) measurements in combination with different oxidizing and reducing treatments are conducted. The charge transport species and mechanisms, type of conductivity, and possible defect species present in the samples are analyzed by electric field, temperature, atmosphere, and time dependent conductivity measurements. These experiments are complemented with temperature and field dependent conductivity measurements while recording XP-spectra.
With these results a first model explaining the electronic structures of sodium and potassium niobate is postulated. Next steps to verify this model are proposed. Therefore, this work provides the basis for further investigations examining the connection between the electronic structure and the antiferroelectric properties to predict new, cheap, and non-toxic antiferroelectric materials.

Contents

1. Motivation

The energy consumption of today's society is continuously increasing. As around $80\,\%$ [1, 2] of this energy is coming from gas, oil, and coal, the CO_2 emission has reached a critical level over the last decades. The world energy consumption and the total CO_2 emission is shown in the first box on the left side of Fig. 1.1. Further increasing CO_2 emission is predicted to raise the average temperature of our planet over $2\,^{\circ}C$ [1, 3]. This would have a drastic impact on life on earth due to environmental changes that could make large parts of the continents uninhabitable. In order to reduce the total CO_2 emission renewable energies, e.g. wind turbines and solar cells, are needed to counteract climate change.

In case of wind turbines, the wind power must be converted into electric power in order to feed it into the electricity grid. However, the generated electric power depends on the wind power and speed, which can result in voltage and frequency spikes. Therefore, the AC-voltage produced by the wind turbines cannot be directly fed in our electricity grid. In this case, an AC/DC/AC-converter is needed to maintain the frequency of the AC-voltage in the grid [4].

In addition, a lot of electric energy will be needed in the transport sector in future. The batteries used in electric vehicles work with DC-voltages. Consequently, the AC-voltage from our grids must be transformed to a DC-signal to charge these batteries, what requires AC/DC/DC-converters. Furthermore, DC/AC-converters are needed to invert the DC-voltage from the battery to a three-phase AC-power for the traction motors during acceleration. In turn, an AC/DC-converter can transform the AC-power from the traction motors back to a DC-signal during braking to recharge the battery of the electric vehicle. During all these charge and discharge cycles voltage spikes can appear, which can damage the battery [5, 6].

In order to prevent such voltage spikes in electric power generators, so-called DC-links are used in the power converters [4, 7]. The DC-links consist of capacitors, which balance the power difference between source and load and reduce the voltage fluctuations. There are different material classes, which can be used as capacitors: aluminum electrolytic capacitors (Al-Caps), metallized polypropylene film capacitors (MPPF-Caps), and high capacitance multi-layer ceramic capacitors (MLC-Caps). Depending on the application and the environmental conditions the right capacitors with the appropriate parameters must be chosen [7].

So-called antiferroelectric (AFE) ceramic materials can be useful as high-energy density capacitors in

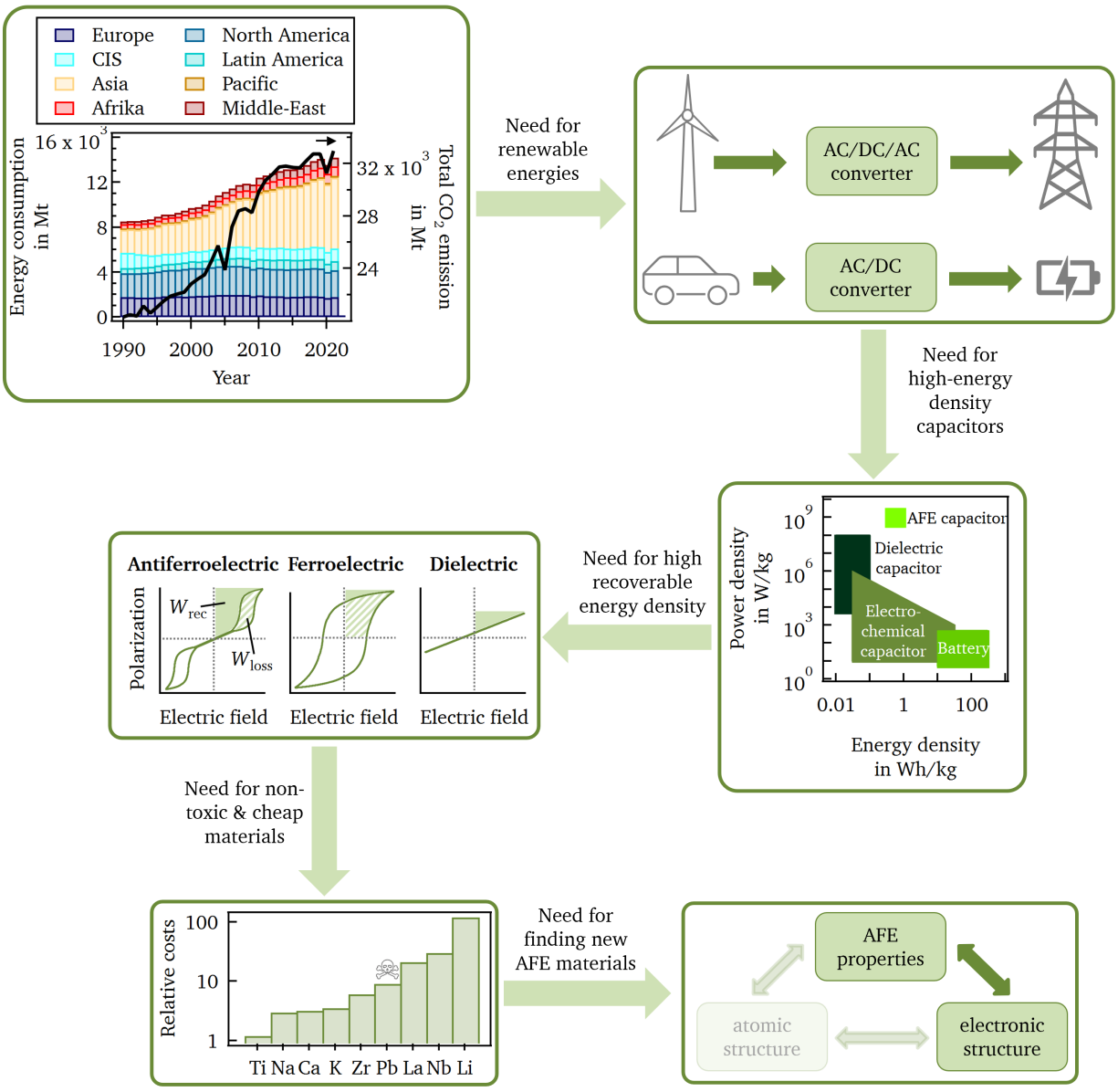

Figure 1.1.: Overview of the motivational aim to find new AFE material systems.

DC-links. In general, the advantage of MLC-Caps over Al- and MPPF-Caps is the reduced size, larger frequency range, and the possibility of higher operating temperatures. However, the dielectric or ferroelectric ceramics used so far suffer from low energy densities [7]. In contrast, AFE capacitors can reach higher energy densities than dielectric capacitors and higher power densities than electrochemical capacitors (e.g. Al-Caps) as shown in the second box on the right side of Fig. 1.1 [8]. Compared to ferroelectrics (FE), which suffer from high energy losses W_{loss} in form of heat indicated by the hysteresis loop, AFEs exhibit a higher recoverable energy W_{rec} [8–11]. The second box on

the left side in Fig. 1.1 illustrates the difference in the polarization-electric-field-behavior between a dielectric, a ferroelectric, and an antiferroelectric material. It is clearly shown that AFEs have a higher recoverable energy (green area) and lower energy losses (hatched area) compared to FEs.
AFE high-energy density capacitors in form of MLC-caps have already been produced by TDK Electronics under the product name CeraLink® [12]. They are based on Pb-containing materials, e.g. Pb(Zr,Sn,Ti)O_3 (PZST) [12]. However, during production toxic species such as PbO or Pb are used or formed [13], which requires more careful handling and safety regulations. In addition, during recycling or in case Pb-containing electronic devices get in contact with the environment, the long term effects on the environment are unclear. Hence, legal restrictions [14] have been put in place to remove toxic elements such as Pb from electronic devices. Therefore, research on non-toxic AFE materials is important.

At the moment, the only non-toxic AFE ceramic materials are $NaNbO_3$ and $AgNbO_3$. However, niobium oxide, which is one precursor of these two materials, is very expensive in comparison to other precursor compounds. The graph in the third box on the left side of Fig. 1.1 compares the relative costs of precursors in form of oxides or carbonates needed for the production of AFEs normalized on the price of TiO_2 [15]. Therefore, the goal is to find new cheap and non-toxic alternatives. Instead of using trial and error methods by preparing a huge variety of different material systems as it is done in practice so far, it would be preferable to find models that can predict new AFE materials. For this purpose, it is important to investigate and understand the structural origin of the AFE properties. Therefore, the aim of the FLAME project, in the context of which this work is carried out, is to better understand the AFE properties by finding connections between them and the atomic and electronic structure. Such fundamental knowledge can potentially lay the foundation for models predicting new AFE material systems.

In this work, the electronic structure of $NaNbO_3$ is investigated as part of the FLAME project. For this purpose, undoped and donor doped $NaNbO_3$ is prepared. For comparison, undoped $KNbO_3$, which is a ferroelectric material, is produced as reference to distinguish potential differences between antiferroelectric and ferroelectric materials. $NaNbO_3$ and $KNbO_3$ differ only in their A-site ions sodium and potassium, which are both alkalines. Hence, it is interesting to understand how the presence of either sodium or potassium changes the atomic and electronic structure that potentially influences the AFE and FE properties.
Another interesting aspect of $NaNbO_3$ and $KNbO_3$ is that they are the parent phases of $K_{0.5}Na_{0.5}NbO_3$, which is studied intensively as a lead free alternative for piezoceramics employed in a lot of applications such as actuators, sensors, and transducer devices [16]. However, hygroscopicity of the precursors Na_2CO_3 and K_2CO_3 requires a very careful processing sequence with a lot of drying steps and organic liquids, e.g. iso-propanol or acetone, as solvent during ball milling instead of water-based solvents [15, 17]. Sintering of ceramics must be done at high temperatures above $1000\,°C$ for a good densification. The relatively low melting temperature of $NaNbO_3$ and $KNbO_3$ of $1422\,°C$ [18] and $1100\,°C$ [18],

respectively, and the high volatility of the alkaline atoms result in a low density and stability as well as high leakage currents of the prepared ceramics [16, 17]. These are the main obstacles, which must be faced during preparation of $K_{0.5}Na_{0.5}NbO_3$-based systems. A lot of additives are analyzed in literature, which might address these problems [17, 19]. However, the real origin of the leakage currents caused by, e.g. high ionic conductivity of alkaline and/or oxygen vacancies or high electronic conductivity of the grain boundaries due to vacancy accumulation, has not been identified so far. In addition, the connection between electronic structure and electrical conductivity, and how additives influence this relation is incompletely understood. Hence, it is interesting to gain more insights into the electronic structure of $NaNbO_3$ and $KNbO_3$ to pinpoint, what is responsible for the high leakage currents and how it can be avoided.

For these purposes, undoped and donor doped $NaNbO_3$ with either calcium or strontium as well as undoped $KNbO_3$ ceramics are prepared. First, the usability of the samples for the investigation and comparison of the electronic structure of $NaNbO_3$ and $KNbO_3$ is validated. The correct composition is verified by means of scanning electron microscopy (SEM), x-ray diffraction (XRD), and x-ray photoelectron spectroscopy (XPS) analyses. In addition, the presence of secondary phases, which would lead to a non-stoichiometry of the samples' composition, is evaluated with SEM and XRD. Surface segregation is examined by XPS.
The microstructure can influence the electronic properties significantly, e.g. the resistance degradation behavior [20], the varistor effect [21], the positive temperature coefficient of resistance (PTCR) effect [22, 23], or the preferred stabilization of a ferroelectric versus an antiferroelectric phase [24]. Hence, knowledge about the morphology of the samples such as the size, shape, and distribution of the grains and pores is of great importance. SEM is utilized within this work to characterize the morphology of the $NaNbO_3$- and $KNbO_3$-based ceramic pellets.
Dopants and defects as vacancies in combination with grain and domain boundaries can modify the polarization behavior [25–27]. Consequently, polarization curves in dependence of the electric field are conducted. The defect distribution can change with time and can have an additional significant effect on the polarization, which is known as aging [28–31]. Therefore, samples in an aged and unaged state are examined. This can give information about possible present defects and their interactions.
Not only the polarization behavior but also the temperature and frequency dependent permittivity is affected by dopants and defects. For example, dopants can lead to a shift of the phase transition temperatures [17, 32, 33]. Furthermore, dopants and vacancies can modify the electronic and/or ionic conductivity, which can have an impact on the dielectric losses due to higher or lower leakage currents [33–36]. Hence, the permittivity behavior in dependence of temperature and frequency of the different sample types are analyzed.
From an electronic structural point of view, dopants and defects, such as vacancies but also polarons, can introduce energy levels into the band gap of semiconductor materials. On the one hand, these

defect levels can increase the electronic and/or ionic charge carriers depending on the Fermi level position, which can raise the electrical conductivity. For example, in $BaTiO_3$ La-doping up to 0.1 mol % helps to increase the conductivity due to a higher electron concentration [37, 38]. However, from a doping concentration of 0.1 mol % on the conductivity is again decreasing because of a changed compensation effect from electronic to ionic compensation [37, 38]. On the other hand, dopants and defects can lead to a Fermi level confinement, which affects the electrical conductivity as, e.g. in $BiFeO_3$ [39, 40]. Polarons coupled to the bismuth and iron host atoms limit the maximal accessible Fermi level and prevent effective n-type doping. Therefore, it is important to gain knowledge about all present defect levels within the band gap of $NaNbO_3$ and $KNbO_3$ because they are mainly influencing the electronic structure. XPS measurements combined with oxidizing and reducing surface treatments are conducted to reveal possible defect states present in the band gap.

In order to understand the nature of AFEs in more detail and how leakage currents in $K_{0.5}Na_{0.5}NbO_3$-based materials can be suppressed, it is important to learn more about the main electrical transport mechanisms and the main conducting species. Hence, DC-conductivity experiments in different atmospheres and temperatures are performed to reveal n- or p-type conduction behaviors [41, 42]. In addition, with a DC-signal only the charge carriers which are transported by the electrodes can be probed. Platinum is commonly used as an electrode for ferroelectric capacitors [43]. By using an electron conductor as the contact material the electronic conductivity can be decoupled from the ionic conductivity and analyzed. For probing the total conductivity of a material, an AC-signal can be used. By means of impedance spectroscopy different transport mechanisms can be untangled due to their different frequency response. [44–47].

Harsh conditions such as high temperatures and electric fields can modify the electrical conduction behavior and lead to resistance degradation effects. For example, in $SrTiO_3$ combination of high electric fields and temperatures lead to a change in the oxygen vacancy concentration near the anode and cathode. This, in turn, affects the concentration of the free charge carriers and increases the conductivity on both sides [20, 48, 49]. Therefore, investigating degradation effects in $NaNbO_3$ and $KNbO_3$ will help to better understand the important transport mechanisms and mobile species. For this purpose, ex situ resistance degradation experiments are performed. Moreover, in situ measurements in the XP-spectrometer are conducted to identify the type of species causing the resistance degradation.

2. Basics

2.1. Ferroelectrics and antiferroelectrics

The majority of information this chapter is based on [50, 51].
In order to define the two terms *ferroelectrics* and *antiferroelectrics* the three following questions are analyzed:

1. What is a ferroelectric or antiferroelectric material?
2. What are characteristics of a ferroelectric or antiferroelectric material?
3. How can we identify ferroelectric or antiferroelectric materials?

Here, the basic definition of ferroelectrics and antiferroelectrics including crystal structure and electrical properties is elucidated.

2.1.1. What is a ferroelectric or antiferroelectric material?

Considering polarization, materials can be divided in four different classes.

1. nonpolar materials
2. polar materials
3. dipolar materials
4. (anti)ferroelectric materials

In a *nonpolar material* the electron cloud can be shifted by exposing it to an electric field. This phenomena occurs in all materials, however, it is the only modification appearing in nonpolar materials, such as elemental materials, upon an electric field. In addition, the ions of a *polar material* can be elastically displaced by an electric field. Hence, polar materials exhibit besides electronic polarization, ionic polarization. Ionic crystals, e.g. alkali halides and some oxides, are examples for polar materials. *Dipolar materials* show electronic, ionic, and orientational polarization meaning that these materials have permanent dipole moments without an applied external electric field. These

permanent dipoles are randomly oriented counterbalancing each other resulting in a net polarization of zero. However, if an electric field is applied, they can be oriented along the direction of this field. Removal of the field causes randomly distributed dipoles and a zero net polarization again. Most dipolar materials are liquids or gases consisting of molecules in which negative (mostly electrons) and positive charge concentrations (mostly nuclei) are not coinciding. As soon as the solidification temperature is reached, the permanent dipoles are fixed and cannot contribute to the orientational polarization anymore.

Nonpolar, polar, and dipolar materials can be summarized in the class of *paraelectric materials*. In contrast, ferroelectrics or antiferroelectrics posses a reversible spontaneous polarization. The origin lays in their electrical ordering of the crystalline structure implying that only crystalline materials with a non-centrosymmetric structure can exhibit spontaneous polarization. In ferroelectrics, these spontaneous dipole moments are aligned in one direction within one domain. Hence, a domain is a group of dipole moments pointing in one direction. On the contrary, the domains of a ferroelectric material are randomly oriented counterbalancing each other resulting in a net polarization of zero. When these materials are introduced into an electric field, the domains can align along the direction of the electric field. In contrast to permanent dipole moments, the alignment of domains does not completely vanish after removing the electric field resulting in a remanent polarization.

According to the Kittel model [52], the difference between ferroelectric (FE) and antiferroelectric (AFE) materials is that antiferroelectrics consists of pairs of dipole moments, which are aligned anti-parallel while ferroelectrics have only single dipole moments pointing in one direction. These pairs of anti-parallel dipole moments can form domains as well. Within one domain all anti-parallel dipole pairs are pointing in one direction. Antiferroelectrics can be transferred into a ferroelectric state by applying a high electric field. However, due to their anti-parallel nature, no remanent polarization is measured after removal of the electric field as it is the case for a ferroelectric material.

The most commonly used (anti)ferroelectric materials have a perovskite structure, which is why in the following only perovskite materials are examined. Oxide perovskites have a ABO_3 composition. The perovskite structure is illustrated in Fig. 2.1a). The B-site cation is octahedrally coordinated by oxygen atoms while the A-site cation is 12-fold coordinated sitting on the corners of the unit cell. Goldschmidt [53] derived a factor which describes the structural stability of the perovskite structure, the so-called Goldschmidt tolerance factor *t*.

$$t = \frac{R_\mathrm{A} + R_\mathrm{O}}{\sqrt{2}(R_\mathrm{B} + R_\mathrm{O})} \tag{2.1}$$

R_A, R_B, and R_O are the ionic radii of A, B, and the oxygen atoms. According to Goldschmidt the perovskite structure is only stable for a tolerance factor between 0.8 and 1.0. Nowadays, perovskite materials stable up to $t = 1.06$ are known [11, 26]. The deviations from a perfect perovskite structure with $t = 1.0$ result often from distortions and tilts of the oxygen octahedra.

2.1.2. What are characteristics of a ferroelectric or antiferroelectric material?

As mentioned above, (anti)ferroelectrics posses an electrical ordering of their spontaneous dipole moments according to the Kittel model [52]. Ferroelectrics are non-centrosymmetric and have a polar axis within their unit cell. This is shown exemplary in Fig. 2.1a) on a tetragonal perovskite unit cell. In contrast, antiferroelectrics exhibit a symmetric unit cell as the anti-parallel dipole moments are centrosymmetric, which is illustrated in Fig. 2.1b) on an orthorhombic perovskite unit cell. However, they still have a polar axis.
These dipole moments can align with each other forming regions with a spontaneous polarization in one direction, which are so-called domains. Ferroelectric domains have a net spontaneous polarization in one direction while antiferroelectric domains exhibit no net polarization. In the virgin state, the domains are oriented randomly and no net polarization exists (point A in Fig. 2.1c) and d)). Applying an electric field orientates the domains along the field direction. In case of a ferroelectric material, a net maximum polarization P_{max} is obtained at point B. When the electric field is decreased to zero the domains remain oriented and a remanent polarization P_{r} persists (point C). Applying the field in the other direction switches the domains when a certain critical field, the so-called coercive field E_{coer}, is applied until the maximum polarization is reached again (point D). Removing the electric field and ramping it up in the positive field direction results in a polarization-electric-field-hysteresis shown in Fig. 2.1c). For a single crystal the hysteresis would result in an almost perfect rectangular shape whereas for polycrystals it is more round because some domains are hampered due to internal stresses and defects.
Antiferroelectric domains align as well along an applied electric field. Nevertheless, the antiparallel orientation of the dipole moments results in a zero net polarization. However, the antiferroelectric domains can be transferred into a ferroelectric state by applying a high enough electric field E_{AF}. With further increasing and decreasing electric field a ferroelectric hysteresis develops. At the backward switching field E_{FA} the domains are transferred back to the antiferroelectric state. For an ideal material no net polarization should be measured in the antiferroelectric state (point C). However, ceramics, which are mainly investigated in this work, are polycrystals and are influenced by stresses, grain boundaries, and defects. This causes a small non-zero remnant polarization. Applying the same electric field in the other direction results in the complete double hysteresis loop illustrated in Fig. 2.1d).

Examining the spontaneous polarization as a function of temperature, displayed in Fig. 2.1e), shows that it is only measurable until a critical temperature T_{C}, which is the so-called Curie temperature. Below this temperature (anti)ferroelectrics exhibit a spontaneous polarization while above T_{C} the spontaneous polarization vanishes. This can be explained by the phase transition to a paraelectric (PE) state. For most perovskite materials, both ferroelectrics and antiferroelectrics, this transition is a first order transition meaning that the change in polarization is discontinuous along with an

entropy and latent heat change. The latent heat has a supercooling or superheating effect when the temperature is decreased or increased close to the phase transition. Therefore, a small temperature hysteresis is observed, which is illustrated in Fig. 2.1e).

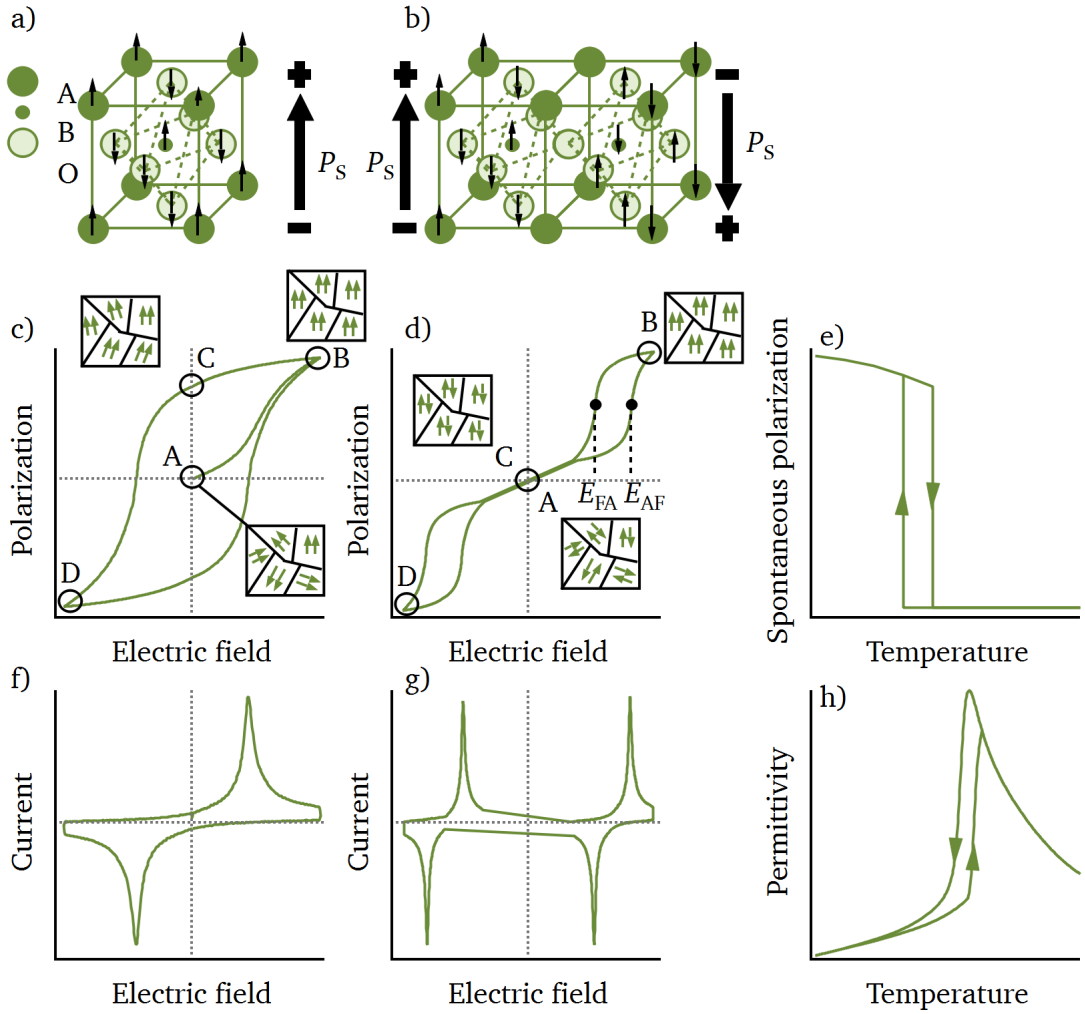

Figure 2.1.: Crystal structure with spontaneous polarization P_s in a) and b), polarization and current hysteresis in dependence of the electric field in c) and d), and f) and g) for a ferroelectric and an antiferroelectric material, respectively. Within the polarization hysteresis loops the domain structure is illustrated for certain states. In e) and h) the spontaneous polarization and permittivity are shown as functions of the temperature. The arrows indicate the heating and cooling direction resulting in a temperature hysteresis.

In general, the polarization P is connected with the electric field E by the electric susceptibility χ, which is a measure of how easily a material can be polarized by an electric field:

$$P = \epsilon_0 \cdot \chi \cdot E \tag{2.2}$$

ϵ_0 is the vacuum permittivity. The susceptibility is in turn related to the materials permittivity ϵ_r by $\chi = \epsilon_\mathrm{r} - 1$. Therefore, the polarization can be written as:

$$P = \epsilon_0 \cdot (\epsilon_\mathrm{r} - 1) \cdot E \tag{2.3}$$

Hence, the permittivity is as well changing when a (anti)ferroelectric material undergoes a phase transition to a paraelectric state. Figure 2.1h) illustrates the permittivity of a (anti)ferroelectric as a function of temperature. Right before the phase transition the permittivity is increasing and exhibits a discontinuous behavior at the transition temperature. In the paraelectric state above T_C, the permittivity behavior can be expressed by the Curie-Weiss law:

$$\epsilon_\mathrm{r} = \frac{C}{T - T_\mathrm{C}} \tag{2.4}$$

C is a constant and T_C is the Curie temperature. Similar to the polarization behavior, the permittivity exhibits a temperature hysteresis shown in Fig. 2.1h) because of the latent heat change at the transition point.

2.1.3. How can we identify ferroelectric or antiferroelectric materials?

Ferroelectric and antiferroelectric materials can be identified by measuring their characteristics introduced in the previous section. A relative easy and direct method is the examination of polarization by varying the electric field. The polarization of a material is compensated by charges. Hence, aligning the spontaneous polarization along the direction of an electric field is accompanied by charging the material. Therefore, the polarization can be defined by:

$$P = \frac{Q}{A} = \frac{1}{A} \int_0^t I \mathrm{d}t \tag{2.5}$$

Consequently, the polarization can be obtained by measuring the current I by knowing the samples area A. The recorded current during polarization of a ferroelectric and antiferroelectric material is shown in Fig. 2.1f) and g), respectively. The current exhibits two distinct peaks for a ferroelectric material, one at positive and one at negative fields, which result from the switching of the polarization when the coercive field is reached. In contrast, an antiferroelectric material shows four current peaks which can be related to the forward and backward switching between AFE and FE state in positive and negative field direction. Hence, (anti)ferroelectrics can be identified by their characteristic current and polarization hysteresis behavior by changing the electric field. However, care must be

taken by analyzing them as defects can influence the switching behavior. As an example, for aged ferroelectrics a pinched double polarization hysteresis with four current peaks can be observed and might be mistaken with an antiferroelectric material [54]. The influence of dopants and defects on the materials' characteristics are examined in more detail in Sections 2.5 and 2.6.

Besides measuring the polarization in dependence of the electric field, the temperature dependent permittivity can be analyzed. By investigating a large temperature range phase transitions including FE-to-PE or AFE-to-PE transitions can be examined. This can be done by measuring the capacitance C of a material, which is directly connected to the permittivity:

$$C = \epsilon_0 \cdot \epsilon_\mathrm{r} \cdot \frac{A}{d} \tag{2.6}$$

A and d are area and thickness of the sample under investigation.

In addition to this experimental characteristics, the tolerance factor combined with the averaged electronegativity difference of a perovskite material can give an indication if a material tends to be ferroelectric or antiferroelectric as found by Halliyal and Shrout [55]. Shimizu et al. [26] illustrated the tolerance factor versus averaged electronegativity difference of different perovskite materials (Fig. 2.2), which shows that materials with $t > 1$ prefer the ferroelectric structure whereas those with $t < 1$ tend to stabilize the antiferroelectric structure. This tendency can be used as a guidance for material preparation for finding new antiferroelectric materials, however, it should be taken with caution as this is not an explanation for the origin of antiferroelectricity. Hence, there might exist exceptions to this rule.

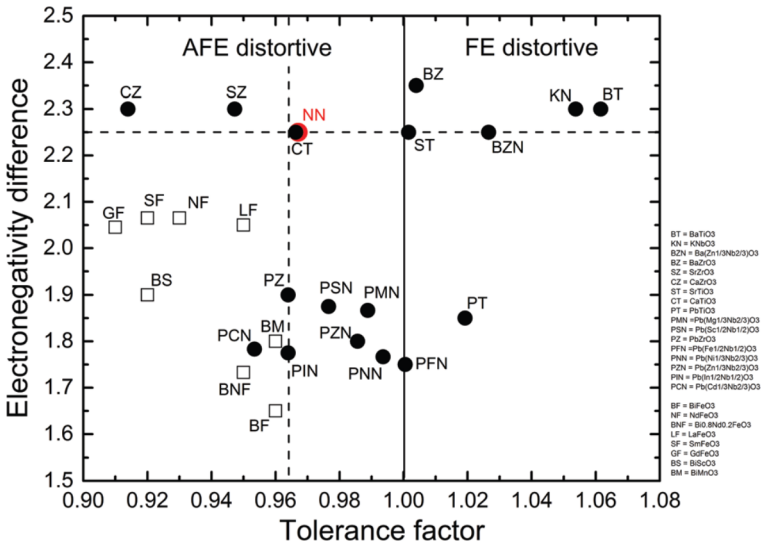

Figure 2.2.: Averaged electronegativity difference versus tolerance factor for different perovskite materials [26].

2.2. Band structure of semiconductor materials

The theoretical principles of the semiconductor band structure can be found in text books about solid state physics like *Physics of Semiconductor Devices* by S. M. Sze and K. K. Ng [56] or *Dielectric Phenomena in Solids* by K. C. Kao [51]. The band structure of a material describes the relation between the energy E and the momentum k within the reciprocal space. It can be obtained by solving the Schrödinger equation, which results for a semiconductor material in broad energy bands separated by an energy gap. Within this gap no energy states exist which can be occupied by an electron. The energy region below the energy gap is called valence band while the one above it is called conduction band. Usually the valence band is occupied by electrons whereas the conduction band is built up by empty states. Close to the band edges the energy bands can be described by a parabolic function:

$$E(k) = \pm\frac{\hbar^2 k^2}{2m^*} \tag{2.7}$$

Here, $\hbar$ is the Planck constant and m^* is the effective mass. Therefore, the curvature of an energy band is given by the inverse of the effective mass of the charge carriers. The energy gap or band gap E_G is defined as the distance between valence band maximum (VBM) and conduction band minimum (CBM). Depending on the position of these in the k-space, a semiconductor has a direct or indirect band gap. If the VBM and CBM have the same location, the band gap is direct. In contrast, an indirect energy gap is established when VBM and CBM are positioned at different k-vectors. Figure 2.3 illustrates the difference between a direct and an indirect semiconductor. In order to excite an electron from the valence to the conduction band, only the energy difference between VBM and CBM has to be overcome in case of a direct band gap. For an indirect semiconductor some momentum must be transferred additionally to the energy.

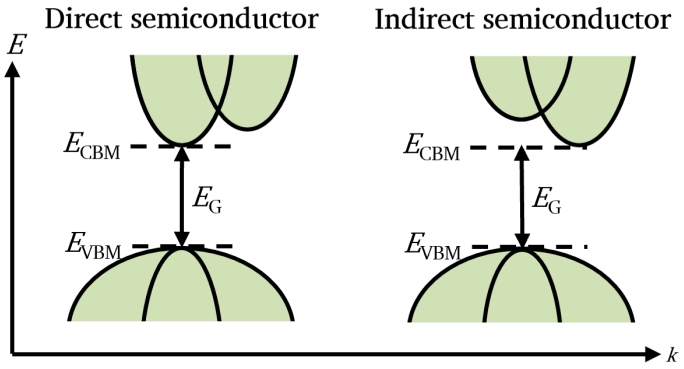

Figure 2.3.: Band structure of a direct and indirect semiconductor.

The number of electrons occupying the conduction band can be calculated by the following equation:

$$n = \int_{E_\mathrm{CBM}}^{\infty} N(E)F(E)dE \tag{2.8}$$

E_CBM is the position of the CBM in energy, $N(E)$ is the density of states, and $F(E)$ is the occupation of the energy states. The occupancy can be derived by the Fermi-Dirac distribution function:

$$F(E) = \frac{1}{1 + \exp\left[\frac{E-E_\mathrm{F}}{k_\mathrm{B}T}\right]} \tag{2.9}$$

In a nondegenerate semiconductor, meaning that the doping or impurity concentration is much smaller than N, the number of positive and negative intrinsic charge carriers is the same. By thermal excitation electrons are excited to the conduction band leaving an equal amount of holes in the valence band. Recombination of these electrons and holes counterbalances the thermal excitation and transfers the system into an equilibrium state. Therefore, the Fermi level is located approximately in the middle of the band gap and the electron n and hole concentration p can be written as follows:

$$n = N_{\mathrm{CB}} \exp\left(-\frac{E_{\mathrm{CBM}} - E_{\mathrm{F}}}{k_{\mathrm{B}} T}\right) \tag{2.10}$$

$$p = N_{\mathrm{VB}} \exp\left(-\frac{E_{\mathrm{F}} - E_{\mathrm{VBM}}}{k_{\mathrm{B}} T}\right) \tag{2.11}$$

$$n = p = n_i = \sqrt{N_{\mathrm{CB}} N_{\mathrm{VB}}} \exp\left(-\frac{E_{\mathrm{G}}}{2 k_{\mathrm{B}} T}\right) \tag{2.12}$$

The density of states for the conduction and valence band are N_{CB} and N_{VB} and the energy of CBM and VBM are given by E_{CBM} and E_{VBM}. n_i is the intrinsic charge carrier concentration. The band structure of an intrinsic semiconductor with its almost mid-gap E_{F} position is illustrated in Fig. 2.4.

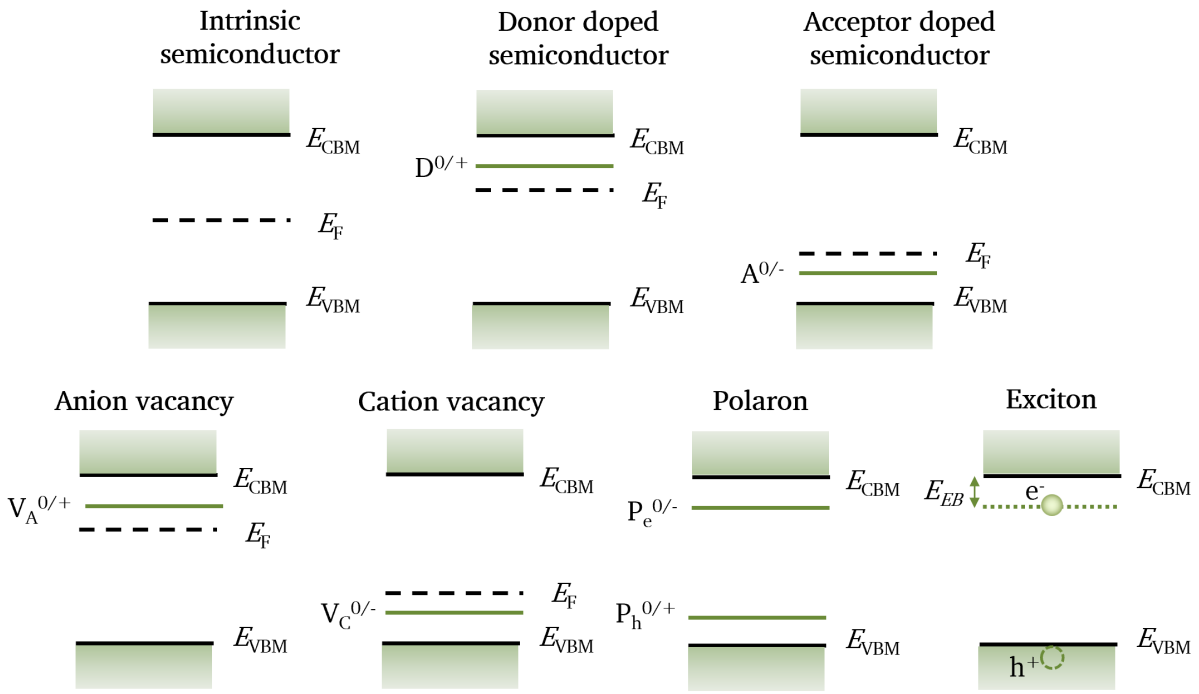

Figure 2.4.: Top: Band structure of an intrinsic, donor and acceptor doped semiconductor with Fermi level E_{F}, donor and acceptor level $\mathrm{D}^{0/+}$ and $\mathrm{A}^{0/-}$. Bottom: Including anion $\mathrm{V}_{\mathrm{A}}^{0/+}$ and cation vacancy level $\mathrm{V}_{\mathrm{C}}^{0/-}$, electron $\mathrm{P}_{\mathrm{e}}^{0/-}$ and hole polarons $\mathrm{P}_{\mathrm{h}}^{0/+}$ as well as an exciton formation.

2.3. Defects

Real materials have always defects, which influence the material properties or even dominate some specific properties. In general, defects can be categorized in point defects, line defects, planar defects, and bulk defects [57]. Examples of some of these defects are illustrated in Fig. 2.5 as a visual overview. As point defects are the major discussed defect type in this thesis, only a rough description of planar, line, and bulk defects are given in this section.

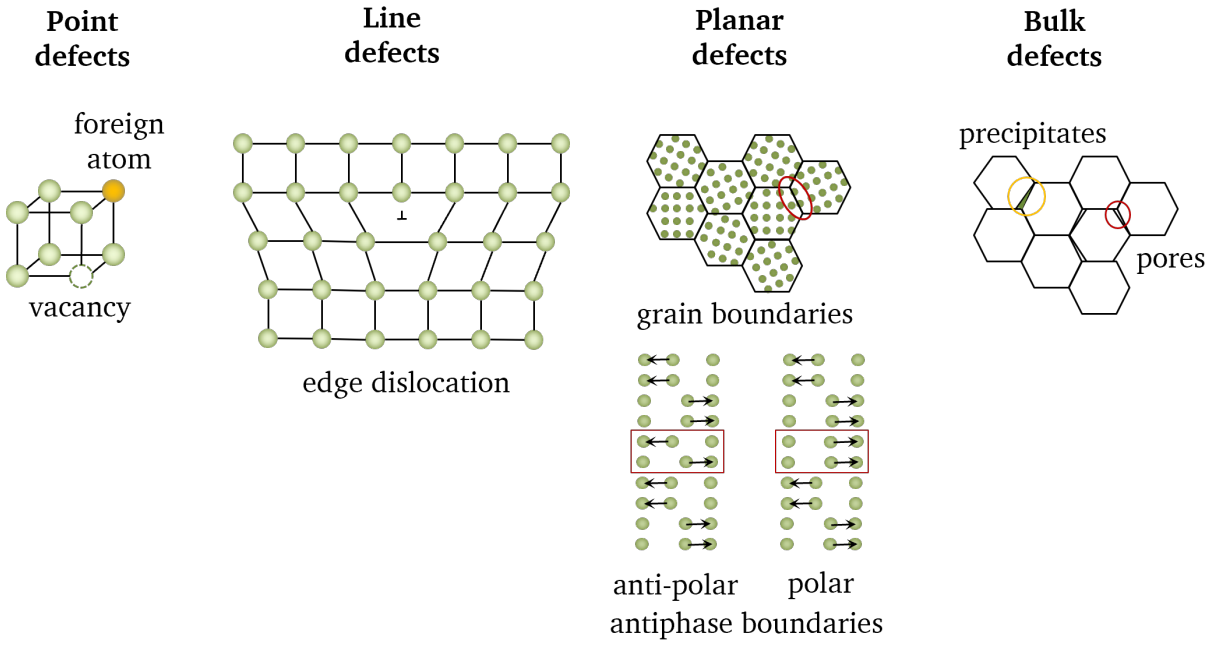

Figure 2.5.: Possible point, line, planar, and bulk defects in polycrystalline materials.

2.3.1. Point defects

Point defects are zero dimensional defects. Examples for point defects are foreign atoms, vacancies, interstitials, antisites, [57, 58], polarons [59–62], excitons [51, 63, 64], and F centers [65]. The main point defects present in oxide perovskites are vacancies, foreign atoms, polarons, and excitons, which is why in the following only these four defect types are explained in more detail. In the end of this section, charge neutrality including all of these point defect types, self-compensation, and Fermi level confinement are discussed.

Foreign atoms

Foreign atoms can be introduced into the materials lattice either intentionally or non-intentionally. Non-intentional foreign atoms are impurities, which are incorporated during sample preparation and/or sample post treatment. In contrast, foreign atoms can also be included intentionally in order to tune the materials properties and go usually on a lattice site in perovskite materials. If the foreign atom has the same valency as the host atom, it is an isovalent substitute. With isovalent substitution the host atom can often be replaced up to $100\,\%$ as in, e.g. (Ba,Sr)TiO_3 [32], which is then called a solid-solution. In case the foreign atom exhibits not the same valency has the host atom, it is a heterovalent substitute and called a dopant. Here, the solubility of the dopants depends on the charge carrier compensation mechanism. This is the reason why in the most cases no $100\,\%$ solubility is reached [66]. Dopants with a higher valency act as donors as they add negative charges to the system while dopants with a lower valency are acceptors because they can capture negative charges, hence, introducing positive charges into the system.
Doping or isovalent substitution with a foreign atom leads to a change in the tolerance factor, hence, the structure can be modified quite significantly. This can have a big impact on properties, e.g. a significant change in the Curie temperature T_C. Co-doping of $2\,$at$\,\%$ calcium on the A- and $2\,$at$\,\%$ zirconium on the B-site in the $NaNbO_3$ lattice leads to a decrease of T_C of about $30\,°$C [26]. However, doping with calcium only can already lower T_C by about $25\,°$C when increasing the doping concentration from $1\,$at$\,\%$ to $4\,$at$\,\%$ [33].

As a donor provides an electron to the conduction band, donor doping increases the Fermi level in a semiconductor. In contrast, an acceptor captures an electron leaving a hole in the valence band, which lowers E_F. Both situations are shown in Fig. 2.4. In addition, a doping level is introduced for both, donors and acceptors. Consequently, doping changes the E_F position. However, the charge state of the dopant depends as well on the E_F location, which can be changed by e.g. oxidizing or reducing conditions. If E_F is higher than the donor level, the donor is occupied and, therefore, neural (D^0). In case of E_F being lower than the donor level, the donor is unoccupied and exhibits a positive charge (D^+). Similar applies for an acceptor. With E_F above and below the acceptor level the acceptor is negatively charged (A^-) and neutral (A^0), respectively. Hence, the doping levels $D^{0/+}$ and $A^{0/-}$ are also called charge transition levels.

Vacancies

In materials crystallizing in the ABO_3 perovskite structure oxygen vacancies are the most common type of vacancies. Oxygen has a valency of 2- in the perovskite lattice. Hence, removing an oxygen atom from the crystal lattice, leaves behind a doubly positively charged oxygen vacancy, which can be written in the Kröger-Vink-notation as $V_O^{\cdot\cdot}$ [67]. In perovskite materials vacancies on the A- or

B-site can also be formed, e.g. in $BaTiO_3$ [68, 69]. These vacancies are usually negatively charged as A- and B-site atoms have positive valencies. In $BaTiO_3$, for example, removing Ba^{2+} or Ti^{4+} from the lattice creates a barium (V''_{Ba}) or titanium vacancy (V''''_{Ti}).

Vacancies can either compensate foreign atoms, which act as donors or acceptors, or behave as a donor or acceptor themselves. The effect of compensating a foreign atom, which is called as well self-compensation or ionic compensation is explained in more detail in Section 2.3.1.
Anion vacancies, e.g. oxygen vacancies, can act as donors providing electrons to the material system, while cation vacancies behave as acceptors capturing electrons. Both situations are illustrated in Fig. 2.4. Similar to foreign atoms functioning as dopants, a doping level of the vacancies is introduced within the band gap. Hence, a variation in the anion and cation concentration changes the E_F position. The charge state of the vacancy depends again on the E_F location. Hence, the doping levels of the vacancies $V_A^{0/+}$ and $V_C^{0/-}$ are called as well charge transition levels. Depending on the valency of the removed element, the vacancy can exhibit more than one charge transition level. For example an oxygen vacancy can transfer from a doubly to a singly positive charged state ($V_O^{\cdot\cdot}/V_O^{\cdot}$) and even further to a neutral state ($V_O^{\cdot}/V_O^0$) [70].

Defect complexes

Defect complexes are associates of two or more charged defects. For example, oxygen vacancies can couple with negatively charged A- or B-site vacancies or negatively charged acceptors [28, 29, 71, 72]. These complexes can, in turn, be charged as well or can be neutral, e.g. for Fe-doped $BaTiO_3$ $(V'_{Fe}\text{-}V_O^{\cdot\cdot})^{\cdot}$ [73] or $(V'_{Fe}\text{-}V_O^{\cdot\cdot}\text{-}V'_{Fe})^x$ [28]. The coupling of such defects influences the behavior of the individual defects itself within the crystal lattice.

Polarons

In general, polarons are charge carriers trapped in a potential well, which results in a distortion of the ion lattice. Therefore, these localized electrons or holes are coupling with phonons. Figure 2.6 shows the potential well of a delocalized conduction electron and the one of a polaron, which is lower in energy. In order to form a polaron, the structural energy E_{St} has to be spend to deform the lattice. When the electron is trapped in the polaron potential well, the electronic energy E_{El} is gained. The difference between E_{El} and E_{St} is the polaron binding energy E_{PB} [62].
Polarons can be divided into small and large polarons. Small polarons (Holstein polarons) exhibit a short-range interaction with phonons and are highly localized. Hence, their deformation of the lattice is in the range of the lattice constant. In contrast, large polarons (Fröhlich polarons) have a long-range interaction with phonons and are less localized, which leads to a larger deformation area of several unit cells. Polarons introduce trap states into the energy gap, which is illustrated in

Fig. 2.4 for an electron (P_e) and a hole polaron (P_h). When the polaron band is occupied the polaron level is charged whereas if it is empty the polaron level is neutral [61, 62].

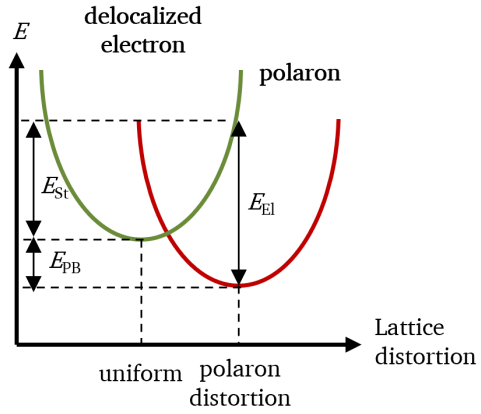

Figure 2.6.: Potential well of a delocalized conduction band electron and a polaron.

Polarons in an ionic crystal can also be described as so-called charge transition levels of the host atoms. Transition metals are known to have localized *d*-orbitals and are forming likely polarons [59, 61]. For example in $LiNbO_3$, electrons can be trapped on the niobium site, which leads to a valence change of the niobium from Nb^{5+} to Nb^{4+} [74–76]. Therefore, the polaron localized on the niobium site can be regarded as charge transition level $Nb^{4+/5+}$.

Large polarons are shallow trap states close to the band edges, which is why they can move almost freely with a high mobility. Similar to conduction band electrons, the mobility of large polarons is decreasing with temperature. On the contrary, small polarons form deep trap states and exhibit a low mobility. Comparable to other hopping processes, the mobility of small polarons is increasing with temperature [59–62]. Table 2.1 sets the main characteristics of small and large polarons in contrast.

Table 2.1.: Main characteristics of small and large polarons [59–62].

	Small polaron	Large polaron
phonon interaction	short-range	long-range
deformation range	$\approx$ unit cell	$\gg$ unit cell
trap states within energy gap	deep ($\sim 1\,\mathrm{eV}$ below E_{CBM})	shallow ($\sim 10\,\mathrm{meV}$ below E_{CBM})
mobility	$< 1\,\mathrm{cm^2\,V^{-1}\,s}$	$> 1\,\mathrm{cm^2\,V^{-1}\,s}$
temperature dependence of mobility	increasing	decreasing

Excitons

When a semiconductor is illuminated by photons with an energy larger than the semiconductor band gap, an electron can be excited from the valence to the conduction band. However, this electron can form an exciton with the hole in the valence band generated by the excitation. This means that the electron is bound to the hole, hence, exhibits an energy state E_{Ex} slightly smaller than the CBM,

which is shown in Fig. 2.4. The binding energy of the exciton E_{EB} is the difference between E_{CBM} and E_{Ex}. Consequently, photons with a smaller energy than the band gap but with a higher energy than $E_{\mathrm{Ex}} - E_{\mathrm{VBM}}$ can excite an exciton [51].
Similar to small and large polarons introduced in the previous section, we can distinguish between short-range (Frenkel excitons) and long-range excitons (Wannier excitons), which are bound stronger and weaker, respectively. Frenkel excitons are more common in organic materials and wide band gap semiconductors with small dielectric constants, whereas Wannier excitons are more present in inorganic materials with large dielectric constants [51, 64].
Excitons can influence the optical absorption spectra of a material quite significantly. In Fig. 2.7a) different excited states of Wannier excitons are shown within the band gap of a semiconductor. These excited states are responsible for additional absorption lines below the band edge as depicted in Fig. 2.7b) in red. The green solid line is the overall measured absorption spectrum while the dashed line represents the absorption from the conduction band. The exciton peak can be clearly identified at low temperatures but with increasing temperature it is smearing out and cannot be observed anymore as shown in Fig. 2.7c) for GaAs as an example. The reason is the scattering of the excited electron with phonons, defects, and impurities with increasing temperature. Hence, after absorption of a photon and excitation to an excitonic state, the electron can absorb phonons, which leads to a further excitation to higher k-vectors and/or to a higher excitonic state [63]. This situation is illustrated in Fig. 2.7a).

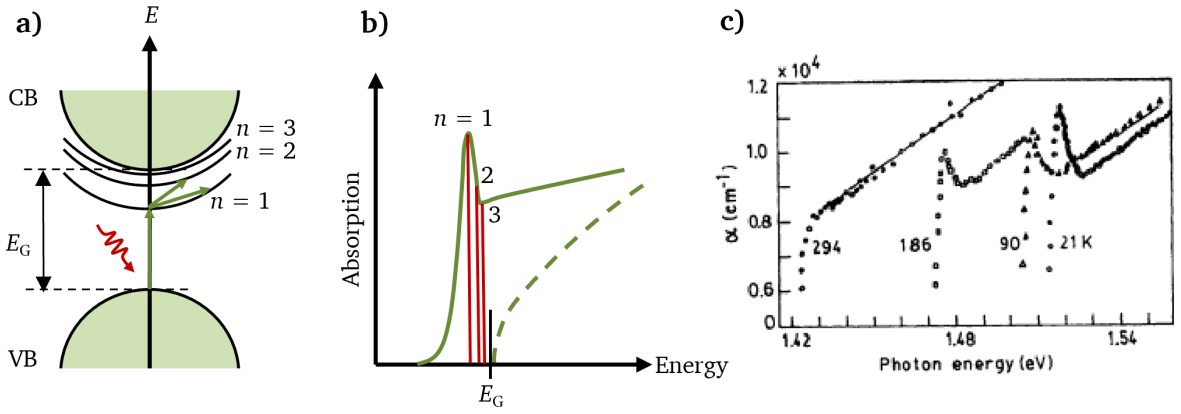

Figure 2.7.: a): Exciton formation with discrete excited states $n = 1, 2, 3, ...$ and further scattering with phonons. b): Measured absorption spectra (green solid line) including exciton lines (red lines) and continuum absorption by the conduction band (dashed green line). c): Absorption spectra of GaAs at different temperatures [63].

Charge neutrality

For all the point defects discussed above, charge neutrality [51, 66] must be fulfilled, which means that all negative charges are counterbalancing all positive charges.

$$n + N_{\mathrm{A}}^{-} + N_{\mathrm{V_C}}^{-} + N_{\mathrm{P_e}}^{-} = p + N_{\mathrm{D}}^{+} + N_{\mathrm{V_A}}^{+} + N_{\mathrm{P_h}}^{+} \tag{2.13}$$

N_{D}^{+}, N_{A}^{-}, $N_{\mathrm{V_A}}^{+}$, $N_{\mathrm{V_C}}^{-}$, $N_{\mathrm{P_e}}^{-}$, and $N_{\mathrm{P_h}}^{+}$ are the numbers of ionized donors, acceptors, anion and cation vacancies, and electron and hole polarons. The variation and interaction of all these charges has to be taken into account.
In case, one species is dominating the whole defect concentration this charge neutrality equation can be simplified. For example, in a purely donor doped (n-type) semiconductor, where vacancy and polaron concentrations are very small, the charge neutrality can be reduced to

$$n = N_{\mathrm{D}}^{+} + p \approx N_{\mathrm{D}}^{+} \tag{2.14}$$

In a purely acceptor doped (p-type) material Equation 2.13 can be shorten to

$$p = N_{\mathrm{A}}^{-} + n \approx N_{\mathrm{A}}^{-} \tag{2.15}$$

At high temperatures ($kT \gg E_{\mathrm{CB}} - E_{\mathrm{D}^{0/+}}$) when the majority of dopants is ionized, we can, therefore, write for a n- and p-type semiconductor with donor concentration N_{D} and acceptor concentration N_{A}:

$$n \approx N_{\mathrm{D}} = N_{\mathrm{CB}} \mathrm{exp}\left(-\frac{E_{\mathrm{CBM}} - E_{\mathrm{F}}}{k_{\mathrm{B}}T}\right) \tag{2.16}$$

$$p \approx N_{\mathrm{A}} = N_{\mathrm{VB}} \mathrm{exp}\left(-\frac{E_{\mathrm{F}} - E_{\mathrm{VBM}}}{k_{\mathrm{B}}T}\right) \tag{2.17}$$

Self-compensation and Fermi level confinement

When a semiconductor is doped with a donor or acceptor an additional free electron or hole is contributed to the system leading to a shift of E_{F} closer to the conduction or the valence band. Charge neutrality is then given by Eq. 2.14 or 2.15. However, with increasing doping concentration it can happen that instead of more free charge carriers, intrinsic defects such as anion ($\mathrm{V_A^{\cdot}}$) and cation vacancies ($\mathrm{V_C^{\prime}}$) are formed for compensation of the dopants. This effect is called self-compensation or ionic compensation. In oxide perovskite materials the anion vacancies are often doubly charged oxygen vacancies ($\mathrm{V_O^{\cdot\cdot}}$), which act as donors. In contrast, cation vacancies function as acceptors. The formation enthalpy of the defects with charge q can be determined by the following equation [77]:

$$\Delta H_{\mathrm{D}}(E_{\mathrm{F}}, \mu) = (E_{\mathrm{D},q} - E_{\mathrm{H}}) + qE_{\mathrm{F}} + \sum_{\infty} n_i \mu_i \tag{2.18}$$

The formation enthalpy depends on the Fermi level E_F and the chemical potential μ_i of the different atomic species i. $E_{D,q} - E_H$ describes the total energy of the system with and without the defect. The formation enthalpy of the cation and anion vacancies can be plotted as function of E_F, which is illustrated in Fig. 2.8a). The slope is determined by the charge of the defect. With increasing donor doping E_F is shifted closer to the conduction band, which results in a decreasing formation enthalpy ΔH_C of V'_C. At $E_{F,max}$ ΔH_C is turning negative, which means that V'_C are formed spontaneously. Hence, any additional donor concentration does not further increase the electron concentration n but the V'_C concentration N_C. Consequently, the Fermi level cannot be shifted closer to the conduction band and is pinned at $E_{F,max}$. This situation can be described as Fermi level pinning. The opposite applies to acceptor doping, which decreases E_F. The lower E_F reduces the formation enthalpy ΔH_O of $V_O^{\cdot\cdot}$. At a certain acceptor concentration ΔH_O turns negative and the Fermi level is pinned at $E_{F,min}$. These self-compensation effects confine the accessible E_F range between $E_{F,min} < E_F < E_{F,max}$ meaning that E_F cannot be varied within the whole band gap [77–79]. In addition, $E_{F,min}$ and $E_{F,max}$ change, when the sample is treated in an oxidizing or a reducing atmosphere. When handling the sample in reducing conditions, the formation enthalpy of $V_O^{\cdot\cdot}$ is decreasing, while for V'_C it is increasing. Hence, the accessible E_F range is shifted to higher energies in a reducing atmosphere compared to oxidizing conditions.

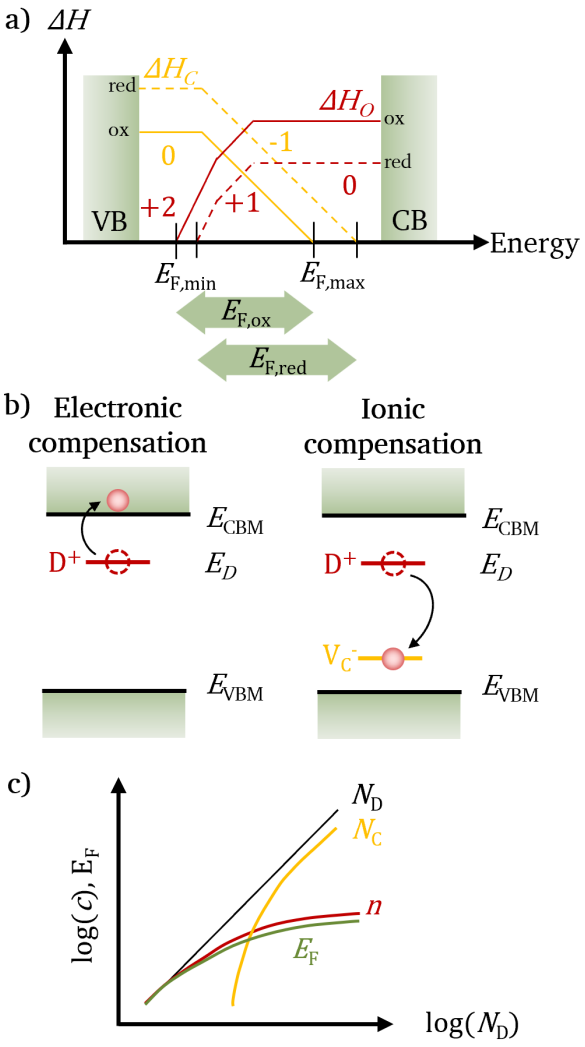

Figure 2.8.: a): Formation enthalpy ΔH of V'_C and $V_O^{\cdot\cdot}$ in dependence of E_F. b) Electronic and ionic compensation leading to an increase in the electron n and the V'_C concentration N_C with increasing donor concentration N_D in c) adapted from [78].

Figure 2.8b) shows the situation for electronic and ionic compensation (self-compensation). In addition, in Fig. 2.8c) the electron n and cation vacancy concentration N_C is plotted as a function of the donor concentration N_D, which demonstrates how a material can change from electronic to ionic or rather mixed electronic-ionic compensation [78].

Not only intrinsic defects but polarons can confine E_F as well [39, 80]. For example when E_F is increased with rising donor concentration reaching the charge transition level of the host atom, e.g. $Nb^{4+/5+}$ in $LiNbO_3$, the formation enthalpy of the polaron is turning negative and E_F is pinned at the polaron level. A higher reduction of the material would lead to such a high polaron concentration (e.g. Nb^{4+}) that the materials would not be stable any longer. In contrast to the self-compensation effect, the formation enthalpy of the polarons is not changing in oxidizing or reducing atmospheres.

2.3.2. Line defects

Line defects are one-dimensional defects [57]. The most prominent line defects are dislocations, which are abrupt changes in the atom arrangement. They can be separated into edge and screw dislocations. Dislocations can facilitate the movement of lattice atoms as well as point defects. Therefore, they can act as sink for lattice defects. However, the evaluation of line defects are extending the scope of this work and will not be further explained nor discussed. The interested reader is referred to [81, 82].

2.3.3. Planar defects

Planar defects are two-dimensional defects, which can be categorized into grain boundaries, domain boundaries, antiphase boundaries, and stacking faults.

Grain boundaries

At grain boundaries the crystal structure is interrupted [57]. Grain boundaries can be sinks for point defects, e.g. vacancies or foreign atoms. Charged point defects can build up potential barriers at the grain boundaries leading to space charge layers within this region. Hence, grain boundaries can have a significant effect on mechanical and electrical properties. Within this thesis grain boundaries are only discussed superficially, hence, the interested reader is referred to [83–86].

Domain boundaries

Domain boundaries can similar to grain boundaries be charged due to accumulation of charged point defects [50]. Therefore, they can highly influence the materials properties, too. As domain boundaries are not subject of this work, the reader is referred to [87, 88]

Antiphase boundaries

A general definition of antiphase boundaries is the boundary between two unit cells which can be described by one half of the unit cell. This implies that the translational vector is $^1/_2$ of the lattice parameter *a* instead of one *a* as in the ordered bulk material. However, in ferroelectric or antiferroelectric materials, the displacement of the atoms resulting in the polarization have to be taken into account. For antiferroelectric materials, e.g. $PbZrO_3$, the antiphase boundaries interrupt the anti-parallel ordering. In bulk $PbZrO_3$ the spontaneous polarization is mainly caused by the displaced Pb ions. Two Pb ions displaced in one direction are followed by two Pb ions displaced in the other direction. At the antiphase boundary this order is interrupted. Depending on the arrangement of the polarization at the antiphase boundary, it is polar or anti-polar as shown in Fig. 2.5 [89, 90]. The materials properties can be influenced by the appearance and density of the antiphase boundaries. For example, Hui Ding proposed in her doctoral thesis that the amount of antiphase boundaries can influence the reversibility of the ferroelectric to antiferroelectric phase transition when applying an electric field [91].

2.3.4. Bulk defects

Bulk defects are three dimensional defects, which are very important especially in ceramic materials. The most common preparation method to produce ceramic samples is the solid state reaction method (see Section 2.7). Bad synthesis and sintering conditions can lead to pores, precipitates, and cracks. All these defects play an important role for several materials properties such has mechanical strength or electrical breakdown strength. Problems resulting from pores or secondary phases as well as strategies to reduce them for $NaNbO_3$ and $KNbO_3$ are shown in Section 2.7.

2.4. Electrical conductivity and transport properties of semiconductors

The electrical conductivity of ionic oxide semiconductors can be divided into electronic conductivity and ionic conductivity. In some materials the electronic conductivity is dominating, e.g. in In_2O_3 [92] or Sn-doped In_2O_3 (ITO) [93], and others exhibit mainly ionic conductivity, e.g. Y-stabilized ZrO_2 [94]. Some materials show a mixed conductivity of both, electronic and ionic conduction, e.g. $(La,Sr)(Co,Fe)_3$ (LSCO) [95]. In the next section electronic and ionic conduction processes are introduced.

2.4.1. Electronic conductivity

Usually electronic conduction means the transport of free electrons in the conduction band in case of a n-type semiconductor or free holes in the valence band for a p-type semiconductor. However, materials which exhibit a high polaron concentration can have a charge transport via a polaron mechanism. In the following both conduction paths are introduced.

Band conduction

The electrical conductivity via band conduction can be expressed by the following equation:

$$\sigma = q\mu_n n + q\mu_p p \tag{2.19}$$

Here, $q = 1.6 \cdot 10^{-19}$ C is the elementary charge, n and p the electron and hole concentration, and μ_n and μ_p the mobility of electrons and holes, respectively. In general, the thermal velocity ν_th can be determined by equating the kinetic and the thermal energy:

$$\frac{1}{2} m^* \nu_\mathrm{th}^2 = \frac{3}{2} k_\mathrm{B} T \tag{2.20}$$

$$\nu_\mathrm{th} = \sqrt{\frac{3 k_\mathrm{B} T}{m^*}} \tag{2.21}$$

T is the temperature and m^* the effective mass of the charge carriers. When an electric field is applied, the charge carriers are accelerated along the electric field resulting in a drift velocity ν_drift:

$$m^* \nu_\mathrm{drift} = qF\tau \tag{2.22}$$

τ represents the mean free time and is defined as the ratio between mean free path $\bar{l}$ and thermal velocity ν_th.

$$\tau = \frac{\bar{l}}{\nu_\mathrm{th}} \tag{2.23}$$

The drift mobility μ can then be calculated by:

$$\mu = \frac{v_\mathrm{drift}}{F} = \frac{q\tau}{m^*} = \frac{q\bar{l}}{m^* \nu_\mathrm{th}} = \frac{q\bar{l}}{\sqrt{3 m^* k_\mathrm{B} T}} \tag{2.24}$$

Hence, the drift mobility is decreasing with rising temperature due to electron-electron scattering by thermal activation. However, the mobility is influenced additionally by impurity and lattice (phonon) scattering. Impurity scattering has a higher impact at low temperatures while lattice scattering influences the mobility dominantly at higher temperatures. Hence, at low temperatures the mobility is increasing with increasing temperature because the effect of impurity scattering is reduced. In

contrast, at high temperatures the mobility is lowered again due to the rising phonon scattering, which slows down the charge carriers.

$$\mu \propto T^{3/2} \qquad \text{impurity scattering} \tag{2.25}$$

$$\mu \propto T^{-3/2} \qquad \text{lattice scattering} \tag{2.26}$$

For intrinsic band conduction with $n_\mathrm{i} = n = p$ Eq. 2.19 can be written as:

$$\sigma = q n_\mathrm{i} (\mu_n + \mu_p) \tag{2.27}$$

Inserting Eq. 2.12 results in:

$$\sigma = \frac{\sigma_0}{T^{3/2}} \cdot \exp\left(-\frac{E_\mathrm{G}}{2 k_\mathrm{B} T}\right) \tag{2.28}$$

σ_0 is a prefactor including the elementary charge and all constants of the mobility and concentration such as density of states of the conduction and valence band. Eq. 2.28 is an Arrhenius-type equation with an activation energy $E_\mathrm{A} = {}^{E_\mathrm{G}}/_{2}$ [51, 56]. The evaluation of an Arrhenius plot is explained in Section 3.9.1.

Polaron conduction

Depending on the type of polarons in the material, the conduction process is performed via small or large polaron transport. Here, we will focus on small polaron conduction because it is the more relevant process for this work. The explanations are based on descriptions in [59, 62, 96, 97].
For polaron conduction the polaron electron or hole has to move from one trapping site to the next trapping site. This is illustrated schematically in Fig. 2.9a) with two potential wells representing site 1 and 2. To move from site 1 to site 2, the electron or hole has to overcome the potential barrier between these two adjacent sites.
Polaron conduction can be divided into an adiabatic and a non-adiabatic (diabatic) regime. In the adiabatic region the frequency of the polaron jumping from one site to the other is much larger than the phonon frequency, which is the case at low temperatures. Hence, the polaron can tunnel from site to site because of an orbital overlap of these two neighboring sites. This orbital overlap results in an electronic coupling strength V_{12}, which is shown in Fig. 2.9a). For the diabatic regime the polaron frequency is much smaller than the phonon frequency, which is the case at high temperatures. Here, the orbital overlap is disturbed by the phonon vibrations. Consequently, the activation energy to overcome the potential barrier is V_{12} lower for an adiabatic process than the for a diabatic process.

In general, the polaron conductivity can be written like:

$$\sigma = c_\mathrm{P} \mu_\mathrm{P} q = \frac{\sigma_0}{T^a} \exp\left(-\frac{E_\mathrm{A}}{k_\mathrm{B} T}\right) \tag{2.29}$$

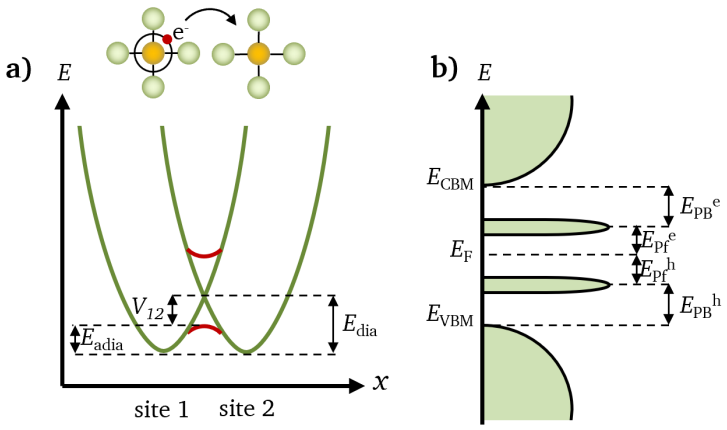

Figure 2.9.: a): Polaron hopping between two adjacent sites for an adiabatic and diabatic case with activation energy E_{adia} and E_{dia}, respectively. V_{12} is the electronic coupling strength. b): Band structure including a hole and an electron polaron band with polaron binding energy E_{PB} and polaron formation energy E_{Pf}.

a equals 1 for the adiabatic regime, while for the diabatic case a is $3/2$. The concentration c_{P} and the mobility μ_{P} of the polaron can be expressed by Equations 2.30 and 2.31.

$$c_{\text{P}} = N_{\text{P}} \exp\left(-\frac{E_{\text{Pf}}}{k_{\text{B}}T}\right) \tag{2.30}$$

$$\mu_{\text{P}} = \frac{\mu_0}{T^a} \exp\left(-\frac{E_{(\text{a})\text{dia}}}{k_{\text{B}}T}\right) \tag{2.31}$$

N_{P} is the number of polaron sites and E_{Pf} is the formation energy of a polaron, which is the energetic distance between the polaron level and E_{F}. In Fig. 2.9b) the formation energy for a hole and an electron polaron is indicated. Here, the polaron binding energy E_{PB} of a hole and an electron, which is the energetic difference between E_{F} and the VBM in case of a hole and the CBM for an electron, is marked as well. The relation between polaron binding energy and (a)diabatic activation energy is given by Eq. 2.32.

$$\begin{aligned} E_{\text{PB}} &= 2(E_{\text{adia}} + V_{12}) && \text{adiabatic regime} \\ E_{\text{PB}} &= 2E_{\text{dia}} && \text{diabatic regime} \end{aligned} \tag{2.32}$$

Therefore, the overall activation energy E_{A} for polaron conductivity is as follows:

$$\begin{aligned} E_{\text{A}} &= E_{\text{Pf}} + E_{\text{adia}} = E_{\text{Pf}} + \frac{E_{\text{PB}}}{2} - V_{12} && \text{adiabatic regime} \\ E_{\text{A}} &= E_{\text{Pf}} + E_{\text{dia}} = E_{\text{Pf}} + \frac{E_{\text{PB}}}{2} && \text{diabatic regime} \end{aligned} \tag{2.33}$$

2.4.2. Ionic conductivity

In general, the ionic conductivity can be expressed similar to the electronic conduction by:

$$\sigma_{\text{ion}} = z_{\text{A}} m_{\text{A}} c_{\text{A}} + z_{\text{C}} m_{\text{C}} c_{\text{C}} \tag{2.34}$$

Here, z is the charge, m the mobility, and c the concentration of the ion, where A and C stands for anion and cation. The mobility and concentration can be expressed by Eq. 2.35 and 2.36.

$$m_{\text{ion}} = \frac{m_0}{T} \exp\left(-\frac{E_{\text{mig}}}{k_{\text{B}} T}\right) \tag{2.35}$$

$$c_{\text{ion}} = N_{\text{ion}} \exp\left(-\frac{E_{\text{ion,f}}}{2 k_{\text{B}} T}\right) \tag{2.36}$$

m_0 is a pre-factor, E_{mig} and $E_{\text{ion,f}}$ are migration and formation energy of the ion, and N_{ion} is the number of ions. Hence, the ionic conductivity can be expressed by:

$$\sigma_{\text{ion}} = \frac{\sigma_0}{T} \exp\left(-\frac{E_{\text{mig}} + \frac{E_{\text{ion,f}}}{2}}{k_{\text{B}} T}\right) \tag{2.37}$$

When an electric field is applied the ions will move to the electrodes according to their charge, which means that anions are moving to the anode while cations are migrating to the cathode. This movement can also be described by the chemical diffusion coefficient $\tilde{D}$, which is connected to the conductivity by the Nernst-Einstein-Equation:

$$\sigma_{\text{DC}} = \frac{z^2 c \tilde{D}_{\text{DC}}}{k_{\text{B}} T} \left(\frac{\delta \ln N}{\delta \ln \mu}\right) \tag{2.38}$$

However, this equation includes all ions meaning all anions and cations. Hence, σ_{DC}, c, and $\tilde{D}_{\text{DC}}$ include all ionic species. ${}^{\delta \ln \mu}/_{\delta \ln N} = \gamma$ is the thermodynamic factor with μ being the chemical potential. The thermodynamic factor is the relation between the chemical diffusion coefficient and the tracer diffusion coefficient D^*.

$$\tilde{D} = D^* \gamma \tag{2.39}$$

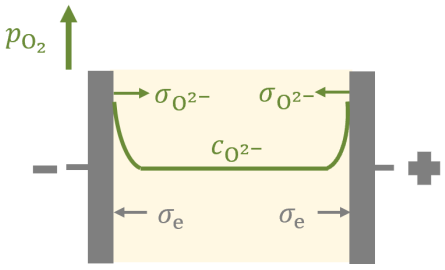

Figure 2.10.: Oxygen and electron diffusion due to an increase in oxygen partial pressure.

Applying a constant electric field at a constant temperature while changing the atmosphere, results in an additional diffusion process due to a change in concentration. If, for example, the oxygen partial pressure is increased, the oxygen concentration at the surface of the sample is higher than in the bulk. This leads to a diffusion of oxygen vacancies $V_{\text{O}}^{\cdot\cdot}$ to the surface and an incorporation

of oxygen into the material, which is then further diffusing into the bulk. This scenario is depicted in Fig. 2.10. The oxygen diffusion induces a diffusion of electrons in the opposite direction due to charge neutrality. Therefore, the oxygen chemical diffusion coefficient $\tilde{D}_{\mathrm{O}}$ cannot be determined anymore by only the ionic (oxygen) conductivity, which is expressed by Eq. 2.40.

$$\tilde{D}_{\mathrm{O}} = \frac{RT}{4F^2} \frac{\sigma_{\mathrm{e}} \sigma_{\mathrm{O}^{2-}}}{\sigma_{\mathrm{e}} + \sigma_{\mathrm{O}^{2-}}} \left(\frac{\gamma_{\mathrm{O}^{2-}}}{c_{\mathrm{O}^{2-}}} + 4 \frac{\gamma_{\mathrm{e}}}{c_{\mathrm{e}}} \right) \tag{2.40}$$

F is the Faraday constant. The electronic conductivity of the electrons has to be considered as well because their movement is connected to the migration of the oxygen ions. Here, we can consider four different cases:

1. $\sigma_{\mathrm{e}} \gg \sigma_{\mathrm{O}^{2-}}$:
   - the electronic conductivity is much higher than the oxygen conductivity due to a high electron concentration and a high electron mobility
   - $\tilde{D}_{\mathrm{O}}$ is mainly determined by the oxygen migration as the rate limiting diffusion process, which depends on the $\mathrm{V}_{\mathrm{O}}^{\cdot\cdot}$ diffusion and concentration
2. $\sigma_{\mathrm{e}} \ll \sigma_{\mathrm{O}^{2-}}$:
   a) $c_{\mathrm{e}} \ll c_{\mathrm{O}^{2-}}$, and $\mu_{\mathrm{e}} \gg m_{\mathrm{O}^{2-}}$:
      - the electronic conductivity is much smaller than the oxygen conductivity because of a low electron concentration
      - $\tilde{D}_{\mathrm{O}}$ is determined by the diffusion of the electrons and oxygen ions

   b) $c_{\mathrm{e}} \gg c_{\mathrm{O}^{2-}}$, and $\mu_{\mathrm{e}} \ll m_{\mathrm{O}^{2-}}$:
      - the electronic conductivity is much smaller than the oxygen conductivity because of a low electron mobility
      - $\tilde{D}_{\mathrm{O}}$ is governed by the diffusion of the electrons and oxygen ions
      - A low electron mobility can be caused by small polarons with a high migration barrier $E_{\mathrm{(a)dia}}$

   c) $c_{\mathrm{e}} \ll c_{\mathrm{O}^{2-}}$, and $\mu_{\mathrm{e}} \ll m_{\mathrm{O}^{2-}}$:
      - the electronic conductivity is much smaller than the oxygen conductivity because of a low electron concentration and a low electron mobility
      - $\tilde{D}_{\mathrm{O}}$ is mainly governed by the migration of the electrons as the rate limiting part
      - A low electron mobility can be caused by small polarons with a high migration barrier $E_{\mathrm{(a)dia}}$

2.4.3. Intrinsic and extrinsic conductivity regime

A common defect in perovskite materials is a Schottky defect, which is the combined formation of cation and anion vacancies. In $NaNbO_3$, for one oxygen vacancy two sodium vacancies are created. The intrinsic formation of Schottky defects occurs at high temperatures at which enough energy can be provided to overcome the formation enthalpy $E_{\text{Schott,f}}$. Therefore, the concentration of cation and oxygen vacancies is influenced by $E_{\text{Schott,f}}$ and the temperature. However, at low temperatures the concentrations can be determined by foreign atoms, e.g. dopants. For an acceptor doped material, the oxygen concentration can be fixed if the dopant is compensated ionically. Consequently, at low temperatures the activation energy of the ionic conductivity is given by the migration energy E_{mig} while at high temperatures it equals the migration energy plus half of the formation energy:

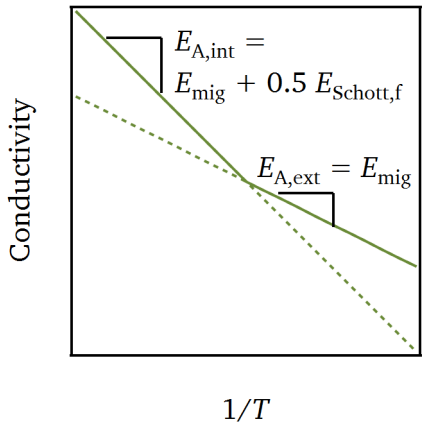

Figure 2.11.: Intrinsic and extrinsic regime of an ion conduction process.

$$\sigma_{\text{ion,ext}} = \frac{\sigma_0}{T}\exp\left(-\frac{E_{\text{mig}}}{k_{\text{B}}T}\right)$$
$$\sigma_{\text{ion,int}} = \frac{\sigma_0}{T}\exp\left(-\frac{E_{\text{mig}} + \frac{E_{\text{Schott,f}}}{2}}{k_{\text{B}}T}\right) \tag{2.41}$$

This relation is illustrated in Fig. 2.11.

2.4.4. Resistance degradation

Resistance degradation is the largest obstacle for today's multi-layer capacitors concerning long-term stability. Exposure to high temperatures and voltages at the same time leads to a significant increase of several orders of magnitude of the leakage current, which can result in a thermal or dielectric breakdown of the device. A characteristic degradation behavior is described by a constant current at constant applied electric field with time, followed by a sudden increase of several orders of magnitude in current after reaching a certain time, which can be defined by the degradation rate. Figure 2.12 illustrates the degradation behavior of a single crystal, a fine- and a coarse-grained sample [85]. The origin for resistance degradation is explained in the most cases by oxygen vacancy migration towards the cathode. This leads to an increase of electrons in this region. In contrast, at the anode a depletion of oxygen vacancies is observed resulting in an accumulation of holes. Hence, a n-type

region near the cathode and a p-type region near the anode is created, which have both a higher electrical conductivity compared to the intrinsic material before, leading to a leakage current. This leakage current is responsible for the observed degradation behavior. Additionally, more oxygen vacancies can be introduced at the anode into the sample causing an overall reduction of the material. In this case, the sample behaves like a n-type material with increased leakage current. Therefore, this explanation is called reduction model [20, 48, 49].

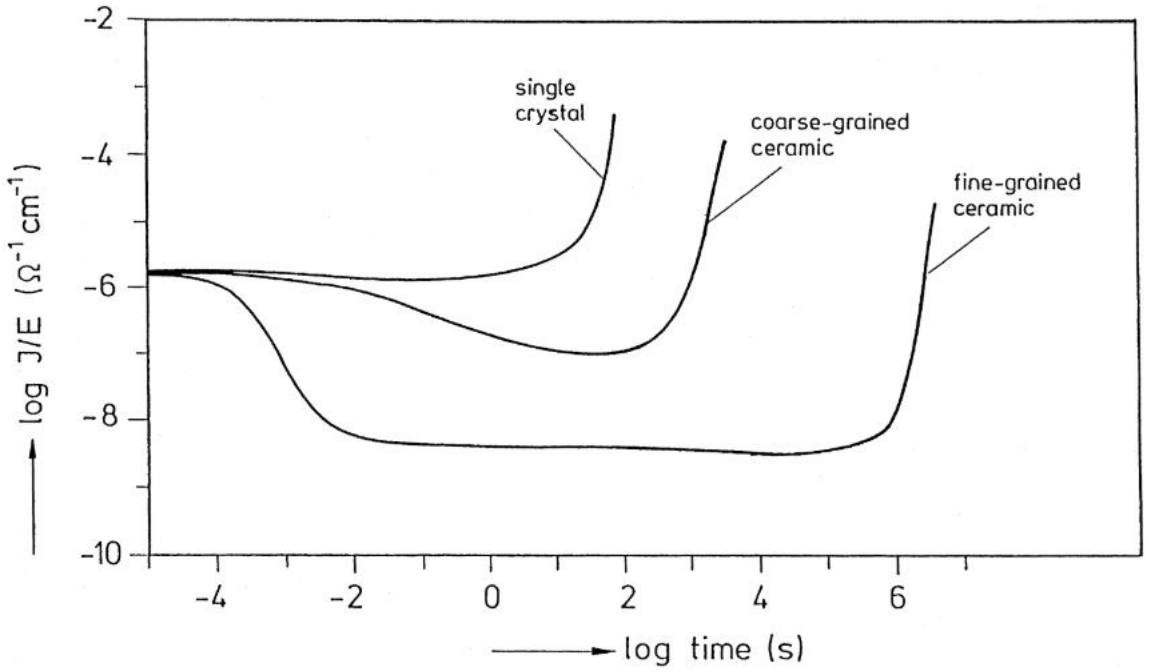

Figure 2.12.: Resistance degradation of a 0.1 at % Ni-doped $SrTiO_3$ single crystal as well as of coarse- and fine-grained ceramic [85].

The degradation rate depends mainly on the composition and the microstructure of the sample. Fine-grained materials degrade slower than samples with larger grains. This phenomenon can be explained by the accumulation of oxygen vacancies at the grain boundaries creating a space charge region depleted of oxygen vacancies. Hence, the decreased oxygen vacancy concentration leads to less diffusion, which slows down the degradation process [98]. Resistance degradation is investigated quite intensively for $BaTiO_3$ and $SrTiO_3$. Doping of these materials showed that acceptor doping is accelerating the degradation process while donor doping is slowing it down. The reason is the different concentration of oxygen vacancies. Acceptors can be compensated by oxygen vacancies, hence, increasing the concentration of these mobile defects. Donors, on the contrary, are compensated by cation vacancies, which are much less mobile [20, 48, 49].

2.5. Sodium niobate

Sodium niobate ($NaNbO_3$) has been reported firstly by Matthias [99] in 1949. Two years later Vousden [100] analyzed it's crystal structure and found that $NaNbO_3$ is in general non-polar, hence, cannot be ferroelectric but exhibits domain movements under applied electric DC-field. In addition, he observed an anti-parallel displacement of Nb ions within the $NaNbO_3$ structure and proposed that $NaNbO_3$ is orthorhombic with space group 22_12. In the same year, Kittel [52] suggested the concept of antiferroelectricity. From this point on several authors including Vousden [101], Megaw [102], and Shirane [103] suggested that $NaNbO_3$ could be antiferroelectric explaining the observations from Vousden. In the following years, the crystal structure was investigated over a broad temperature range mainly by the group of Megaw who summarized the structural analyses and described the seven phases in $NaNbO_3$ [104]. In addition, Megaw corrected the room temperature space group indicated by Vousden and identified it as Pbma space group [102]. All polymorphs of $NaNbO_3$ are illustrated in Fig. 2.13 including space group, dielectric state, and all tilts observed in the corresponding structure according to Glazer's notation [105].

In Glazer's notation the three positions a, b, and c correspond to the tilts about the directions $[100]$, $[010]$, and $[001]$, respectively. The letter a, b, and c express the magnitude of these tilts, while the subscripts $+$, $-$, and 0 indicate if two consecutive oxygen octahedra are tilted in the same or the opposite direction about the axis or have a zero tilt. This implies that a $a^-b^+a^-$ tilt system as in the P phase has tilts of the same magnitude in $[100]$ and $[001]$ direction which are different from the tilt in the $[010]$ direction. The tilts along the $[100]$ and $[001]$ are alternating while the octahedra along the $[111]$ direction are always tilted in the same manner.

Both antiferroelectric phases, P and R phase, exhibit a very complicated tilt system. The P phase consists of pairs of $a^-b^+a^-$ layers alternating with pairs of $a^-b^-a^-$ layers. Pairs of $a^-b^+c^+$ layers in a row with single $a^-b^0c^+$ layers build the R phase. In general, it can be observed that the number of tilt and displacement components is decreasing from polymorph to polymorph with increasing temperature [106]. Above $480\,°C$ all phases are paraelectric while below $-100\,°C$ $NaNbO_3$ undergoes a transition to a ferroelectric rhombohedral phase [107].

Two room temperature phases exist in $NaNbO_3$, an antiferroelectric and a ferroelectric one, which are called P and Q phase, respectively. The P phase is orthorhombic with space group Pbcm [108] and the Q phase is orthorhombic with space group $P2_1ma$ [109], which are both shown in Fig. 2.14 adapted from [110]. The lattice parameters of the P phase are $a = 5.506\,Å$, $b = 5.566\,Å$, and $c = 15.520\,Å$ [102]. For the Q phase lattice parameters of $a = 5.569\,Å$, $b = 7.790\,Å$, and $c = 5.518\,Å$ are determined [109]. Both polymorphs have corner-shared NbO_6-octahedra which spaces are filled by the Na atoms. The Nb atoms located in the octahedra are shifted from the central position towards the in-plane oxygen atoms along the pseudocubic $[110]$ direction. In case of the Na atoms, there exist two kinds of sodium position, Na(1) and Na(2). Na(1) is shifted in the same direction as the Nb atoms with an even larger displacement. In contrast, Na(2) is only slightly displaced. The

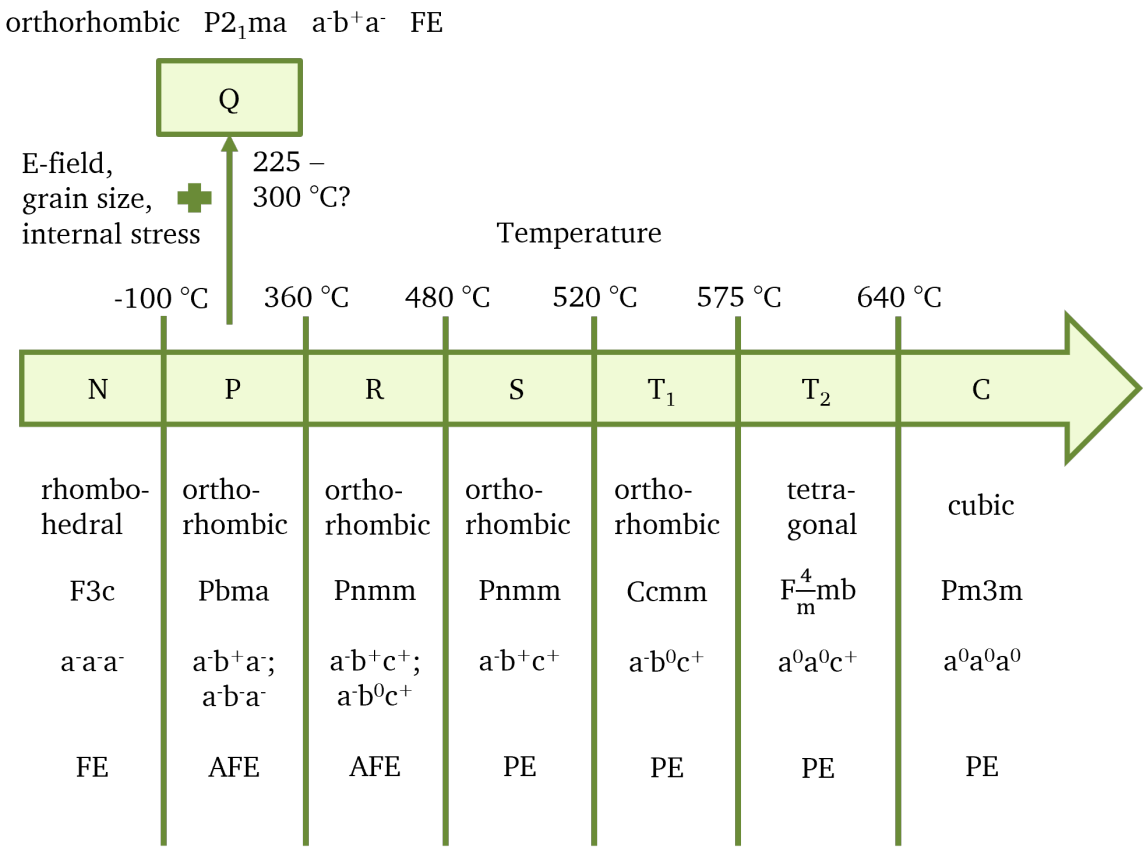

Figure 2.13.: All polymorphs of $NaNbO_3$ including crystal structure, space group, Glazer's notation, and dielectric state. The metastable Q phase, which can be introduced by a high electric field, a small grain size, or internal stresses, is added as well. The transition temperature is unclear and marked by a question mark [104, 106, 107].

displacements of Nb and Na atoms are indicated by blue and orange arrows in Fig. 2.14. In the P phase, Na(1) is displaced in the same direction as the Nb atoms above and below it. The next row includes only Na(2) atoms (layer 1 and 2). The next block of Nb, Na(1), and Nb atoms (layer 3 and 4) is shifted in the opposite direction as the block before. In contrast, these atoms are displaced in the same direction as the ones in layer 1 and 2 in the Q phase. Hence, in the P and Q phase an anti-parallel and parallel displacement is formed, respectively. Consequently, the unit cell of the P phase is almost doubled in c-direction in comparison to the unit cell of the Q phase [108].
The P phase is energetically more stable than the Q phase. However, the energy difference of about 1 meV [26] is not large, which is why both phases can coexist at room temperature. Nevertheless, the majority is mostly present in the P phase. The Q phase can be induced by applying a high electric field [111], by preparing polycrystalline samples with small grain sizes [24, 112], or by introducing internal stresses [113]. If the Q phase is achieved by a high electric field, the P phase can be restored by heating above 300 °C [111, 114].

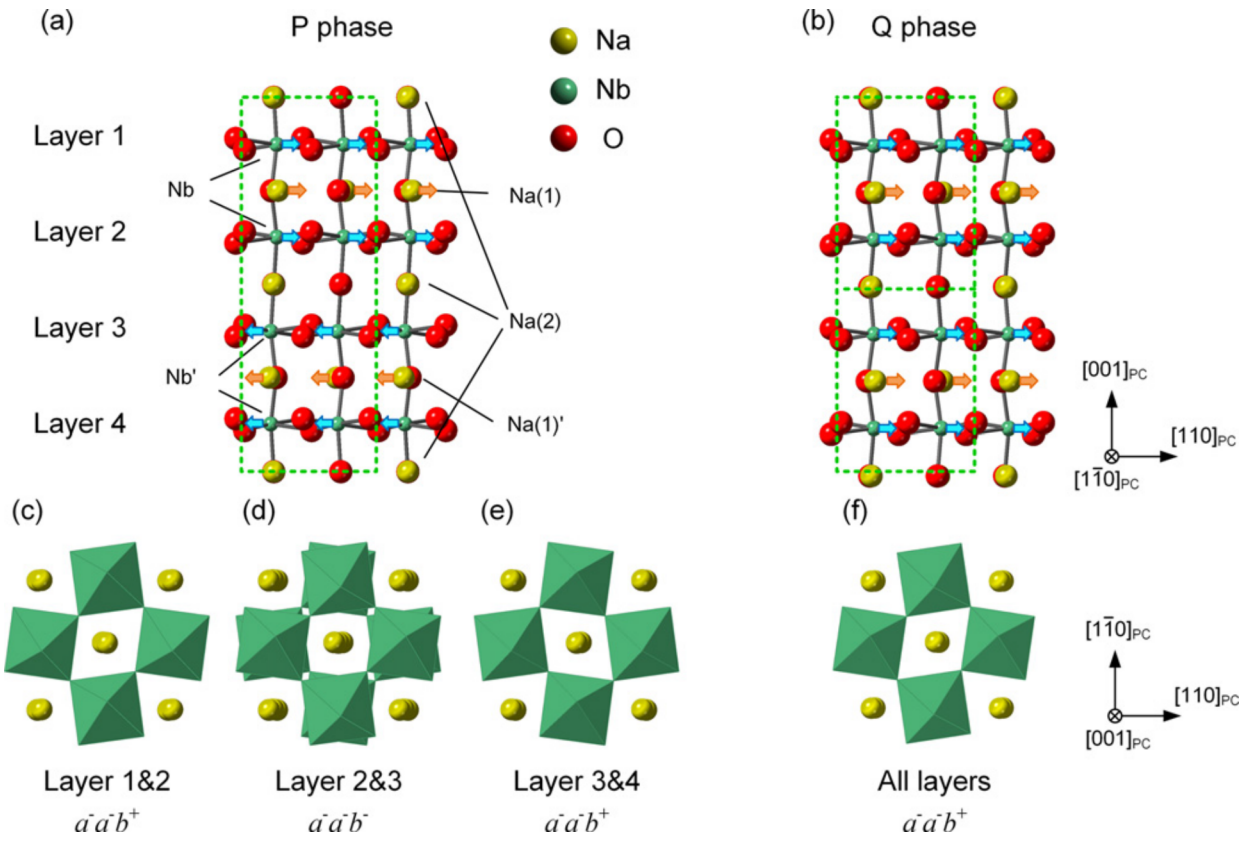

Figure 2.14.: Crystal structure of P and Q phase represented in a) and b) with Na and Nb displacements indicated by orange and blue arrows, respectively. In c)–f) the tilts of the oxygen octahedra are illustrated for the different layers including the Glazer's notation. The figure is adapted from [110].

In Fig. 2.13 the Q phases is included with an upper phase transition temperature ranging from 225 °C to 300 °C. Several experiments, e.g. XRD[115], differential scanning calorimetry [116], and temperature-dependent permittivity measurements [114, 117] have been conducted to identify transition temperatures. However, different values have been reported in literature for the Q phase [114–117] and no definite transition temperature could be pinpointed, yet.

2.5.1. Band structure

The orthorhombic band structure of the P phase with space group Pbcm has not been investigated by many scientist so far. Villa and Albe [70] calculated recently it's band structure and density of states (DOS) by density functional theory (DFT) using the Vienna ab initio simulation package (VASP), which is shown in Fig. 2.15. The highest occupied valence state is at the S point while the CBM can be found at the Γ point. Hence, the band gap of $NaNbO_3$ is an indirect band gap. Villa

and Albe determined the band gap by means of the Perdew-Burke-Ernzerhof (PBE) formalism of the generalized-gradient approximation (GGA). The resulting band gap of orthorhombic $NaNbO_3$ is 2.48 eV. It is known that this kind of functional is often underestimating the band gap of materials. Indeed, much higher experimental values of 3.4 eV to 3.5 eV are examined by optical spectroscopy [118–127].

To the best of my knowledge, only the cubic band structure was investigated theoretically and experimentally besides the orthorhombic band structure. A band gap of 2.927 eV [128] and 3.120 eV [129] was calculated by the Heyd–Scuseria–Ernzerhof (HSE) hybrid functional. This value is much larger than the calculated orthorhombic band gap of 2.48 eV [70] but is quite close the experimentally determined band energy of 3.290 eV [130] of the cubic structure, which was measured by UV-vis spectroscopy.

The DOS diagram of the orthorhombic structure shown on the right side of Fig. 2.15 illustrates clearly the contribution of the sodium, niobium, and oxygen orbitals to the valence and conduction bands. The valence band is mainly formed by the O p orbitals especially at the VBM, whereas the conduction band is mainly composed of Nb d orbitals, which significant influence the CBM.

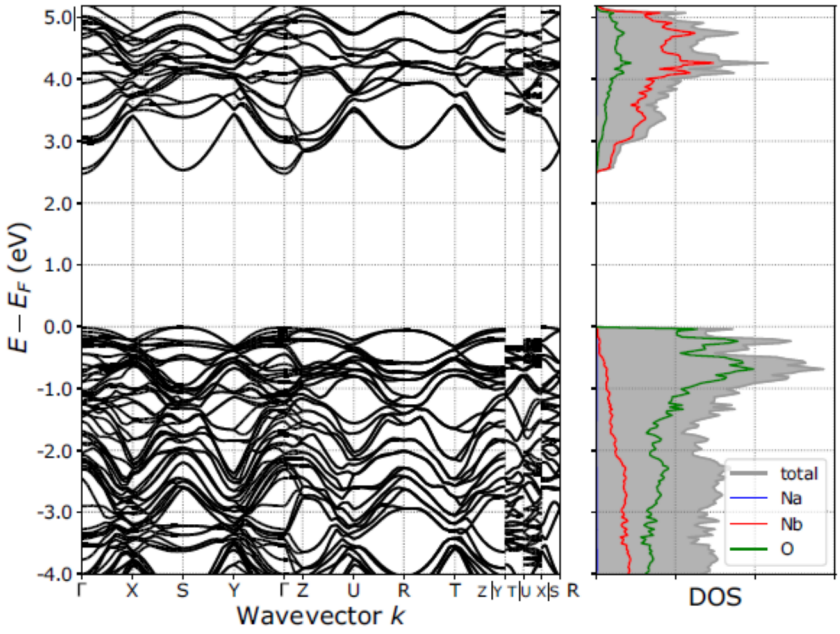

Figure 2.15.: Band structure and density of states of orthorhombic $NaNbO_3$ with space group Pbcm adapted from [70].

2.5.2. Polarization hysteresis loops

As already mentioned above, $NaNbO_3$ is an antiferroelectric material. Hence, double polarization hysteresis loops should be observed if an electric field is applied. In fact, not many double loops have been reported in literature for pure $NaNbO_3$ and all the samples were single crystals [131, 132]. Cross and Nicholson [131] measured the first double polarization loop on a $NaNbO_3$ single crystal but only when the field was applied perpendicular to the c-axis. Their recorded P-E-loop is shown in Fig. 2.16a). In polycrystalline samples no complete double hysteresis loops without isovalent or heterovalent substitution could be achieved so far. However, the AFE-to-FE transition for the first poling process was recently observed [133, 134] and is illustrated in Fig. 2.16b). Afterwards, the ceramic material stays in the ferroelectric state and exhibits only ferroelectric polarization loops. Hence, the AFE-to-FE transition is an irreversible transition in polycrystalline samples. This irreversible change from P to Q phase is also confirmed by transmission electron microscopy (TEM) [135]. Furthermore, several studies show that although a ferroelectric polarization hysteresis is measured, not all crystallites change to the Q phase but remain in the P phase meaning that P and Q phase coexist after applied electric field [111, 133]. The reason for this phenomenon is explained by internal stress clamping some of the domains, which are hindered to undergo a phase transition. Internal stresses develop due to the volume expansion from AFE to FE phase [133].

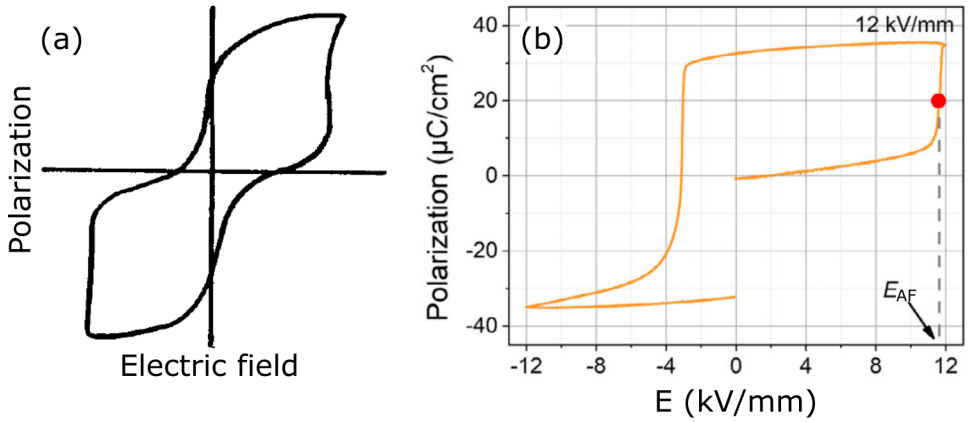

Figure 2.16.: Polarization versus electric field hysteresis of a single crystal measured perpendicular to the c-axis in a) [131] and of a ceramic sample in b) [27].

Quite some effort has been made in order to stabilize the double polarization loop in $NaNbO_3$. This has been mostly achieved by substitution of both, A- and B-site cation. The addition of different material systems, such as $CaZrO_3$ [26, 135], $SrZrO_3$ [136], $CaHfO_3$, [137], $SrSnO_3$ [27], $Ba_{0.5}Na_{0.5}TiO_3$ [134], and $BaZrO_3$ with $CaZrO_3$ [138], lead to measurable double hysteresis loops. In contrast, doping with only one element, e.g. Sr or Ca, does not result in the stabilization of the antiferroelectric phase [33, 139]. Therefore, it is not clear why these substitutes help to maintain a double polarization loop. One

explanation could be that they form defect dipoles with intrinsic defects, e.g. V'_{Na} or $V_O^{\cdot\cdot}$, resulting in pinched loops. This would mean that the observed double P-E-loops are not due to AFE-FE and FE-AFE back-switching but rather because of pinned ferroelectric domains as suggested by Arioka et al. [140]. However, TEM [135] and in situ high-energy XRD measurements [141] suggest that the substitutes indeed stabilize the FE-AFE back-switching. In addition, Tan et al. proposed that defect dipoles might influence the phase transition and stabilize the double polarization loop [72].
Another explanation why substitutes can stabilize the AFE phase is given by Shimizu et al. [26]. They proposed that decreasing the tolerance factor by substituting with larger A- and B-site atoms should stabilize the AFE phase over the FE phase. By adding Ca^{2+} on the Na-site and Zr^{4+} on the Nb-site the tolerance factor can be lowered quite effectively. Shimizu et al. verified their theory by preparing $(Na_{1-x}Ca_x)(Nb_{1-x}Zr_x)O_3$ samples and showing the stabilization of the AFE phase by the appearance of AFE superlattice reflections, dielectric measurements, XRD and TEM analysis of domain structures, and the appearance of double polarization hysteresis loops.
A similar study by Zhang et al. [27] showed that with addition of $SrSnO_3$ to the $NaNbO_3$ material the AFE phase can be put in favor over the FE phase. Sr^{2+} is occupying the Na-site while Sn^{4+} goes on the Nb-site. Both ions are larger than the corresponding host ions increasing the overall cell volume, which leads to a decreased tolerance factor as in the work of Shimizu et al. [26]. Zhang et al. suggested that this increased cell volume with a more disordered but less distorted local structure of the Na-site induced by the Sr^{2+} and Sn^{4+} ions stabilizes the AFE structure. This is supported by their first-principle calculations showing that the AFE phase is more stable than the FE phase by an energy difference of $1.4\,\mathrm{meV\,f.u.}^{-1}$. In addition, they measured double polarization hysteresis loops for the $SrSnO_3$-substituted samples, which further supports their theory.

Different forward switching fields E_{AF} and maximum polarization P_{max} values can be found in literature for single crystals and ceramic samples. For the single crystal shown in Fig. 2.16a) a E_{AF} of $8.75\,\mathrm{kV\,mm^{-1}}$ and a P_{max} of $11.4\,\mu\mathrm{C\,cm^{-2}}$ [131] is examined while in case of the ceramic sample shown in Fig. 2.16b) values of about $11.6\,\mathrm{kV\,mm^{-1}}$ and $38\,\mu\mathrm{C\,cm^{-2}}$ [133] are observed, respectively. However, both is influenced by the frequency at which the polarization loop is measured [133]. In case of substitution by other A- and B-site elements, E_{AF} is enhanced while P_{max} is decreased with increasing substitution content [26, 27, 136, 137].

2.5.3. Electrical conductivity

Only a few studies concerning the electrical conductivity of $NaNbO_3$ can be found in literature. The majority is conducted by impedance spectroscopy [142–146, 148, 150]. To the best of my knowledge there are only two experiments performed with a direct current (DC)-signal [147, 151]. Furthermore, single crystals [41, 145, 147, 151] as well as polycrystalline ceramics [142, 143, 146, 148–150, 152] have been investigated. Primarily, the temperature dependence of the electrical conductivity has been analyzed and activation energies over a wide temperature range from room temperature up to $800\,°C$ have been determined. The results of a view studies are illustrated in Fig. 2.17. Solid and dashed lines represent polycrystals and single crystals, respectively. The colors indicate the different electrodes used for the measurements. Above the conductivity curves, the different polymorphs of $NaNbO_3$ stable at different temperatures are shown.

In general, a low conductivity of $1 \times 10^{-12}\,S\,cm^{-1}$ to $1 \times 10^{-3}\,S\,cm^{-1}$ is measured in this temperature window. Thereby, the activation energies E_A vary from $0.1\,eV$ to $1.9\,eV$. However, most of the authors report at least two to three activation energy regimes. A clear change in E_A appears around the P-to-R phase transition temperature at $360\,°C$. Below this temperature E_A is approximately $0.83\,eV$ to $0.97\,eV$ [142, 146–148, 152] while above $360\,°C$ it is increased to $1.2\,eV$ to $1.8\,eV$ [142, 143, 147, 150]. Pisarski et al. [145] found another change in E_A from $1.0\,eV$ to $0.5\,eV$ when crossing $220\,°C$ with increasing temperature, respectively. A lower value ranging from $0.11\,eV$ to $0.53\,eV$ was also observed by

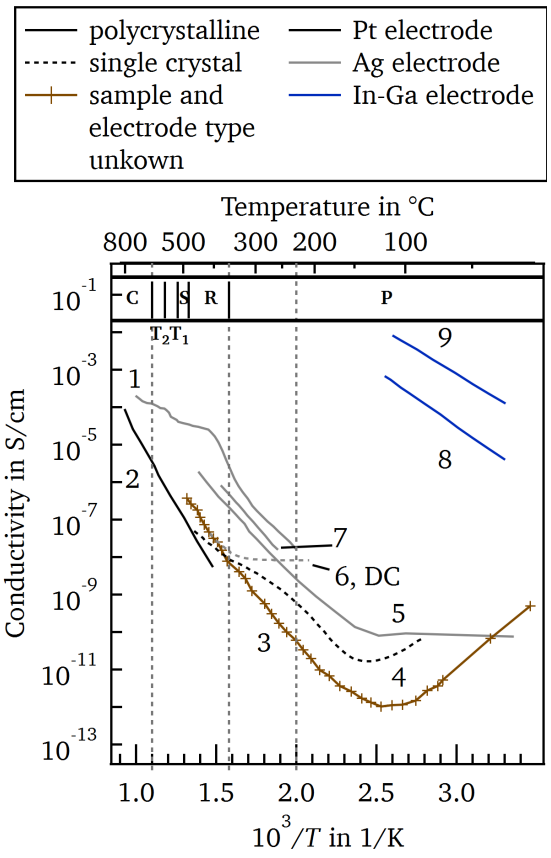

Figure 2.17.: Conductivity versus the inverse temperature $^1/_T$ for polycrystals (solid line) and single crystals (dashed lines) measured with different electrode materials. The numbers are linked to the corresponding reference: 1 [142], 2 [143], 3 [144], 4 [145], 5 [146], 6 [147], 7 [148], 8 ($Na_{0.99}Ca_{0.01}NbO_3$) and 9 ($NaNbO_3$) [149]. Curve 6 was probed with a DC-signal. All other measurements were conducted with an AC-field. The vertical dashed lines indicate changes in E_A.

Macutkevic et al. [142] at temperatures between $130\,°C$ and $430\,°C$ for reduced oxygen deficient $NaNbO_3$. Similar, $E_A = 0.55\,eV$ was measured by Raevski et al. [149] in case of reduced Ca-doped $NaNbO_3$ for Ca concentrations up to $1.5\,mol\,\%$ below $125\,°C$.
Lanfredi et al. [143] studied the conductivity at high temperatures and detected a E_A change at the T_2-to-C phase transition around $640\,°C$. E_A was $1.4\,eV$ from $400\,°C$ to $640\,°C$ and increased above $640\,°C$ to $1.67\,eV$. In addition, they investigated the influence of the porosity of the samples, which lead to a reduction of the activation energies in both temperature regimes. Doping with lithium results in the same effect [150]. All three temperature regimes are marked by dashed lines in Fig. 2.17.

Ruf et al. [146] had a closer look on the influence of sodium deficiency on the conductivity of $NaNbO_3$ by preparing samples with slightly different compositions. They observed an increase in E_A between $225\,°C$ and $400\,°C$ from $0.84\,eV$ to $1.22\,eV$ comparing the stoichiometric and the Na deficient composition. In contrast, the sodium enriched sample had a lower E_A of $0.49\,eV$ from $175\,°C$ to $400\,°C$. Hence, with increasing Na deficiency the activation energy is increasing.

A few studies examined the conductivity under reducing conditions e.g. heating in hydrogen [151] or in vacuum at a pressure of 10^{-1} Pa to 10^{-2} Pa [41, 149], which significantly increases the conductivity. In Fig. 2.17 the results from Raevski et al. [149] are shown for an undoped (No. 9) and a Ca-doped sample (No. 8), which were reduced by heating in vacuum at 10^{-1} Pa.
Molak et al. [41] measured the conductivity in dependence of the oxygen partial pressure. It clearly showed a n-type behavior when heating between $630\,°C$ and $780\,°C$. With decreasing oxygen partial pressure the conductivity increased. In addition, the whole conductivity profile exhibit higher values when measuring at higher temperatures.

In Table 2.2 all important information of the above mentioned references are summarized.

No clear explanation for the different observed activation energies and their origin is given so far. The majority interprets the observations with small polaron motion [144, 145, 149, 150, 152]. Pisarski et al. [145] interpreted the change in E_A at $360\,°C$ as a transition from polaron band conduction to hopping conduction. In the same way Bak et al. [144] explained the minimum at around $150\,°C$ (No. 3 in Fig. 2.17) with a change from tunneling to hopping conductivity of small polarons. In contrast, Macutkevic et al. [142] suggest that at least at high temperatures where E_A reaches $1.8\,eV$, which is approximately half of the band gap of $NaNbO_3$, might be due to intrinsic carrier conduction. Only Ye et al. [148] explain their observed E_A of about $1\,eV$ measured by impedance spectroscopy with oxygen ion migration.

Table 2.2.: Conductivity measurements reported in literature with important information including the conductivity at $500\,°C$ $\sigma_{500\,°C}$, activation energies within the temperature window of the P phase $E_{A,P}$, R to T_2 phase $E_{A,R-T_2}$, and C phase $E_{A,C}$, and conduction type.

sample type	electrode material	setup type	$\sigma_{500\,°C}$ in S cm^{-1}	$E_{A,P}$ in eV	$E_{A,R-T_2}$ in eV	$E_{A,C}$ in eV	conduction type	No. in Fig. 2.17	ref.
ceramic	Ag	AC	$3.8 \cdot 10^{-5}$	0.83	1.80	–	polaron	1	[142]
ceramic	Pt	AC	$1.0 \cdot 10^{-7}$	–	1.40	1.67	electronic	2	[143]
?	?	AC	$4.0 \cdot 10^{-7}$	–	1.60	–	small polaron hopping	3	[144]
crystal	Pt	AC	$5.0 \cdot 10^{-8}$	$T > 360\,°C$: 0.7 $360 > T > 220\,°C$: 0.5 $T < 220\,°C$: 1.0	–	–	small polaron hopping small polaron band mobility –	4	[145]
ceramic	Ag	AC	–	0.84	–	–	–	5	[146]
crystal	Ag	DC	–	0.97	1.15	–	–	6	[147]
ceramic	Ag	AC	–	0.95	–	–	$V_O^{\cdot\cdot}$ migration	7	[148]
Ca-doped ceramic	In-Ga	?	–	0.55	–	–	small polaron	8	[149]
ceramic	In-Ga	?	–	0.55	–	–	small polaron	9	[149]
Li-doped ceramic	Pt	AC	–	–	1.06	1.54	small polaron hopping	–	[150]

To the best of my knowledge, no studies specifically examining the differentiation between electronic and ionic conductivity exist. There have been some attempts to explain the observations by, e.g. polaron, free electron, or oxygen vacancy conduction as mention above. Some studies identify the ionization of oxygen vacancies as source for the free electrons [41, 146] or electron polarons [142, 149], which increase the conductivity in certain temperature windows.

2.6. Potassium niobate

Potassium niobate ($KNbO_3$) was investigated firstly by Matthias [99] in 1949, who reported it's ferroelectricity. Wood [153] analyzed the crystal structure and the phase transitions between room temperature and $500\,°C$ two years later. She identified the room temperature phase to be orthorhombic changing at around $225\,°C$ to a tetragonal structure, which becomes cubic at $435\,°C$ upon heating. During cooling Wood observed a shift to smaller transition temperatures of $200\,°C$ and $420\,°C$. Hence, $KNbO_3$ exhibits a temperature hysteresis at the phase transitions. Shirane et al. [154] later confirmed these phase transitions by temperature dependent permittivity measurements. In

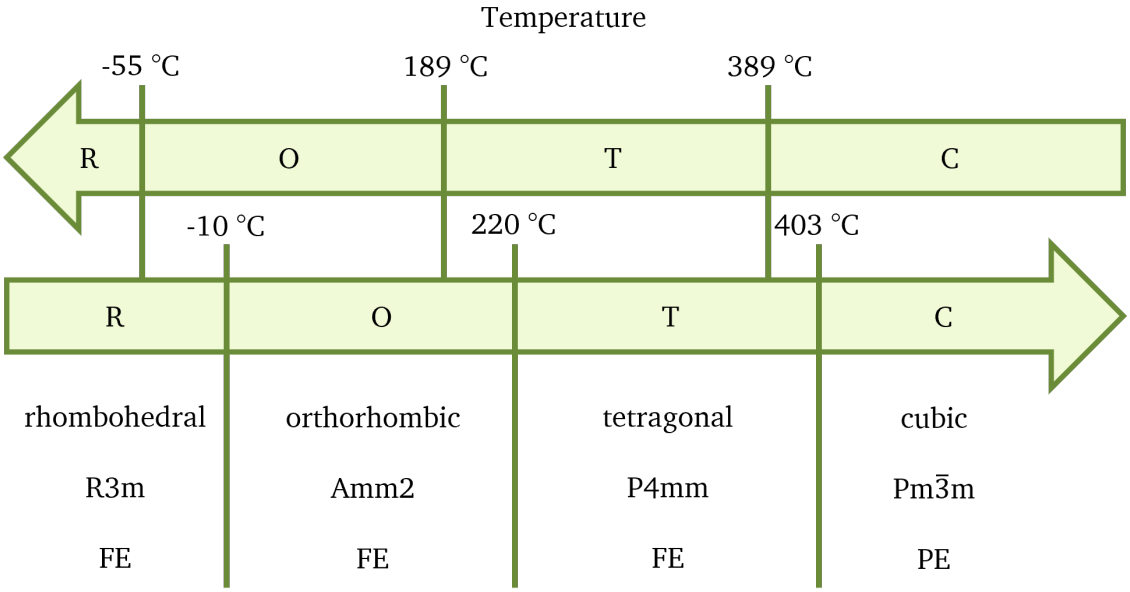

Figure 2.18.: All polymorphs of $KNbO_3$ including crystal structure, space group, and dielectric state. Transition temperatures of both, heating and cooling cycle, are included.

addition, they identified a low temperature rhombohedral phase with phase transition temperatures of $-10\,°C$ and $-55\,°C$ upon heating and cooling, respectively. Further NMR [155], neutron diffraction [156], and XRD analysis [157] confirmed and further refined the phase transition temperatures, which are illustrated in Fig. 2.18. Hewat [156] examined the four phases of $KNbO_3$ in more detail by neutron diffraction and found that the space groups of the rhombohedral, orthorhombic, tetragonal,

and cubic phase are R3m, Amm2, P4mm, and Pm3m, respectively. All phases except for the cubic structure are ferroelectric, hence, the Curie temperature T_C is around the tetragonal-cubic-phase transition.

The lattice parameters of the orthorhombic unit cell of $KNbO_3$ are $a = 3.973\,Å$, $b = 5.695\,Å$, and $c = 5.721\,Å$ [103, 156, 158, 159]. This structure is ferroelectric with a spontaneous polarization parallel to the orthorhombic c-axis. The spontaneous polarization results mainly from the displacement of the Nb atoms parallel to the c-axis while the oxygen octahedra remain almost unchanged. Two long and two short O-Nb bonds are formed due to the Nb displacements [156–158]. Figure 2.19 illustrates the room temperature structure of $KNbO_3$ perpendicular to the b-axis in a) and to the a-axis in b) and c). The yellow arrows indicate the displacement of the Nb atoms from the central position in the oxygen octahedra and the unit cells are marked by black rectangular. In b) and c) two orthorhombic unit cells are shown for a better identification of the pseudocubic unit cell colored in blue. From Fig. 2.19 the spontaneous polarization parallel to the c-axis is clearly visible. In addition, the arrangement in c) demonstrates that the Nb displacement and, hence, the spontaneous polarization are directed along the pseudo-cubic [011] direction.

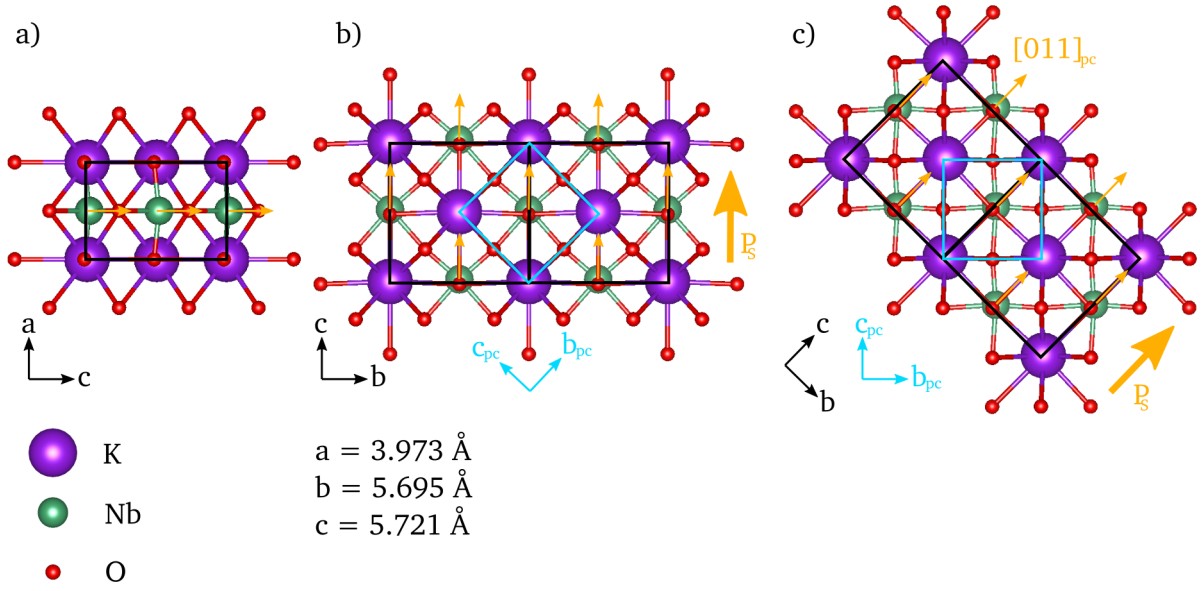

Figure 2.19.: Amm2 crystal structure of room temperature $KNbO_3$ perpendicular to the *b*-axis in a) and to the *a*-axis in b) and c). Arrows indicate the displacement of the Nb atoms and the direction of the resulting spontaneous polarization. The orthorhombic and pseudo-cubic unit cells are indicated by black and blue rectangular, respectively. The structures are visualized by the program Visualization for Electronic and Structural Analysis (VESTA) [160].

2.6.1. Band structure

The band structure and DOS of all $KNbO_3$ phases has been investigated by Schmidt et al. [161] with the Vienna Ab initio Simulation Package (VASP) using the Heyd-Scuseria-Ernzerhof (HSE) screened-Coulomb-potential hybrid functional based on structural data determined by PBEsol functionals. In Fig. 2.20 the results of the room temperature orthorhombic phase with space group Amm2 is shown. The valence band is mainly formed by hybridized Nb *d* and O *p* states. Here, the VBM is dominated by the O *p* orbitals. In contrast, the Nb *d* states are mainly contributing to the CBM, while at higher energies antibonding Nb *d* and O *p* orbitals are forming the conduction band [159, 161, 162]. VBM and CBM are indicated by red lines in Fig. 2.20. The gray shaded area is the total band structure calculated by means of the conventional Perdew-Burke-Ernzerhof (PBE) functional for comparison reason. $KNbO_3$ has an calculated electrical indirect band gap of 3.59 eV to 3.63 eV [161, 163] between the T point at the VBM and the Γ point at the CBM. The experimentally determined optical band gap is about 0.2 eV to 0.5 eV smaller in energy [121, 126, 127, 164–167]. Schmidt et al. [163] explained this discrepancy with exciton states, which lower the CBM and decrease the optical band gap probed by optical methods. Optical measurements are based on the absorption of a photon for band gap determination. However, an excitonic state can decrease the energy difference between the created electron-hole-pair, which results in a lower detected optical band gap. Schmidt et al. calculated an exciton binding energy of 0.5 eV and an electrical band gap of 3.63 eV. This explains perfectly the 0.2 eV to 0.5 eV smaller optical band gap.

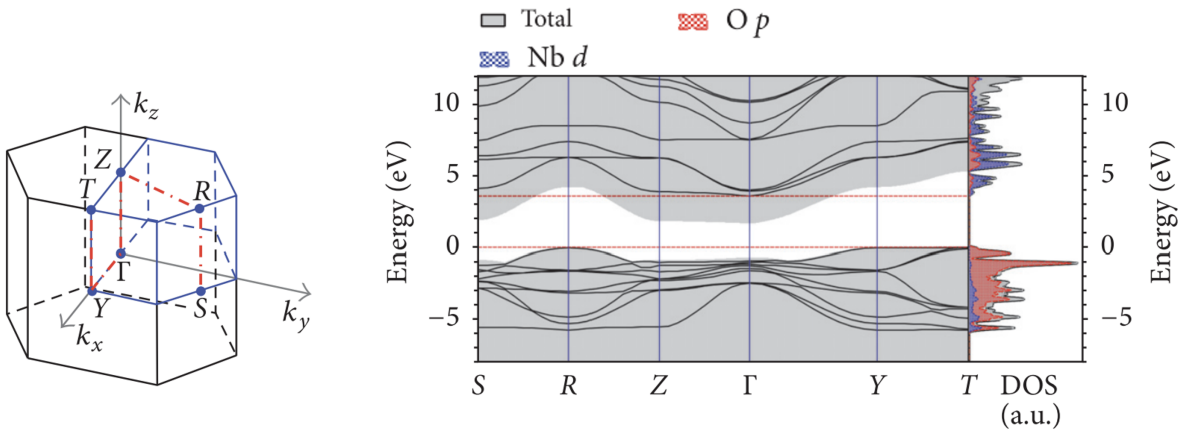

Figure 2.20.: First Brillouin zone, band structure, and density of states of orthorhombic $KNbO_3$ with space group Amm2 adapted from [161].

In addition, Schmidt et al. [161] calculated the band gap of the tetragonal and cubic structure. They obtained an energy value of 3.23 eV and 3.14 eV for the tetragonal and cubic lattice with space group

P4mm and $Pm\bar{3}m$, respectively. Both values are in good agreement with experimentally determined band gaps by UV-vis diffuse reflectance measurements [167]. Here, a band gap of 3.08 eV and 3.24 eV are detected for the tetragonal and cubic phase, respectively.

2.6.2. Polarization hysteresis loops

$KNbO_3$ is a ferroelectric material in which the spontaneous polarization mainly results from the displacement of the niobium atoms from the central position within the oxygen octahedra [158, 168]. Hence, for undoped $KNbO_3$ a ferroelectric polarization hysteresis loop is obtained by applying an electric field as shown in Fig. 2.21(a). Triebwasser [169] was the first author reporting spontaneous polarization values of $26\,\mu C\,cm^{-2}$ at the orthorhombic to tetragonal phase transition. Later investigations found that a spontaneous polarization of more than $40\,\mu C\,cm^{-2}$ can be measured [170, 171]. However, these experiments were conducted on single crystals. In contrast, ceramics usually exhibit much smaller maximum polarization values from $10\,\mu C\,cm^{-2}$ to $20\,\mu C\,cm^{-2}$ [172–174].
It is not easy to prepare dense $KNbO_3$ ceramics due to the high volatility of potassium at temperatures above $800\,°C$ [175–177]. Therefore, sintering aids [174, 178] or dopants [172, 179] are used in order to improve the densification. These additives can significantly influence the polarization-electric-field-behavior due to aging effects [71, 180, 181]. Figure 2.21(b) illustrates an unaged and aged $1\,mol\,\%$ Mn-doped $K(Nb_{0.9}Ta_{0.1})O_3$ sample [180]. Such effects are observed in other ferroelectric materials as well [28, 30, 73, 182].

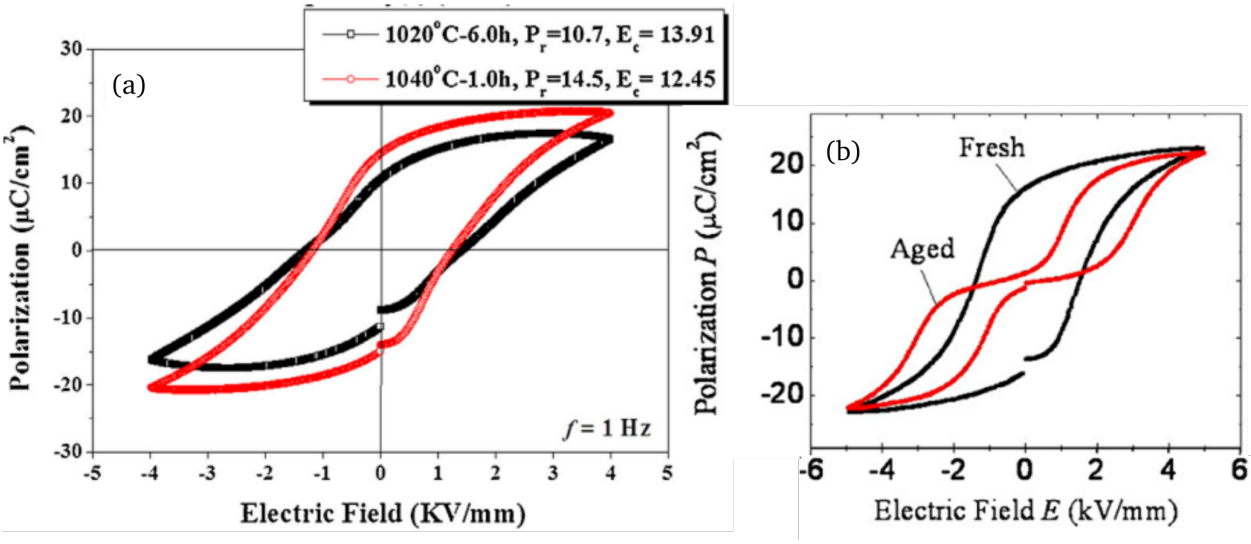

Figure 2.21.: Polarization versus electric field for an undoped $KNbO_3$ sample in (a) [173] and a $1\,mol\,\%$ Mn-doped $K(Nb_{0.9}Ta_{0.1})O_3$ sample in an unaged and aged state in (b) [180].

Three different origins were discussed in the past being responsible for the observation of aging effects [28–31]:

1. Volume effect: Electrical and/or mechanical dipoles align to the original direction of the spontaneous polarization forming a dipole polarization P_{D}, which acts as internal restoring force.
2. Domain effect: Point defects diffuse into the domain walls during aging time and pin the domain walls, which hinders the domain wall movement and, hence, the domain switching behavior.
3. Grain boundary or surface effect: Interface or surface states can attract charged defects and form space charge regions, which create an electric field influencing the domain switching behavior.

However, surface and domain effects could be often excluded as origin for aging leaving volume effects as predominant reason [29, 30, 73]. Usually aging is explained by defect dipoles aligning over time along the spontaneous ferroelectric polarization direction and forming a dipole polarization P_{D}. During electric field cycling the defect dipoles cannot follow the field, hence, staying in their original orientation. However, they facilitate and hamper domain switching depending on their orientation, which results then in a pinched double P-E-loop behavior. The defect dipoles are mostly composed of acceptor dopants and oxygen vacancies formed due to charge compensation of the acceptor states [29, 30, 73, 180].

2.6.3. Electrical conductivity

Similar as for $NaNbO_3$, not many reports of the electrical conductivity behavior can be found for undoped $KNbO_3$. The few results presented in literature are mainly conducted with an AC-signal. In Fig. 2.22 some results are illustrated in one graph. Solid lines represent polycrystalline materials, while dashed lines indicate single crystals. The colors specify the different electrodes used in the experiments. All samples show in the tetragonal and cubic phase a similar trend with activation energies ranging from $1.01\,\text{eV}$ to $1.40\,\text{eV}$. Table 2.3 summarizes electrode material, setup type, electrical conductivity at $500\,°\text{C}$, activation energy, and conduction type of the measurements shown in Fig. 2.22.

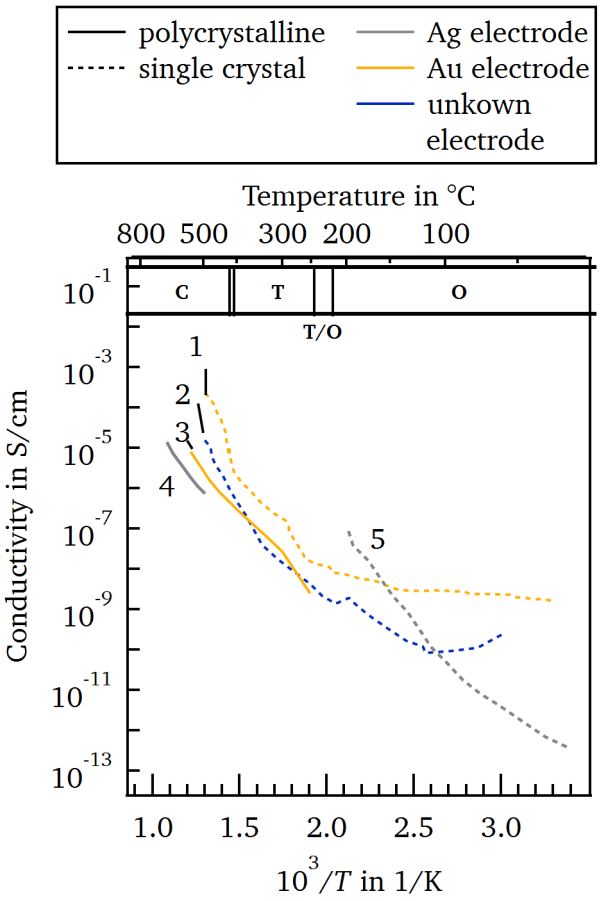

Figure 2.22.: Conductivity versus the inverse temperature $^1/_T$ for polycrystals (solid line) and single crystals (dashed lines) measured with different electrode materials. The numbers are linked to the corresponding reference: 1 [183], 2 [184], 3 [185], 4 [35], and 5 [186].

The conduction process and activation energies are either explained with ionic motion of mainly oxygen vacancies, [35, 185] or by small polaron hopping on the niobium site [183, 184]. Handerek et al. [184] observed a kink at the tetragonal-to-cubic phase transition and interpreted it as a change in the conduction mechanism from polaron band conductivity to polaron hopping conduction. Lee et al. [183] discovered as well a kink in the temperature dependent conductivity around the tetragonal-to-cubic phase transition. However, they explained the high temperature part with polaron conduction on the Nb-site while the low temperature regime was attributed to vacancies of alkali metal ions. It is clear that not a lot of attention has been drawn to the electrical transport mechanism in $KNbO_3$ resulting in the different explanations for the conduction behavior. To the best of my knowledge, no studies specifically examining the differentiation between electronic and ionic conductivity exist. In addition, no literature reports investigating the conduction behavior in dependence of the oxygen partial pressure have been performed so far.

Table 2.3.: Conductivity measurements reported in literature with important information including the conductivity at $500\,°C$ $\sigma_{500\,°C}$ and activation energy within the temperature window of the tetragonal phase $E_{A,T}$.

sample type	electrode material	setup type	$\sigma_{500\,°C}$ in S cm^{-1}	$E_{A,T}$ in eV	conduction type	No. in Fig. 2.17	ref.
crystal	Au	AC	$2.3 \cdot 10^{-4}$	1.02	small polaron hopping	1	[183]
crystal	?	?	$1.5 \cdot 10^{-5}$	1.40	small polaron hopping	2	[184]
ceramic	Au	AC	$2.5 \cdot 10^{-6}$	1.01	$V_O^{\cdot\cdot}$ migration	3	[185]
ceramic	Ag	AC	$7.4 \cdot 10^{-7}$	1.20	$V_O^{\cdot\cdot}$ migration	4	[35]
crystal	Ag	?	–	–	–	5	[186]

2.7. Preparation methods

The preparation of alkaline niobates has turned out to be quite challenging due to many difficulties, e.g. volatility [187] and sensitivity to moisture of the alkaline materials [188, 189] and the relative low melting point of alkaline niobates [18]. These can lead to problems such as sintering temperatures close to the melting point [173, 189–191], poor densification [173, 190, 192], non-stoichiometry [189], secondary phases [146, 187, 193], and abnormal grain growth [146, 173, 187, 190, 194]. A lot of different synthesis and sintering routes addressing these obstacles have been proposed, e.g. sol-gel [146, 195], hydrothermal [196], glycothermal [197], microemulsion-mediated [198], and mechanochemical processes [88] for synthesis and hot-pressing [195, 199] and spark-plasma sintering [200, 201] as alternative sintering routes. However, in this work only the standard solid state synthesis and normal sintering is used and described in the following.

For $NaNbO_3$- and $KNbO_3$-based ceramics usually Na_2CO_3, K_2CO_3, and Nb_2O_5 are used as precursor powders. It was shown that orthorhombic Nb_2O_5 results in a homogeneous composition, while the monoclinic polymorph leads to an inhomogeneity [191]. Therefore, it should be taken care of the polymorph of Nb_2O_5 during sample preparation. The precursors are mixed with a solvent and milled to ensure a homogeneous particle size distribution, which is very crucial for a good synthesis [191], and the right particle size, which is very important in regard of the initial sintering process dominated by grain growth [192, 194]. After milling the powders are dried, sieved, and mixed together in the right ratio. Here, great care must be taken because alkaline carbonates are very hygroscopic [188, 189], which can result in wrong weighing and non-stoichiometric ratio of Na/Nb and K/Nb, respectively. However, a precise stoichiometric ratio of 1:1 is very important to avoid the formation of secondary phases [189]. In addition, humidity is facilitating the evaporation of K_2O and Na_2O above $800\,°C$ [175, 189], which is unfavorable for preparing highly dense ceramics.
After homogenization, the powders are milled, dried, sieved, and pressed into pellets for calcination.

During calcination the following reactions take place in case of $NaNbO_3$:

$$Na_2CO_3 \rightarrow 2Na^+ + O^{2-} + CO_2 \tag{2.42}$$

$$2Nb_2O_5 + 2Na^+ + O^{2-} \rightarrow Na_2Nb_4O_{11} \tag{2.43}$$

$$Na_2Nb_4O_{11} + 2Na^+ + O^{2-} \rightarrow 4NaNbO_3 \tag{2.44}$$

The alkaline ions diffuse into the Nb_2O_5 powder reacting to $Na_2Nb_4O_{11}$ creating a shell around the Nb_2O_5 particles at temperatures higher than $500\,°C$. Afterwards, this shell is reacting further to $NaNbO_3$ above $700\,°C$ [202]. Therefore, the calcination temperature should be at least $700\,°C$. The synthesis reactions for $KNbO_3$ are much more complex as for $NaNbO_3$ because more reaction products are forming. Malič et al. [202] could identify $K_6Nb_{10.88}O_{30}$, $K_{5.75}Nb_{10.85}O_{30}$, and $K_4Nb_6O_{17}$ as intermediate reaction products. In addition, $KNbO_3$ starts to form already at $600\,°C$. Preparation of $K_{0.5}Na_{0.5}NbO_3$ showed that the potassium ions diffuse slower than the sodium ions, hence, being the growth limiting species [191, 202]. Calcination can be done several times to ensure that all precursor powders reacted to $NaNbO_3$ and $KNbO_3$. Between each step, the powders are milled, dried, sieved, and pressed into pellets again to further decrease and homogenize the particle size for a better sinterability. Finally, a greenbody is formed from the calcined powders and sintered in a dry oxygen-containing atmosphere. In case of $NaNbO_3$, below $950\,°C$ no densification can be observed. Grain growth starts at temperatures between $950\,°C$ to $1150\,°C$ [194]. Given that the melting point of $NaNbO_3$ is at $1422\,°C$ [18], the sintering window is very narrow. $KNbO_3$ starts to shrink already at $850\,°C$ [203, 204], however, the melting temperature of $1100\,°C$ [18] is lower as well compared to $NaNbO_3$. Therefore, the temperature range for a good sintering behavior is very limited.
One obstacle during sintering is the high volatility of the alkalines. Potassium and sodium evaporate already at around $800\,°C$ mostly in the form of an oxide [175, 177]. This can lead to the undesired formation of secondary phases [146, 193]. In addition, high sintering temperatures can result in further evaporation of K_2O and Na_2O, which can induce a liquid phase at the grain boundaries. Liquid phases enhance the sinterability, however, with an anisotropic thermodynamic trend favoring abnormal grain growth [146, 173, 190]. That sodium and potassium evaporation enhances the formation of abnormal grains is confirmed by the lower sodium and potassium concentration detected in abnormal grains [187]. On the one hand, high sintering temperatures are necessary to promote grain growth for highly dense ceramics. On the other hand, it facilitates the volatilization of sodium and potassium, which works against densification and supports abnormal grain growth. Furthermore, long sintering times enhance the creation of abnormal grains but are favorable for the preparation of dense ceramics [173, 194]. In the majority of the cases all these effects have a negative impact on the samples properties, e.g. dielectric and piezoelectric responses [187, 190]. Consequently, various approaches, e.g. using sacrificial powder [190, 205] or different sintering aids, e.g. CuO [72, 178, 206, 207], ZnO [174, 207, 208], MnO_2 [209], or MoO_3 [210] have been proposed. Sintering aids are not only helping for a better densification but modify the microstructure and electrical properties as well as they can simultaneously be a dopant. For some dopants the grain size is decreasing with

higher doping concentration [33, 211–213] while for other doping elements it is increasing [178, 209, 210]. Depending on the type of dopant, the polarization behavior, the permittivity, and the piezoelectric coefficients can be drastically changed [72, 178]. Furthermore, some sintering aids and/or dopants can help to reduce the leakage current of the material [206]. For more information on different substitution elements and how they are influencing the microstructure and electrical properties of the sample, the reader is referred to [16, 17, 214].

3. Characterization methods

3.1. Laser granulometry

Experimental objectives:

- Checking particle size of powders
- Analyzing particle size distribution

Laser granulometry is used to determine the particle size d of powders by means of laser diffraction. Figure 3.1 illustrates a basic setup of a laser granulometer. Laser light typically with a wavelength λ of 632 nm is focused on the sample cell, where it is diffracted by the particle probes. A multi-element array detector or multiple detectors convert the measured diffraction pattern into a size distribution information. Depending on the size of the particles in relation to the laser wavelength different models are used for the information conversion:

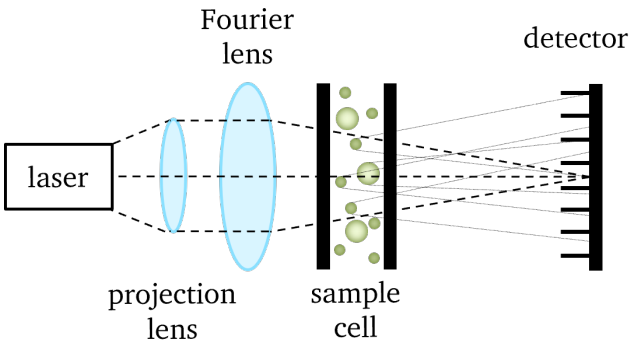

Figure 3.1.: Setup of a laser granulometer for particle size analysis.

- $d >> \lambda$: Fraunhofer model is applied.
- $d << \lambda$: Rayleigh scattering model is used.
- $d < \lambda$: Rayleigh-Gans optical model is employed.

These models and the information conversion are based on the following assumptions:

- All particles have a spherical shape.
- There is no interaction of the scattered light coming from different particles.

- The diffraction pattern measured at the detector is the sum of all scattering patterns from all particles.

Based on these assumptions, it is important that the sample contains well milled powder and to avoid agglomeration. For this purpose, the powder is mixed with some solvent in the sample cell, which is equipped with an ultrasonicator and a pumping system.
The interested reader is forwarded to [215] for more information about the technique, limitations, and the conversion models.

3.2. Optical dilatometry

Experimental objectives:

- Examination of shrinkage behavior during calcination and sintering of a ceramic probe
- Estimation of a suitable calcination and sintering temperature

The synthesis and sintering behavior of ceramic samples can be analyzed by an optical dilatometer. A schematic of the setup is shown in Fig. 3.2. For this purpose, the ceramic powder is pressed into cylindrical pellets and put into a furnace. While heating the probe up, a light source, e.g. a low voltage filament or a halogen lamp, is illuminating the sample. A camera takes periodically pictures of the sample. By evaluating the change in diameter the shrinkage and expansion behavior can be analyzed by means of Eq. 3.1 [216].

$$\frac{\Delta l}{l} = \frac{l_{\mathrm{RT}} - l_T}{l_{\mathrm{RT}}} \cdot 100 + CLTE \cdot 100 \cdot (T - T_{\mathrm{RT}}) \tag{3.1}$$

l_{RT} and l_T is the diameter of the sample at room temperature T_{RT} and the measured temperature T, respectively. $CLTE$ is the coefficient of linear thermal expansion.
For more information the reader is referred to [217].

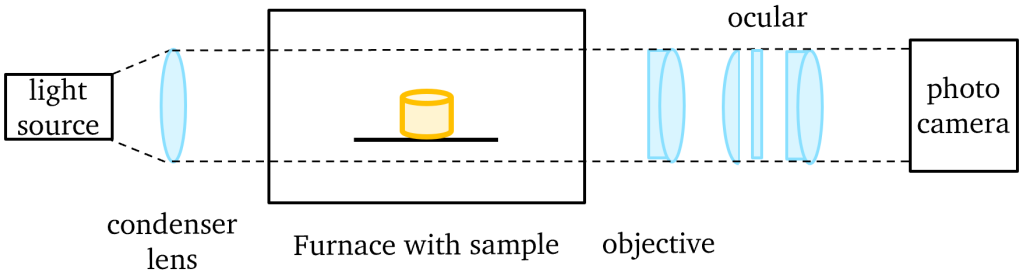

Figure 3.2.: Setup of an optical dilatometer for investigating shrinkage and expansion behavior of ceramic pellets during synthesis and sintering.

3.3. Archimedes method

Experimental objectives:

- Determination of the relative densification of ceramic samples

The density can be evaluated by the Archimedes method, which requires weighing of a ceramic sample in three different conditions:

1. In a completely dry state (m_{air})
2. In a completely soaked state measured in distilled water ($m_{\text{H}_2\text{O}}$)
3. In a completely soaked state measured in air ($m_{\text{H}_2\text{O,air}}$)

For the first weight measurement, the sample is weighted in a completely dry state. Afterwards, the sample is immersed in distilled water in a beaker. In order to remove all air trapped in the pores the beaker is put under a vacuum bell jar. Then, the sample is weighted in distilled water ($m_{\text{H}_2\text{O}}$). For the last weight measurement, the sample is taken out of the distilled water, dried with a clean wipe, and put on a scale in air ($m_{\text{H}_2\text{O,air}}$). Figure 3.3 shows the schematic setup.

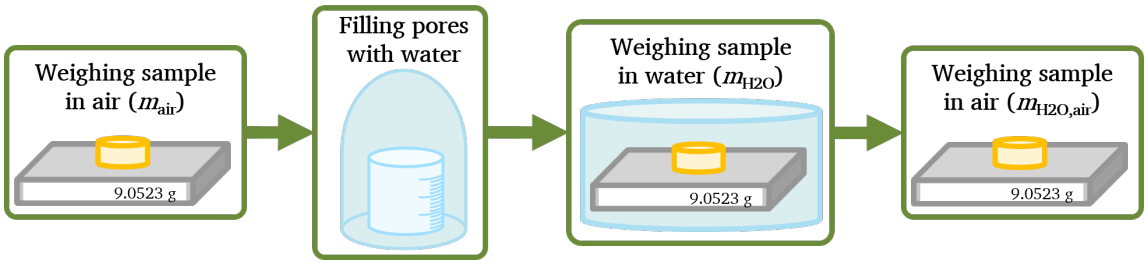

Figure 3.3.: Setup of the Archimedes principle for measuring the sample's density.

The density of the sample ρ can be calculated by means of these three weight measurements and Eq. 3.2 [218]:

$$\rho = \frac{\text{dry weight of sample}}{\text{weight loss in water}} \cdot \text{density of water} = \frac{m_{\text{air}}}{m_{\text{H}_2\text{O,air}} - m_{\text{H}_2\text{O}}} \cdot \rho_{\text{H}_2\text{O}} \tag{3.2}$$

Hence, the relative densification ρ_{rel} can be determined by:

$$\rho_{\text{rel}} = \frac{\rho}{\rho_{\text{theo}}} \cdot 100 \tag{3.3}$$

Here, ρ_{theo} is the theoretical density of the sample calculated by means of the atomic masses, the crystal structure, and the lattice parameters taken from XRD data.

3.4. Secondary electron microscopy

Experimental objectives:

- Determination of sample morphology, e.g. size, shape, and distribution of grains, precipitates, and pores
- Identification of secondary phases

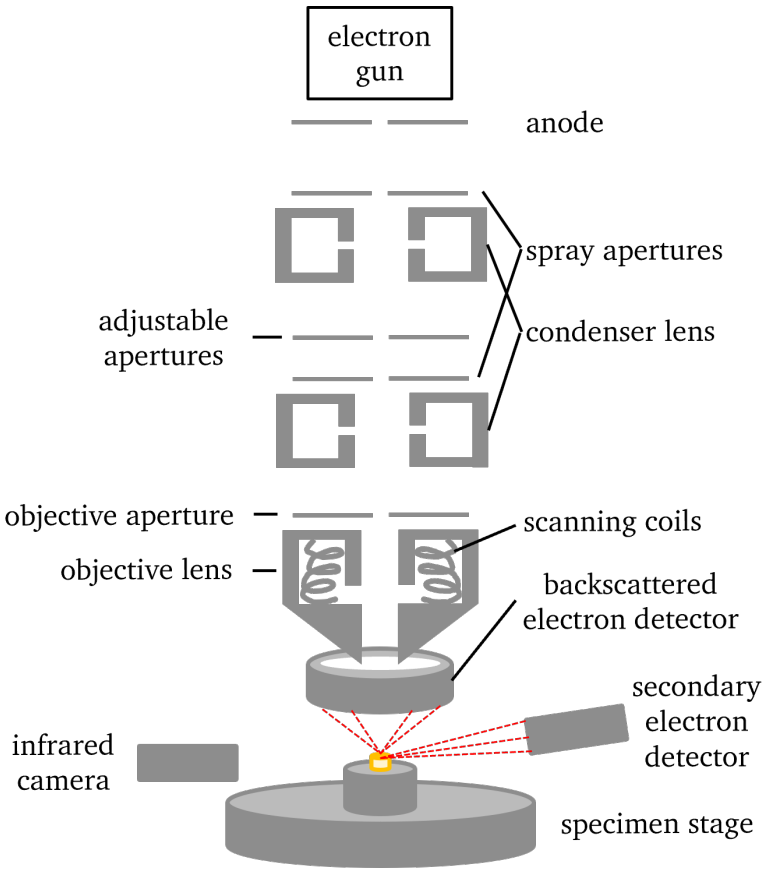

Figure 3.4.: Typical setup of a secondary electron microscope adapted from [219].

A secondary electron microscope can be used to image a sample with a high magnification up to 200000 times. Hence, the sample's morphology, e.g. grain size and shape or precipitate size, surface topography, and pore size, shape, and distribution can be analyzed. The setup of a typical SEM is illustrated in Fig. 3.4. Most parts are kept under vacuum to ensure electron generation and to avoid scattering events with other particles.
An electron beam is generated by an electron gun. Typical electron guns used in a SEM are tungsten filament, LaB_6 emitter, Schottky field emission, and cold field emission guns. In this work a Schottky field emitter is used, which consists of a sharp tungsten tip connected to a tungsten wire. The high negative voltage applied at the cathode lowers the work function of the material because of the high electric field generated due to the small tip size. In addition, the emitter is heated up by a current flow. The thermal energy is due to the lowered work function high enough to emit electrons (thermionic emission). Furthermore, the tungsten tip is coated with ZrO_x, which further reduces the work function.
The diameter of the electron beam must be confined and focused for a good resolution, which is

done by electromagnetic lenses. Scan coils are used in order to screen the sample. The electron beam interacts with the sample by creating secondary, backscattered, and Auger electrons, and characteristic x-rays. The secondary electrons used for imaging are generated near the surface of the probe in a depth of around 100 nm. These electrons exhibit a low kinetic energy. Therefore, a positive voltage is applied at a Faraday cage, which covers the front of the detector, in order to collect all secondary electrons.
The detector is usually an Everhart-Thornley (E-T) detector, which consists of a scintillator and a photomultiplier. At the scintillator, the collected electrons are converted into photons. Their number depends on the kinetic energy of the incoming electrons. These photons are directed through a quartz glass window out of the SEM-chamber to the photomultiplier, which is located outside the vacuum chamber. Here, the photons are transformed back to photoelectrons by interacting with a photocathode. These low energy photoelectrons are amplified by an array of dynodes. By impacting at a dynode the photoelectrons create two or more secondary electrons, which are accelerated to the next dynode. By this cascade effect, the signal gets amplified for a strong image contrast. The interested reader is forwarded to [219] for more information.

3.5. X-ray diffractometry

Experimental objectives:

- Determination of the sample's crystal structure
- Identification of secondary phases

The descriptions in this section are mainly based on the book *Moderne Röntgenbeugung* written by Lothar Spieß et al. [220].
Analysis of the crystal structure and identification of secondary phases can be done by XRD, which is based on the diffraction of an incident x-ray beam by the crystal lattice planes. This situation is illustrated in Fig. 3.5. Two reflected beams from two different lattice planes are either annihilating (destructive interference) or enhancing each other (constructive interference) depending on the wavelength of the incident photons and the distance between the lattice planes, hence, the crystal structure. As a consequence, every crystal structure is creating it's own diffraction pattern, which can be used as identification.

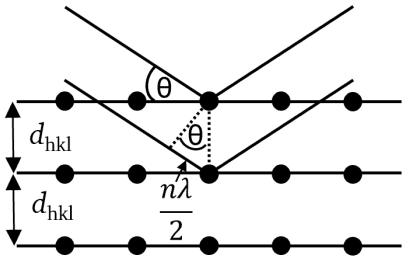

Figure 3.5.: Two incident x-ray beams, which get diffracted at the crystal lattice planes illustrating the relation of the Bragg equation.

Only constructive interference leads to a measurable signal, which can be described by the Bragg Equation.

$$2d_{hkl} \cdot \sin(\Phi_{hkl}) = n \cdot \lambda \tag{3.4}$$

d_{hkl} is the distance between the lattice planes with the Miller indices hkl. Φ_{hkl} and λ are the angle and the wavelength of the incident x-rays, respectively. n is an integer giving the order of the interference. The distance $n \cdot \lambda$ between two diffracted beams leads to a constructive interference.

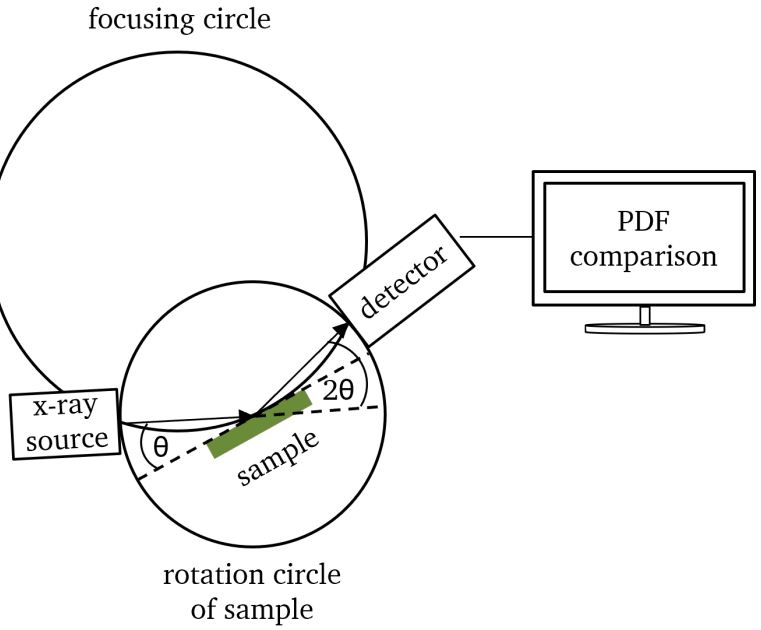

Figure 3.6.: Schematic of a x-ray diffractometer with Bragg-Brentano geometry of a theta-2 theta-goniometer.

A typical setup of a x-ray diffractometer is shown in Fig. 3.6. The x-rays are created in a x-ray tube frequently employing a Cu anode. A single crystal monochromator filters the Cu $K\alpha_1$ and $K\alpha_2$ radiation with a photon energy of $8047.78\,\text{eV}$ and $8027.83\,\text{eV}$, respectively. By means of a slit diaphragm the energetically lower $K\alpha_2$-line can be blocked. The photons of the $K\alpha_1$-line can interact in different ways with the sample. Besides elastic scattering, which is required for the diffraction, inelastic scattering and absorption can take place. These processes adding up to a continuous background signal, which must be subtracted before analysis of the diffractogram. The diffracted beam is focused to the detector, which is in the most cases a proportional counter tube or a scintillator.
The goniometer used in this work is a theta-2 theta-goniometer meaning that the x-ray source is fixed in position while sample stage and detector can be moved. In order to scan the whole 2θ-range, the probe is rotated with the angular speed ω whereas the detector is moved with 2ω along the focusing circle. Samples in form of powder can be filled in a small container covered with a protection foil. Furthermore, the Bragg-Brentano arrangement is applied within this work applicable for polycrys-

talline sintered pellets. Here, x-ray source, sample, and detector are located on a focusing ring, which has a decreasing radius with increasing 2θ-angle. However, only the grains with the lattice planes parallel to the surface are measured.
The detector counts the x-rays for each 2θ-angle. The resulting diffractogram can be compared with a database of powder diffraction files (PDF). By checking the position and intensity ratios of the measured reflexes with the PDFs of the relevant materials, the composition and crystal structure of the samples can be confirmed and secondary phases can be identified.

3.6. Polarization hysteresis

Experimental objectives:

- Examination of the probe's poling behavior, e.g. dielectric, (anti)ferroelectric, relaxor
- Identification of sample's state, e.g. aged or unaged
- Determination of material characteristics such as remanent P_r and maximum polarization P_{max} and coercive field E_{coer}

In order to check whether a material is dielectric, ferroelectric or antiferroelectric the change in polarization with applied electric field can be measured. The polarization can be indirectly examined by measuring the accumulated charge of the sample, which is in series to a linear capacitor, or by detecting the displacement current by means of the voltage drop over a known resistor in series. The former is done via a so-called Sawyer-Tower circuit [221], which is illustrated in Fig. 3.7. With the sample's area and Eq. 2.5 the polarization can be calculated. By measuring the voltage drop over a resistor with a known resistance, the displacement current of the sample can be examined with the so-called virtual ground method. This method utilizes a current-to-voltage converter and is very useful when measuring small capacitors [54, 222].

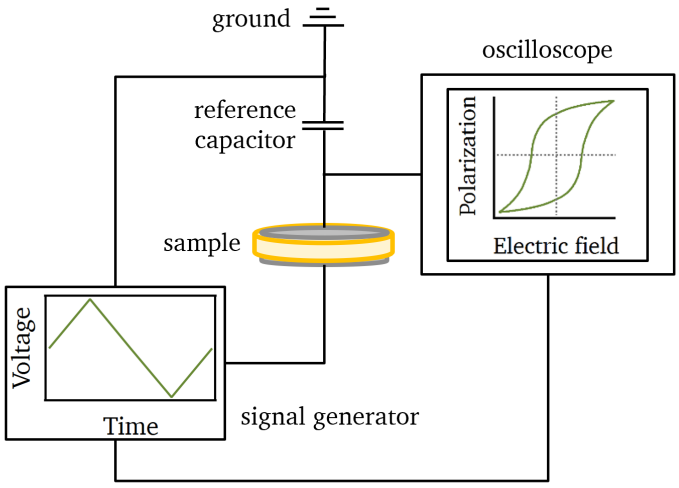

Figure 3.7.: Schematic of a Sawyer-Tower circuit used for polarization hysteresis loop measurements.

3.7. Permittivity

Experimental objectives:

- Determination of temperature and order of phase transitions
- Analyze influence of leakage currents

The permittivity is a material characteristic, which connects the polarization with the electric field. It is both frequency and temperature dependent. Hence, measuring the permittivity as function of frequency and temperature can give information about, e.g. temperature and order of a phase transition, relaxation processes, leakage currents, and influences of dopants [50].
In this work, the permittivity is examined by recording the capacitance of the sample with a LCR meter. By means of Equation 2.6 and the known sample geometries, the permittivity can be calculated.

$$C = \epsilon_0 \cdot \epsilon_\mathrm{r} \cdot \frac{A}{d}$$

The sample is heated in an oven and the temperature is controlled by a thermocouple element. The covered frequency range can be set at the LCR meter.

3.8. Photoelectron spectroscopy

Experimental objectives:

- Determination of the sample's composition
- Investigation of Fermi level positions and boundaries of the Fermi level, e.g. Fermi level confinement due to trap states
- Examination of segregation effects
- Analysis of interface reactions and interface behavior to different electrode materials
- Finding possible correlations between electronic structure and (anti)ferroelectric properties

The major description in this section is based on the content of the textbook *Photoelectron spectroscopy - Principles and Applications* written by Stefan Hüfner [223].
XPS measurements are examined to determine the composition and the Fermi level of the investigated samples before and after oxidizing or reducing treatments. For this purpose, high energy x-rays are emitted by a x-ray tube with an aluminum anode. A monochromator filters the x-rays with a photon energy of $1486.6\,\mathrm{eV}$ corresponding to the Al $K\alpha$-line with an energy width of $0.85\,\mathrm{eV}$. These

monochromized x-rays hit the sample and are absorbed by it. The energy of the x-ray photons is high enough to excite core level electrons into electronic states above the vacuum level out of the sample. These so-called photoelectrons are accelerated towards the analyzer, which separates them by their kinetic energy. The analyzer used in this work is a spherical capacitor analyzer (SCA), which allows only electrons with the right pass energy to reach the detector. By using an electrostatic lens before the entrance slit of the analyzer, the incoming electrons can be retarded or accelerated to the pass energy. Applying different voltages to the lens enables to scan the whole energy range of the photoelectrons. After passing the analyzer, the electrons are counted at the detector, which is a multi channel detector in this work. The whole XPS-setup is shown in Fig. 3.8. The binding energy of the photoelectrons E_{BE} can be calculated by subtracting their kinetic energy E_{kin} and the work function of the analyzer Φ_{A} from the energy of the x-ray photons $h\nu$.

$$E_{\mathrm{BE}} = h\nu - E_{\mathrm{kin}} - \Phi_{\mathrm{A}} \tag{3.5}$$

As the sample is electrically connected to the spectrometer during the measurements E_{kin} is only

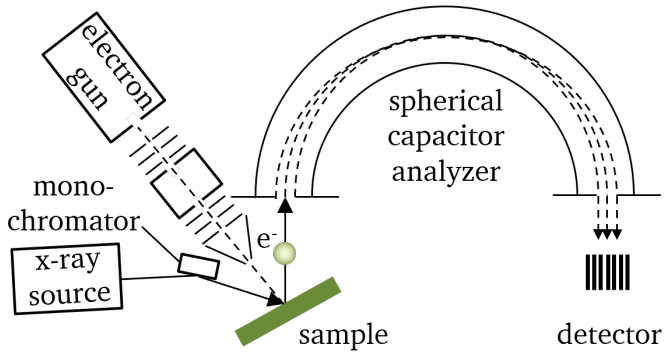

Figure 3.8.: Schematic of a XP-spectrometer.

depending on the workfunction of the spectrometer, which is calibrated by setting the Fermi edge of a clean metal calibration sample to $0\,\mathrm{eV}$. In addition, this electrical connection allows for electrons to flow from the spectrometer to the sample's surface to balance the positive charge created by the excited photoelectron. In case of insulating samples, an accumulation of positive charges can occur because the electron transfer is too slow. This results in overestimated binding energies of the photoelectrons and deformed peak shapes. In the worst case the sample cannot be measured at all. Here, an electron gun can be used to compensate for the positive surface charge. However, the binding energy can still be wrong due to over- or undercompensation.

XPS is a surface sensitive method. The penetration depth of the incoming photons is larger than the information depth d_{i} because the excited photoelectrons are slowed down by mainly electron-electron collisions, which are called plasmons, resulting in a small mean free path λ within the solid probe. Figure 3.9 illustrates the mean free path of the electrons as a function of their kinetic energy. The

minimum results from excitation of the plasmons, which is highest around $50\,\text{eV}$. The information depth of XPS is considered to be $d_\text{i} \approx 3\lambda$, hence, ranging from a few atomic layers to about $10\,\text{nm}$. This small information depth requires clean surfaces without a lot of absorbents on the surface to ensure a high signal intensity. Therefore, an ultrahigh vacuum atmosphere is essential for a good measurement. In addition, an ultrahigh vacuum atmosphere ensures that the emitted photoelectrons do not collide with gas phase species on their way from the sample to the detector, maintaining their kinetic energy.

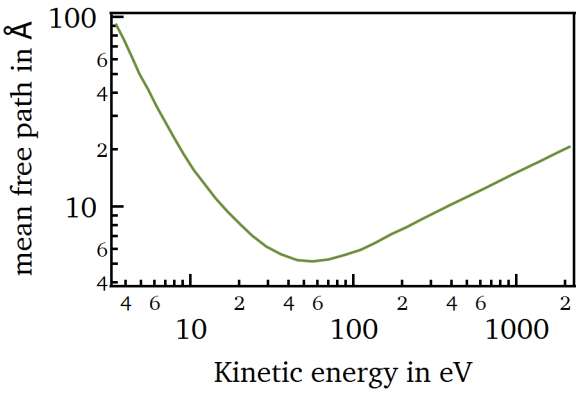

Figure 3.9.: Mean free path λ of the photoelectrons within a solid sample in dependence of their kinetic energy.

The information depth depends on the angle between sample and detector:

$$d_\text{i} = 3 \cdot \lambda \cdot \sin(\alpha) \tag{3.6}$$

Collecting the photoelectrons at different angles is used to gain information as a function of depth and is called angle resolved x-ray photoelectron spectroscopy (ARXPS). A $90°$ angle between sample surface and detector reveals information of subjacent layers of the surface, while a smaller angle corresponds to a highly surface-sensitive measurement of the surface-near layers. Comparing the peak intensity of a subjacent layer and a surface-near layer related measurement, shows if an element is only absorbed on the surface or part of the material. In addition, segregation of a species can be identified.

The whole process of generating a photoelectron can be explained in more detail by means of the three-step model, which divides the creation of a photoelectron into the following three steps:

1. Photoexcitation of the electron

2. Transport of the electron to the surface

3. Penetration of the electron through the surface and escaping into the vacuum

When a photoelectron is emitted, a photohole is left behind at the inner atomic shell of the atom. Consequently, the atom is not in its ground state any longer, which is the so-called final state. The energy state before photoemission is called initial state. The binding energy of the photoelectron E_BE can then be calculated by the energy difference of final state E_final having (N-1) electrons and

the initial state E_{inital} with N electrons.

$$\begin{aligned} E_{\text{BE}} &= E_{\text{final}}(N-1) - E_{\text{inital}}(N) + \Delta E_{\text{c}} - E_{\text{r}} \\ &= |\epsilon_{\text{i}}| + \Delta E_{\text{c}} - E_{\text{r}} \\ &\approx |\epsilon_{\text{i}}| \end{aligned} \tag{3.7}$$

Initial and final state energies can be calculated by the Hartree-Fock approximation, which neglects correlation interactions. Hence, these interactions must be included by the correction factor ΔE_{c}. In addition, the remaining electrons in the system will relax according to a different screening of the nucleus due to the created photohole. This leads to an extra term E_{r} compensating for this relaxation effect. Furthermore, according to Koopmans' theorem [224] the energy difference between initial and final state determined by the Hartree-Fock approximation equals the eigenstate value of the initial state ϵ_{i}. ΔE_{c} and ΔE_{r} are almost canceling each other out. Hence, the photoelectron binding energy can be approximated by the eigenvalue of the initial state.
The photoelectron binding energy can be influenced by different processes, which can be separated into initial- and final-state effects. Initial-state effects directly affect $|\epsilon_{\text{i}}|$ from the beginning by alteration of the density of states of the initial state. A change in the oxidation state of an atom is such an initial-state effect and is called the chemical shift. In general, the higher the positive charge of an atom the higher the binding energy [225].
During the different steps of the three-step model, the electron can interact in various ways loosing some of its kinetic energy, which results in a splitting or a change in the shape of the emission line. This phenomenon is called final-state effect. It can be distinguished between intrinsic and extrinsic final-state effects. Intrinsic final-state effects are processes occurring during step one, while extrinsic final-state effects are interactions with the photoelectron appearing after step one [223, 225]. Table 3.1 summarizes all possible final-state effects including the information if they are intrinsic or extrinsic and how they are influencing the emission lines. Besides initial- and final-state effects, artifacts can occur in the measured XP-spectrum and are listed in Table 3.1 as well.

Table 3.1.: Final-state effects and measurement artifacts, which can appear in a XP-spectrum.

final-state effect	type	impact	description
spin-orbit coupling	intrinsic	line splitting or broadening	The magnetic moment of an electron due to its spin s can couple with the orbital angular momentum l of the electron created by its movement with the orbit. An emitted photoelectron leaves an unpaired electron in the orbit. The spin-orbit coupling of this unpaired electron influences E_{kin} of the photoelectron. Taking the total angular momentum $j = \|s+l\|$ into account, leads to two possible states for each orbital type (except for the s-orbital), which results in an emission line splitting. The intensity ratio of these two lines is given by the ratio of the number of degenerate states $(2j + 1)$.
spin-spin coupling	intrinsic	line splitting or broadening	The magnetic moment of an electron due to its spin s can couple as well with the spin of the valence shell resulting in two final states, which are responsible for a splitting or broadening of the emission line.
photohole screening	intrinsic	line splitting or broadening	Adjustment of the localized electrons of the atom and of the delocalized valence electrons to the suddenly present electrostatic potential.
plasmons	intrinsic or extrinsic	line splitting or broadening	Plasmons are collective vibrations of the electron gas, which can be excited intrinsically, when the delocalized valence electrons screen a photohole, or extrinsically by the photoelectron on its way out of the sample in step two and three. The photoelectron looses some of its kinetic energy, which produces a higher measured binding energy. A satellite line appears at higher binding energies in the spectrum. The distance between main and satellite line equals the plasmon energy.
shake-up line	intrinsic or extrinsic	line splitting or broadening	The photoelectron can excite a second electron to a higher energy side by transferring some of its energy. This results as for the plasmons in a satellite peak at higher binding energies.

shake-off line	intrinsic or extrinsic	line splitting	The photoelectron can also excite a second electron above the vacuum level by loosing some of its energy, which leads to a second final state.
phonon interaction	intrinsic or extrinsic	line broadening	Phonons can interact intrinsically with the created photohole or extrinsically by scattering inelastic with the photoelectron in step two and three.
artifact	**type**	**impact**	**description**
inelastic scattering	extrinsic	intensity loss	The photoelectron is scattering inelastically during step two with other electrons or ions, which leads to a loss of kinetic energy. The amount of energy loss depends on the number of scattering events, which is visible as continuous energy tail instead of a discrete satellite line. The energy tails of different emission lines add up to a background intensity with increasing binding energy.
secondary electrons	extrinsic	intensity loss	Secondary electrons are emitted by an energy transfer from the kinetic energy of the photoelectron. These secondary electrons appear similar to the inelastic scattering effects as continuous energy tail on the higher binding energy side of each emission line and contribute to the background intensity.
charging effect		line shift and broadening	The generated photoholes create a positive surface charge, which must be refilled by electrons. For metals, electrons can be easily supplied. In contrast, in case of insulators electrons cannot be provided fast enough, which induces a positive surface charge. This surface charge reduces the kinetic energy of the photoelectron, which increases the measured binding energy of the emission lines. Therefore, charging effects lead to an energy shift of the peak position and a broadening of the line shape. In case of very high charging effects, the emission line cannot be recorded at all and is ”running away” from the measured spectrum.

In general, a photoelectron can be created by exciting and emitting a localized inner electron or a delocalized valence electron, which results in a core level emission line or an emission line adding to the measured valence band. Furthermore, Auger electrons generated by an energy release of a second electron filling the photoelectron can be detected. The Auger electrons are indexed with *XYZ*. *X*, *Y*, and *Z* indicate the shell from which the photoelectron is excited, the higher energy shell from which a second electron is filling the created photohole, and the higher energy shell from which the Auger electron is then emitted, respectively. The energy release of the second electron is the energy difference between shell *X* and *Y*, which is then transferred to the Auger electron. Figure 3.10 shows a XP-spectrum recorded over the whole energy range including the core level and Auger emission lines, valence band, final-state effects, and measurement artifacts.

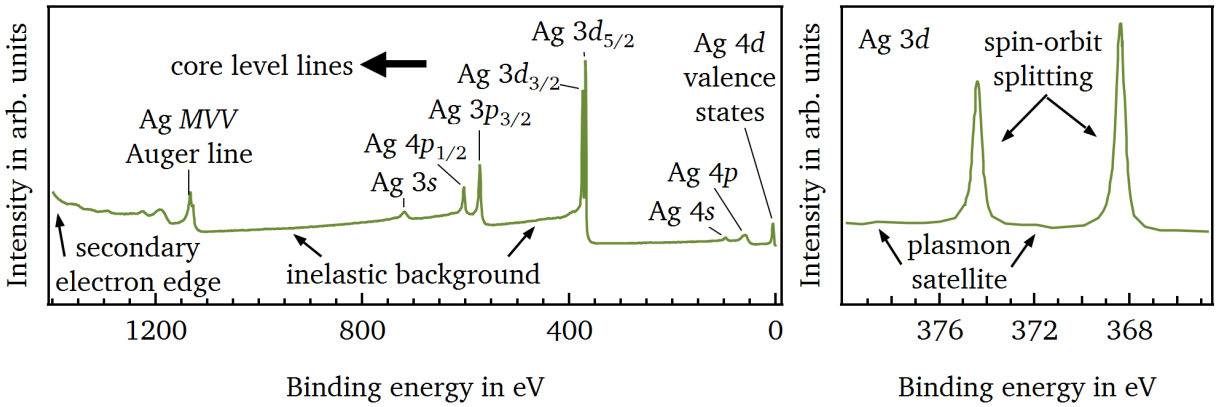

Figure 3.10.: Survey spectra of silver with all characteristic emission lines, final-state effects, and measurement artifacts (left) and a detailed spectra of the Ag 3*d* core level (right). Please not the absence of carbon emissions at $285\,\mathrm{eV}$ binding energy, which is achieved by $3\,\mathrm{min}$ to $5\,\mathrm{min}$ Ar-sputtering.

3.8.1. Quantitative analysis

XPS can be used to check quantitatively the composition of a material. The atomic fraction c_x of each element can be calculated by Eq. 3.8.

$$c_\mathrm{x} = \frac{I_\mathrm{x}/ASF_\mathrm{x}}{\sum_\mathrm{x} I_\mathrm{x}/ASF_\mathrm{x}} \tag{3.8}$$

Here, I_x is the integrated area of the most intense core level peak of an element. The atomic sensitivity factor ASF_x is a correction factor, which includes instrumental influences such as the angle between photon source and detector, the detector efficiency, and the photon flux and sample

specific contributions, e.g. the density of atoms in the detected area, the photoionization cross-section, and the mean free path of the photoelectrons λ [226]. In order to calculate I_x the background must be subtracted from the peak intensity. There are different functions, e.g. the Shirley function [227], which mimic the increase of the background with each photo emission line. However, it is not easy to correctly describe the background with these functions especially if satellite structures superimpose the core level peak. Therefore, the evaluated compositions should be taken with cautions.

3.8.2. Determination of the band gap

The energy gap of a material can be determined by the energy loss of the photoelectrons, which loose energy by plasmon and band-to-band excitation. These electrons appear in the XP-spectrum at higher binding energies because they reach the analyzer with a lower kinetic energy. Hence, the minimum energy loss equals the band gap of the material and is represented by the energy distance between the main line and the onset of the energy loss part [228, 229]. This situation is illustrated in Fig. 3.11. The intensity is plotted on a logarithmic scale for better identification of the energy loss onset. However, this evaluation requires no interference with other emission lines. Usually this evaluation is carried out on the O 1*s* peak [228, 229].

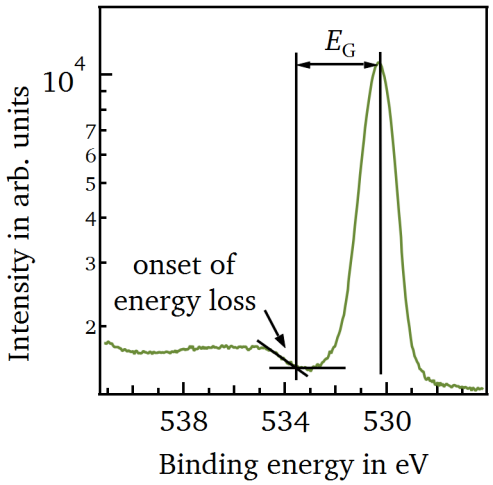

Figure 3.11.: Determination of E_G by the energy loss of the core level electrons exciting band-to-band transitions using the O 1s emission line of a $NaNbO_3$ sample as an example.

3.8.3. Fermi level shift and interface experiments

With XPS the position of the Fermi level at the surface of a material can be evaluated. As the sample is in electrical contact with the spectrometer, the Fermi levels will align and be set to $0\,\mathrm{eV}$ in the binding energy diagram. Hence, the recorded valence band edge of a semiconductor material is a measure for the distance between VBM and Fermi level, which is illustrated in Fig. 3.12. Combined with in-situ oxidizing or reducing treatments, Fermi level variations can be investigated by means of XPS [230, 231]. If a material is annealed in an oxidizing atmosphere the Fermi level is shifted closer to the valence band, while in a reducing environment it is shifted in direction to the conduction band. Therefore, the energy distance between valence band edge and Fermi level gets smaller and larger, respectively. The difference between the initial Fermi level and oxidized (reduced) Fermi level position in regard to the valence band edge is defined as the Fermi level shift ΔE_F.
As the Fermi level shift affects not only the valence band edge but the whole XP-spectrum, it can be extracted from each core level peak, which is shown in Fig. 3.12. However, this requires that no other energy shifts, e.g. chemical shifts, alter the emission line energy. Under such conditions, the distance between the valence band edge and the individual core level line ($E_\mathrm{CL} - E_\mathrm{VBM}$) is a constant value. The direction of the peak shift tells whether the sample is oxidized or reduced. Oxidation and reduction leads to a peak change to lower and higher binding energies, respectively.

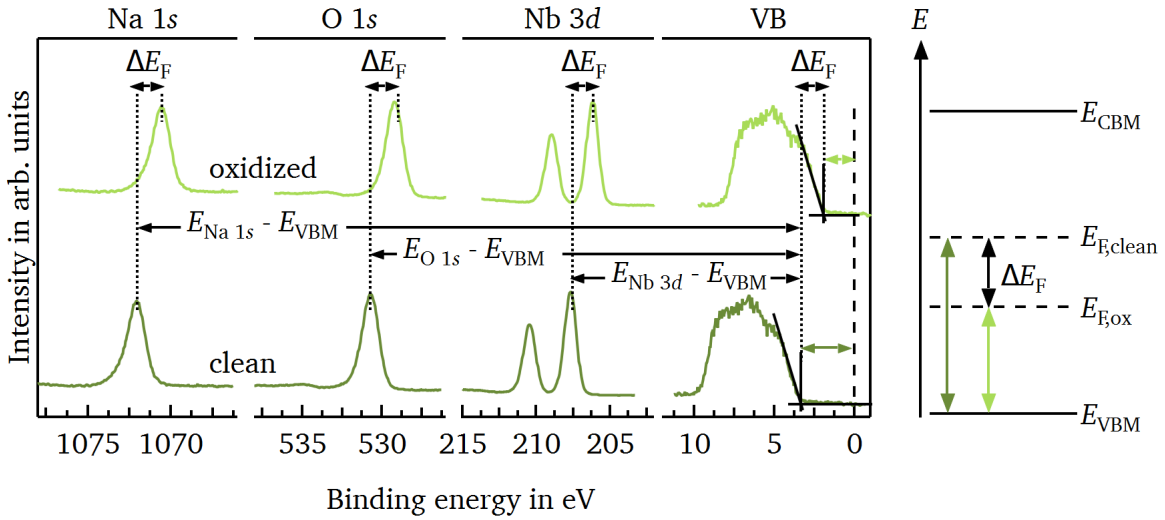

Figure 3.12.: Measured emission lines of a clean $NaNbO_3$ ceramic sample and after oxidation with Fermi level shift ΔE_F and constant core-level-VBM-distance $E_\mathrm{CL} - E_\mathrm{VBM}$. Cleaning was done by heating in a low pressure oxygen atmosphere. The oxidized spectra are the same as the cleaned ones and shifted to lower binding energies for illustration purposes. The band diagram on the right side illustrates the Fermi level positions in perspective to the band edges.

So-called interface experiments can be performed to probe the interface properties such as Schottky barriers between two materials, e.g. the contact between insulator and electrode. In addition, Fermi level shifts can be examined due to the bending of the band edges of the semiconductor at the interface. Hence, the maximum induced Fermi level shift can be analyzed, which can reveal a possible Fermi level pinning due to trap states located within the band gap. However, Fermi level pinning due to interfacial reaction between electrode and sample should be avoided. Metal electrodes are

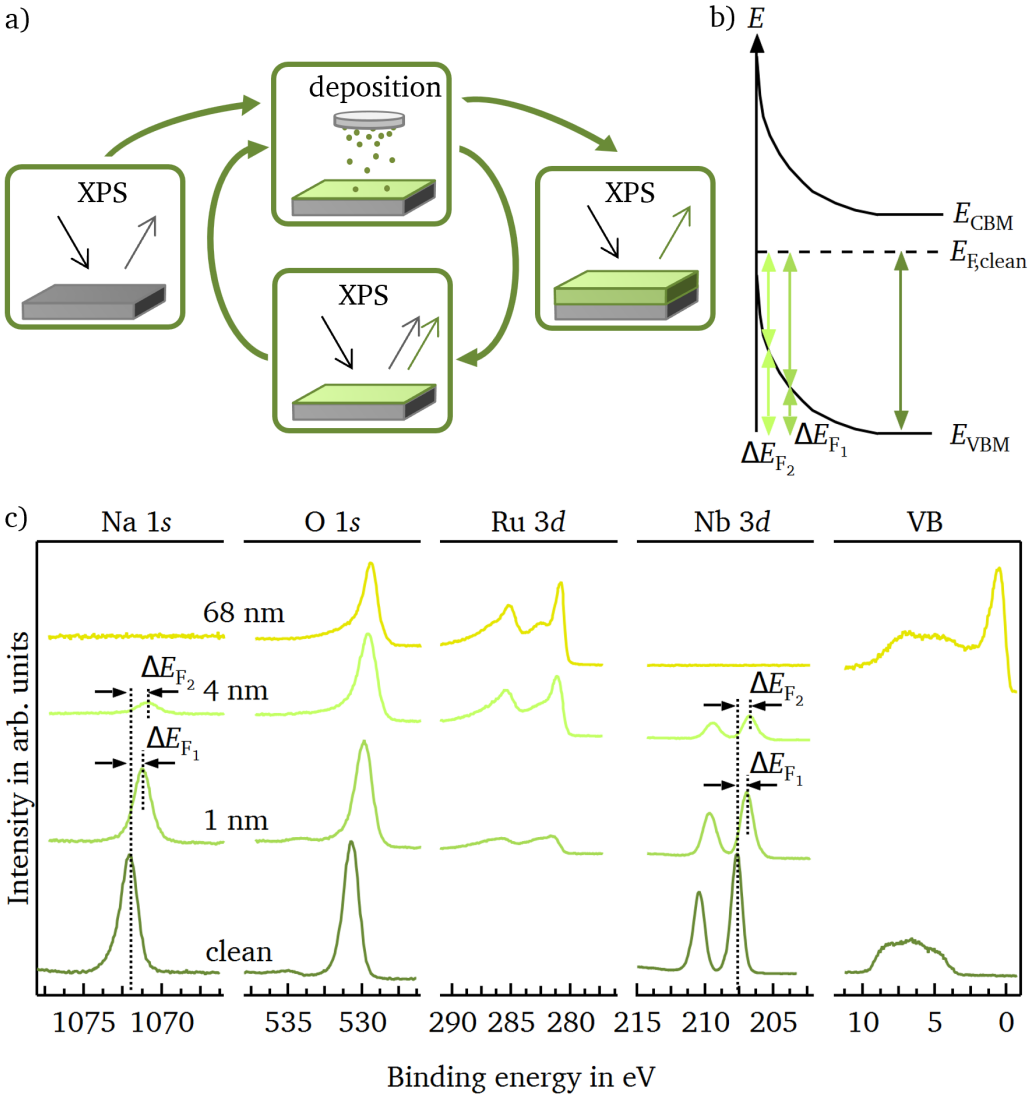

Figure 3.13.: a): Schematic drawing of the experimental procedure of an interface experiment. b): Band bending at the sample-contact-interface with measured Fermi level shifts ΔE_F. c): Recorded XP-emission lines of substrate and thin film with ΔE_F after each deposition step.

prone to create interfacial trap states, which is why oxide electrodes are the better alternative to investigate perovskite oxides [232]. The upper Fermi level limit close to the conduction band can be examined with low work function materials, e.g. ITO ($\Phi = 4.5\,\text{eV}$ [233]), and the lower Fermi level limit near the valence band with high work function materials such as RuO_2 ($\Phi = 5.6\,\text{eV}$ [231]).

The experimental process is illustrated schematically in Fig. 3.13a). First, the core level lines and the valence band of the clean substrate are measured. Afterwards, the sample is transferred into a deposition chamber, in which a thin layer of the contact material is deposited on top of the sample's surface. Another XP-measurement including all core level lines of substrate and thin film elements is conducted after moving the sample back into the XP-chamber. This deposition-XP-measurement-sequence is repeated until the upper layer is thick enough that no signal of the substrate is detected anymore. In this case, a detailed spectra of the valence band of the thin film is recorded as well.
As mentioned above, the Fermi level shift can be extracted from the valence band edge and each core level line. However, the elements present in both, substrate and thin film, as well as the valence band edge cannot be used for the determination of the Fermi level because of a mixture of the two contributions from substrate and thin film. In this case, only the unique elements can be used as a measure for the Fermi level shift. In addition, an overlap of different emission lines from one element with the main lines of the other element should be avoided for a high quality analysis. Graph c) in Fig. 3.13 shows the recorded emission lines with corresponding Fermi level shifts after each deposition step. In Fig. 3.13b) these Fermi level shifts are put in relation to the band bending. With increasing layer thickness a larger band bending is measured due to the limited information depth.

3.9. Electrical Conductivity

Experimental objectives:

- Identification of type of charge carriers
- Analysis of conduction mechanisms
- Examination of application duration
- Finding possible correlations between electronic structure and (anti)ferroelectric properties
- Identifying species or specific conduction behaviors required for a material being ferroelectric or antiferroelectric

3.9.1. DC-conductivity

DC-conductivity experiments are conducted to gain knowledge about the electronic structure of a material. For ceramic samples usually the 2-point-method is used. Here, two electrodes are deposited on both sides of the samples covering almost the whole surface. A small gap without electrode is left towards the edges in order to avoid any electric flashovers as shown in Fig. 3.14 [234]. A voltage V is applied between the two electrodes while the flowing current I is measured. By means of Ohm's law (3.9) [235], electrode area A, and sample thickness d, the conductivity σ can be calculated:

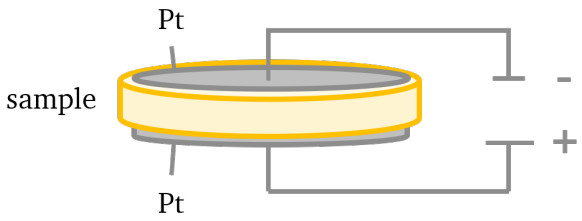

Figure 3.14.: Sample with sputtered Pt-electrodes.

$$U = R \cdot I \tag{3.9}$$

$$\sigma = \frac{1}{\rho} = \frac{d}{R \cdot A} = \frac{I \cdot d}{U \cdot A} \tag{3.10}$$

R is the resistance of the sample and depends on the sample geometry while the resistivity ρ is independent on it. However, this equation is neglecting any contact resistances. During the measurements temperature T and atmosphere in particular the oxygen partial pressure p_{O_2} can be varied.

In general, with a DC-signal only the charges which are conducted by the electrodes can be measured. Hence, with metal electrodes such as Pt only electronic conductivity can be probed. In order to examine ionic conductivity of, e.g. oxygen ions oxygen conducting electrodes as Y-stabilized ZrO_2 [236] are required.

Temperature dependent measurements

Temperature dependent measurements are usually performed with a constant heating and cooling rate while applying a constant electric field. As described in section 2.4, both electronic and polaron conduction are thermally activated processes with an activation energy E_A, which can be described by Eq. 3.11.

$$\sigma = \frac{\sigma_0}{T^{3/2}} \exp\left(-\frac{E_A}{k_B T}\right) \tag{3.11}$$

This equation is an Arrhenius equation. Consequently, the activation energy can be determined by an Arrhenius plot as shown on the left side of Fig. 3.15 [237]. Plotting the multiplication of σ and $T^{3/2}$ on a natural logarithmic scale as function of $\frac{1}{T}$ results in a simple evaluation of the activation energy from the slope as illustrated by Eq. 3.12 and Fig. 3.15.

$$\ln\left(\sigma T^{3/2}\right) = \ln(\sigma_0') - \frac{E_A}{k_B} \cdot \frac{1}{T} \tag{3.12}$$

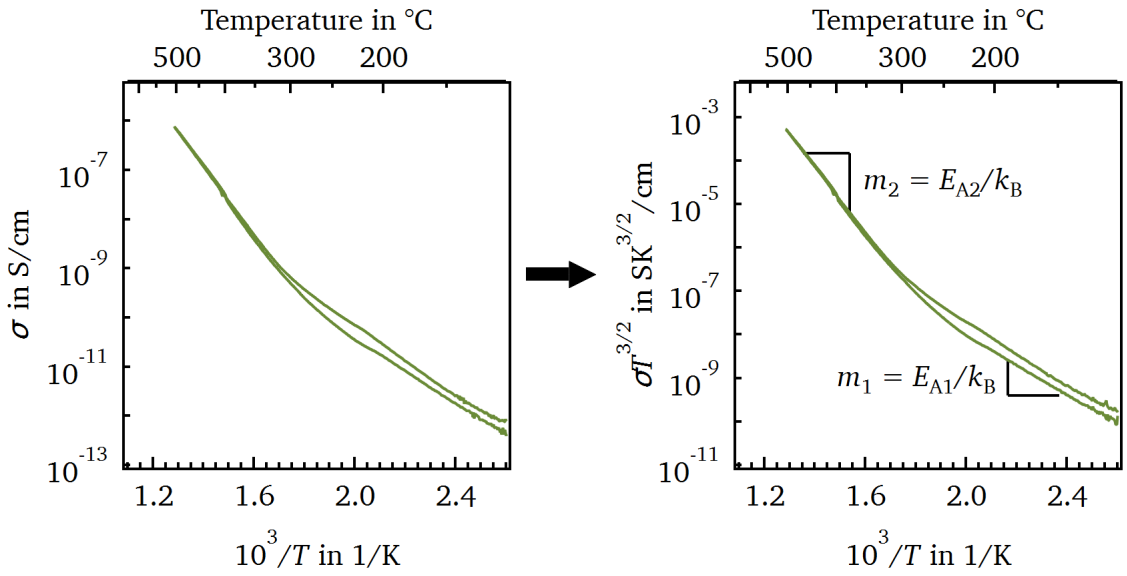

Figure 3.15.: Conductivity as function of temperature. Left: Arrhenius plot. Right: Modified Arrhenius plot with temperature independent pre-factor.

Relaxation experiments

Relaxation experiments are conducted in order to investigate how a sample adapts to a change in atmosphere. Therefore, the sample is heated at a certain temperature while applying a constant electric field and measuring the current until an equilibrium state has developed. Afterwards, the atmosphere meaning the oxygen partial pressure is changed and kept constant until a new equilibrium state establishes. From such an experiment, it can be observed if a sample is n-type conducting (conductivity is increasing with lower oxygen partial pressure) or p-type conducting (conductivity is decreasing with lower oxygen partial pressure). In Fig. 3.16 the relaxation curve of a n-type sample is shown when changing from N_2 to dry air atmosphere.

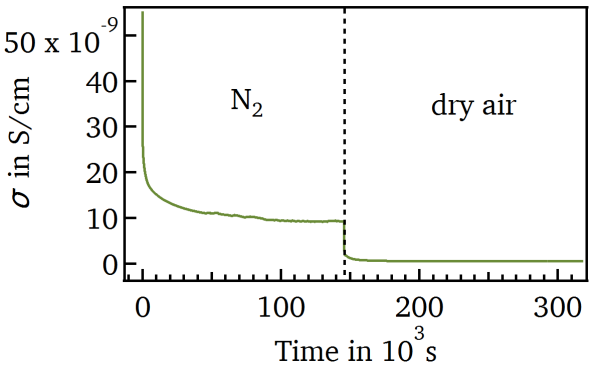

Figure 3.16.: Conductivity as function of time of a n-type sample while changing the atmosphere from N_2 to dry air.

Resistance degradation experiments

Resistance degradation can appear in a material after a certain application duration as, e.g. multilayer ceramic capacitors [238], which could lead to a failure of the whole component. Hence, it is important to investigate the resistance degradation process. High electric fields can be applied while heating at a constant temperature in order to accelerate the occurrence of resistance degradation. In the beginning of a measurement it is unknown at which combination of electric field and temperature resistance degradation starts to develop. Therefore, an electric field profile is applied, which increases the electric field in a certain time interval at constant temperature.

Fig. 3.17 illustrates this profile and the corresponding conductivity as function of time. When the electric field is changed, the sample is charged accordingly. A charging peak can be identified within the first few seconds, which is shown in the inset of Fig. 3.17. For the first three time intervals the conductivity is decaying exponentially after the charging peak until an equilibrium state is reached. This is not the case for the fourth step. Here, the conductivity is increasing very rapidly after a certain time period, which is an indication for resistance degradation. The same electric field profile can be applied at different temperatures in order to analyze the influence of temperature. However, when a degradation process is developed, a post-annealing step should be conducted at high enough temperatures in

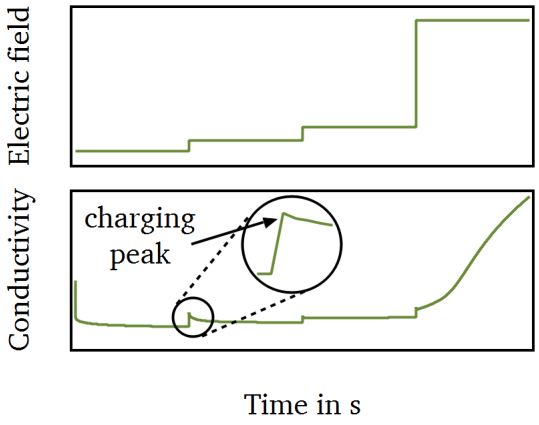

Figure 3.17.: Electric field profile and measured conductivity as a function of time in order to investigate a resistance degradation process.

order to redistribute the defects within the material. In addition, it should be checked if the same room temperature resistivity as in the initial state is established again. If this is not the case the post-annealing treatment was most likely not performed long enough, at insufficient high temperatures, or an irreversible change of the sample, e.g. the formation of precipitations, occurred.

3.9.2. Impedance spectroscopy

The main information for this section are based on the textbooks *Impedance Spectroscopy - Applications to Electrochemical and Dielectric Phenomena* written by Vadim F. Lvovich [239] and *Impedance Spectroscopy - Theory, Experiment, and Applications* edited by Evgenij Barsoukov and J. Ross Macdonald [240].

Impedance spectroscopy is used in order to separate different possible conduction mechanism, e.g. bulk and grain boundary conductivity. These processes dominate at different frequencies. With impedance spectroscopy the conductivity is examined in dependence of frequency. Hence, the conduction mechanisms can be separated by measuring from low to high frequencies, typically between 10^{-2} Hz to 10^{7} Hz. As for the DC-measurements, two electrodes are deposited on both sides of the samples covering almost the whole surface. A sinusoidal voltage signal V is applied at the electrodes. The resulting current I and the phase shift Φ between voltage and current is recorded. Voltage and current signal including the phase shift are shown in Fig. 3.18. The impedance $Z^{\star}$ is similar to the resistance defined as the ratio of voltage and current:

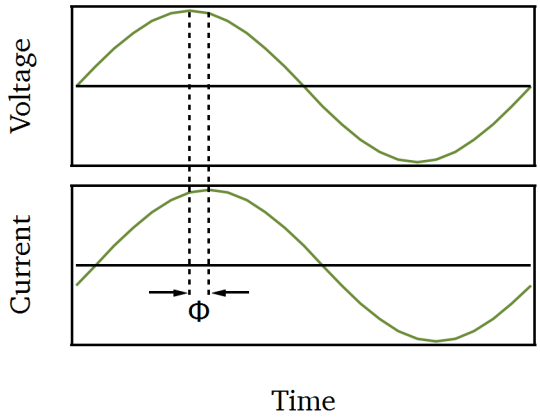

Figure 3.18.: Voltage and current signal which are phase shifted by Φ.

$$\begin{aligned} Z^{\star} &= \frac{V(t)}{I(t)} \\ &= \frac{V_{\mathrm{A}}\sin(\omega t)}{I_{\mathrm{A}}\sin(\omega t + \Phi)} \\ &= Z_{\mathrm{A}}\frac{\sin(\omega t)}{\sin(\omega t + \Phi)} \end{aligned} \tag{3.13}$$

Voltage and current, and therefore, the impedance are dependent on the time t. ω is the radial frequency. Eq. 3.13 can also be expressed in following form:

$$Z^{\star} = Z_{\mathrm{A}}\exp(j\Phi) = Z_{\mathrm{A}}(\cos\Phi + j\sin\Phi) = Z' + jZ'' \qquad \tan\Phi = \frac{Z''}{Z'} \tag{3.14}$$

Z'' and Z' are imaginary and real part of the impedance.
The electrical response of a material can often be described by a combination of different resistance and capacitance elements in series and parallel. A pure resistor can be described by one resistance element leading to an impedance only determined by its real part $Z^\star = Z' = R$. In contrast, a pure capacitor can be expressed by one capacitance element with $Z^\star = Z'' = {}^1/_{j\omega C}$. One way to graphically illustrate the impedance of a material is the so-called impedance Nyquist plot shown for a simple RC-circuit on the top left of Fig. 3.19. It connects imaginary and real part of the impedance

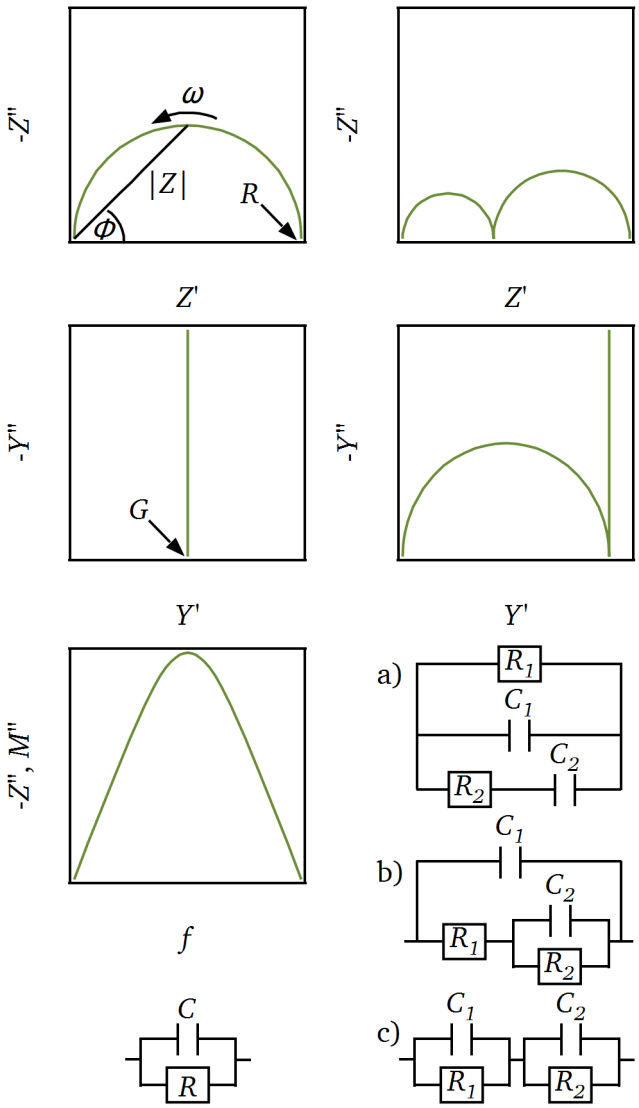

Figure 3.19.: Impedance (top) and admittance nyquist plot (middle) as well as equivalent circuits (bottom). Left: Simple RC-element including the impedance and modulus Bode plots. Right: All three equivalent circuits result in the same impedance and admittance plot. a) Maxwell (parallel) circuit, b) Randles circuit, and c) Voigt (series) circuit.

and is always a half semicircle for a single RC-element. From the intercept with the Z'-axis at low frequencies the resistance of the circuit can be evaluated. Furthermore, the relation between Z'', Z', and the phase angle Φ can be identified from Fig. 3.19.
Other impedance related functions are the admittance $Y^\star$, the permittivity $\epsilon^\star$, and the modulus $M^\star$, which are given by the following equations:

$$Y^\star = \frac{1}{Z^\star} = Y' + jY'' \tag{3.15}$$

$$\epsilon^\star = \frac{1}{j\omega\epsilon_0 Z^\star} = \epsilon' + j\epsilon'' \tag{3.16}$$

$$M^\star = \frac{1}{\epsilon^\star} = j\omega\epsilon_0 Z^\star = -\omega\epsilon_0 Z'' + j\omega\epsilon_0 Z' = M' + jM'' \tag{3.17}$$

The admittance Nyquist plot is shown on the left side of Fig. 3.19 for a simple RC-element. Similar to the impedance, the intercept of the Y'-axis marks the conductance of the circuit [239, 240]. Furthermore, showing the imaginary part of the impedance and the modulus as a function of frequency, a so-called Bode plot, can elucidate a conduction process more clearly. For a simple RC-element, as illustrated in Fig. 3.19, both, Z'' and M'', exhibit a maximum. The peak height is proportional to R and to $1/C$ for Z'' and M'', respectively. If the impedance of a material is dominated by a long range conductivity, the peaks of Z'' and M'' overlap in frequency while in case of a localized relaxation process they are separated in frequency. Moreover, the impedance emphasizes the most resistive part while the modulus highlights the element with the lowest capacitance. This can be very helpful in identifying different processes, which might overlap in frequency [44–47].

On the right side of Fig. 3.19 the impedance and admittance Nyquist plots of an impedance measurement dominated by two processes is illustrated. These spectra can be expressed by three different equivalent circuits a)–c). a) is called Maxwell circuit and represents elements happening in parallel. In contrast, the Voigt circuit shown in c) describes two components in series. In b) the so-called Randles circuit is illustrated, defining a material including processes in parallel and series. Being able to explain the shown impedance and admittance Nyquist plots by three different equivalent circuits, makes clear that the conduction process cannot be explained by performing only impedance measurements. Other characterization methods are required in order to decide for an appropriate equivalent circuit explaining all measured results [239].

In contrast to DC-measurements, with an AC-signal all mobile charges within the sample can be probed. Hence, the type of electrode is not important to examine electronic and ionic conductivity. This means that with impedance spectroscopy both, electronic and ionic conductivity are measured if present in the material.

4. Experimental

In this work the major analysis was done on ceramic samples. However, some XPS measurements were conducted on thin films for comparison reason. All ceramic samples were prepared during a research visit supported by the German Academic Exchange Service (DAAD) in the electronic ceramics group of Prof. Dr. Barbara Malič at the Jozef Stephan Institute (JSI) in Lubljana, Slovenia. The thin films were either provided by Thorsten Schneider from the advanced thin film group of Prof. Dr. Lambert Alff at the Technical University of Darmstadt, Germany, or by Dr. Jutta Schwarzkopf from the thin oxide films group at the Leibniz-Institut für Kristallzüchtung (IKZ) in Berlin, Germany. Concerning the characterization of all samples, granulometry, optical dilatometry, SEM, scanning transmission electron microscopy (STEM), and XRD were conducted at JSI. Density measurements via the Archimedes method, polarization hysteresis curves, permittivity analysis, XPS, and all electrical conductivity measurements were performed at the Technical University of Darmstadt. Electron energy loss spectroscopy were conducted by Hongguang Wang at the Max Planck Institute for Solid State Research in Stuttgart, Germany.

4.1. Sample preparation of ceramics

All ceramics were prepared by the conventional solid-state reaction synthesis route and subsequent sintering of the synthesized powders. Othorhombic Nb_2O_5 ($99.9\,\%$, Sigma-Aldrich), Na_2CO_3($99.9\,\%$, ChemPur), and K_2CO_3 ($99.9\,\%$, ChemPur) were used as precursor powders. Calcium and strontium were included as donor dopants on the A-site of $NaNbO_3$. Here, $CaCO_3$ ($99.95\,\%$, Alfa Aesar) and $SrCO_3$ ($99.994\,\%$, Alfa Aesar) was added during synthesis. Figure 4.1 illustrates schematically the complete processing chain.

First, the precursor powders were milled by planetary milling except for Nb_2O_5, which was milled by attrition milling. For planetary milling the powders were added to acetone and yttria-stabilized zirconia balls and were crushed for $4\,\mathrm{h}$ with a rotational frequency of $200\,\mathrm{min}^{-1}$. In case of attrition milling, the Nb_2O_5 powder was mixed with isopropanol and yttria-stabilized zirconia balls and milled for $2\,\mathrm{h}$ at a rotational frequency of $500\,\mathrm{min}^{-1}$. Afterwards, the powders were dried at $105\,^{\circ}\mathrm{C}$ for $1\,\mathrm{h}$

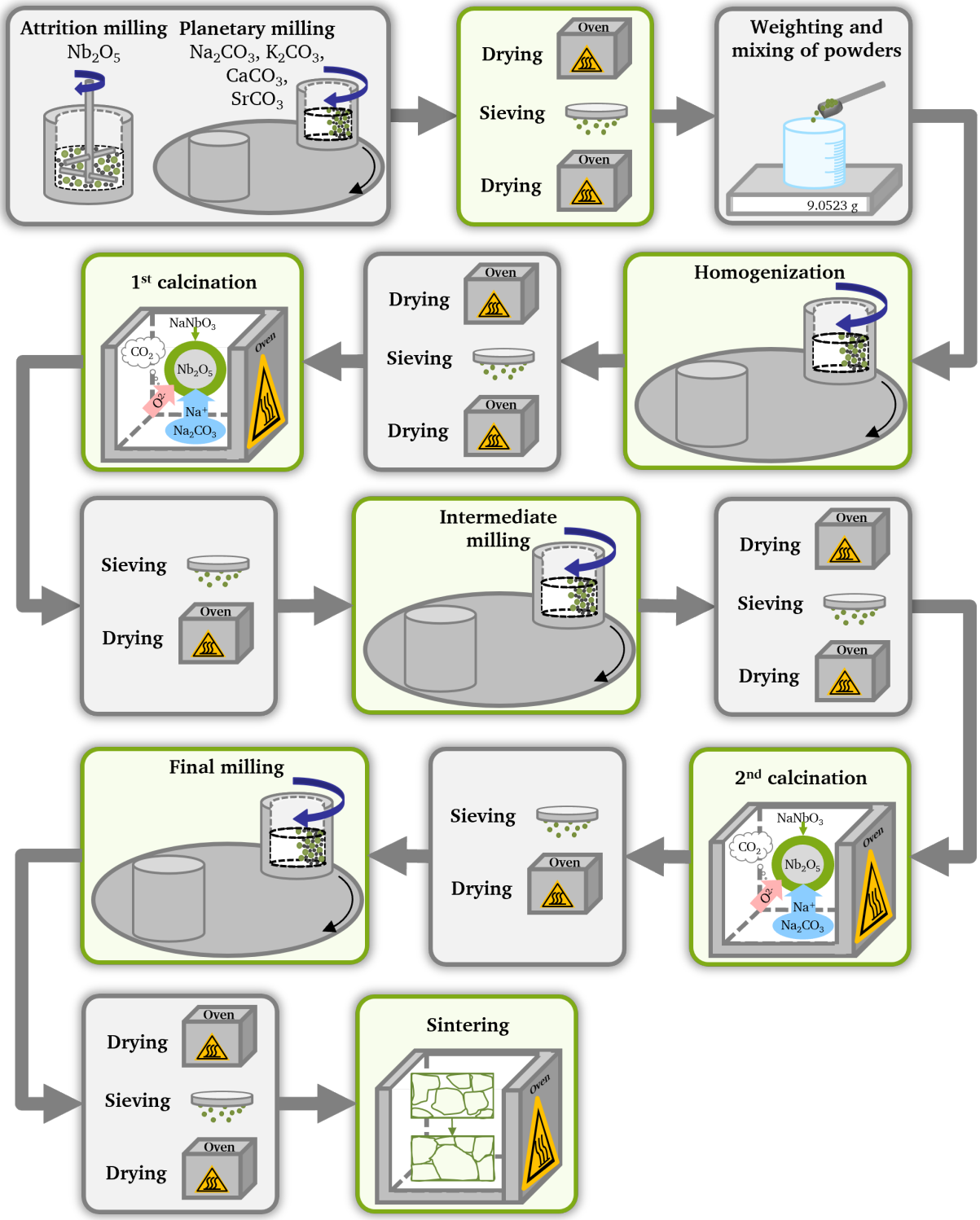

Figure 4.1.: Processing chain for the solid-state synthesis route and the subsequently performed sintering procedure.

and additional for 2 h at 200 °C. Then, the powders were sieved and dried again at 200 °C for 2 h. For homogenization, the powders were weighted according to the final composition in a Labmaster 130 glove box (MBraun, Garching, Germany). $CaCO_3$ and $SrCO_3$ was added corresponding to a 1 mol % doping concentration in case of the donor doped $NaNbO_3$ samples. Homogenization and all milling steps mentioned in the following were conducted by planetary milling at 200 min^{-1} for 3 h. For this the powders were mixed with acetone and yttria-stabilized zirconia balls. Drying of the powders was performed first at 105 °C for 1 h followed by a 2 h heating step at 200 °C. Then, the powders were sieved and dried again at 200 °C for 2 h. This procedure was conducted after each milling step.
After homogenization and drying of the powders, the powders were pressed uniaxially with 50 MPa to cylinders with a diameter of about 2 cm. These cylinders were put on a Pt-foil in an Al_2O_3 container, which was placed in an oven for the first calcination step. During calcination the solid-state reaction takes place as described in section 2.7. First, the oven was heated with 5 K min^{-1} up to 200 °C in air. The temperature was hold for 2 h. Afterwards, the oven was raised up with the same heating rate to the final calcination temperature and hold for 4 h at this temperature. For undoped $NaNbO_3$, donor doped $NaNbO_3$, and $KNbO_3$ a calcination temperature of 700 °C, 950 °C, and 800 °C was used, respectively. Then, the oven was cooled down with a cooling rate of 5 K min^{-1}. The cylinders were crushed by a mortar, sieved, and dried at 200 °C for 1 h before the powders were milled, dried, and sieved again. To ensure a complete reaction to the final product, a second calcination step was performed with the same parameters as the first calcination after pressing the powders to cylinders as described above. A final milling step was conducted before sintering, which leads to densification via grain growth of the powders. Therefore, the powders were pressed uniaxially with 100 MPa and then isostatically with 200 MPa in a cylindrical form with a diameter of about 8 mm. These cylinders were placed on a Pt-foil in an Al_2O_3 container, which is pushed into an Al_2O_3 tube furnace. First, the samples were heated at 200 °C for 2 h. Then, the temperature was raised to the sintering temperature and the samples were sintered for 2 h. Undoped $NaNbO_3$ and $Na_{0.99}Sr_{0.01}NbO_3$ were sintered at 1250 °C while $Na_{0.99}Ca_{0.01}NbO_3$ had a sintering temperature of 1320 °C. $KNbO_3$ was densified at 1010 °C. The heating and cooling rate was 5 K min^{-1}. Calcination T_{cal} and sintering temperature T_{sint} for all samples are listed in Table 4.1.

Table 4.1.: Calcination T_{cal} and sintering temperature T_{sint} of all ceramics.

	$NaNbO_3$	$Na_{0.99}Ca_{0.01}NbO_3$	$Na_{0.99}Sr_{0.01}NbO_3$	$KNbO_3$
T_{cal} in °C	700	950	950	800
T_{sint} in °C	1250	1320	1250	1010

For further analysis, the cylinders were cut into 1 mm-thick disks by a diamond saw, ground, and polished. The final polishing step was done with diamond paste with a particle size of 0.25 µm. In order to eliminate the stress introduced by grinding and polishing, a stress-release-heating was performed. The samples were heated at 600 °C for 1 h in air. Heating and cooling temperatures

were set to $5\,\mathrm{K\,min^{-1}}$ and $1\,\mathrm{K\,min^{-1}}$, respectively. The outer ends of the cylinders were crushed by a mortar and used for XRD-analysis.

4.2. Laser granulometry

After each milling step the particle size was determined by a laser granulometer (Microtrac S3500 Particle Size Analyzer, Montgomeryville, PA, US). Therefore, a small amount of powder was mixed after sieving with isopropanol and introduced drop-wise with a pipette into the granulometer.

4.3. Optical dilatometry

In order to determine the correct calcination and sintering temperature, some portion of the homogenized and calcined powder was pressed to a small cylinder and analyzed by a hot stage microscope (Leica Microsystems GmbH, Wetzlar, Germany), respectively. The cylinders formed of the homogenized powder were heated with $10\,\mathrm{K\,min^{-1}}$ in case of $NaNbO_3$ and $KNbO_3$, while donor doped $NaNbO_3$ was heated with $5\,\mathrm{K\,min^{-1}}$ up to $1350\,^{\circ}\mathrm{C}$. The temperature during the analysis of the calcined cylinders was raised with $5\,\mathrm{K\,min^{-1}}$ up to $1350\,^{\circ}\mathrm{C}$ for all material systems. A picture of the cylinder's profile was taken every $10\,^{\circ}\mathrm{C}$. By checking the diameter of the cylinder, shrinkage and expansion of the sample was calculated by means of Eq. 3.1.

4.4. Archimedes method

The density of the samples was determined by means of the Archimedes principle. First, the sample's weight is measured in a completely dry state. Afterwards, the sample was immersed for $20\,\mathrm{min}$ in distilled water under the vacuum bell jar. Then, the ceramic pellet was weighted under distilled water. Finally the sample's weight was measured again in air after drying it with a clean wipe.

4.5. Scanning electron microscopy

The microstructure of the ceramic samples was investigated by means of a SEM using a JSM 7600F (Jeol, Tokyo, Japan). Prior to the measurements, the samples were thermally etched by heating $100\,^{\circ}\mathrm{C}$ below the sintering temperature. Carbon paste was used to avoid charging of the sample's surface during SEM-analysis.
The scanning electron microscope was utilized to examine the grain size, pore distribution, and

the appearance of secondary phases. By means of the line intercept method the particle size of the samples was determined.

4.6. X-ray diffraction

Analysis of the crystal structure was conducted by powder x-ray diffraction using the Bragg-Brentano method. Calcined and sintered powders were investigated at room temperature by a X'Pert PRO MRD diffractometer with Cu $K\alpha_1$ radiation (PANalytical, Almelo, Netherlands). A 2θ-region from $10°$ to $90°$ was recorded in $0.17°$-steps.
After first and second calcination some powder was removed after sieving for XRD analysis. In case of the sintered material, the edges of the sintered rods were cut off and crushed by a mortar. The sintered powder was annealed at $600\,°$C for $1\,$h to release stresses introduced by the mortar. This could not be done for the calcined powders as the temperature is too close to the calcination temperature, hence, possible modification during stress-release-annealing could not be excluded.

4.7. Polarization hysteresis

In order to confirm the antiferroelectric or ferroelectric nature of the prepared samples, polarization hysteresis loops were examined at low and high frequencies. The low frequency behavior ranging from $0.3\,$Hz to $1.0\,$Hz was measured by a common Sawyer-Tower setup while at high frequencies of $1\,$kHz the virtual ground method was used. For the Sawyer-Tower configuration, a triangular field was applied and amplified by a 20/20C amplifier (Trek inc, Lockport, NY, US). The reference capacitor had a capacitance of $2.2\,$µF. In case of the virtual ground method, a TF Analyser 2000 (aixACCT Systems GmbH, Aachen, Germany) in combination with a high voltage amplifier 20/20C was used. Aged and equilibrated samples were analyzed as well by the TF Analyser.
Prior to the measurements, the ceramics were ground to a thickness of $0.25\,$mm and annealed at $600\,°$C for $1\,$h to release the introduced stresses. Afterwards, Pt contacts were deposited by a Q300TD sputter coater (Quorum, Laughton, East Sussex, UK). Finally, the samples were cut into $1.5\,$mm $\times$ $1.5\,$mm rectangular by a diamond saw. In Table 4.2 all samples used for the polarization hysteresis loops are listed.

4.8. Permittivity

Temperature and frequency dependent permittivity and dielectric loss were probed by a HP4284A LCR meter (Keysight technologies, Santa Rosa, CA, US). An AC voltage amplitude of $0.05\,$V was

applied at frequencies ranging from $100\,\mathrm{Hz}$ to $1\,\mathrm{MHz}$. The temperature was raised up to $600\,^{\circ}\mathrm{C}$ and down again to room temperature with a heating and cooling rate of $1\,\mathrm{K\,min^{-1}}$.
Prior to the measurements the samples were ground to a thickness of $0.25\,\mu\mathrm{m}$, stress-release-annealed, sputtered with Pt, and cut into $1.5\,\mathrm{mm} \times 1.5\,\mathrm{mm}$ rectangular as described in the previous section. In Table 4.2 all samples used for the permittivity measurements are listed.

Table 4.2.: Samples used for P-E-loop and permittivity measurements including sample thickness d and area A.

type of experiment	sample type	sample	d in mm	A in mm^2	setup
P-E-loops	$NaNbO_3$	NB111	0.24	2.4	Sawyer-Tower
	$Na_{0.99}Ca_{0.01}NbO_3$	NB130	0.23	2.4	
	$Na_{0.99}Sr_{0.01}NbO_3$	NB129	0.24	2.0	
P-E-loops	$NaNbO_3$	NB113	0.25	2.2	Virtual ground method
	$Na_{0.99}Ca_{0.01}NbO_3$	NB139	0.28	2.2	
	$Na_{0.99}Sr_{0.01}NbO_3$	NB138	0.24	2.2	
	$KNbO_3$	NB120	0.25	2.3	
Permittivity	$NaNbO_3$	NB113	0.27	2.3	–
	$Na_{0.99}Ca_{0.01}NbO_3$	NB139	0.29	2.3	
	$Na_{0.99}Sr_{0.01}NbO_3$	NB138	0.26	2.5	
	$KNbO_3$	NB120	0.25	2.4	

4.9. Electron energy loss spectroscopy

The optical band gap was determined by electron energy loss spectroscopy (EELS) performed by a SESAM microscope from ZEISS (Wetzlar, Germany) in TEM mode. The microscope is equipped with an electrostatic Ω-type monochromator (CEOS GmbH, Heidelberg, Germany) and an in-column MANDOLINE energy filter. Here, an acceleration voltage of $200\,\mathrm{kV}$ and an energy resolution of $60\,\mathrm{meV}$ was used.
Before conducting the measurements, the samples were mechanical polished and subsequently argon ion milled at liquid nitrogen temperature by a precision ion polishing system (PIPS, model 691, Gatan, Pleasanton, CA, US).
These experiments have been conducted by Hongguang Wang at the Max Planck Institute for Solid State Research in Stuttgart.

4.10. The Darmstadt Integrated System for Materials Research

The **Da**rmstadt **I**ntegrated **Sy**stem for **Mat**erial Research (DAISY-MAT) is an ultra-high vacuum cluster tool for the preparation and analysis of thin films. It consists of a distribution chamber, several preparation chambers in which the layers can be deposited via magnetron sputtering, atomic layer deposition (ALD), and chemical vapour deposition (CVD), and one analyzing chamber, which includes a photoelectron spectrometer. The complete cluster tool is schematically illustrated in Fig. 4.2. Furthermore, the deposited thin films as well as ex-situ prepared samples can be treated in

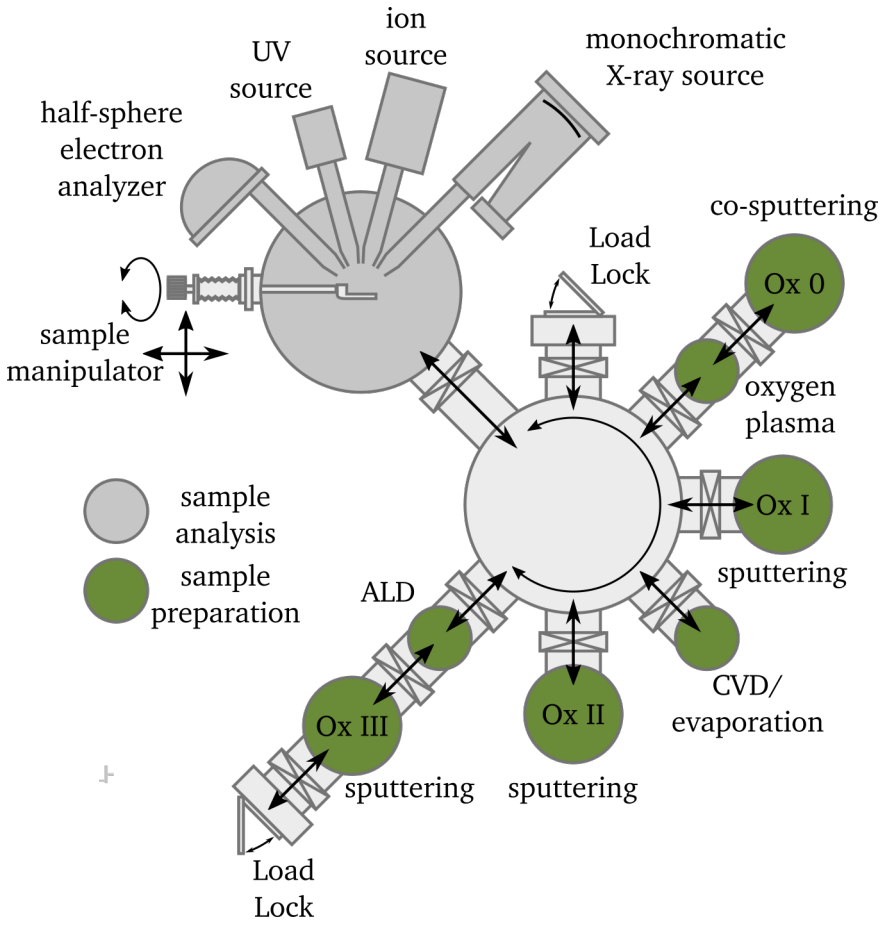

Figure 4.2.: Schematic presentation of the DAISY-MAT including the analyzing and all preparation chambers.

different oxidizing and reducing atmospheres within the preparation chambers and subsequently examined with the photoelectron spectrometer. The big advantage of this system is that samples can be prepared, treated, and analyzed without breaking the vacuum, hence, preventing contamination from carbon or hydroxide adsorbents. This is an unique opportunity to investigate clean surfaces and interfaces. In many other studies published in literature, cleaning via, e.g. argon sputtering has to be performed in order to get rid of any adsorbents on the surface. However, such energetically

intense treatments can modify the surface and influence the photoelectron spectroscopy results.

4.10.1. Thin film preparation

Thin films can be deposited by means of radio frequency (RF)- or DC-magnetron sputtering in the chambers Ox 0, Ox I, Ox II, and Ox III. All chambers have a heating lamp powered by a power supply SM7020-D from Delta Elektronika (Terneuzen, Netherlands), which can be controlled by a temperature regulator 2416 from Eurotherm (Worthing, UK). Argon, oxygen, and an argon/oxygen-mixture are available as processing gases. The gas flows are adjusted by mass flow controllers of type PR 4000 from MKS instruments (Andover, MA, US). In the following the deposition process of ITO and RuO_2 will be explained because these are the two relevant materials used in this work as electrode materials.
ITO was prepared by RF-sputtering in pure argon in the Ox II chamber at room temperature or at higher temperatures up to $400\,°C$. A power of $25\,W$ was applied to an ITO-target with $10\,wt\,\%$ Sn manufactured by Lesker (Jefferson Hills, PA, US) by means of a PFG 300 RF-generator from TRUMPF Hüttinger GmbH + Co. KG (Freiburg im Breisgau, Germany). Argon gas flow and chamber pressure were 5 sccm and $0.5\,Pa$. The distance between ITO-target and sample was set to $10\,cm$, which results in a sputtering rate of $5\,nm\,min^{-1}$. Both, room temperature and $400\,°C$-deposition, were conducted in this work.
A MDX-500 DC-plasma source (Advanced Energy Industries Inc., Denver,CO, US) was used for depositing RuO_2 with a power of $10\,W$. Here, a Ru-target produced by MaTeck (Jülich, Germany) was positioned in Ox I, hence, oxygen gas had to be introduced into the chamber in order to receive RuO_2. Oxygen and argon flow were set to 0.75 sccm and 9.25 sccm at a chamber pressure of $1\,Pa$. The RuO_2 deposition was done at room temperature with a target-to-sample-distance of $9.4\,cm$, which results in a sputtering rate of $3.3\,nm\,min^{-1}$.

4.10.2. Sample treatments

Samples can be treated in different oxidizing and reducing atmospheres. Oxidizing conditions are heating in a low pressure oxygen atmosphere in one of the chambers Ox 0 to Ox III or by an oxygen plasma treatment with a plasma source located in Ox 0. For reduction of the samples' surfaces, vacuum annealing in the XPS or in one of the sputter chambers or water deposition in the ALD-chamber was used. The reducing effect of water has been observed in several works in the research group [39, 80, 241], however, it is not completely understood why it is behaving reductive. In addition, interface experiments can be conducted in order to shift the Fermi level at the sample's surface closer to the valence or conduction band. This can be seen as a physically oxidation or reduction of the surface.

Heating in oxygen

Heating in a low pressure oxygen atmosphere was primarily used for cleaning ex-situ prepared samples. Here, the oxygen flow was set to 5 sccm at 0.5 Pa. The sample was heated up to $400\,^{\circ}$C with $5\,\mathrm{K\,min^{-1}}$ and annealed for 2 h. This was done to get rid of the carbonaceous and hydroxide species absorbed on the surface. The effect is illustrated in Fig. 6.1 in Section 6.1. As oxidizing post-annealing step the samples were heated up to $300\,^{\circ}$C with the same heating rate and oxidized for 3 h.

Oxygen plasma

An oxygen plasma was created at room temperature by a tectra Gen II hybrid plasma source (tectra GmbH, Frankfurt am Main, Germany) used in the atom mode, which is further enhanced by a magnetic field in the ECR mode. The oxygen flow was 2.5 sccm and the sample was treated for 10 min.

Heating in vacuum

Heating in vacuum was performed in one of the deposition chambers with a chamber background pressure in the range of 1×10^{-6} Pa at $400\,^{\circ}$C for 1 h. The heating and cooling rates were set to $5\,\mathrm{K\,min^{-1}}$. In contrast, annealing in the XPS-chamber was conducted with a room temperature background pressure of 1×10^{-7} Pa for 3 h. The temperature was increased manually, which is why no exact heating and cooling rates can be given.

Interface experiments

In order to shift the Fermi level closer to the valence and conduction band the high and low work function material RuO_2 and ITO are deposited step-wise as described in section 3.8.3. The thin films were deposited in the way as outlined in section 4.10.1. In case of ITO, the first deposition step was 10 s while for RuO_2 it was 20 s. For the consecutive steps, the deposition time was always doubled. The last thick layer was deposited for 20 min. After each deposition step a XP-spectra was recorded.

4.10.3. Photoelectron spectroscopy

The photoelectron spectrometer located in the analyzing chamber of the DAISY-MAT system was used in order to characterize the surfaces and interfaces of the samples under investigation. It is part of a Physical Electronic PHI 5700 multi-technique surface analysis system (Feldkirchen, Germany). The

x-ray source was monochromatic Al K_α-radiation with a photon energy of $1486.6\,\text{eV}$ and a resolution of $600\,\text{meV}$, which was determined from the Gaussian broadening of a clean silver sample. X-ray source and detector are positioned in a $90°$ angle while the photons hit the sample under a $45°$ angle. The vacuum pressure was maintained in the high 10^{-10} mbar to low 10^{-9} mbar region.
In this work different types of spectra were recorded. A so-called survey spectra including the whole measurable binding energy regime and detailed spectra of the valence band and the elements' core levels of interest were measured. Figure 4.3 illustrates the different types of spectra for silver as an example. In Table 4.3 all parameters of the respective measuring modes are listed. The measuring

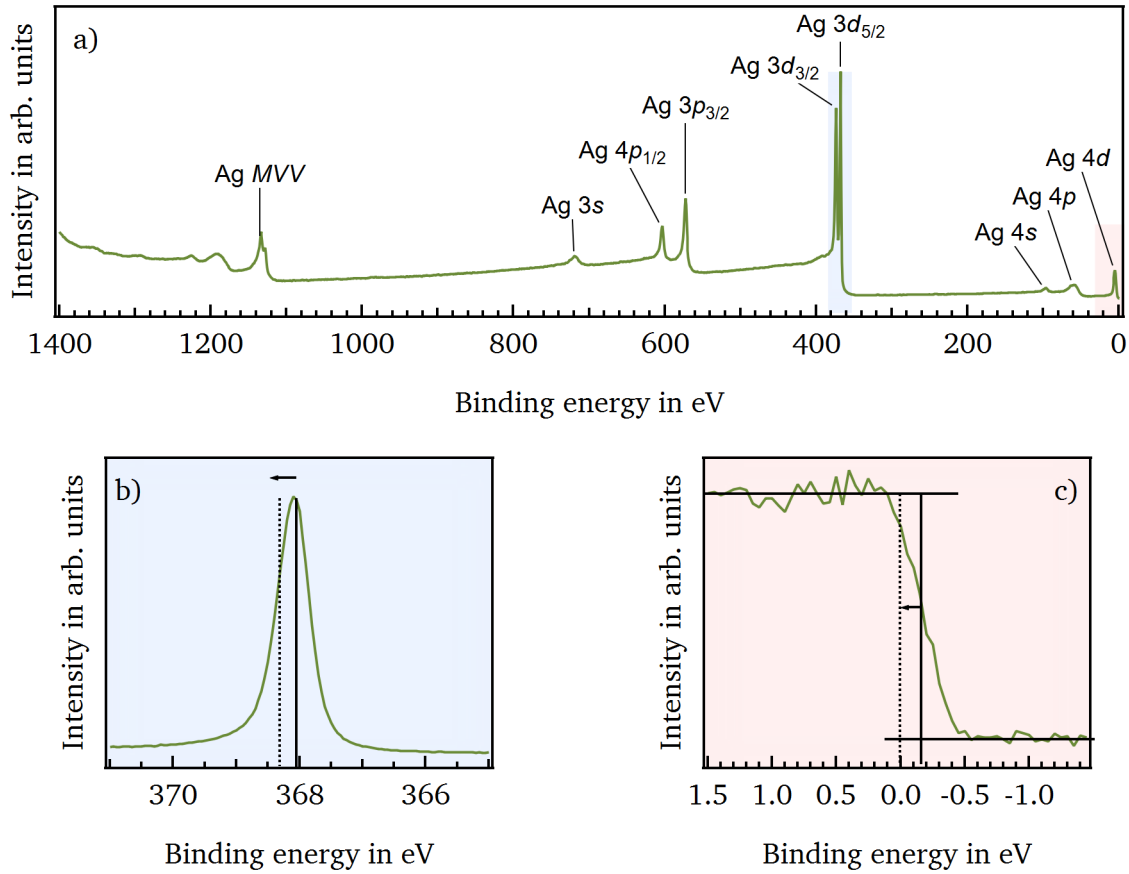

Figure 4.3.: XP-spectra of a silver sample for calibration. a) Survey spectra; b) Ag $3d_{5/2}$ core level line; c) valence band. The arrows in b) and c) indicate the calibration offset.

range for the detailed spectra varied upon the investigated core level.
All spectra were calibrated with respect to the Fermi edge of a sputter cleaned silver standard. Figure 4.3b) shows the offset of the Fermi edge to the origin. However, for a metal like silver it should pass through $0\,\text{eV}$. As the whole spectrum is influenced by the offset, it can be also seen in the shifted position of the Ag $3d_{5/2}$ emission line. In order to determine the correct core level binding energies all recorded spectra have to be adjusted by the measurement day's offset.

Table 4.3.: Parameters of XPS measuring modes.

measuring mode	range in eV	pass energy in eV	step width eV step^{-1}	$^{\text{time}}/_{\text{step}}$ in ms
survey	-1 – 1400	187.75	0.80	100
detailed	variable	5.85	0.05	100

Background subtraction and calculation of the composition

In order to calculate the correct integrated area for the determination of the sample's composition, the background has to be subtracted from the recorded core level emission lines. Figure 4.4 illustrates background subtractions for the Na $1s$, O $1s$, K $2p$, and Nb $3d$ peaks. The colored areas represent the integrated areas. By means of this area, the atomic sensitivity factors ASFs for each element, and Eq. 3.8, the samples' compositions can be determined. The atomic sensitivity factors matching with the instrument settings of the photoelectron spectrometer used in this work, are included in Fig. 4.4.

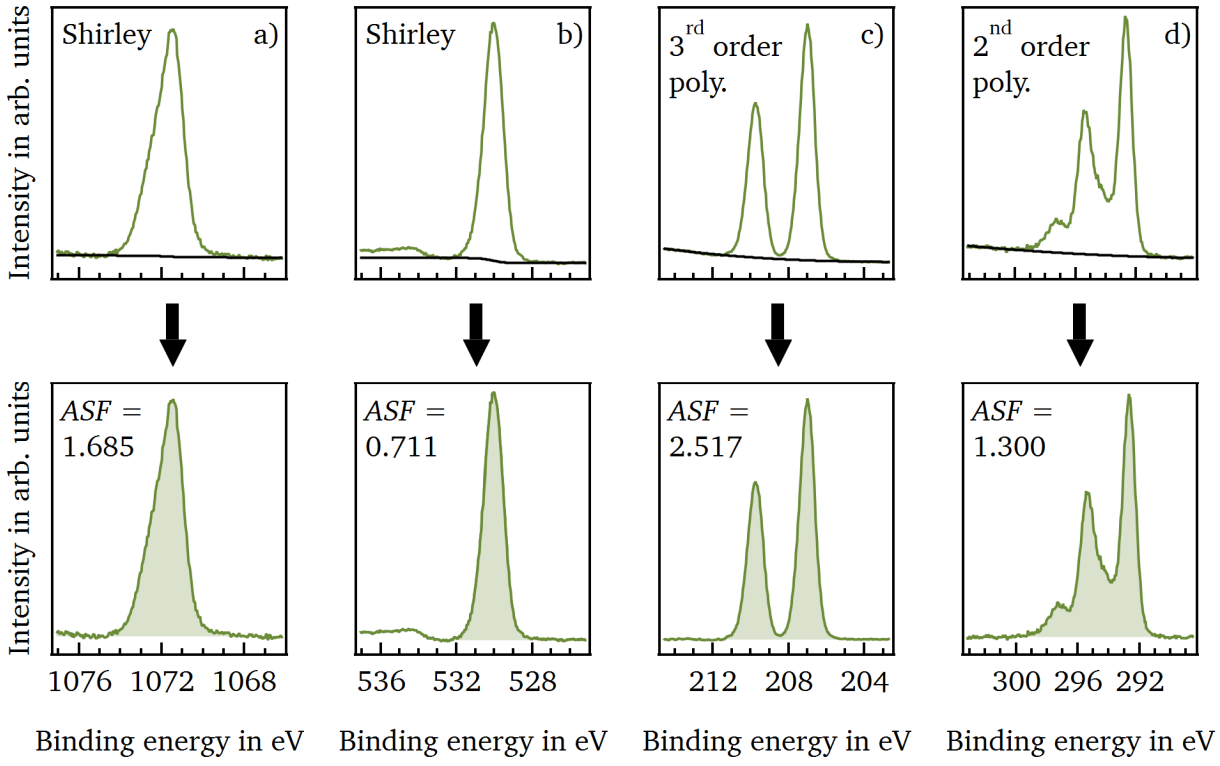

Figure 4.4.: Background subtraction for a) Na $1s$, b) O $1s$, c) Nb $3d$, and d) K $2p$ peak. Top: Measured spectra with background line. Bottom: Emission lines with already subtracted background.

4.11. Direct current conductivity measurements

Except for the high-voltage measurements at room temperature, all DC-conductivity measurements were conducted in a homemade oven in which either dry air or nitrogen can be used as the experimental atmosphere. Figure 4.5 illustrates this setup.

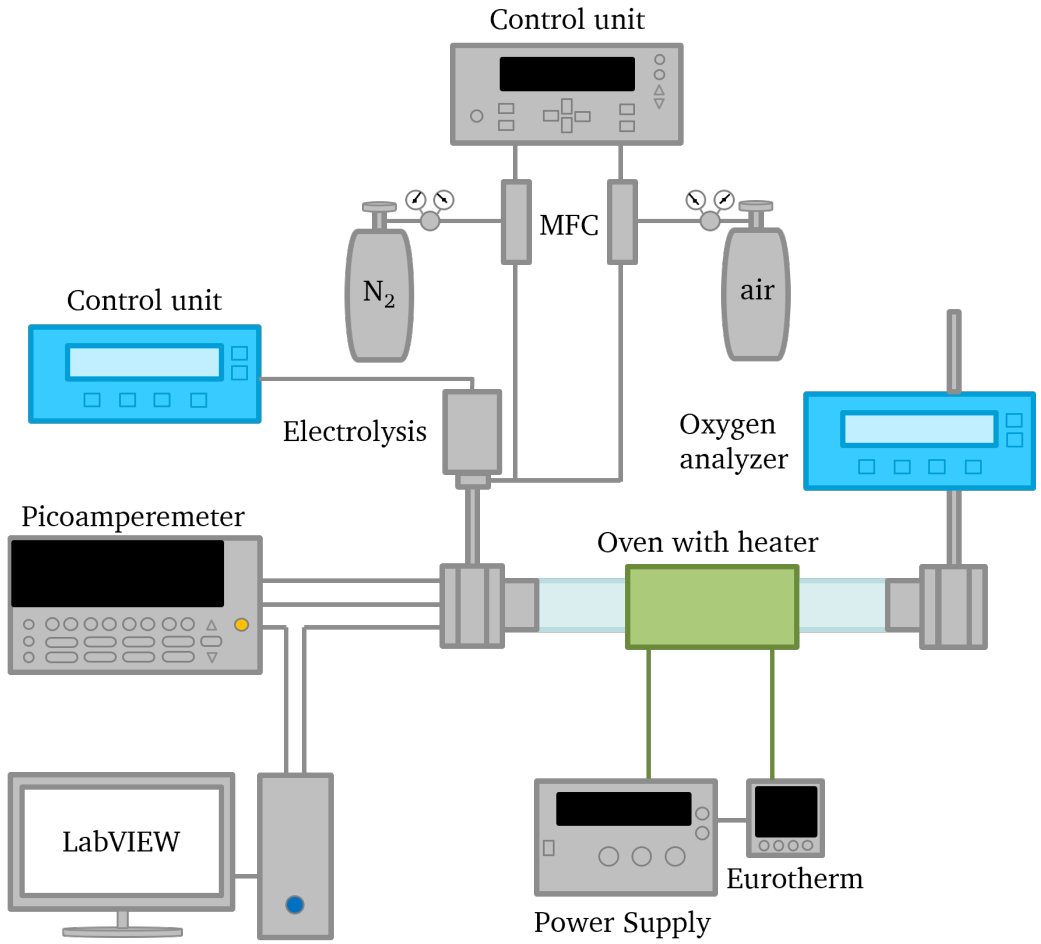

Figure 4.5.: Setup for DC-conductivity measurements.

The oven consists of a tube made of quartz glass with a DN 16 CF stainless steal flange on both sides, which is a custom-made product from LewVac company. The quartz glass tube has a length of $240\,\mathrm{mm}$ and a diameter of $14.3\,\mathrm{mm}$. Gas inlet and outlet from Swagelok are welded to spacers, which are mounted on the stainless steal flanges and closed by end flanges. Dry air or nitrogen can be introduced into the oven by mass flow controllers type PR 4000 (MKS instruments, Andover, MA, US). The oxygen partial pressure is adjusted by an ZIROX electrolysis (ZIROX Sensoren & Elektronik GmbH, Greifswald, Germany) and can be varied within a range of $1.0 \times 10^{-6}\,\mathrm{bar}$ to $2.1 \times 10^{-1}\,\mathrm{bar}$. A SGM_5T oxygen analyzer (ZIROX Sensoren & Elektronik GmbH, Greifswald, Germany) measures

the oxygen content at the gas outlet, which shows that the oxygen partial pressure within the oven can be changed from 8×10^{-6} bar to 2.1×10^{-1} bar.
The temperature is regulated by a homemade heating element, which is based on a resistance heating and adjusted by a Elektro-Automatik digital power supply 3065-05 B (Viersen, Germany). For further information about the structure of the heating element the reader is referred to the dissertation of Mareike Frischbier [242]. The temperature in the oven is controlled by means of a thermocouple of type E (NiCr/CuNi).

For conducting the experiments, a sample was mounted on the sample holder. Prior to the measurements Pt electrodes were deposited by a Q300TD sputter coater (Quorum, Laughton, East Sussex, UK). The diameter of the Pt electrodes was around $6\,\mathrm{mm}$. Between the two contacts a voltage was applied by a 6487 picoammeter (Keithley Instruments, Solon, Ohio, USA), which was measuring the current through the sample as well. All relevant parameters including voltage V, sampling rate r, electrode diameter D, and sample thickness d were set in a self-written Laboratory Virtual Instrumentation Engineering Workbench (LabVIEW) program provided by National Instruments. Applied voltage V, temperature T, current I, and conductivity σ were recorded with time by the LabVIEW program.

4.11.1. High-voltage measurements

As mentioned above the DC-measurements with high-voltages at room temperature were not conducted at the setup explained above but at a home-made setup in the high voltage laboratories at the Technical University of Darmstadt. Here, the DC-voltage was applied using an universal high voltage power supply PNChp 30000-2 mup (Heinzinger, Rosenheim, Germany) while the current was measured by a B2985A electrometer/picoamperemeter (Keysight Technolo- gies, Böblingen, Germany). The starting electric field of $0.4\,\mathrm{kV\,m^{-1}}$ was increased in $0.2\,\mathrm{kV\,m^{-1}}$ or $0.4\,\mathrm{kV\,m^{-1}}$ steps after relaxation of the conductivity.
Just like the samples for the polarization hysteresis measurements, the ceramic pellets were ground to a thickness of $0.25\,\mathrm{mm}$ and annealed at $600\,^{\circ}\mathrm{C}$ for $1\,\mathrm{h}$ to release the introduced stresses prior the high-voltage conductivity experiments. Afterwards, Pt contacts were deposited by a Q300TD sputter coater (Quorum, Laughton, East Sussex, UK). Finally, the samples were cut into $1.5\,\mathrm{mm} \times 1.5\,\mathrm{mm}$ rectangular by a diamond saw. These experiments are called *HV* in Table 4.4, which includes all relevant parameters.

Table 4.4.: Relevant parameters for all DC- and AC-conductivity measurements.

type of experiment	sample type	sample	d in mm	V in V	T_{max} in °C	$r_{heat/cool}$ in K min^{-1}	t_{hold} in min	f_{air} in sccm	f_{N_2} in sccm	$p_{O_2}(N_2)$ in bar	atmosphere
HV	$NaNbO_3$	NB111	0.23	100 - 1100	RT	–	–	–	–	–	air
	$Na_{0.99}Ca_{0.01}NbO_3$	NB130	0.23	100 - 900	RT	–	–	–	–	–	air
	$Na_{0.99}Sr_{0.01}NbO_3$	NB129	0.24	100 - 1300	RT	–	–	–	–	–	air
T-loops	$NaNbO_3$	NB162	0.79	0.1	500	1	2	5	50	$8 \cdot 10^{-6}$	air, N_2, air
	$Na_{0.99}Ca_{0.01}NbO_3$	NB153	0.72	0.1	600	1	2	5	50	$8 \cdot 10^{-6}$	air, N_2, air
	$Na_{0.99}Sr_{0.01}NbO_3$	NB176	0.65	0.1	500	1	2	5	50	$8 \cdot 10^{-6}$	air, N_2, air
	$KNbO_3$	NB172	0.68	1.0	500	1	2	5	50	$8 \cdot 10^{-6}$	air, N_2, air
Relaxation	$Na_{0.99}Ca_{0.01}NbO_3$	NB153	0.72	0.1	350	5	5300	5	50	$8 \cdot 10^{-6}$	N_2, air
		NB153	0.72	0.1	400	5	12674	5	50	$8 \cdot 10^{-6}$	N_2, air
		NB136	0.67	0.3	460	5	431	5	5	$5 \cdot 10^{-3}$	N_2, air, N_2
		NB136	0.67	0.1	470	5	166	5	5	$5 \cdot 10^{-3}$	N_2, air, N_2
		NB136	0.67	0.05	540	5	200	5	5	$5 \cdot 10^{-3}$	air, N_2, air
		NB136	0.67	0.05	560	5	180	5	5	$5 \cdot 10^{-3}$	air, N_2, air
Degradation	$NaNbO_3$	NB162	0.79	0.01 - 400	RT - 500	5	270	–	–	–	air
	$Na_{0.99}Ca_{0.01}NbO_3$	NB136	0.67	0.01 - 400	RT - 500	5	140	–	–	–	air
	$Na_{0.99}Sr_{0.01}NbO_3$	NB135	0.66	0.10 - 400	RT - 400	5	130	–	–	–	air
	$KNbO_3$	NB119	0.48	0.01 - 400	RT - 300	5	160	–	–	–	air
Impedance	$NaNbO_3$	NB114	0.34	0.1 – 1.0	600	5	30	–	–	–	air
	$Na_{0.99}Ca_{0.01}NbO_3$	NB136	0.67	0.1 – 1.0	600	5	30	–	–	–	air
	$Na_{0.99}Sr_{0.01}NbO_3$	NB135	0.66	0.1 – 1.0	600	5	30	–	–	–	air
	$KNbO_3$	NB180	0.68	0.1 – 1.0	600	5	30	–	–	–	air

4.11.2. Temperature and atmosphere dependent measurements

Temperature dependent conductivity plots were recorded for all $NaNbO_3$- and $KNbO_3$-based ceramic samples in dry air. A voltage of $0.1\,V$ and $1.0\,V$ was applied to the $NaNbO_3$- and $KNbO_3$-based samples, respectively. Every $30\,s$ the current was measured while the sample was heated up to a maximum temperature T_{max} of $500\,°C$ or $600\,°C$ with a heating rate r_{heat} of $1\,K\,min^{-1}$ at an air flow f_{air} of $5\,sccm$. After holding the maximum temperature for $2\,min$ (t_{hold}) the sample was cooled down with an cooling rate r_{cool} of $1\,K\,min^{-1}$. This heating cycle was repeated five to ten times. Afterwards, the atmosphere was changed to nitrogen with a flow f_{N_2} of $50\,sccm$ and the oxygen partial pressure was set to the minimum reachable value of $8 \times 10^{-6}\,bar$. Once again, the conductivity was examined for five to ten heating cycles. Finally, the atmosphere was changed back to pure dry air and five to ten heating cycles were performed while determining the conductivity. All relevant parameters including the thickness of the measured samples d are listed in Table 4.4. The temperature dependent conductivity plots described within this section are called *T-loops* in Table 4.4.

4.11.3. Relaxation experiments

Relaxation experiments were performed on $Na_{0.99}Ca_{0.01}NbO_3$ samples. The samples were heated up to a certain temperature with $5\,K\,min^{-1}$ in either dry air or nitrogen with an oxygen partial pressure of $5 \times 10^{-3}\,bar$ or $8 \times 10^{-6}\,bar$ while a voltage between $0.05\,V$ to $0.30\,V$ was applied. After reaching the target temperature the conductivity was measured until an equilibrium state was developed. Then, the atmosphere was changed either to nitrogen or dry air depending on what was the starting condition. The conductivity was again monitored until an equilibrium value was reached. For some temperatures a last step with the starting atmosphere conditions was conducted. Afterwards, the same procedure was performed at a higher temperature. The exact parameters for each measured sample can be looked up in Table 4.4. In total, the samples were measured in a temperature range from $100\,°C$ to $560\,°C$. However, in Table 4.4 only the measurements are listed, which are important for the later analysis of this work.

4.11.4. Resistance degradation experiments

In order to analyze the resistance degradation behavior an electric field profile is applied to a sample at a constant temperature. These experiments were conducted on all ceramics under investigation in this work. The samples were post-annealed at $500\,°C$ for $1\,h$ after each electric field cycle in order to ensure for a homogeneous defect concentration over the whole sample. For some samples, a second cycle was performed at the same temperature without post-annealing. In addition, the electrode of the $NaNbO_3$ sample were grounded for a few seconds after each electric field profile to remove any

surface charges, which could influence the following measurement. Unfortunately, this was not done for the other samples.
The electric field profile was applied at temperatures from room temperature up to $600\,°C$. The heating and cooling rate prior and after the measurements were $5\,K\,min^{-1}$. Each electric field step was 10 min long. All relevant parameters and important information are listed in Table 4.4 in which the resistance degradation experiments are called *degradation*.

4.12. Impedance spectroscopy

Impedance measurements were performed in air on all four sample types $NaNbO_3$, $Na_{0.99}Ca_{0.01}NbO_3$, $Na_{0.99}Sr_{0.01}NbO_3$, and $KNbO_3$. The temperature was increased from $125\,°C$ to $600\,°C$ and decreased back to $125\,°C$ again in $25\,°C$-steps. The heating and cooling rate $r_{heat/cool}$ was $5\,K\,min^{-1}$. At each temperature T the impedance was recorded with an amplitude-voltage V of $0.1\,V$ to $1.0\,V$ within a frequency range of $0.1\,Hz$ to $3 \times 10^6\,Hz$. For the experiments, an Alpha-A impedance analyzer (Novocontrol Technologies GmbH & Co. KG, Montabaur, Germany) was used. Prior to the measurements, Pt electrodes with a $6\,mm$ diameter were sputtered by a Q300TD sputter coater (Quorum, Laughton, East Sussex, UK) on both sides of the samples. All relevant parameters including sample thickness d are listed in Table 4.4.
The impedance measurements were conducted by Maryam Azadeh in the working group Nonmetallic-Inorganic Materials at TU Darmstadt.

4.13. Combined XPS and DC-conductivity measurements

In order to investigate the electrode-sample interface XPS-measurements were conducted combined with a DC-conductivity analysis at elevated temperatures. Prior to the experiments a $3\,nm$ thick ITO-electrode with a diameter of $6\,mm$ was deposited on top of the sample to ensure a conductive enough electrode to prevent charging during the XPS-measurements while still being able to detect a signal of both, electrode and sample. The ITO-film was deposited in the Ox II-chamber of the DAISY-MAT at $400\,°C$ after cleaning the sample at the same temperature for $2\,h$ in a low pressure oxygen atmosphere of $0.5\,Pa$ with an oxygen flow of 5 sccm. Then, the gas was changed to pure argon with a flow of 10 sccm at $0.5\,Pa$. For ITO-deposition the power of the RF-generator was set to $25\,W$ and the sample-to-target distance was $10\,cm$. The ITO-layer was deposited for $36\,s$, which results in the required sample thickness of $3\,nm$ with a deposition rate of $5\,nm\,min^{-1}$. A thick platinum layer with a diameter of $6\,mm$ was used as bottom electrode, which was deposited by a Q300TD sputter coater (Quorum, Laughton, East Sussex, UK). Afterwards, the sample was mounted on a special sample holder in order to perform the simultaneous XPS and conductivity measurements

while heating the sample. The sample holder is shown in Fig. 4.6. The inner contact was separated from the outer part of the holder by ceramic plates and was connected with the bottom platinum electrode. The sample was fixed on the holder by the mask, which was simultaneously connecting the ITO-top-electrode with the outer part of the sample holder. After mounting the sample on the sample holder, it was transferred into the XPS-chamber, where the sample holder was positioned on the XPS holder, which is illustrated in Fig. 4.6. Here, the sample could be heated up by a heating wire, which was powered by a Elektro-Automatik digital power supply 3032-10 B (Viersen, Germany). The outer clamp fixture and the inner pin were in contact with outer and inner part of the sample holder, respectively. A voltage was applied between outer clamp and inner pin by a 6487 picoammeter (Keithley Instruments, Solon, Ohio, USA).

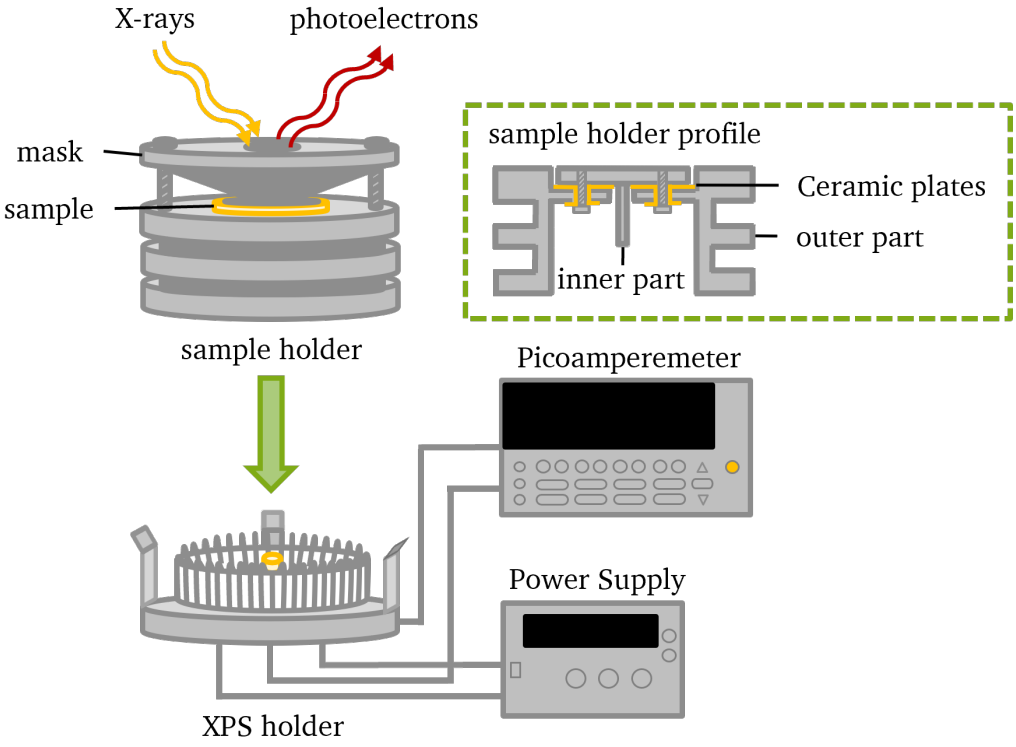

Figure 4.6.: Setup for combined XPS and DC-conductivity measurements.

A complete XP-spectra over the whole energy scale as well as detailed spectra of the sample's and ITO-electrode's core levels are measured before, while, and after heating and applying a voltage in a Physical Electronic PHI 5700 multi-technique surface analysis system as described in section 4.10.3. With this method changes in peak position, shape, and intensity during heating and DC-conductivity measurements were examined, which could be informative about possible interactions between electrode and sample. Furthermore, potential mechanisms causing a resistance degradation could be monitored.
The measurements are conducted with the top electrode being the anode or the cathode. Table 4.5

lists all relevant parameters including sample thickness d, applied voltage V, voltage for the heating wire V_{heat}, and temperature T for each experiment.

Table 4.5.: Relevant parameters combined XPS and DC-conductivity measurements.

type of electrode	sample type	sample	d in mm	V in V	V_{heat} in V	T in °C	atmosphere
anode	$Na_{0.99}Ca_{0.01}NbO_3$	NB160	0.67	10	3.30	100	vacuum
cathode	$Na_{0.99}Ca_{0.01}NbO_3$	NB160	0.50	15	3.30	100	vacuum
				30	3.30	100	vacuum
				30	6.95	200	vacuum
				30	–	RT	vacuum

5. Sample preparation and basic characterization

In this section, the sample preparation and the basic structural and electrical characterization of the produced samples by means of SEM, XRD, and measurements of polarization hysteresis loops and permittivity will be presented and discussed. The main aspects examined in this chapter can be summarized as following.

This chapter has the aim to ...

- ... validate the samples' condition (composition, crystal structure, (anti)ferroelectric state, electrical conductivity).
- ... analyze the morphology of the samples including size, shape, and distribution of grains, pores, and possible secondary phases.
- ... examine segregation and depletion due to sodium and potassium volatility.

5.1. Particle size and densification

First, the sample preparation is qualified by examining the particle size after each milling step and analyzing the shrinkage behavior during calcination and sintering. This allows for determination of the right calcination and sintering temperature.
As introduced before, the particle size of the precursor powders as well as the powder after homogenization and calcination has a big impact on the synthesis and the microstructure of the sintered samples. A homogeneous particle distribution with small particle size is preferred. Therefore, the particle size of the powders were investigated after each milling step. Fig. 5.1 illustrates the particle size distribution after homogenization, 1st and 2nd calcination for all four sample types.

After homogenization, a large variation of the particle size ranging from $0.1\,\mu m$ to $10\,\mu m$ can be observed. The milling step after the 1st calcination leads already to a quite uniform particle distribution, which is further improved by an additional milling after the 2nd calcination. In case of the $KNbO_3$ powder, the particle size distribution does not change significantly after the final milling step.

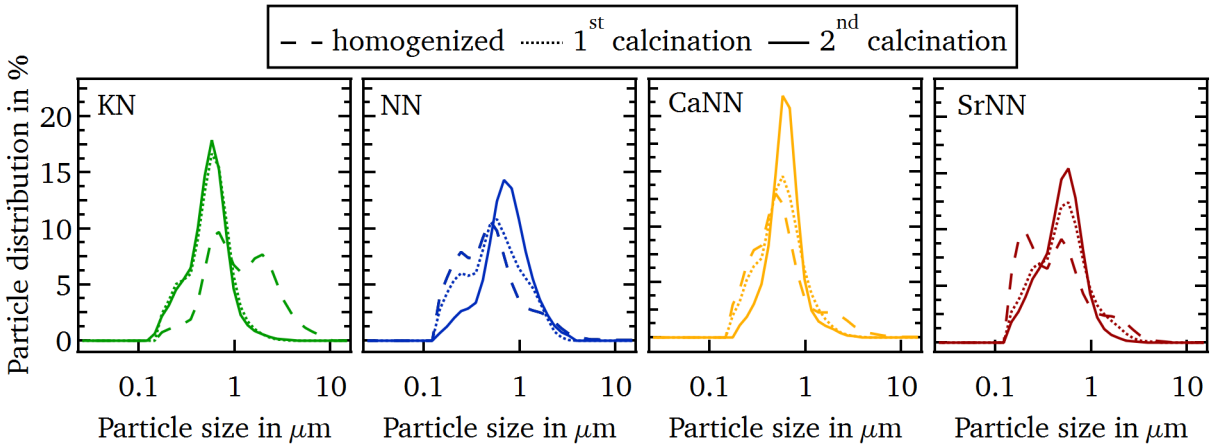

Figure 5.1.: Particle size distribution of the powders after homogenization, 1st and 2nd calcination for the four different materials.

The mean particle size has a value around $0.69\,\mu m$ for $NaNbO_3$ whereas for the other materials it is distributed around $0.58\,\mu m$. In any case, some particles have a smaller size going down to $0.1\,\mu m$. Overall it can be stated that a homogeneous particle distribution around $0.6\,\mu m$ to $0.7\,\mu m$ is achieved, which should result in a good synthesis and sintering behavior.

In order to determine a suitable calcination temperature, the shrinkage behavior of the homogenized powder is analyzed by means of a heating stage microscope. On the left side of Fig. 5.2 the corresponding curves are shown for $KNbO_3$, $NaNbO_3$, $Na_{0.99}Ca_{0.01}NbO_3$, and $Na_{0.99}Sr_{0.01}NbO_3$. The heating rate was $10\,K/min$ for $KNbO_3$ and $NaNbO_3$ while it was $5\,K/min$ for the doped $NaNbO_3$ samples. Dotted lines mark the temperatures at which a change in slope can be observed. At around $400\,°C$ the materials start to expand indicating the begin of the solid-state reaction. The maximum expansion is reached at around $600\,°C$ for the $NaNbO_3$-based samples while for $KNbO_3$ it is already obtained at $540\,°C$. In case of the $NaNbO_3$-based samples both, the onset of expansion as well as the maximum expansion, exhibit lower values for the doped samples compared to the undoped one. The expansion of the materials is caused by decomposition of the carbonates and the formation of the reaction layer on the niobium pentoxide particles. $2\,mol$ of the product material is formed by $1\,mol$ niobium pentoxoide. Therefore, the theoretical expansion can be calculated by the following equations [191]:

$$\frac{\Delta r}{r} = \sqrt[3]{\frac{2V_M(\text{product})}{V_M(Nb_2O_5)}} - 1 \tag{5.1}$$

$$V_M = \frac{M}{\rho} \tag{5.2}$$

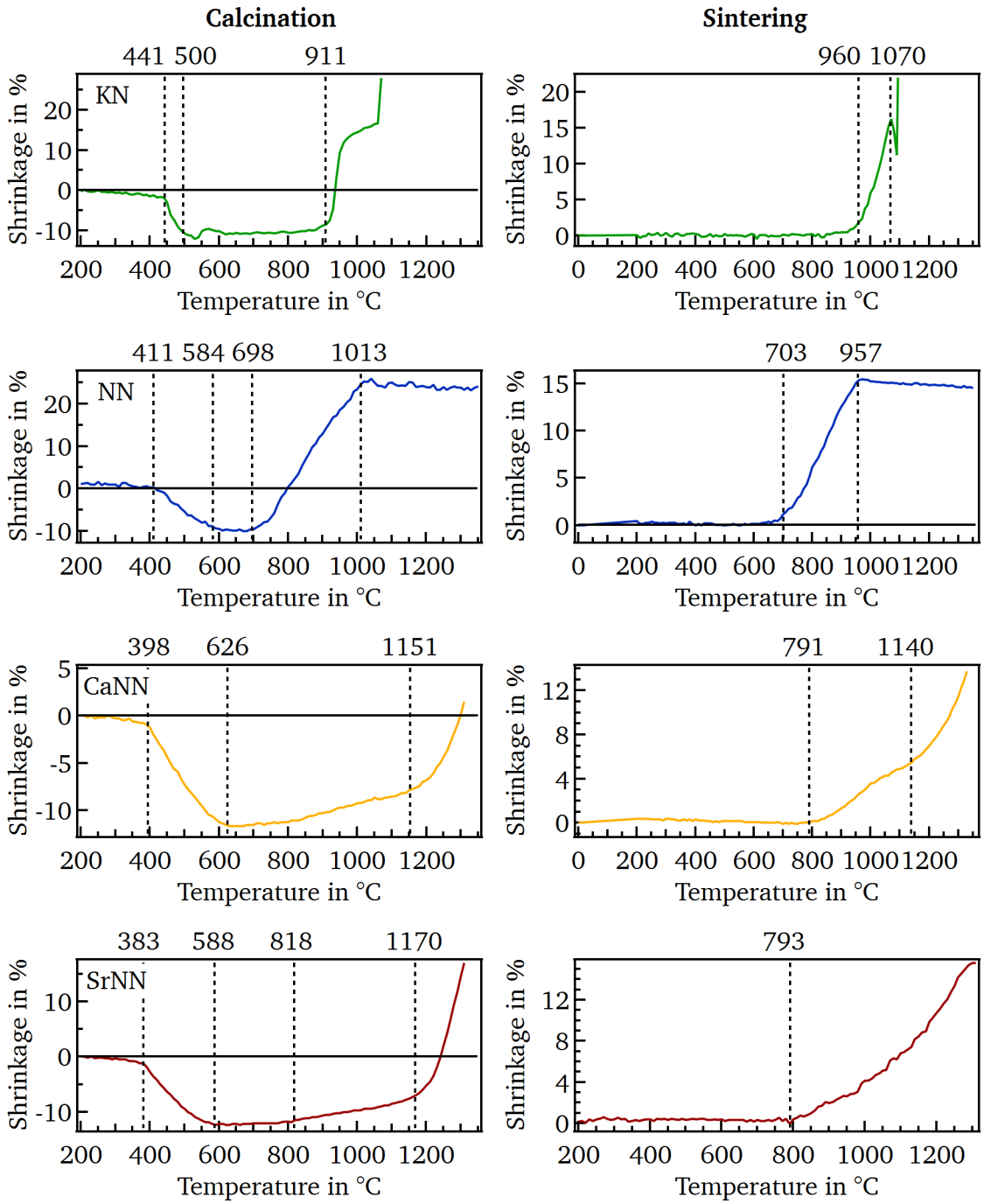

Figure 5.2.: Shrinkage of a green body in dependence of temperature before calcination (left side) and before sintering (right side) for $KNbO_3$, $NaNbO_3$, $Na_{0.99}Ca_{0.01}NbO_3$, and $Na_{0.99}Sr_{0.01}NbO_3$. The dotted lines indicate changes in the shrinking behavior.

where V_M is the molar volume in $cm^3\,mol^{-1}$, M is the molar mass in $g\,mol^{-1}$, and ρ is the theoretical density in $g\,cm^{-3}$. Theoretical densities of $4.55\,g\,cm^{-3}$[18] and $4.64\,g\,cm^{-1}$[18] for $NaNbO_3$ and

$KNbO_3$ are taken, respectively. According to Equations 5.1 and 5.2 the maximum theoretical expansion for $NaNbO_3$ is $12.1\,\%$. Doping with 1 mol% calcium and strontium leads to slightly larger theoretical expansions of $12.2\,\%$ and $12.3\,\%$, respectively. The experimental values of $11.5\,\%$ and $12.3\,\%$ for $Na_{0.99}Ca_{0.01}NbO_3$ and $Na_{0.99}Sr_{0.01}NbO_3$ are in relatively good agreement with the theoretical values. In contrast, the experimentally determined maximum expansion of $9.9\,\%$ for $NaNbO_3$ deviates more from the theoretical value. A similar behavior can be observed for $KNbO_3$ with a measured value of $12.0\,\%$ and a theoretical value of $14.9\,\%$. In order to ensure a complete reaction of all starting materials a calcination temperature above the maximum expansion, but below a significant densification occurs, is chosen. Therefore, the $KNbO_3$ powder is calcined at $800\,°C$. The calcination temperature of pure $NaNbO_3$ is set to $700\,°C$ while the one for the doped $NaNbO_3$ powders is $250\,°C$ higher.

Before sintering, a shrinkage curve with the same heating rate of $5\,K/min$ used during sintering is measured to identify a suitable sintering temperature. The corresponding curves are plotted on the right side of Fig. 5.2 for the investigated materials. $KNbO_3$ shows a narrow shrinkage region from $960\,°C$ to $1070\,°C$ followed by a small expansion and a steep shrinkage. This behavior can be attributed to the melting point of $KNbO_3$ at $1100\,°C$ [18]. In Fig. A.1 in the appendix, pictures of a pellet at $1070\,°C$, $1080\,°C$, and $1100\,°C$ are displayed. It can be clearly seen that at $1080\,°C$ the edges of the pellet start to soften and at $1100\,°C$ the sample melts. Melting results in a decrease of the measured diameter explaining the sudden increase in the shrinkage curve. Similar shrinkage curves have been described in literature [203, 204]. Acker et al. [204] investigated the influence of potassium and niobium excess on the shrinkage behavior as well as on densification. According to them, K-excess leads to a reduction of the temperature range in which the material shrinks whereas Nb-excess increases this temperature range compared to stoichiometric $KNbO_3$. By heating with $5\,K/min$ the stoichiometric sample starts to shrink at $742\,°C$ and reaches its maximum at $947\,°C$ while the Nb-rich material starts to shrink at $960\,°C$ and has not got to the maximum point before melting. The behavior of the Nb-rich sample is similar to the one observed in this thesis. Therefore, it might indicate that the $KNbO_3$ samples are deficient in potassium. Possible causes could be evaporation during calcination and/or an error during weighting of the K_2CO_3 precursor powder due to adsorbed water. Nevertheless, the sintering temperature was determined from the measured shrinkage curve. To stay below the melting point but still ensure a high densification a sintering temperature of $1010\,°C$ was chosen.

The $NaNbO_3$-based samples start to densify at lower temperatures around $700\,°C$ for pure $NaNbO_3$ and around $790\,°C$ for the doped samples. Furthermore, the shrinkage range is larger compared to $KNbO_3$. Undoped $NaNbO_3$ shrinks up to $950\,°C$ whereas the doped samples are still shrinking until a temperature of $1300\,°C$. For $Na_{0.99}Ca_{0.01}NbO_3$ it seems that the maximum of the shrinkage is even not reached at $1300\,°C$. This is why a higher sintering temperature of $1320\,°C$ was chosen. The sintering temperature for $NaNbO_3$ and $Na_{0.99}Sr_{0.01}NbO_3$ was set to $1250\,°C$.

5.2. Microstructure

The microstructure is analyzed to investigate the homogeneity of the grains as well as size and distribution of the grains and pores. By scanning for the appearance of secondary phases it is verified that all precursors fully reacted to $NaNbO_3$ or $KNbO_3$ during calcination. In addition, the density of the samples is checked to evaluate the densification behavior during sintering.

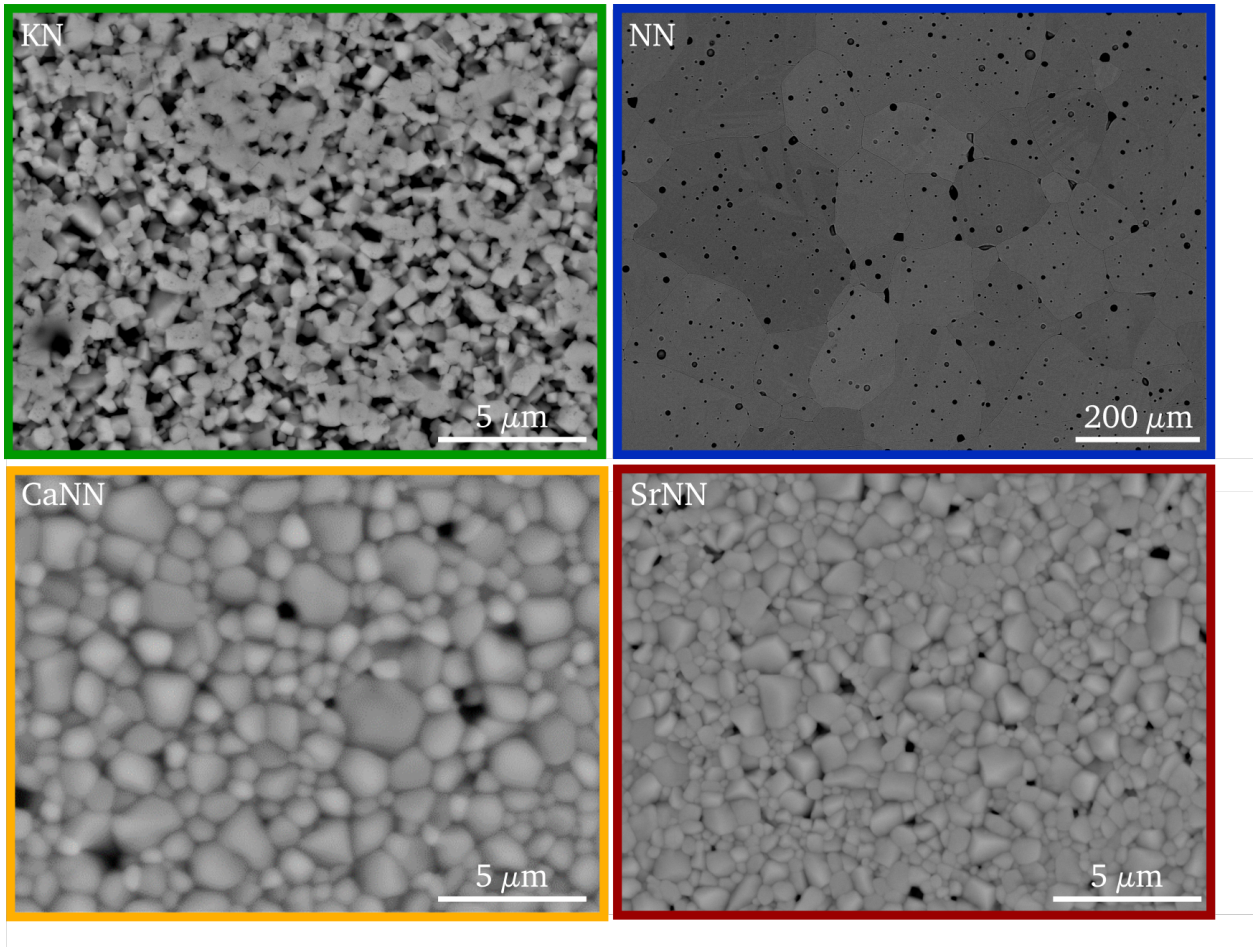

Figure 5.3.: SEM pictures of $KNbO_3$ (green), $NaNbO_3$ (blue), $Na_{0.99}Ca_{0.01}NbO_3$ (yellow), and $Na_{0.99}Sr_{0.01}NbO_3$ (red).

The microstructure was analyzed by SEM while the density was measured by means of the Archimedes density method as described in Section 3.3. Figure 5.3 illustrates the SEM pictures of the investigated material systems. $NaNbO_3$ exhibits large grains around $90\,\mu m$ in diameter and a relative density of $94.5\,\%$. In addition, pore inclusions within the grains can be observed. Such an abnormal grain growth combined with pore inclusions is detected in pure $NaNbO_3$ in literature as well [146, 194]. Doping with Ca and Sr leads to a tremendous reduction in grain size to $1.5\,\mu m$ and $0.9\,\mu m$ and an

increase in density to $96.1\,\%$ and $96.0\,\%$, respectively. Similar effects are observed in literature for Sr-doped $K_{0.5}Na_{0.5}NbO_3$ [212, 243]. Hrescak et al. [212] detected no secondary phase until a doping content of 2 mol% Sr. This agrees with the observation of this work, in which no secondary phases are identified via SEM for 1 mol% Ca or Sr doping.
In general, it seems that A-site donor dopants with a valency of $+2$ such as Ca, Sr, or Ba reduce the grain size in $NaNbO_3$-based materials [10, 138, 211, 244]. This might not be surprising as it is already known for $BaTiO_3$ that A-site donor doping leads to smaller grains [38, 245, 246].

Evaluating the grain size of the $KNbO_3$ bulk ceramic with the line intercept method is difficult due to the high porosity of the sample. Therefore, it is estimated from the SEM picture to be 0.5 µm to 1.0 µm. The relative density determined by the Archimedes density method is $88.7\,\%$. The microstructure is comparable to microstructures one can find in literature for samples prepared at similar sintering conditions. Kim et al. [173] obtained small grain sized $KNbO_3$ with a low density at a sintering temperature of $1020\,°C$ and a sintering time of $2\,h$. In contrast, Acker et al. [204] received large grains ranging from 150 µm to 500 µm with a high relative density of $94.4\,\%$ sintered at $1030\,°C$ for $2\,h$ for a stoichiometric $KNbO_3$ composition. Nb-excess, however, leads to a decrease in both, density ($89.8\,\%$) and grain size including very small grains ranging from 1 µm to 2 µm and medium grains of maximum 15 µm. As discussed in the previous Section 5.1, the $KNbO_3$ samples prepared in this work might be K-deficient indicated by their shrinkage behavior. The small grain size and high porosity support this fact. A clear statement whether or not the samples exhibit a K-deficiency can yet not be made as the microstructure depends on many sintering parameters such as temperature, time, rate, and atmosphere as well as on the conditions of the calcined powder examined in the next section.

5.3. X-ray Diffraction

In order to determine the crystal structure, all present phases, and the appearance of possible secondary phases, XRD was conducted on $NaNbO_3$ and $KNbO_3$ powders after first and second calcination as well as after sintering. Here, the as-calcined pellets as well as the cut-off edges of the as-sintered rod were crushed by a mortar. Then, XRD was performed on the powders by the Bragg-Brentano method described in Section 3.5.

Fig. 5.4 shows the measured intensity of the reflections of pure $NaNbO_3$ powder on a logarithmic scale over the whole 2θ-region from $10°$ to $90°$. On first glance, the pattern after calcination and sintering do not differ much. It can be noticed that the powders are phase pure and there are no secondary phases, as already observed with SEM. In order to distinguish whether the samples crystallize in the antiferroelectric P or the ferroelectric Q phase, one has to analyze some parts of the diffraction pattern in more detail. In literature, the 2θ-ranges from $35.0°$ to $38.0°$, $42.5°$ to $44.0°$, and $54.0°$ to $56.0°$ are usually investigated to differentiate between the two phases [112, 116, 118, 133, 247].

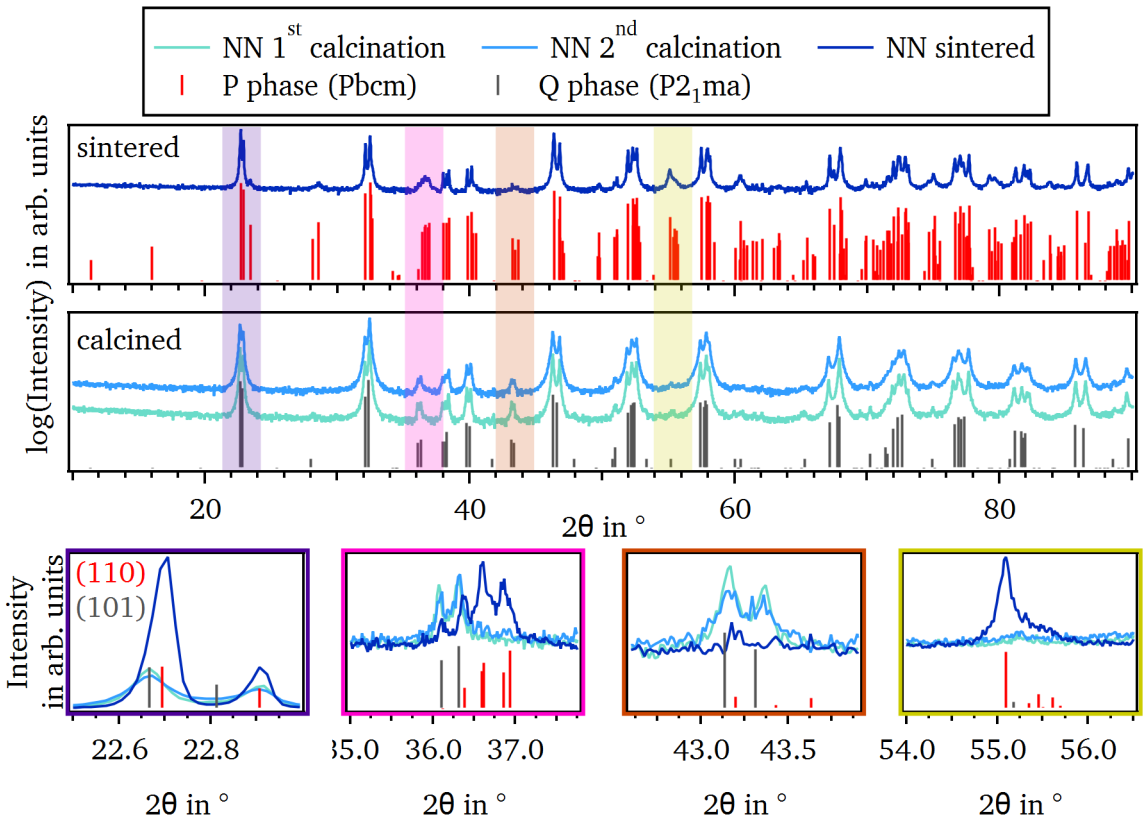

Figure 5.4.: X-ray diffraction pattern of pure $NaNbO_3$ after first and second calcination and after sintering. The reflections of the antiferroelectric P phase with space group Pbcm (red) was calculated by the program VESTA [160] while the lines of the ferroelectric Q phase with space group $P2_1ma$ (grey) correspond to the powder diffraction file JCPDS 01-082-0606 [109]. The measured patterns are aligned in position according to the (110)- and (101)-reflection located around $26.7°$ of the reference patterns of P and Q phase, respectively.

These regions are enlarged in Fig. 5.4. It can be clearly seen that the calcined powders crystallize in the ferroelectric Q phase with space group $P2_1ma$ while after sintering the powder is mostly present in the antiferroelectric P phase with space group Pbcm, which was also observed by Koruza et al. [116]. Only a small amount of Q phase can be identified after sintering. It should be mentioned that for better comparison the measured diffraction patterns shown in Fig. 5.4 are shifted according to the (110)- and (101)-line of the reference patterns of P and Q phase, respectively. The illustrated reference diffraction lines for the P phase are calculated by the program VESTA [160] while the ones for the Q phase correspond to the powder diffraction file JCPDS 01-082-0606 [109].
These two patterns were chosen after a detailed analysis of the diffraction patterns calculated by VESTA and the corresponding powder diffraction files for both, P (JCPDS 01-073-0803 [108]) and

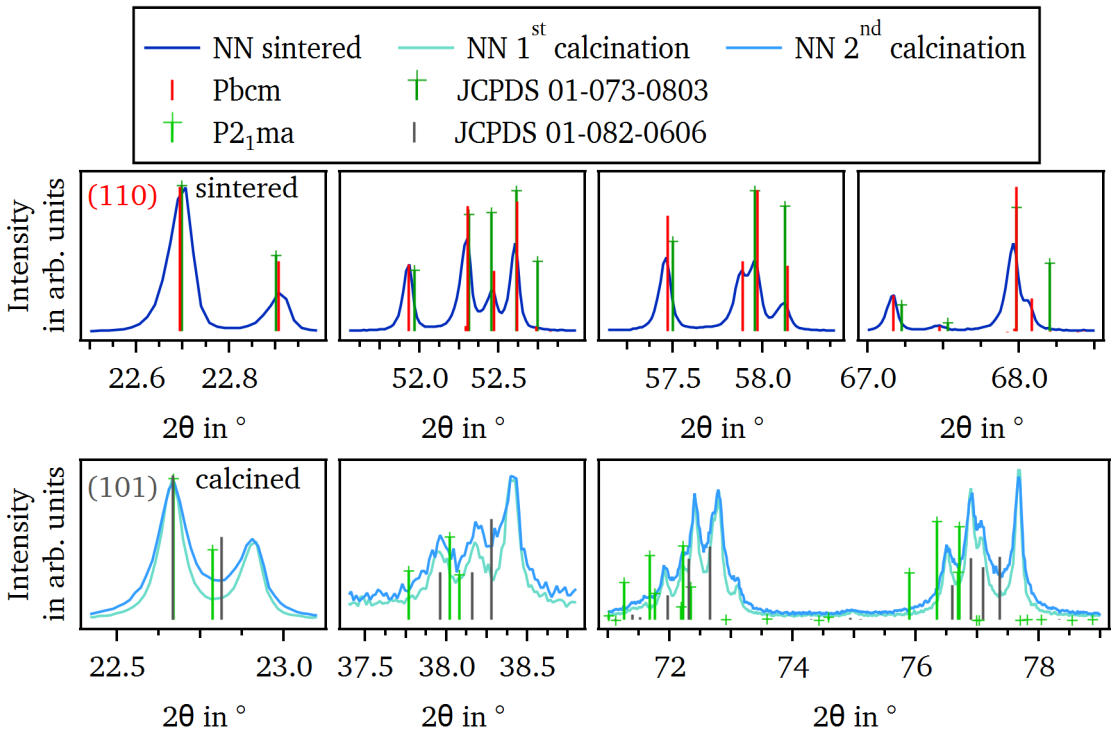

Figure 5.5.: Selected 2θ-regions for comparison of the measured diffraction patterns after calcination and sintering of pure $NaNbO_3$ powder to calculated patterns by the program VESTA [160] and the corresponding powder diffraction patterns from literature. For the antiferroelectric P phase (Pbcm) and the ferroelectric Q phase ($P2_1ma$) the JCPDS file 01-073-0803 [108] and 01-082-0606 [109] were chosen, respectively. All patterns are normalized in intensity and aligned in position according to the (110)- and (101)-reflection located around $26.7°$ of the reference patterns of P and Q phase, respectively.

Q phase (JCPDS 01-082-0606 [109]). In Fig. 5.5 the differences between these patterns and the ones for the calcined and sintered powders are examined for selected regions. The lines of the sintered powder match well with the calculated reflections. In contrast, the calcined powders can be described better with the powder diffraction pattern JCPDS 01-082-0606 [109]. Consequently, these two patterns are taken to identify the P and Q phases in Fig. 5.4. It should be mentioned that in Fig. 5.5 the line positions are aligned and the intensities are normalized according to the (110)- and (101)-reflection at around $22.7°$ for P and Q phase, respectively. From Fig. 5.5 we can clearly see that the intensities of the measured patterns do not match for all diffraction lines with the reference patterns. This effect can most likely be explained by a non-homogeneous grain size distribution of large grains resulting in a texture due to an insufficient grinding with the mortar. A homogeneous grain size distribution below $5\,\mu m$ is desired for a high accuracy of the line intensities [220]. Furthermore, a broader full width at half maximum (FWHM) is observed after the second

calcination compared to the first calcination. This can have multiple reasons such as internal stress resulting from crushing with the mortar or very small grain sizes. However, internal stresses seem to be the more probable cause as we have just referred the intensity differences to the large grain size distribution. Another indication for a stress related broadening of the diffraction lines are the shifted line positions compared to the reference lines. It makes sense that some residual stresses are left in the calcined powders as no stress-release heating step was performed before the XRD measurements. In contrast, the sintered powder was heated for $1\,\mathrm{h}$ at $600\,^{\circ}\mathrm{C}$ before conducting the XRD measurement. Hence, the diffraction lines match quite well in position with the reference lines due to the stress-release during heating.

In case of $Na_{0.99}Ca_{0.01}NbO_3$ and $Na_{0.99}Sr_{0.01}NbO_3$, similar observations as for pure $NaNbO_3$ can be made. The calcined powders crystallize in the ferroelectric Q phase while after sintering the powders take the antiferroelectric P phase. This can be seen in Fig. A.2 and Fig. A.3 in the appendix. Torres-Pardo et al. [139] investigated the influence of Sr-doping on the stabilization of the Q phase by using following formula $Na_{1-x}Sr_{x/2}\square_{x/2}NbO_3$ with $x = 0, 0.1, 0.2, 0.3$, and 0.4. Up to $x = 0.1$ they were able to assign the P phase to their measured XRD pattern. A doping of $x = 0.2$ led to the stabilization of the ferroelectric Q phase. According to their results, the samples, which were prepared within this work with 1 mol% Sr-doping should still be in the AFE region. This, indeed, could be verified by the XRD measurements shown in Fig. A.3 in the appendix, which illustrate that the $Na_{0.99}Sr_{0.01}NbO_3$ samples mostly crystallize in the antiferroelectric P phase. Similar observations have been reported for Ca-doped $NaNbO_3$ in the work of Liu et al. [33]. They incorporated Ca according to following formula $(Na_{1-2x}Ca_x)NbO_3$ with $x = 0.01, 0.02, 0.04,$ and 0.08 compensating the additional charges by sodium vacancies. Up to $x = 0.04$ the samples showed the antiferroelectric superlattice reflections. At $x = 0.08$ the intensity of this reflection line was decreased. Consequently, there seems to be a limit for Ca-incorporation until which antiferroelectricity can be sustained. Passing this limit destabilizes the antiferroelectric phase. Interestingly, Liu et al. prepared a sample without sodium vacancy compensation ($(Na_{0.96}Ca_{0.04})NbO_{3.02}$) for comparison, which did not show the superlattice reflection characteristic of the antiferroelectric phase. We doubt that the written formula is correct because it is very unlikely that oxygen will fill an interstitial site in a perovskite material. Nevertheless, they concluded from these results that compensation with sodium vacancies plays a crucial role for maintaining the antiferroelectric phase. However, from the results in this work it can be seen that up to 1 mol % Ca-doping the P phase still remains.

Comparing the sintered powders of $NaNbO_3$ with Ca- and Sr-doped $NaNbO_3$, a shift of the diffraction patterns towards higher angles for the doped samples is observed. This shift can be clearly seen in Fig. 5.6, which shows the (110)-reflection. Na^+ has an ionic radius of $1.39\,\text{Å}$ [248] for a 12-fold coordination. In comparison, those of Sr^{2+} and Ca^{2+} are $1.44\,\text{Å}$ [248] and $1.34\,\text{Å}$ [248]. Considering the Bragg equation 3.4, it falls into place that the diffraction lines of $Na_{0.99}Ca_{0.01}NbO_3$ are shifted towards higher angles. Due to the smaller ionic radius of Ca^{2+} compared to Na^+, the lattice can relax resulting

in slightly smaller lattice parameters. This in turn, will influence the reflections appearing at higher 2θ-values.

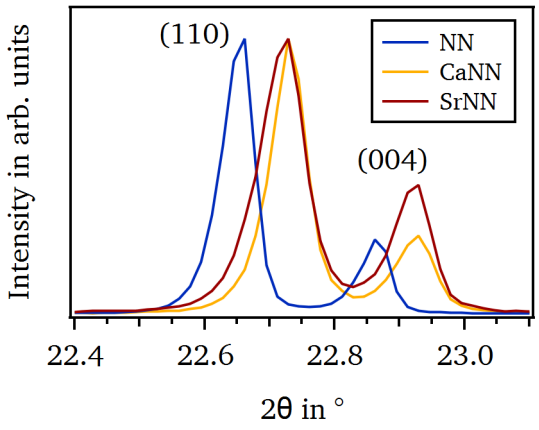

Figure 5.6.: (110)- and (400)-diffraction line for $NaNbO_3$ (blue), $Na_{0.99}Ca_{0.01}NbO_3$ (yellow), and $Na_{0.99}Sr_{0.01}NbO_3$ (red).

Hence, the effect should be the opposite for $Na_{0.99}Sr_{0.01}NbO_3$ as Sr^{2+} has a larger ionic radius than Na^{+}. On the contrary, a shift towards higher 2θ-values is observed as well for $Na_{0.99}Sr_{0.01}NbO_3$. This can most likely be explained by the high amount of Ca found on the surface of $Na_{0.99}Sr_{0.01}NbO_3$ ceramics, which is affecting the pattern. The Ca-concentration is larger on the surface than the Sr-concentration because of Ca segregation towards the surface, which will be shown later in Section 6.1. As the investigated powders for XRD are cut off from the edges of the calcined and sintered rods, it seems very reasonable that the powder is highly affected by Ca segregation. Nevertheless, due to the absence of secondary phases, besides the ferroelectric Q phase, and the shifted reflections of the doped samples it is concluded that Ca and Sr were sufficiently incorporated into the $NaNbO_3$ system.

The crystal structure of the ferroelectric material $KNbO_3$ is much simpler as the one of $NaNbO_3$. Only one phase exists at room temperature, which can be attributed to an orthorhombic structure with space group Amm2. In Fig. 5.7 the powder diffraction patterns are illustrated after first and second calcination and after sintering. All reflections fit to space group Amm2 (JCPDS 01-071-0946 [156]) which can be seen in more detail for four different selected regions shown in Fig. 5.7. The measured patterns were shifted and normalized according to the (111)-reflection of the powder diffraction file. Similar to the observations for the $NaNbO_3$ samples a broadening of the diffraction lines of the calcined powders is noticed. This can be most likely attributed again to internal stresses as no stress-release heating was performed before the XRD measurements. Nevertheless, the reflection positions fit quite well. Differences in the line intensities compared to the reference lines are detected, which are probably caused by an insufficient milling with the mortar.

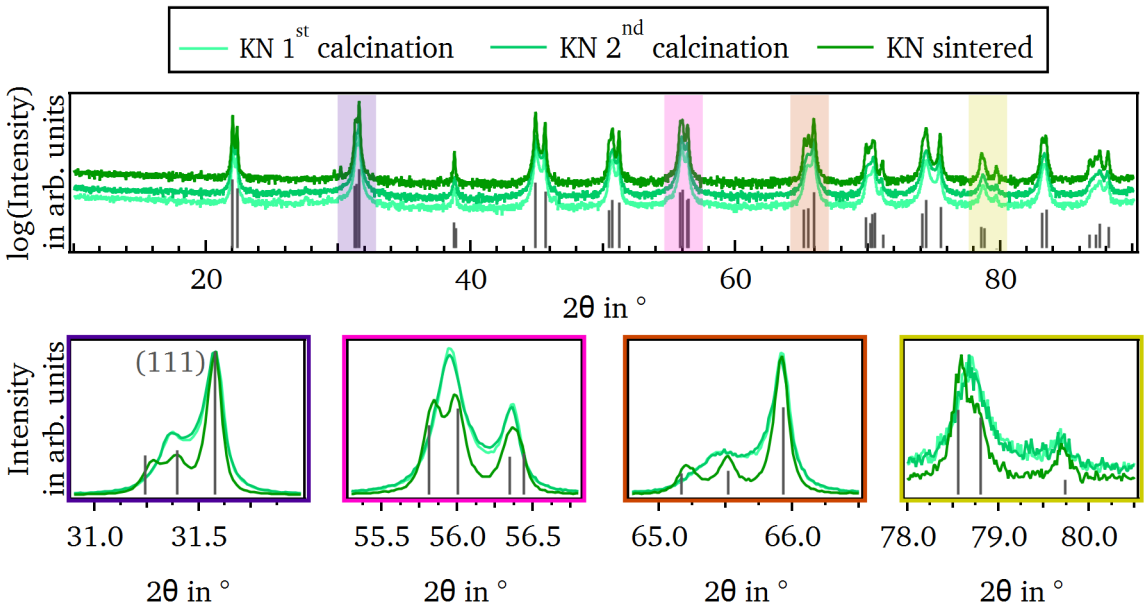

Figure 5.7.: X-ray diffraction patterns of $KNbO_3$ after first and second calcination and after sintering. All reflections can be referred to an orthorhombic crystal structure with space group Amm2 (grey, JCPDS 01-071-0946 [156]). The measured patterns are aligned in position and normalized in intensity according to the (111)-reflection of the reference pattern located around $31.6°$.

5.4. Polarization and current hysteresis loops

For verification of the antiferroelectricity and ferroelectricity of the $NaNbO_3$ and $KNbO_3$ samples, polarization and current hysteresis loops are conducted. Here, the polarization behavior can be studied in more detail.

As concluded from the section before, all $NaNbO_3$-based samples are mainly in the antiferroelectric P phase. To confirm this, polarization- and current-electric-field loops are measured. Experiments executed at low frequencies between $0.3\,\mathrm{Hz}$ and $1.0\,\mathrm{Hz}$ result in balloon-like shaped polarization curves for the doped samples, which are shown in Fig. A.4. Obviously, the samples are too conductive in order to be measured at low frequency due to a high leakage current corrupting the polarization-electric-field loop. Undoped $NaNbO_3$ does not show a high leakage contribution, however, no complete loop can be examined as all samples experience breakdown beforehand. Hence, polarization- and current-hysteresis loops are conducted at a higher frequency of $1\,\mathrm{kHz}$. Here, it should be mentioned that the loops at low frequencies were recorded with a common Sawyer-Tower setup measuring the charge whereas the hysteresis curves at high frequency are taken by an TF Analyzer 2000 using the virtual ground method.

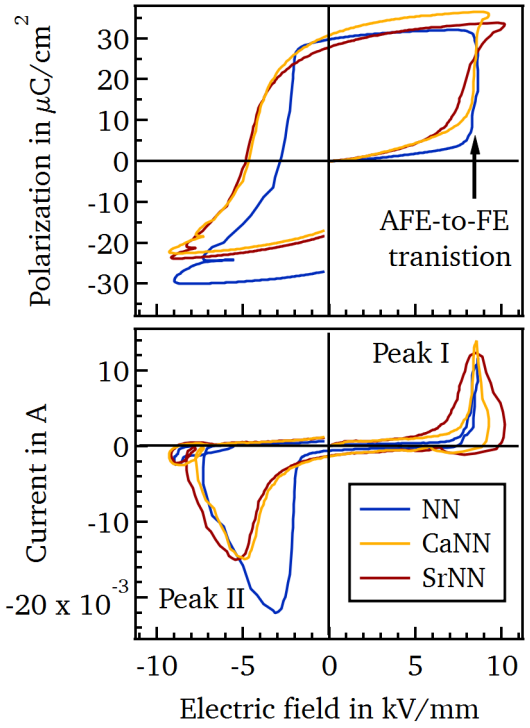

Figure 5.8.: Virgin polarization and corresponding current hysteresis loops for $NaNbO_3$ (blue), $Na_{0.99}Ca_{0.01}NbO_3$ (yellow), and $Na_{0.99}Sr_{0.01}NbO_3$ (red) measured at 1 kHz. Hysteresis loops conducted at lower frequencies are shown in Fig. A.4 in the appendix.

With this method the polarization current is directly obtained instead of the charge.

The first loops for $NaNbO_3$, $Na_{0.99}Ca_{0.01}NbO_3$, and $Na_{0.99}Sr_{0.01}NbO_3$ are illustrated in Fig. 5.8. The polarization is linearly increasing up to ca. $8.5\,\mathrm{kV\,mm^{-1}}$ followed by a sudden increase up to approximately $30\,\mu\mathrm{C\,cm^{-2}}$. This jump is caused by the transition from the antiferroelectric to the ferroelectric state. After reaching the maximum polarization the curve follows a ferroelectric characteristic meaning that the ferroelectric phase is stabilized and is not switching back to the antiferroelectric state. This irreversible antiferroelectric-to-ferroelectric transition is observed regularly in literature [26, 27, 133–135, 137, 138, 249]. Quite some studies are testing doped and/or isovalent substituted $NaNbO_3$ with different elements, which mainly decrease the tolerance factor in order to stabilize the antiferroelectric phase [10, 26, 27, 134, 135, 137, 138, 249–251]. However, it is not completely clear whether the antiferroelectric phase is stabilized or defect-dipoles are formed, which influence the polarization behavior. Furthermore, the maximum and remanent polarization ranging from $32\,\mu\mathrm{C\,cm^{-2}}$ to $36\,\mu\mathrm{C\,cm^{-2}}$ and $27.8\,\mu\mathrm{C\,cm^{-2}}$ to $30.8\,\mu\mathrm{C\,cm^{-2}}$ for $NaNbO_3$, $Na_{0.99}Ca_{0.01}NbO_3$, and $Na_{0.99}Sr_{0.01}NbO_3$ are in the same region as in literature [27, 112, 133–135, 138, 252], respectively.

In the corresponding current hysteresis loops two peaks appear. The first current peak (Peak I) in the second quadrant results from the antiferroelectric-to-ferroelectric transition whereas the second peak (Peak II) in the fourth quadrant is caused by the change of polarization direction of the ferroelectric phase along the electric field.

Second and last measured polarization- and current-electric-field loops are displayed in Fig. 5.9. It can be clearly seen that the ferroelectric phase is stabilized for all samples indicated by the ferroelectric polarization loops and the shift of the first current peak to lower electric fields. In all three cases the

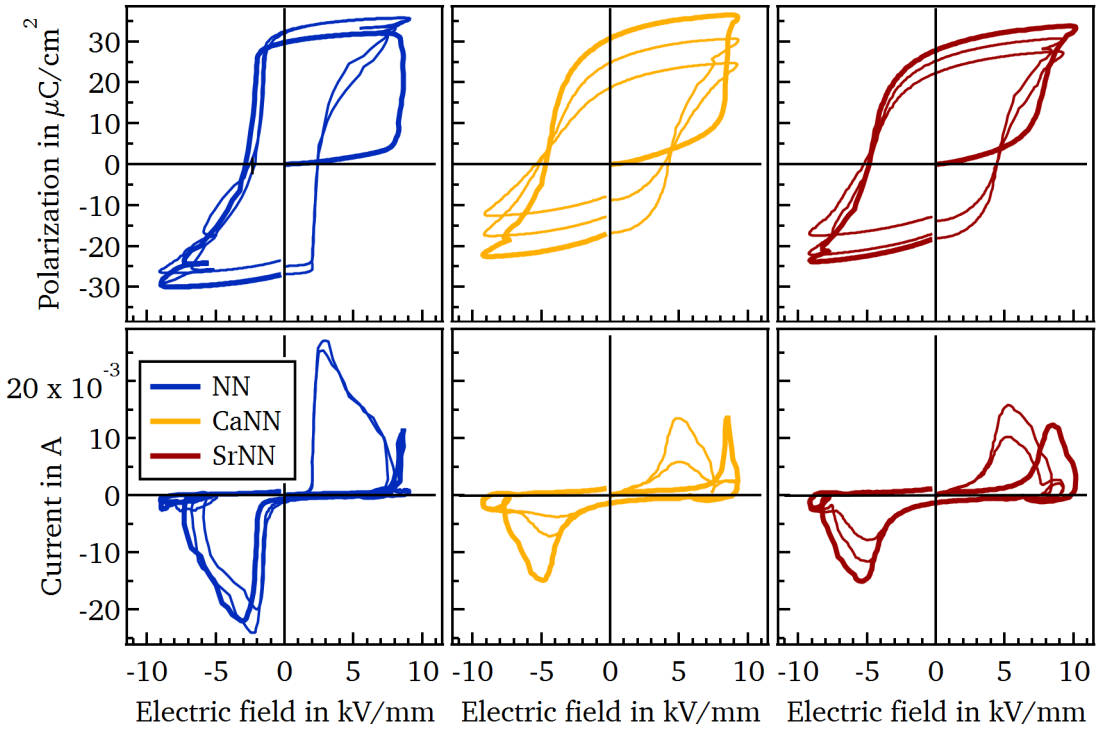

Figure 5.9.: Polarization and current hysteresis loops of $NaNbO_3$ (blue), $Na_{0.99}Ca_{0.01}NbO_3$ (yellow), and $Na_{0.99}Sr_{0.01}NbO_3$ (red). The thick curves show the first virgin loop.

current peaks are very broad, which can have several reasons. A common explanation in literature is the formation of so-called dead layers, which have a lower permittivity than the ferroelectric material itself [54]. This in turn lowers the electric field in the ferroelectric material. The existence of dead-layers would also explain the decreased value of the remanent polarization due to a decreased internal electric field leading to prematurely backswitching of the domains. However, the current peaks in Fig. 5.9 are not only broadened, they are also asymmetric indicating an overlap of two or more current peaks located at different electric fields. The occurrence of more than one current peak can be explained by effects, which hinder the switching of some domains. These effects are usually attributed to defects, which can pin domain walls, impede or ease the domain switching due to different local defect concentrations, or form defect dipoles affecting the switching behavior [28–31, 54]. All these contributions cannot be excluded in $NaNbO_3$-based ceramics as defects such as sodium (V'_{Na}) and oxygen vacancies ($V^{\cdot\cdot}_{O}$) are very likely to be present due to evaporation during sintering [177, 187]. Furthermore, in the Ca- and Sr-doped samples the dopants can also contribute to such effects. Indeed, there seem to be different mechanisms being responsible for the current peak shape in undoped $NaNbO_3$ and the donor doped samples. In $Na_{0.99}Ca_{0.01}NbO_3$ and $Na_{0.99}Sr_{0.01}NbO_3$ the current peak is decreasing in intensity, which is accompanied by a lowered maximum and remanent polarization after a few cycles. In contrast, these values are more or less constant for pure $NaNbO_3$.

A reasonable explanation could be that charge carriers are more mobile within the doped samples. The charge carriers could easily redistribute themselves while an electric field is applied leading to a higher number of pinned domains with increasing cycling number. As a consequence, a fatigue effect is observed meaning that a decreasing number of domains add to the overall measured polarization [181].
In pure $NaNbO_3$ it seems that the charge carriers are less mobile. The asymmetric peak shape could, therefore, result from the formation of defect dipoles, e.g. $(V'_{Na}\text{-}V_O^{\cdot\cdot}\text{-}V'_{Na})^x$ or $(V'_{Na}\text{-}V_O^{\cdot\cdot})^{\cdot}$, creating an internal electric field. Such defect dipoles are much less mobile and cannot follow the applied AC-field, hence, maintaining their initial alignment along the orientation of the spontaneous polarization. These "frozen" defect dipoles hamper or facilitate the switching of some domains depending on their orientation causing pinched P-E-loops and broader current peaks. This is called an aging effect [28–31, 54]. In contrast to a fatigue effect, aging appears with time without applied electric field resulting in a lowered remanent and maximum polarization of the initial state while fatigue emerges with applied electric field and increasing cycling number. Therefore, it might be that undoped $NaNbO_3$ is less affected by fatigue and more by aging because of the broader current peak and the stable remanent and maximum polarization values.
In order to figure out if aging has a more pronounced effect on undoped $NaNbO_3$ than on donor doped $NaNbO_3$, P-E-loops were measured on a sample, which was not touched for approximately one year, and on a sample freshly annealed at $600\,°C$ for $1\,h$. The corresponding P-E- and I-E-loops are illustrated in Fig. A.5 in the appendix. Indeed, differences in the polarization behavior between aged and equilibrated samples are observed. The aged sample of undoped $NaNbO_3$ exhibits slightly pinched loops with lower remanent and maximum polarization compared to the equilibrated sample. For doped $NaNbO_3$ the aged samples show also altered loops, however, they are not pinched but slanted with lower remanent and maximum polarization. Therefore, it seems that all samples are influence by aging while doped $NaNbO_3$ is additionally affected by fatigue effects.

Having a closer look on the coercive fields, slightly different values for positive and negative electric fields are obtained for all samples. The exact values for the last measured loop can be found in Table 5.1. Different coercive fields are a consequence of shifted current peaks and an indication for an internal bias field. Such internal electric fields can develop from defect dipoles aligned with the original domain structure or from space charge layers at grain or domain boundaries. The difference is much more pronounced in the doped samples as can be seen from Table 5.1. Internal bias fields E_{bias} can be calculated by Eq. 5.3 with negative and positive coercive field E_{c-} and E_{c+}, respectively [29].

$$E_{\text{bias}} = \frac{E_{c-} + E_{c+}}{2} \tag{5.3}$$

The evaluated values are listed in Table 5.1. It might be that the Sr-and Ca-dopants or compensating

defects, such as V'_{Na}, segregate during sintering to the grain and/or domain boundaries leading to space charge regions, which create an internal electric field. Segregation of dopants or A-site vacancies towards grain boundaries is always an issue if it comes to polycrystalline ceramics and is discussed quite extensively in literature especially for $BaTiO_3$ as a perovskite material [23, 68, 69, 253, 254]. However, TEM measurements conducted on Ca- and Sr-doped samples do not reveal any segregation of the dopants towards the grain boundaries within the resolution limit of 0.1 mol %. Corresponding pictures and element concentrations are illustrated in Fig. A.7 and A.8 in the appendix. Hence, it is not completely clear why the donor doped samples exhibit larger internal bias fields than undoped $NaNbO_3$.
Nevertheless, we should not forget that $NaNbO_3$ is mainly present in the antiferroelectric phase before poling. Therefore, it could be that some parts of the sample undergo a reversible antiferroelectric-to-ferroelectric transition resulting in the observed polarization and current behavior.

$KNbO_3$ is a ferroelectric material and should, therefore, possess a ferroelectric polarization and current behavior. Indeed, the corresponding hysteresis loops demonstrated in Fig. 5.10 look much different compared to the ones of the $NaNbO_3$-based ceramics. A slim ferroelectric polarization-electric-field curve is observed. Compared to literature [172–174, 255], the remanent and maximum polarization are in the same range and have values of $8.6\,\mu C\,cm^{-2}$ and $14.6\,\mu C\,cm^{-2}$, respectively.
The current-electric-field-plot exhibits four switching peaks. This is usually obtained for antiferroelectric materials as switching of the antiferroelectric to the ferroelectric state and backswitching from the ferroelectric to the antiferroelectric state occurs for both, positive and negative electric field directions. However, as already discussed earlier, defects can be responsible for internal electric fields. It is not surprisingly that defects influence the loop behavior as potassium is even more volatile than sodium [177, 187] and, therefore, V'_K and $V^{\cdot\cdot}_O$ can be easily formed during sintering. The observation of two switching peaks is usually attributed to either defect dipoles or different defect concentrations within the sample [28–30, 54, 73]. In the case of defect dipoles, domain switching is hardened due

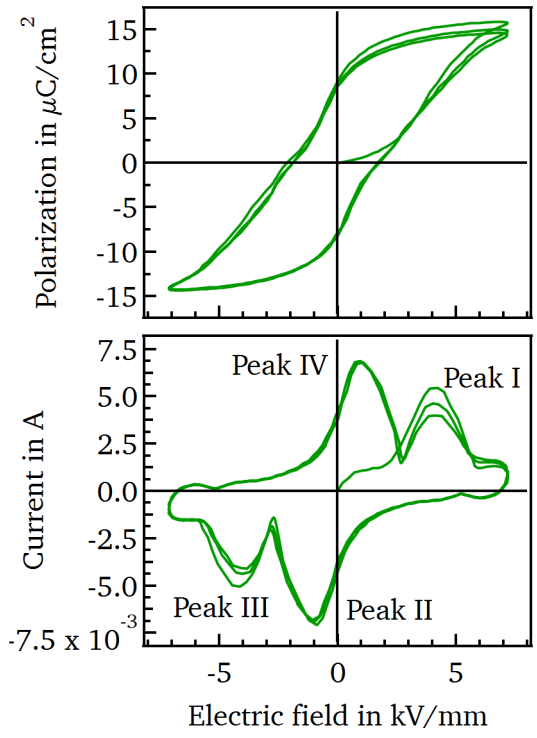

Figure 5.10.: Polarization and corresponding current hysteresis loops for $KNbO_3$.

to an internal bias field created by the defect-dipoles, which are aligned to the original direction of the spontaneous polarization within the sample. V'_K and $V^{\cdot\cdot}_O$ could form such defect dipoles, e.g. $(V'_K\text{-}V^{\cdot\cdot}_O\text{-}V'_K)^x$ or $(V'_K\text{-}V^{\cdot\cdot}_O)^{\cdot}$. A different defect concentration facilitating and hindering the domain switching in different parts of the sample could also be a possible explanation. To the best of my knowledge no aging effects of undoped $KNbO_3$ have been reported in literature so far, but in Mn- and Cu-doped $KNbO_3$ aging is observed [71, 180, 181]. In these materials the aging effect is attributed to defect dipoles composed of Mn- or Cu-dopants and oxygen vacancies.
Similar to undoped $NaNbO_3$ positive and negative coercive fields (Table 5.1) are different resulting in a small internal bias field. In addition, a small fatigue effect decreasing slightly remanent and maximum polarization is visible. In Section 5.1 it has already been suggested that the $KNbO_3$ samples are potassium deficient. Hence, it is very likely that defects play a role affecting the polarization and current hysteresis behavior.
The influence of possible aging effects are examined by recording P-E-loops on a sample, which was left alone for approximately one year, and on a sample prior equilibrated at $600\,°C$ for $1\,h$. The measured polarization and current loops in dependence of the electric field are illustrated in Fig. A.5 in the appendix. In contrast to the $NaNbO_3$-based ceramics, clear aging effects are visible for the non-annealed sample. Nicely pinched P-E-loops with a maximum polarization of $17.6\,\mu C\,cm^{-2}$ and four broad current peaks are obtained. In contrast, the equilibrated sample exhibits no pinching but is slanted. Although the sample was annealed above the Curie temperature, which should ensure well distributed defects, $100\,\%$ elimination of all defect effects cannot be reached. In addition, a small fatigue behavior is observed for the equilibrated sample. Consequently, $KNbO_3$ is highly influenced by aging, e.g. defect dipoles formed of potassium and oxygen vacancies, and only slightly altered by fatigue processes.

Table 5.1.: Remanent P_r and maximum polarization P_{max}, positive E_{c+} and negative coercive field E_{c-}, and internal bias field E_{bias} of $NaNbO_3$, $Na_{0.99}Ca_{0.01}NbO_3$, $Na_{0.99}Sr_{0.01}NbO_3$, and $KNbO_3$.

	P_r in $\mu C\,cm^{-2}$	P_{max} in $\mu C\,cm^{-2}$	E_{c+} in $kV\,mm^{-1}$	E_{c-} in $kV\,mm^{-1}$	E_{bias} in $kV\,mm^{-1}$
$NaNbO_3$	32.1	35.8	2.38	-2.54	-0.08
$Na_{0.99}Ca_{0.01}NbO_3$	18.7	24.8	3.88	-5.41	-0.77
$Na_{0.99}Sr_{0.01}NbO_3$	22.3	27.5	4.41	-5.27	-0.43
$KNbO_3$	8.6	14.6	1.75	-1.9	-0.08

5.5. Room temperature conductivity

In order to check the electrical state of all prepared ceramics meaning the evaluation of a highly efficient capacitor with a high resistivity and a low leakage current, DC-conductivity measurements were carried out at room temperature as a function of electric field. Figure 5.11a) and b) show three electric field steps and their corresponding current behavior as an example. When the electric field is raised, the current peaks out, followed by a slow relaxation process. After reaching a steady-state behavior, the next electric field step was adjusted. Fields up to $6.2\,\mathrm{kV\,mm^{-1}}$ were applied. Conductivity values of $NaNbO_3$, $Na_{0.99}Ca_{0.01}NbO_3$, and $Na_{0.99}Sr_{0.01}NbO_3$ calculated from the equilibrium currents for each step are displayed in Fig. 5.11c). The conductivity of all samples increases nearly linearly with electric field, but remains below $5 \times 10^{-10}\,\mathrm{S\,cm^{-1}}$. Consequently, a low conductivity over a wide electric field range is measured. The linear increase can mainly be attributed to some resistive heating of the samples due to the high applied voltages. To the best of my knowledge, there are no published values concerning the room temperature conductivity of $NaNbO_3$-based samples. Only Yun et al. [256] reported very low currents in the nano-ampere region examined at room temperature by conductive atomic force microscopy. From Fig. 5.11c) it is evident that the donor doped samples exhibit an one order of magnitude higher electrical conductivity compared to pure $NaNbO_3$. Nevertheless, they possess a low conductivity up to 4.1×10^{-10} eV for $Na_{0.99}Ca_{0.01}NbO_3$ and 2.9×10^{-11} eV for $Na_{0.99}Sr_{0.01}NbO_3$. Therefore, donor doping with calcium or strontium does not increase the conductivity significantly. However, it seems to be high enough to result in a leaky polarization loop behavior at low frequencies as observed in the previous section.

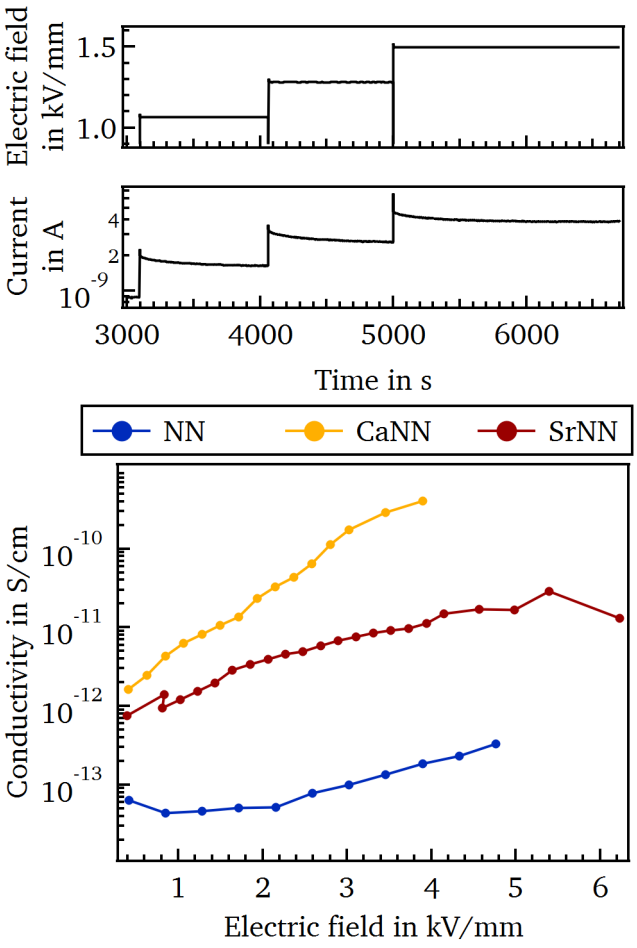

Figure 5.11.: Recorded electric field in a) and corresponding current steps in b) for room temperature conductivity measurements of $NaNbO_3$ (blue), $Na_{0.99}Ca_{0.01}NbO_3$ (yellow), and $Na_{0.99}Sr_{0.01}NbO_3$ (red). The conductivity values are calculated by means of the equilibrium currents.

Unfortunately, no such measurements were conducted on $KNbO_3$ bulk ceramics. Conductivity values from $5\,\mathrm{mS\,cm^{-1}}$ to $100\,\mathrm{mS\,cm^{-1}}$ [164] are reported in literature for $KNbO_3$ single crystals. These values are significantly higher than the ones measured in this work for $NaNbO_3$-based ceramics and would indicate a large difference in the electrical conductivity behavior between $NaNbO_3$ and $KNbO_3$. However, one has to keep in mind that in ceramics the conductivity can be influenced by different effects, e.g. grain boundaries.

5.6. Temperature dependent permittivity

Permittivity and permittivity loss have been measured in dependence of temperature at several frequencies in order to determine the phase transition temperatures, the effect of possible leakage currents, and how both are influenced by doping. In Fig. 5.12 the corresponding curves measured at frequency of $100\,\mathrm{Hz}$, $10\,\mathrm{kHz}$, and $1\,\mathrm{MHz}$ are illustrated for pure $NaNbO_3$ (blue) and Ca- (yellow) and Sr-doped $NaNbO_3$ (red).
For all three samples a peak related to the phase transition of the antiferroelectric orthorhombic P to the antiferroelectric orthorhombic R phase is observed. The corresponding temperature is the Curie temperature T_C of $NaNbO_3$. This phase transition shows a thermal hysteresis meaning that the peak occurs at higher temperatures for the heating cycle than for the cooling cycle, which is indicated by arrows in Fig. 5.12. For pure $NaNbO_3$ the transition appears at $376\,^\circ\mathrm{C}$ ($353\,^\circ\mathrm{C}$) while heating (cooling). These values lie in the temperature range of $323\,^\circ\mathrm{C}$ to $386\,^\circ\mathrm{C}$, which can be found in literature for the P-R phase transition [26, 27, 33, 112, 116, 133, 134, 249, 251, 252, 257]. Doping with $1\,\mathrm{mol\,\%}$ Ca and Sr leads to a shift to lower temperature values of $357\,^\circ\mathrm{C}$ ($300\,^\circ\mathrm{C}$) and $325\,^\circ\mathrm{C}$ ($296\,^\circ\mathrm{C}$) upon heating (cooling), respectively. Hence, the temperature hysteresis is enlarged when doping with Ca. The permittivity is increased with doping at both, T_C and room temperature. A decrease in the transition temperature and a higher room temperature permittivity in doped $NaNbO_3$ samples containing Ca or Sr is also seen in literature. However, a higher permittivity value at T_C is only obtained if the material is doped on the A-site with Ca or Sr [139] without simultaneous substitution of the B-site with, e.g. zirconium.
A closer investigation of the permittivity curves, reveals further phase transitions in the temperature range up to $600\,^\circ\mathrm{C}$. For pure $NaNbO_3$ the material changes to the orthorhombic S, the tetragonal T1, and the tetragonal T2 phase at $494\,^\circ\mathrm{C}$, $535\,^\circ\mathrm{C}$, and $580\,^\circ\mathrm{C}$, respectively. In contrast to the P-R phase transition, not all phase transitions seem to be affected in the same way by doping. Hence, a decreased phase transition temperature cannot be stated for all of them. Interestingly, a dielectric anomaly at around $130\,^\circ\mathrm{C}$ can be identified for $Na_{0.99}Ca_{0.01}NbO_3$, marked by a circle in Fig. 5.12, which cannot be observed for $NaNbO_3$ and $Na_{0.99}Sr_{0.01}NbO_3$. A dielectric anomaly around $150\,^\circ\mathrm{C}$ is shown in several publications. The origin is not completely understood so far and still under debate.

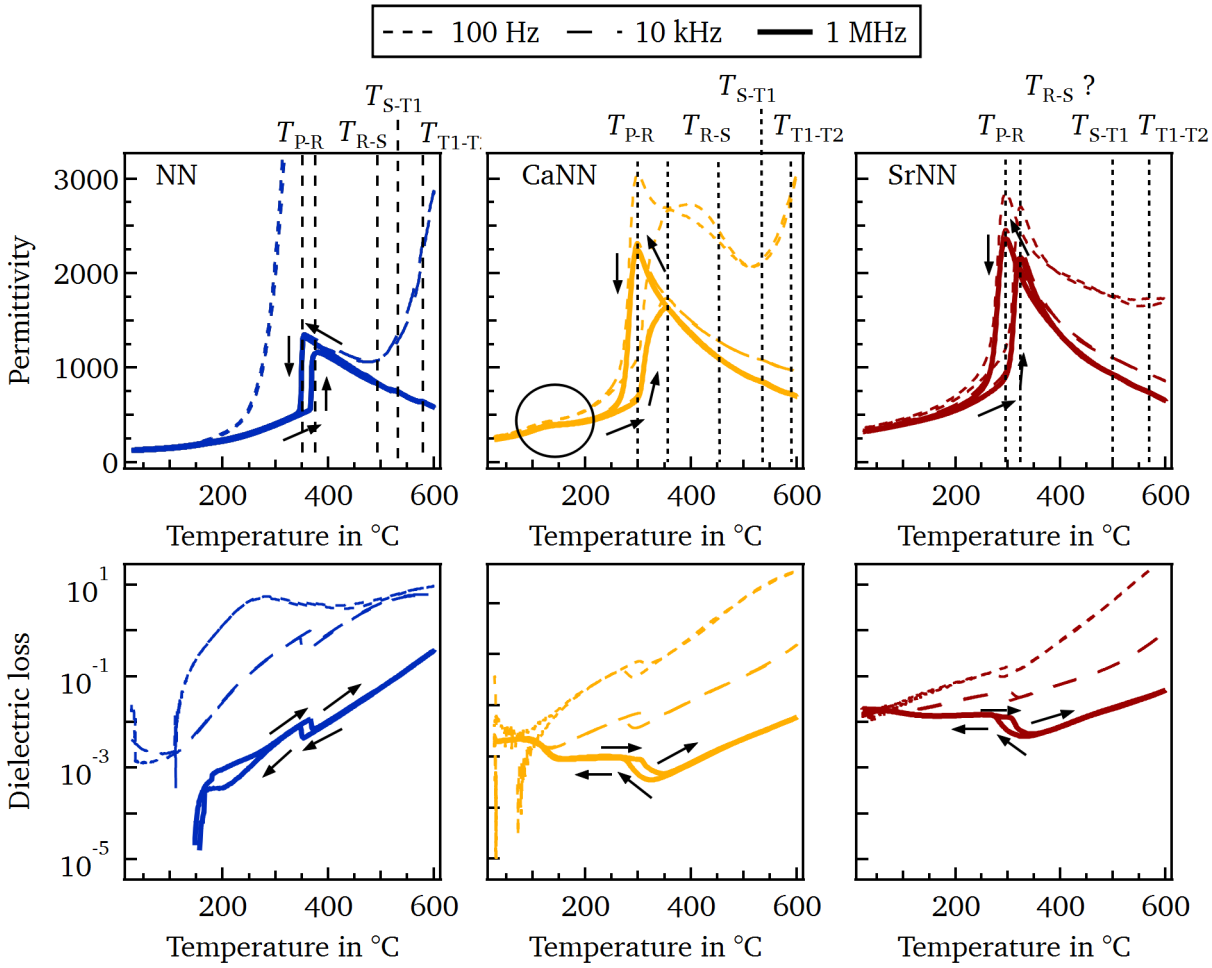

Figure 5.12.: Permittivity and permittivity loss in dependence of temperature measured at a frequency of 100 Hz, 10 kHz, and 1 MHz for $NaNbO_3$ (blue), $Na_{0.99}Ca_{0.01}NbO_3$ (yellow), and $Na_{0.99}Sr_{0.01}NbO_3$ (red). The arrows indicate the heating/cooling direction of the measured curves.

However, it is often explained by either an incommensurate phase [114, 136] or the appearance of ferroelectric nanodomains within an antiferroelectric matrix [112, 116].
Furthermore, a much larger frequency dispersion is observed in undoped $NaNbO_3$. In order to grasp the dimension of this dispersion, the permittivity-temperature-dependence for $NaNbO_3$ is shown in Fig. A.6 in the appendix for different permittivity scales. A less pronounced frequency dispersion controls the permittivity behavior in the doped samples. A frequency dispersion appears also in the dielectric loss curves and is also more pronounced in case of pure $NaNbO_3$. Consequently, in the lower frequency range much higher losses are observed compared to high frequencies. Frequency dispersion with high permittivity losses are usually explained in literature by highly mobile

charge carriers and a high conductivity [35, 258, 259]. The question is why does undoped $NaNbO_3$ exhibit a much more pronounced dispersion when it has a lower room temperature conductivity as shown in the previous section. A closer look on the low temperature regime of the permittivity and the permittivity loss reveals that indeed both, frequency dispersion and permittivity loss, are lower for undoped $NaNbO_3$ than for the doped samples. Above $\sim 200\,°C$ both are significantly increasing. In chapter 7 it will be illustrated that the conductivity of undoped $NaNbO_3$ is undoubtedly higher above $\sim 200\,°C$ and lower below $\sim 200\,°C$ than that of the Ca- and Sr-doped $NaNbO_3$.

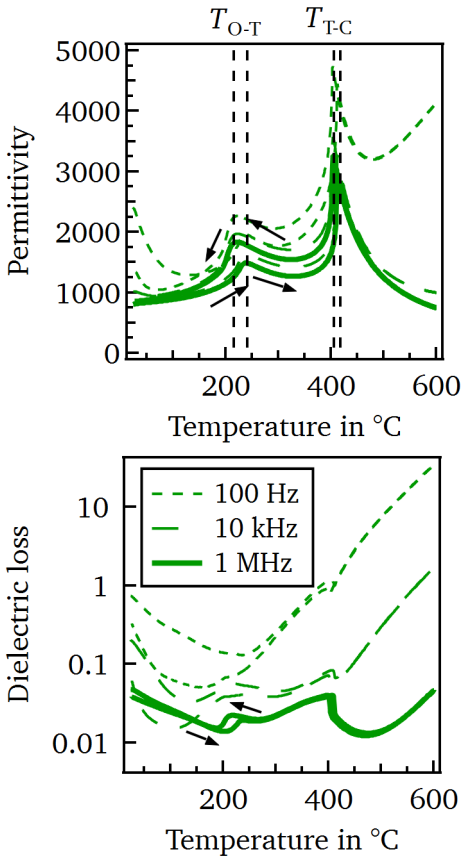

Figure 5.13.: Permittivity and permittivity loss as function of temperature measured at $100\,Hz$, $10\,kHz$, and $1\,MHz$ for $KNbO_3$.

This increase of electrical conductivity fits well to the observations shown here.

$KNbO_3$ has a much simpler crystal structure than $NaNbO_3$ without so many polymorphs. Therefore, only two phase transitions are identified in Fig. 5.13, which illustrates the permittivity and dielectric loss in dependence of the temperature. The orthorhombic-to-tetragonal transition occurs at $243\,°C$ for the heating cycle and at $217\,°C$ when the temperature is decreased again. Hence, a small temperature hysteresis is visible. The tetragonal-cubic phase transition is located at $419\,°C$ ($407\,°C$) when the sample is heated up (cooled down). Both phase transition temperatures agree with values reported in literature [172, 185, 260, 261]. Compared to the $NaNbO_3$-based samples a much higher room temperature permittivity of approximately 800 and higher dielectric loss values over the complete temperature region are determined. In addition, a frequency dispersion is observed.

5.7. Sample preparation and basic characterization - Summary

In this chapter, analysis during sample preparation including particle size, calcination, and sintering curves as well as basic characterization of the prepared ceramics covering SEM, XRD, polarization hysteresis loops, room temperature DC-conductivity, and temperature dependent permittivity measurements were investigated and discussed. In the following the main results and conclusions are summarized.

Table 5.2.: Main results of sample preparation and basic characteristics including composition, crystal structure, (anti)ferroelectric state, and electrical conductivity.

	pure $NaNbO_3$	**changes induced by Ca- and Sr-doping**	**pure $KNbO_3$**
composition	phase pure $NaNbO_3$ without secondary phases	none	potassium deficient but phase pure $KNbO_3$
crystal structure	AFE P phase with very small traces of FE Q phase and $T_C = 376\,°C$	decrease of T_C	FE orthorhombic phase with space group Amm2 and $T_C = 419\,°C$
micro-structure	abnormal grain growth with large average grain size of $90\,\mu m$ and a relative density of $94.5\,\%$	decreased grain size of about $1.5\,\mu m$ and $0.9\,\mu m$ and increased relative density of $96.0\,\%$	small grains of $0.5\,\mu m$ to $1.0\,\mu m$ with low relative density of $88.7\,\%$
(anti-) ferroelectric state	AFE polarization behavior with irreversible FE transition leading to a fully FE polarization behavior including aging effects most likely induced by defect dipoles such as $(V'_{Na}\text{-}V_O^{\cdot\cdot})^{\cdot}$ or $(V'_{Na}\text{-}V_O^{\cdot\cdot}\text{-}V'_{Na})^{x}$	none	reproducible FE behavior altered by fatigue phenomenons but highly influenced by aging effects probably induced by defect dipoles, e.g. $(V'_K\text{-}V_O^{\cdot\cdot})^{\cdot}$ or $(V'_K\text{-}V_O^{\cdot\cdot}\text{-}V'_K)^{x}$
electrical conductivity	low RT conductivity of $4.4 \times 10^{-14}\,S\,cm^{-1}$ to $3.3 \times 10^{-13}\,S\,cm^{-1}$	slightly increased RT conductivity to $7.6 \times 10^{-13}\,S\,cm^{-1}$ to $4.1 \times 10^{-11}\,S\,cm^{-1}$	

dielectric properties	increased frequency dispersion and dielectric losses above 200 °C	frequency dispersion and dielectric losses are increased below 200 °C and decreased above 200 °C	increased frequency dispersion and higher dielectric losses than $NaNbO_3$ over the whole temperature range

In summary, phase pure samples were prepared with an initial antiferroelectric and ferroelectric state in case of $NaNbO_3$ and $KNbO_3$, which can be used for further investigations of the electronic structure, the transport properties, and degradation behavior, respectively.

6. Electronic structure

In the following chapter room temperature XPS measurements of pure $NaNbO_3$, $Na_{0.99}Ca_{0.01}NbO_3$, $Na_{0.99}Sr_{0.01}NbO_3$, and $KNbO_3$ will be analyzed. The goals of this section can be summarized as following.

This chapter has the aim to ...

- ... confirm the composition of the investigated materials.
- ... determine the band gap of $NaNbO_3$ and $KNbO_3$.
- ... find the accessible Fermi level range of these materials.
- ... propose possible origins, which confine the Fermi level in case Fermi level limitations are found.
- ... find a first model for the band structure of $NaNbO_3$ and $KNbO_3$.

The analysis of these aims will show if there is already a fundamental difference in the electronic structure between the antiferroelectric $NaNbO_3$ and the ferroelectric $KNbO_3$ system.
In order to verify the composition of $NaNbO_3$ and $KNbO_3$ complete survey spectra are recorded over the whole binding energy range as well as detailed spectra of the sample elements' core levels and the valence band. As XPS is a surface sensitive method, a special focus is put on the surface analysis. In this regard, anomalies observed in the sodium and potassium core level lines are examined and possible origins are discussed.
The band gaps are investigated via XPS and TEM. It is shown that the energy gaps can be determined from the electron energy loss spectrum measured with the transmission electron microscope but not with the XP-spectrometer. Reasons why this analysis cannot be done for the electron energy loss spectrum recorded with XPS are presented.
Interface experiments to the low work function material ITO and the high work function material RuO_2 as well as other oxidizing and reducing treatments are discussed to reveal possible Fermi level limitations. First sources responsible for the confinement of the Fermi level are proposed. However, their validity is examined in more detail in the later chapters.

On the basis of the extracted band gap values and the Fermi level limitations a first model for the band structure of $NaNbO_3$ and $KNbO_3$ is proposed.

6.1. XP spectra and composition analysis of clean samples

First, the composition with a special focus on the surface is examined. Possible contamination are identified. For this purpose, an overview of all elements present in the samples is given by measuring a survey spectra over the whole binding energy range. Fig. 6.1 shows these spectra for a $NaNbO_3$, a Ca- and Sr-doped $NaNbO_3$, and a $KNbO_3$ ceramic sample.

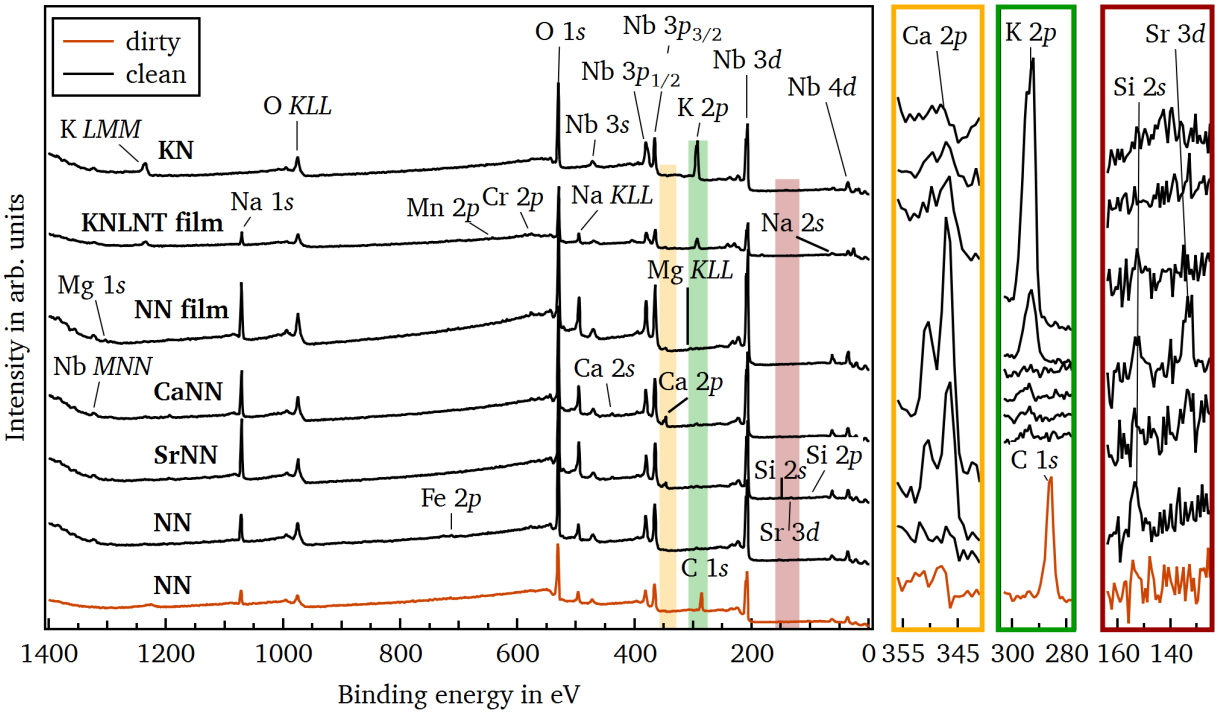

Figure 6.1.: Survey spectra of a $NaNbO_3$, $Na_{0.99}Ca_{0.01}NbO_3$, $Na_{0.99}Sr_{0.01}NbO_3$, and $KNbO_3$ ceramic as well as of a $NaNbO_3$ and a $0.95(K_{0.49}Na_{0.49}Li_{0.02})(Nb_{0.8}Ta_{0.2})O_3$-$0.05CaZrO_3$ with $2\,wt\,\%$ MnO_2 thin film. In brown the survey spectra of the as-prepared sample are colored while the samples cleaned in a low pressure oxygen atmosphere at $400\,°C$ are marked in black. Magnified views of the colored areas show the emission lines of the impurities and dopants in more detail.

For comparison, the XP survey spectra of a $NaNbO_3$ thin film and a $0.95(K_{0.49}Na_{0.49}Li_{0.02})(Nb_{0.8}Ta_{0.2})O_3$-$0.05CaZrO_3$ with 2 wt % MnO_2 (KNLNT) thin film are plotted. The thin films were measured to identify the exact binding energies of the core levels as charging is compromising the values of the ceramic samples. However, the main focus in this work is on the ceramics.
In Fig. 6.1 the survey spectra of an as-prepared $NaNbO_3$ sample (brown) and after cleaning this sample in a low pressure oxygen atmosphere at $400\,°C$ (black) are displayed. Sodium, oxygen, carbon, and niobium can be identified for the as-prepared sample. After cleaning, no carbon species are detected, which can be clearly seen in the green inset in Fig. 6.1 in which the samples' emission lines are intensified. The removal of the carbon species reveals small traces of impurities as iron, potassium, and silicon. Silicon is most likely a residual of the silicon carbide paper after grinding. The same impurities are visible for the doped samples. In the case of the thin films, chromium, calcium, and magnesium are additional impurities.
In the magnified view of the yellow area, a clear Ca 2*p* peak is visible for the Sr- and Ca-doped sample. In the case of $Na_{0.99}Ca_{0.01}NbO_3$, it is not surprising to see calcium, however, for a 1 mol % doping the intensity is too high. For $Na_{0.99}Sr_{0.01}NbO_3$ small impurity traces as for the thin films or $KNbO_3$ could be expected. In contrast, a Ca 2*p* emission line almost intense as the one for $Na_{0.99}Ca_{0.01}NbO_3$ is clearly visible. This suggests that calcium contamination is introduced by adding the $SrCO_3$ powder during synthesis. It should be noted that by comparing the peak intensities of the Ca 2*p* and the Sr 3*d* emission lines in the magnified views of the yellow and red area, the amount of calcium is higher than that of strontium.

6.1.1. Sodium niobate based samples

The Na 1*s*, O 1*s*, and Nb 3*d* core levels and the valence band of a $Na_{0.99}Sr_{0.01}NbO_3$ sample and a thin $NaNbO_3$ film are shown as an example for all $NaNbO_3$-based samples in Fig. 6.2. The spectra are not influenced by the dopants, hence, can be used as representatives. In brown and black the emissions of the as-prepared sample and after cleaning are illustrated, respectively. The emission lines of the ceramic samples are shifted to higher binding energies compared to the ones of the thin film. This shift is indicated by the arrows in the Nb 3*d* core level lines and the valence band. It can be explained by charging of the ceramic sample during XPS measurements. Although a platinum contact covering half of the sample's surface is deposited prior to the XPS investigations, charging cannot be completely avoided. Hence, the peak positions and the VBM are determined only for the thin films. In the following, mean values of all clean thin films are given as representatives of the core level binding energies and the VBM for all $NaNbO_3$-based samples.

The Na 1*s* peak has the highest binding energy with 1071.6 eV. Furthermore, it can be decomposed into three components. The most intense component with the lowest binding energy of 1071.5 eV, colored in blue, can be related to the bulk [262, 263]. Its binding energy is slightly higher compared

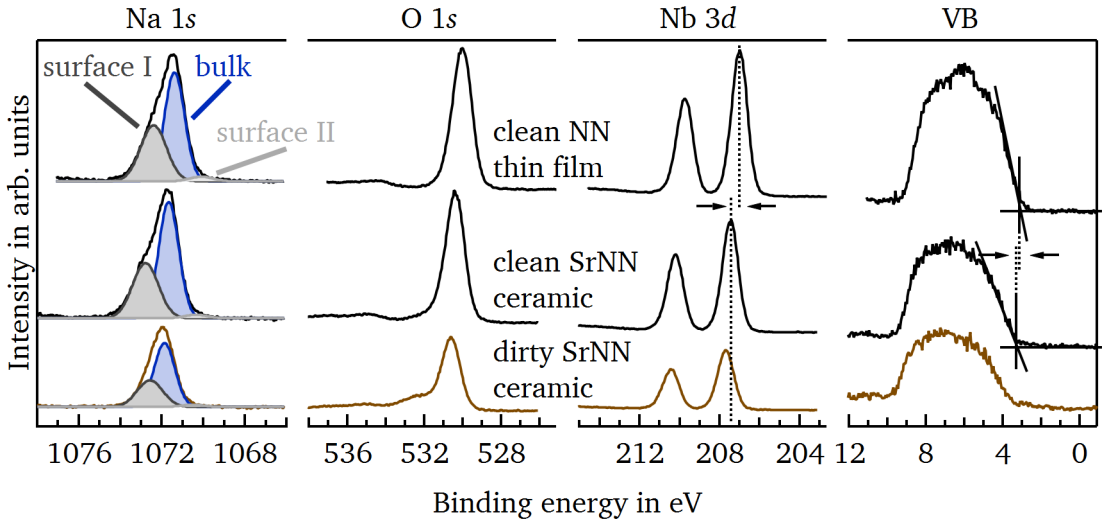

Figure 6.2.: Na 1*s*, O 1*s*, and Nb 3*d* core levels as well as the valence band of an as-prepared $Na_{0.99}Sr_{0.01}NbO_3$ sample (brown), after cleaning (black) and a clean $NaNbO_3$ thin film (black). Within the Na 1*s* peak the bulk component is marked in blue while surface component I and II are colored in dark and light gray, respectively.

to values reported in literature ranging from 1070.5 eV to 1071.2 eV [247, 262–264]. Unfortunately, only Kruczek et al. [262] showed valence band spectra, which exhibit an about 1 eV lower VBM compared to the ones measured in this work. Most likely this difference results from a different Fermi level, which shifts the whole spectrum and explains also the 1 eV smaller binding energy of the Na 1*s* peak measured by Kruczek.

The two emissions on the higher and lower binding energy side are attributed to the surface [262, 263]. In this thesis, the one at higher and lower binding energies will be called *surface component I* (dark gray) and *surface component II* (light gray), respectively. All three components are visible for each $NaNbO_3$-based sample. As can be clearly observed from Fig. 6.2, surface component I is much more intense as surface component II and has a slightly increased intensity after cleaning. Possible origins for the appearance of these surface components are discussed in Section 6.4.

The O 1*s* peak is very symmetric and can be associated with one single bulk component located at 530.2 eV, which is similar to the Na 1*s* peak slightly higher in energy compared to literature values ranging from 529.3 eV to 529.8 eV [247, 262–264]. This observation agrees with the explanation of different Fermi levels of the samples.

Before cleaning, a shoulder at the higher binding energy side is observed, which can be attributed to carbonate and hydroxide groups adsorbed on the surface. These adsorbents are successfully removed with the cleaning procedure revealing a clean surface. This is indicated by the disappearance of the O 1*s* shoulder and the C 1*s* peak after cleaning shown in Fig. 6.1. However, a small shoulder remains, which is shown and discussed in Section 6.2.

Similar to the O 1*s* emission line, the Nb 3*d* peak is very symmetric and can be correlated to one bulk component. However, due to the spin-orbit-coupling a peak splitting into the more intense $3d_{5/2}$ and the less intense $3d_{3/2}$ peak occurs. Out of simplicity this thesis is only referring to the main $3d_{5/2}$ line, which has a binding energy of 207.2 eV. As for the Na 1*s* and O 1*s* peak, the binding energy of the Nb 3*d* emission line is higher than the values of 206.6 eV to 206.8 eV reported in literature [247, 262–264], which can be attributed to different Fermi level positions.

The valence band maximum can be determined from the valence band as shown in Section 3.8. Its mean value extracted from all clean thin films is 3.2 eV. This value is an indirect measure of the Fermi level as explained in Section 3.8. Consequently, the Fermi level is located 3.2 eV above the VBM.

The sample composition can be evaluated using equation 3.8, which includes the integrated peak areas after subtracting the background divided by the atomic sensitivity factor ASF. In Fig. 4.4 the background subtraction is demonstrated for each core level line. The corresponding compositions can be taken from Fig. 6.3. For a stoichiometric sample without any secondary phases, the amount of sodium and niobium should equal one while the one of oxygen should be three. For the undoped $NaNbO_3$ ceramics a clear sodium deficiency is observed. This deficiency is less pronounced for the doped samples while the $NaNbO_3$ thin films are either sodium deficient or sodium rich. The lower concentration of sodium could be caused by a larger amount of V'_{Na} or by a sodium deficient second phase forming at the surface.

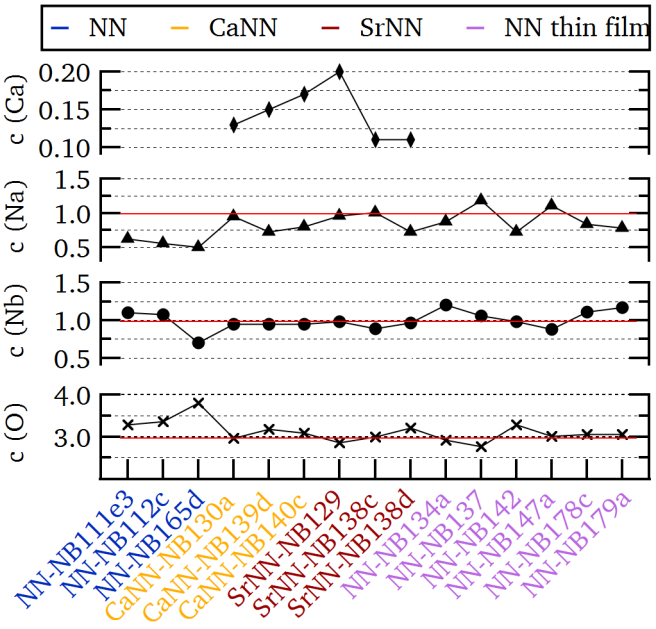

Figure 6.3.: Composition of clean $NaNbO_3$-based samples. The red lines indicate the nominal amount of the specific element.

In the case of the Ca- and Sr-doped samples the amount of calcium was quantified as well resulting in 10 mol % to 20 mol % calcium concentration. This amount is much higher than the intended doping concentration of strontium and calcium. TEM measurements along the cross section of a $Na_{0.99}Ca_{0.01}NbO_3$ sample have been conducted in order to determine whether calcium is only enriched at the surface or throughout the bulk. Figure A.9 in the appendix illustrates that the calcium concentration is about 20 mol % in the first 20 nm of the sample, which agrees with the XPS

measurements. In the bulk, however, the calcium amount equals approximately 0.5 mol %, which is about half of the intended doping concentration. This high calcium concentration on the surface can have two possible origins. First, a surface contamination as result from surface preparation during grinding and polishing and second, a segregation of calcium towards the surface during stress-release-annealing. A surface contamination can most likely be ruled out as this should apply for all ceramic samples. However, such high calcium concentrations are not observed for undoped $NaNbO_3$. Hence, segregation of calcium towards the surface during stress-release-annealing is the more plausible origin of the high amount of calcium at the surface. The TEM investigations show additionally a high concentration of dislocations at the surface, which are most likely introduced by grinding and polishing of the sample surface. These dislocations could facilitate the calcium migration leading to the calcium segregation at the surface.

6.1.2. Potassium niobate based samples

The O 1*s*, K 2*p*, and Nb 3*d* core levels and the valence band of an as-prepared $KNbO_3$ ceramic (brown) and after cleaning the sample in oxygen at 400 °C (black) are displayed in Fig. 6.4. Since no pure $KNbO_3$ thin film could be investigated, the corresponding emissions of a clean KNLNT thin film are shown for comparison in Fig. 6.4. Comparing the peak and valence band positions, a shift to higher

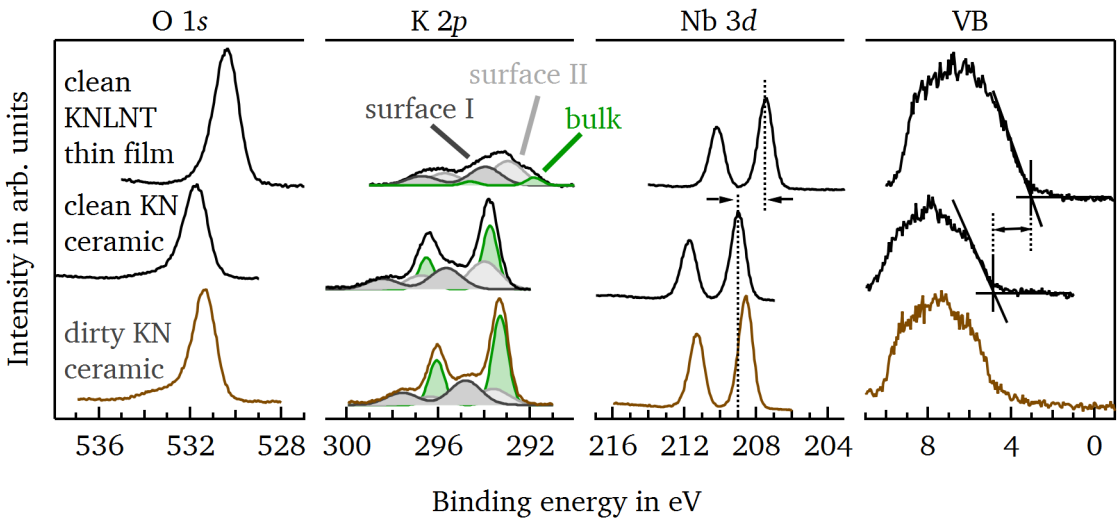

Figure 6.4.: O 1s, K 2*p*, and Nb 3*d* core levels as well as the valence band of an as-prepared $KNbO_3$ sample (brown), after cleaning (black) and a clean KNLNT thin film (black). In the K 2*p* peak the bulk component is marked in green while surface component I and II are colored in dark and light gray, respectively.

binding energies in case of the $KNbO_3$ emissions is observed indicated by arrows in the Nb 3*d* and the valence band spectrum. This effect can again be explained by charging of the ceramic although a

Pt-contact was deposited beforehand. On the basis of this charging issue of the ceramic samples, mean values for the core level and VBM binding energies are extracted only from the clean KNLNT thin films for all $KNbO_3$-based samples. Nevertheless, we have to keep in mind that the binding energies for pure $KNbO_3$ could be slightly different.

The O 1*s* peak has, similar to the $NaNbO_3$-based samples, a very symmetric shape and is located at around $530.3\,\text{eV}$. Before cleaning, a shoulder on the lower binding energy side is visible, which can be again attributed to carbonates and hydroxides adsorbed on the surface. The shoulder is not completely removed after the cleaning procedure. No carbon is detected, which is clearly seen in Fig. 6.1. Hence, the origin of the shoulder must be something different, which will be discussed in more detail in Section 6.2.

Due to the p-orbital character, the K 2*p* emission line shows a peak splitting into the $2p_{3/2}$ peak at lower binding energies and the $2p_{1/2}$ peak at higher binding energies. In addition, it can be decomposed into three components similar to the Na 1*s* peak in $NaNbO_3$. The one with the lowest binding energy at around $291.7\,\text{eV}$ is associated with the bulk while the two components located at higher binding energies are attributed to the surface [265, 266]. For the bulk component a binding energy of $292.0\,\text{eV}$ is reported in literature [265, 266], which fits quite well with the measured position here. In this thesis, the peak at higher and lower binding energies will be called *surface component I* (dark gray) and *surface component II* (light gray), respectively. On average, surface component I is positioned at $293.7\,\text{eV}$ and surface component II at $292.6\,\text{eV}$. It is quite striking that the surface components are much more intense for the KNLNT thin film than for the pure $KNbO_3$ ceramic. However, possible causes for the appearance of the surface components as well as the different intensity ratios will be given in Section 6.4.

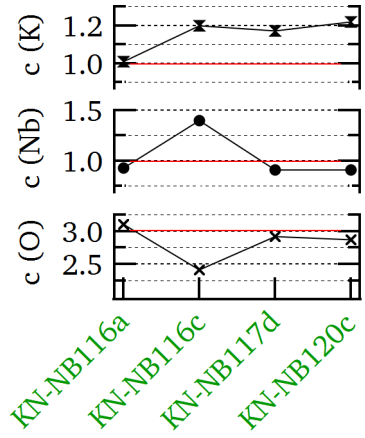

Figure 6.5.: Composition of clean $KNbO_3$ samples. The red lines indicate the nominal amount of the specific element.

The Nb 3*d* core level has a symmetric shape and is split into $3d_{5/2}$ and $3d_{3/2}$ component. The main $3d_{5/2}$ line is located at $207.2\,\text{eV}$ as the one for $NaNbO_3$ and is close to values reported in literature ranging from $207.0\,\text{eV}$ to $208.0\,\text{eV}$ [265, 266].

The VBM is extracted from the valence band spectra and has a mean value of $3.1\,\text{eV}$. Consequently, the Fermi level is located $3.1\,\text{eV}$ above the VBM, which is almost the same value found in $NaNbO_3$.

The composition of the investigated $KNbO_3$ samples is illustrated in Fig. 6.5. The potassium and niobium amount should equal one while the amount of oxygen should be three for a stoichiometric sample without any secondary phases. In contrast, the amount of potassium is much higher than one for the majority of the samples. It is unclear if this high concentration is representative for the complete bulk material or if a segregation is responsible for these high values. The same consideration, which has been made for the high calcium concentration in $Na_{0.99}Ca_{0.01}NbO_3$ and $Na_{0.99}Sr_{0.01}NbO_3$ apply for this case. Potassium could segregate either to the surface and/or the grain boundaries. However, a segregation towards the surface is as likely as to the grain boundaries as potassium is very volatile [175, 177, 187]. Therefore, it is possible that potassium diffuses to the surface at $600\,^{\circ}C$, which is the temperature used during stress-release heat treatment. Due to the high volatility of potassium it is, therefore, very likely that the high concentration of potassium measured with XPS is caused by segregation. This in turn would explain why the bulk material is potassium deficient as already indicated by the sintering curve and the microstructure in Section 5.1 and 5.2. Unfortunately, no TEM analysis were conducted, which could confirm the potassium segregation to the surface. However, for future investigations this would be very interesting and helpful for compositional analysis of this material.

6.2. Determination of the nominal band gap using energy electron loss spectroscopy

The nominal band gap E_G of the investigated materials was determined from the electron energy loss spectrum measured by XPS and TEM. We call this examined band gap *nominal band gap* because it will be discussed in Section 6.6 that the band gap measured with XPS and TEM is not the distance between VBM and CBM. In the following section the nominal band gap values determined by the two methods are analyzed and compared with literature values mainly measured by optical spectroscopy.

6.2.1. Nominal band gap analysis by x-ray photoelectron spectroscopy

The band gap of a material can be determined from the onset of the energy loss part of the O 1*s* peak. These measured electrons represent the O 1*s* photoelectrons, which lost some of their kinetic energy by band-to-band excitation. Hence, the kinetic energy loss of the O 1*s* electrons correspond to the band gap energy, which is the energetic difference between the O 1*s* emission line and the onset of the energy loss part [228, 229].

In Fig. 6.6 the O 1*s* core levels of pure, Ca- and Sr-doped $NaNbO_3$, two $NaNbO_3$ and KNLNT thin films, and two $KNbO_3$ ceramics are shown on a logarithmic scale for a better separation of the onset of the energy loss part from the main component. For pure, Ca- and Sr-doped $NaNbO_3$ values of

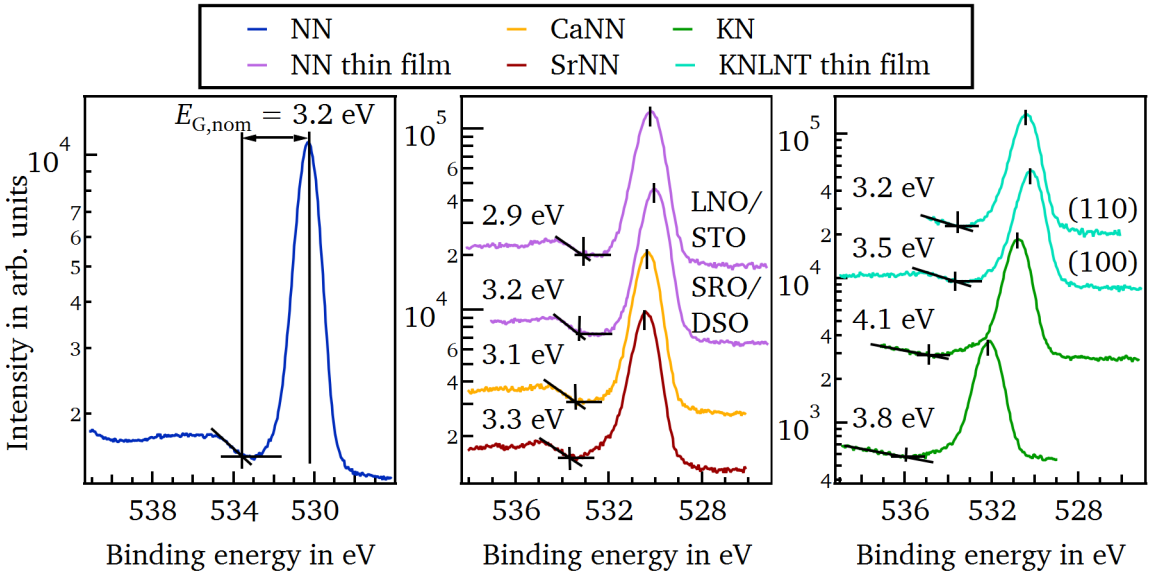

Figure 6.6.: O 1s core levels for pure, Ca- and Sr-doped $NaNbO_3$, two $NaNbO_3$ and KNLNT thin films, and two $KNbO_3$ ceramics on a logarithmic scale. The energetic difference between the O 1s emission line and the onset of the energy loss part corresponds to the nominal band gap energy.

(3.2 ± 0.1) eV, (3.3 ± 0.1) eV, and (3.1 ± 0.1) eV are identified, respectively. These values are quite consistent for all measured samples but are to some extent smaller than the values published in literature ranging from 3.4 eV to 3.5 eV determined by optical spectroscopy [118–127]. In contrast, the extracted nominal band gap energies for the $NaNbO_3$ and KNLNT thin films and the $KNbO_3$ ceramics deviate more between different samples. The nominal band gap values of these materials lie within a range of (2.9 ± 0.1) eV to (3.2 ± 0.1) eV, (3.2 ± 0.1) eV to (3.5 ± 0.1) eV, and (3.8 ± 0.1) eV to (4.1 ± 0.1) eV, respectively. Here, the determined nominal band gap values are higher compared to the band gap energies of 3.1 eV to 3.4 eV for $KNbO_3$ [121, 126, 127, 164–167] and 3.0 eV to 3.2 eV for $K_{0.5}Na_{0.5}NbO_3$ [121, 267] reported in literature. Therefore, a difference of more than 0.5 eV in the nominal band gap energy between $NaNbO_3$ and $KNbO_3$ is identified by XPS.

A clear shoulder can be observed on the high binding energy side of the O 1*s* emission line for $KNbO_3$ and $K_{0.5}Na_{0.5}NbO_3$. Fitting of the O 1*s* peak with one symmetric component by a Voigt line reveals at least one second component at higher binding energies for these two materials, which is shown in Fig. 6.7. This is evidence for another oxide appearing in the samples or at the surface. As previously seen from Fig. 6.1 no carbon is visible after the cleaning procedure any more. Hence, the second component cannot be attributed to some adsorbed carbonaceous species on the surface. One explanation could be the formation of some potassium oxide species at the surface, e.g. K_2O, K_2O_2, K_2O_3, or KO_2. For the KNN thin film the second component is located at around 531.3 eV. According to literature this would refer to K_2O_2 with binding energies ranging from 531.0 eV to

531.7 eV [268–270].
Fig. 6.7 illustrates also the O 1*s* peak and the corresponding fit with one Voigt line for $NaNbO_3$. Interestingly, a second component at higher binding energies can be identified as well although it is not clearly visible at first glance in Fig. 6.6. This species could be also an indication for an oxide, e.g. Na_2O.

In Section 6.4 possible origins for the surface components visible in the K 2*p* and Na 1*s* peaks are discussed. One explanation is the formation of some oxide species, which agrees with the shoulder on the higher binding energy side of the O 1*s* emission lines of both $KNbO_3$- and $NaNbO_3$-based samples. This shoulder most likely interferes with the background line leading to a large error in the determination of the nominal band gap. In case of $NaNbO_3$, however, the second component could also result from an overlap of the Na *KLL* Auger line, which is very broad with features at around 530 eV. Hence, this Auger line could also interfere with the O 1*s* peak causing an error in the extracted nominal band gap values.

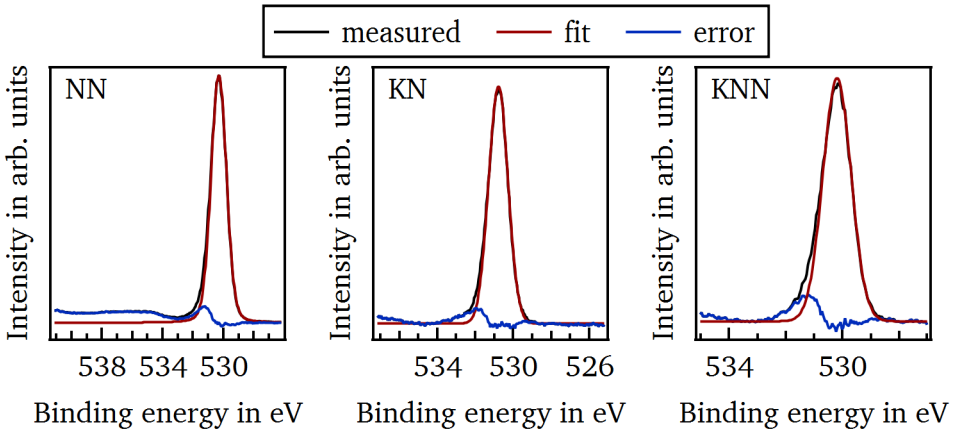

Figure 6.7.: O 1s peaks of $NaNbO_3$, $KNbO_3$, and KNLNT. All tree emission lines are fitted by one single voigt function. The deviation from the measured curves is indicated as well.

6.2.2. Nominal band gap analysis by electron energy loss spectroscopy

The band gap can also be determined by the electron energy loss signal measured with TEM. Fig. 6.8 illustrates the EELS signal recorded for a pure (blue) and a Sr-doped $NaNbO_3$ sample (red). Both exhibit a nominal band gap value of around 3.5 eV. This value agrees with the ones reported in literature ranging from 3.4 eV to 3.5 eV [118–127] analyzed by optical spectroscopy. In the previous section, possible reasons for the deviation of the values extracted from the O 1*s* emission line have already been discussed and are most likely attributed to some oxide species appearing at the surface and/or

the Na *KLL* Auger line. An explanation why the oxide species, e.g. Na_2O, interfere with the XPS results but not with the EELS measurements could be the different information depth of the two methods. XPS is a very surface sensitive method and, therefore, easily affected by some oxide species forming on the surface. In contrast, EELS measures the bulk properties, hence, it is much less influenced by these oxides.

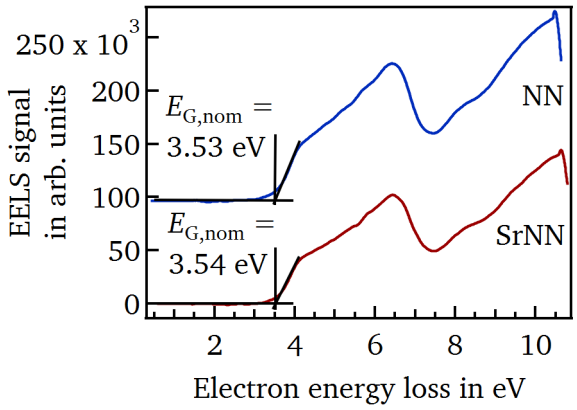

Figure 6.8.: EELS spectrum of pure (blue) and Sr-doped $NaNbO_3$ (red) with extracted nominal band gap values $E_{G,nom}$.

In conclusion, the nominal band gap values determined by EELS seem much more trustworthy and agree with values published in literature. Therefore, in the next sections, a nominal band gap of 3.5 eV will be used for further analyses. Unfortunately, no EELS measurements were carried out on $KNbO_3$ bulk ceramics. Thus, an average nominal band gap of 3.2 eV calculated by means of values identified in literature [121, 126, 127, 164–167] is taken as a measure in the following sections.

6.3. Interface experiments

Interface experiments were conducted in order to investigate the accessible Fermi levels within $NaNbO_3$ and $KNbO_3$. For this purpose, the low work function material ITO or the high work function material RuO_2 is deposited step-wise on the investigated material's surface. The deposition of ITO typically leads to a downward bending of the substrate's bands at the interface while in case of RuO_2 an upward bending is induced. Consequently, with ITO the upper Fermi level limit is examined whereas with RuO_2 the lower Fermi level limit is elucidated.

Figures 6.9 and 6.10 illustrate the recorded core levels and valence band spectra during interface formation of $Na_{0.99}Sr_{0.01}NbO_3$ to ITO and of $Na_{0.99}Ca_{0.01}NbO_3$ to RuO_2 as an example for all measured $NaNbO_3$-based samples. ITO was deposited at $400\,°C$ while RuO_2 was prepared at room temperature. From both figures it can be observed that the peak intensities of Na 1*s* and Nb 3*d* are decreasing with increasing ITO or RuO_2 film thickness while the ones of In 3*d*, Sn 3*d*, and Ru 3*d* are raised in intensity. After depositing an approximately $70\,nm$ to $100\,nm$ thick layer, no signal of $NaNbO_3$ is detected anymore.
In addition to the decrease in intensity, the peak shape of the Na 1*s* emission line changes with

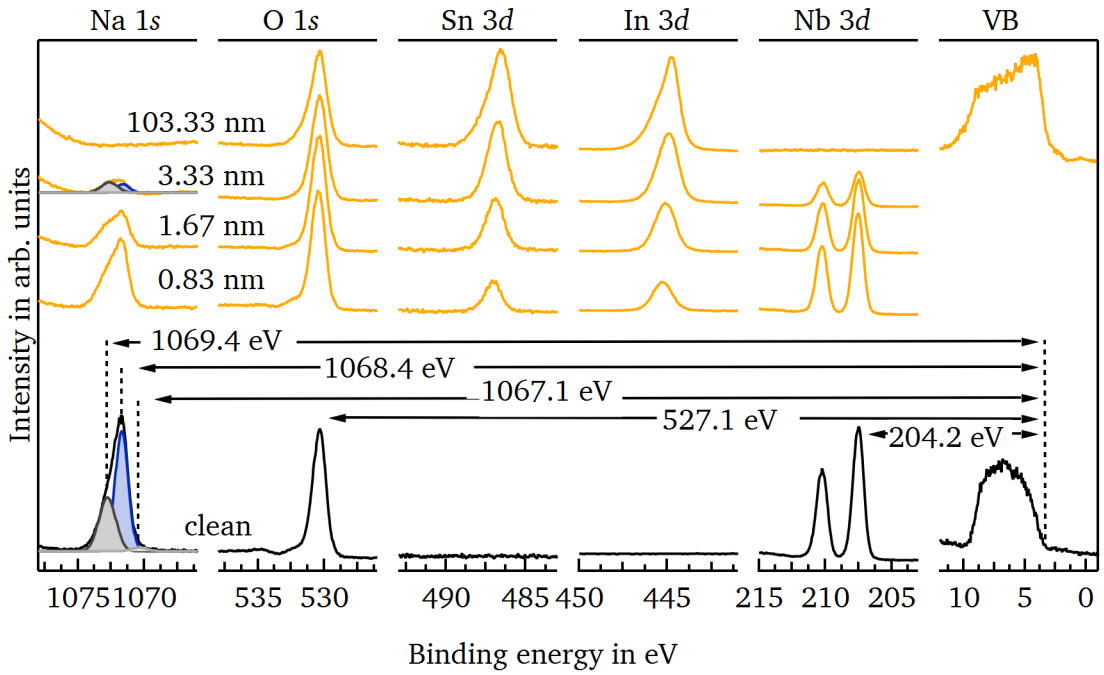

Figure 6.9.: Na 1*s*, O 1*s*, Sn 3*d*, In 3*d*, and Nb 3*d* core level and valence band spectra of a Sr-doped $NaNbO_3$ bulk ceramic sample in the course of ITO deposition. The black lines belong to the cleaned sample, whereas the yellow spectra are measured after depositing a few nanometers of ITO on top. The bulk and surface components of the Na 1*s* emission line are colored in blue and gray in the clean and the last but one XP spectrum. Arrows mark the core-level-to-VBM-distance for each core level of the clean sample.

deposition time. In case of ITO, the intensity ratio of surface component I to the bulk component is getting larger with increasing film thickness whereas for RuO_2 the intensity ratio of surface component II to the bulk component is enhanced. This behavior is also observed for pure $NaNbO_3$, which is illustrated in Fig. A.11 and Fig. A.14. For $Na_{0.99}Sr_{0.01}NbO_3$ the intensity ratio of surface component II to the bulk component is as well increased with RuO_2 layer thickness shown in Fig. A.15. Instead, $Na_{0.99}Ca_{0.01}NbO_3$ does not show such clear increase in the surface component I with ITO layer thickness as for pure $NaNbO_3$ and $Na_{0.99}Sr_{0.01}NbO_3$ (Fig. A.12).
Besides the Na 1*s* peak, the peak shape of the Nb 3*d* emission line is getting more asymmetric on the lower binding energy side with RuO_2 deposition. This applies to the Nb 3*d* core level emissions of all $NaNbO_3$-based samples. The peak shape of Nb 3*d* stays unchanged when ITO is deposited on the surface.

Interface experiments of $KNbO_3$ to ITO and RuO_2 were conducted as well. The corresponding XP-spectra are displayed in Fig. A.13 and A.16. Similar observations are done for the ITO interfaces. Surface component I is gaining in intensity with longer ITO deposition, while surface component II

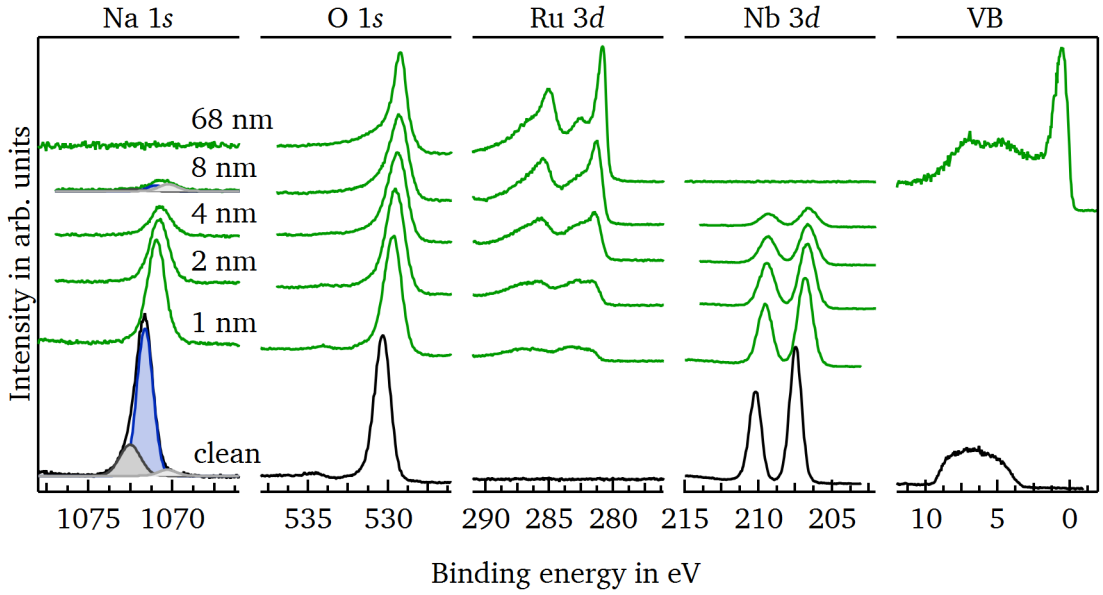

Figure 6.10.: Na 1*s*, O 1*s*, Ru 3*d*, and Nb 3*d* core level and valence band spectra of a Ca-doped $NaNbO_3$ bulk ceramic sample in the course of RuO_2 deposition. The black lines belong to the cleaned sample, whereas the green spectra are measured after depositing a few nanometers of RuO_2 on top. The bulk and surface components of the Na 1*s* emission line are colored in blue and gray in the clean and the last but one XP spectrum.

and the bulk component are decreasing. Interestingly, after depositing a 100 nm thick ITO layer a signal of surface component I is still detected. Possible causes for this phenomenon will be discussed in the next section.

When RuO_2 is used to form an interface to $KNbO_3$ no modifications of the peak shapes, neither of the K 2*p* nor the Nb 3*d* emission line, are identified. Only the peak intensity decreases with the RuO_2 film thickness. This observation is quite different to the one made for $NaNbO_3$.

6.4. Surface characterization

In this section the above mentioned surface components observed for the Na 1*s* and K 2*p* peak are analyzed and discussed in very detail. This is done because surface components have been observed in other perovskite oxide materials, such as $BaTiO_3$ and $SrTiO_3$, in this working group over the last fifteen years. However, no clear explanation has been found so far, which is why all observations done for $NaNbO_3$ and $KNbO_3$ are examined with great care for future investigations. Readers who are interested in detailed analysis of surface components in $BaTiO_3$ and $SrTiO_3$ are referred to the theses of Robert Schafranek [271] and Karsten Rachut [272].

In this part, some results, which will be studied in Section 7.4.3, are already introduced in order to

discuss possible origins for the appearance of the surface components. First, the K 2*p* core level lines of $KNbO_3$ ceramics and KNLNT thin films will be investigated and then the Na 1*s* emission line of $NaNbO_3$ ceramics as well as KNLNT thin films will be analyzed.

6.4.1. K 2*p* emission line

Figure 6.11 shows K 2*p* emission lines of $KNbO_3$ ceramics for an interface formation to ITO at room temperature in a) and at 400 °C in b) as well as after sample preparation in c). In order to get a consistent description for the different components, for all spectra the three components bulk (green), surface I (dark gray), and surface II (light gray) are fitted with the same fitting procedure and parameters as described in more detail in the appendix.

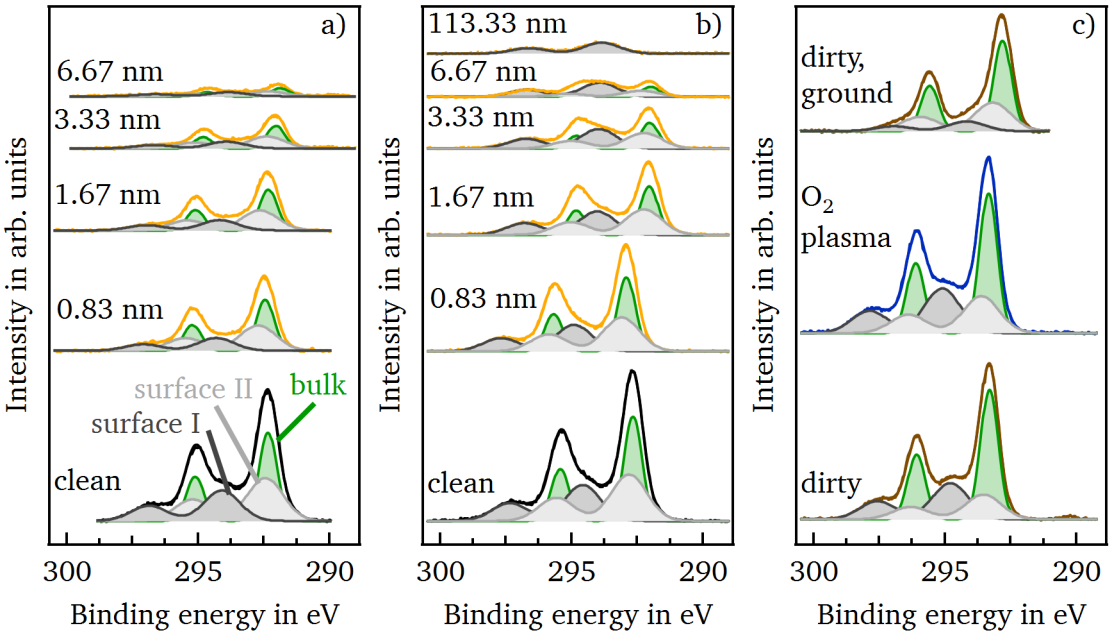

Figure 6.11.: K 2*p* emission lines for an interface formation to ITO at a) room temperature and b) 400 °C, and for a ceramic sample after grinding with stress-release-annealing, after an oxygen plasma treatment and after grinding without stress-release-annealing in c). Bulk component (green), surface component I (dark gray), and surface component II (light gray) are fitted for each peak.

The interface experiment conducted at room temperature exhibits a continuous decrease in intensity of all three components. Unfortunately, no XP-spectrum was recorded after the deposition of an approximately 100 nm thick ITO layer, however, in Section 7.4.3 a room temperature deposition of a 100 nm thick ITO film on a KNLNT sample reveals the disappearance of all KNLNT containing elements. The same observation of decreasing K 2*p* peak intensities of all contributions is made

with increasing film thickness of a RuO_2 film shown in Fig. A.17 in the appendix. The RuO_2 layer was also deposited at room temperature. In contrast, for the ITO-interface formation at $400\,°C$ bulk and surface component II are reduced in intensity with ITO deposition while surface component I is raising in intensity relative to the bulk contribution. Interestingly, this component can be still detected when a more than $100\,nm$ thick ITO layer is deposited on top of the sample at $400\,°C$.
Both surface components are already visible before the cleaning procedure as shown in Fig. 6.11c) (dirty spectrum). The K 2*p* core level is measured after sample preparation meaning after cutting, grinding, polishing, and stress-release-annealing at $600\,°C$. After an oxygen plasma treatment no big differences besides a larger binding energy separation of bulk and surface component I can be identified. Heating the sample at elevated temperatures seems to enhance the first surface component suggesting that this contribution is a potassium species forming on the surface of the sample. In order to verify this hypothesis, the oxygen plasma treated $KNbO_3$ ceramic is ground once again without the stress-release-post-annealing. Figure 6.11c) shows evidently that the intensity of surface component I is much smaller than before grinding. Hence, it is very likely that surface component I is formed by a second phase on the surface of the samples.
The question is what kind of second phase could be formed during heating. With a binding energy between 293.1 eV and 294.1 eV surface component I agrees with literature values found for potassium oxides like K_2O and K_2O_2 [268, 269, 273]. Here, the binding energies of the KNLNT thin films and the K 2*p* emission line measured on top of the thick ITO layer are considered because the $KNbO_3$ ceramics are most likely influenced by charging of the samples. Hence, the binding energies of the ceramics are not completely reliable. On first glance, the formation of K_2O_2 sounds not very likely, however, several indications support the creation of K_2O_2 instead of K_2O. First, the appearance of the shoulder at around $532\,eV$ in the O 1*s* peak shown in Fig. 6.7 in Section 6.2.1 fits better to oxygen in form of K_2O_2. K_2O_2 exhibits a O 1*s* binding energy of 530.3 eV to 531.7 eV while K_2O has a O 1*s* core level line located at much lower energies of 527.2 eV to 528.3 eV [268, 269]. Second, in literature it has been shown by annealing experiments that K_2O_2 is much more stable than other potassium oxide compounds [268]. And finally, K_2O_2 has a lower formation enthalpy than K_2O, which explains the higher stability of this compound [18]. These indications suggest that surface component I can be referred to K_2O_2.

Still the question remains what might be the origin for surface component II. In order to discuss possible reasons for the appearance of this contribution, let us first have a look on the K 2*p* core level lines of KNLNT thin films on different oriented Nb-doped $SrTiO_3$ substrates. Figure 6.12 illustrates the K 2*p* peak on a (100)-, (110)-, and (111)-oriented substrate before cleaning in a) and after cleaning in b). In addition, more bulk and more surface sensitive measurements are shown in c) and d), respectively. Before cleaning the sample in a low pressure oxygen atmosphere at $400\,°C$, only surface component II is visible. After the cleaning procedure, surface component I has developed and exhibits a much higher intensity in the surface sensitive measurement. This is in line with the

observations made above and agrees with a potassium oxide species forming during annealing on the samples' surfaces. Interestingly, surface component II is much more pronounced in the KNLNT thin films compared to the $KNbO_3$ ceramics. Therefore, an explanation for the appearance of surface component II could be a changed surrounding due to other A-site atoms such as lithium and sodium. In the $KNbO_3$ ceramics, small traces of sodium, which are not visible in the survey spectrum, cannot be excluded but might be responsible for the observation of surface component II.

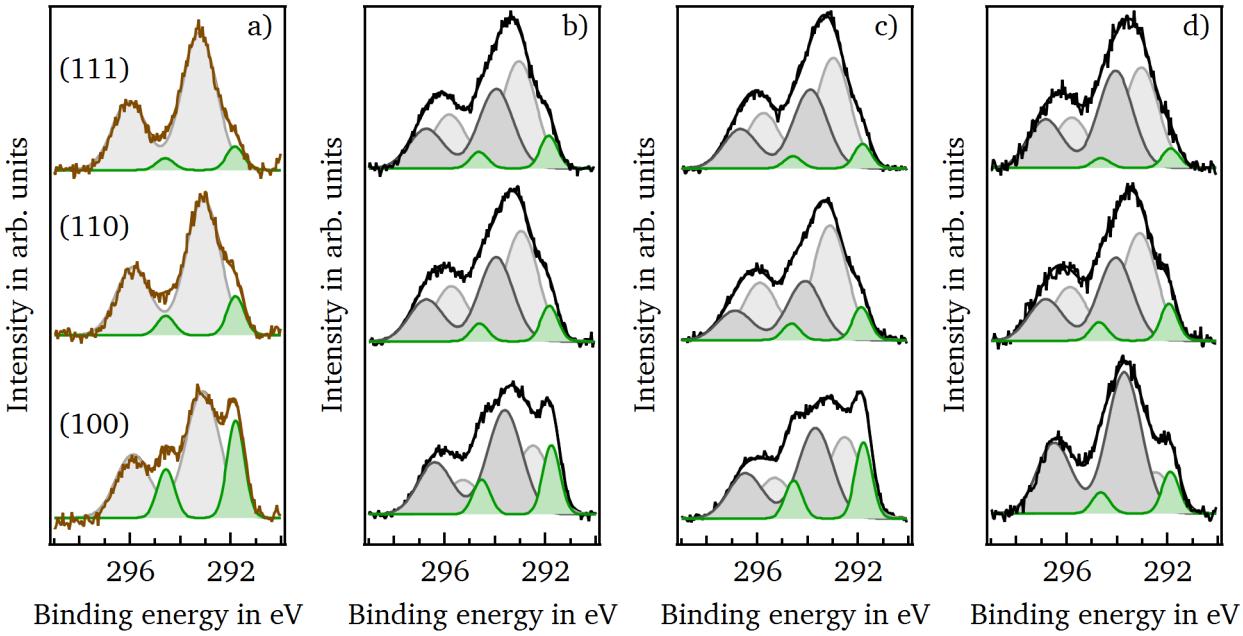

Figure 6.12.: K 2*p* peaks of KNLNT thin films on different oriented Nb-doped $SrTiO_3$ substrates in a) before and in b) after cleaning as well as for a more bulk in c) and more surface sensitive setup arrangement in d). For all emission lines bulk (green), surface I (dark gray), and surface II (light gray) components are fitted.

Moreover, the substrate orientation might play a role because the intensity ratio of surface component II to the bulk part is much larger in case of the (110)- and (111)-oriented substrates than for the (100)-oriented substrate. Final state and screening effects could be further possible origins. The emitted photoelectron can lose some energy to, e.g. other electrons, which can be excited to higher energy states. From Eq. 3.5 it is clear that a smaller kinetic energy translates to a higher binding energy at constant x-ray photon energy. Consequently, a signal at higher binding energies is detected. In literature the existence of surface components is attributed to K_2CO_3 [266] or a more metallic-like form of potassium [265]. Both explanations seem not realistic for this work. K_2CO_3 can be excluded because no carbon peak is visible in the survey spectra shown in Fig. 6.1. In addition, it would not explain why surface component II is enhanced for the KNLNT thin films. Metallic potassium can

also be ruled out as no clear Fermi edge is observed in the valence band of the clean KNLNT films (Fig. 6.15) as it should be in case of a metal component. In addition, metallic potassium should be located at 294.4 eV [273], which is a much higher binding energy as the range of 291.9 eV to 293.0 eV determined for surface component II.
Hence, it is not clear what the origin of surface component II is. The most probable explanations are a changed surrounding due to other A-site atoms, different crystal orientations, final state or screening effects.

6.4.2. Na 1s emission line

In Fig. 6.13 Na 1*s* emission lines for an interface formation of $Na_{0.99}Sr_{0.01}NbO_3$ to ITO in a) and of $Na_{0.99}Ca_{0.01}NbO_3$ to RuO_2 in b) and after water exposure of a $NaNbO_3$ thin film in c) are displayed. It should be mentioned that neither doping nor sample preparation (ceramic or thin film) have a

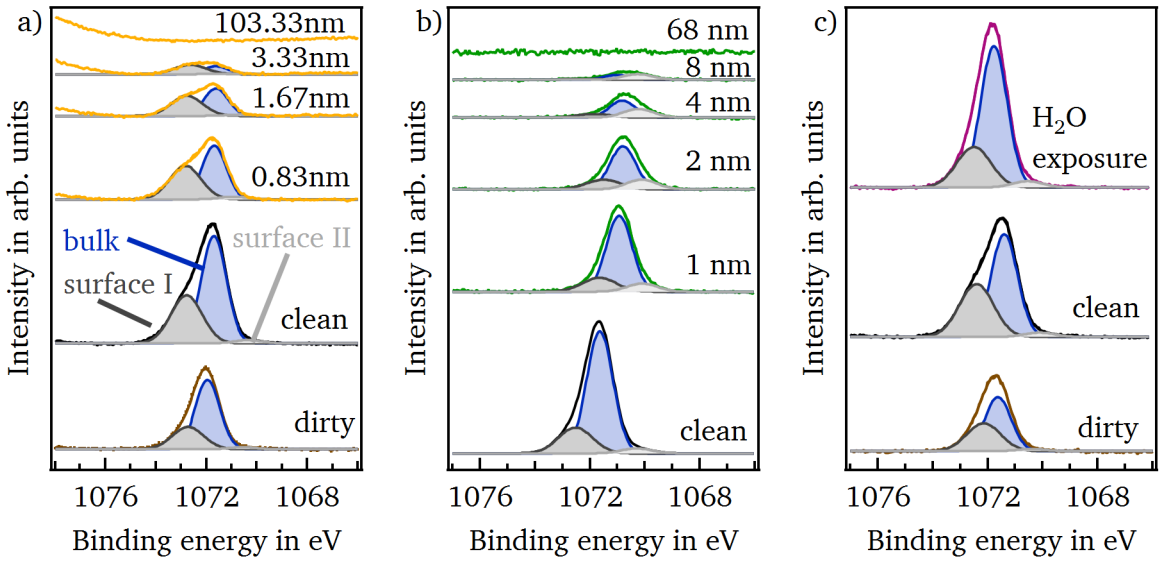

Figure 6.13.: Development of the Na 1s peak of $Na_{0.99}Sr_{0.01}NbO_3$ during an interface formation to ITO deposited at 400 °C in a), of $Na_{0.99}Ca_{0.01}NbO_3$ during step-by-step room temperature deposition of RuO_2 in b), and of a $NaNbO_3$ thin film after exposure to water in c). Bulk (blue), surface I (dark gray) and surface II components (light gray) are fitted for each individual emission line.

significant influence on the behavior of the peak shape. Therefore, only those experiments, which show the influences of sample treatments on the peak shape most clearly, are illustrated for the sake of simplicity.
Two surface components are observed, however, surface component II cannot be easily identified for the as-prepared and cleaned samples. The ITO-film was deposited at 400 °C while RuO_2 was

prepared at room temperature. Similar to the observations made for the K 2*p* emission line during the interface formation of $KNbO_3$ with 400 °C-ITO, bulk and surface component II of the Na 1*s* peak decrease in intensity with increasing ITO layer thickness whereas surface component I is intensified. However, for $NaNbO_3$ no sodium signal is detected after depositing a 100 nm thick ITO film on top. Interestingly, in case of the RuO_2 interface bulk and surface component I are lowered in intensity while surface component II is gaining intensity relative to the bulk part. Nevertheless, no traces of sodium can be found after depositing a thick RuO_2 film on the $NaNbO_3$ ceramic sample. Exposing $NaNbO_3$ to water leads to a decrease of surface component I in comparison to the bulk contribution. Here we must note that this decrease is much more pronounced for the thin film sample shown in Fig. 6.13c) as for the ceramic samples, which are not included in this work.

For the KNLNT thin films deposited on Nb-doped $SrTiO_3$ substrates with different orientations surface component I of the Na 1*s* peak is much less pronounced while surface component II is clearly more visible. The corresponding spectra are shown in Fig. 6.14 before and after cleaning in a) and b), respectively. After performing the cleaning procedure both surface contributions have decreased in intensity relative to the bulk part. However, no clear trend with, e.g. substrate orientation, can be identified.

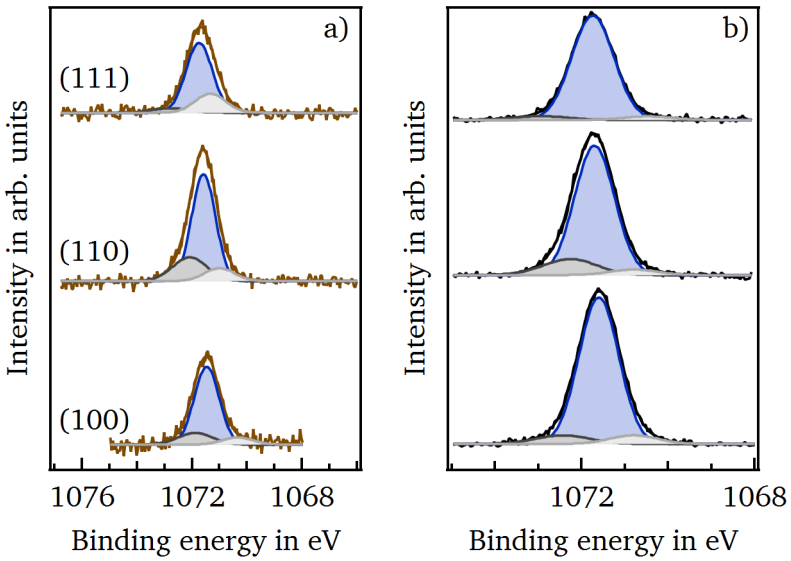

Figure 6.14.: Na 1*s* emission lines of KNLNT thin films on different oriented Nb-doped $SrTiO_3$ substrates in a) before and in b) after cleaning. For all emission lines bulk (blue), surface I (dark gray), and surface II (light gray) components are fitted.

The evaluation of possible origins for the surface components is even more difficult for sodium than for potassium. Surface component I could be attributed to some metallic or oxide species forming on the surface similar as for surface component I of the K 2*p* emission line.

In literature, binding energies of metallic sodium are ranging from 1070.8 eV to 1071.8 eV [274, 275]. For sodium oxide a binding energy of 1072.0 eV is reported [275]. In this work, binding energies between 1072.2 eV and 1073.0 eV are measured for surface component I. Again, only the values of the clean $NaNbO_3$ and KNLNT thin films are taken into account as charging of the ceramics cannot be excluded. The recorded positions of surface component I suggest the formation of sodium oxide on the surface. This agrees with the measured valence band maxima illustrated in Fig. 6.15 of the clean $NaNbO_3$ thin film. In case of a metallic sodium contribution a Fermi edge should be observed at 0 eV, which is not detected here. Hence, it is more likely that surface component I of the Na 1*s* peak has more oxidic character.

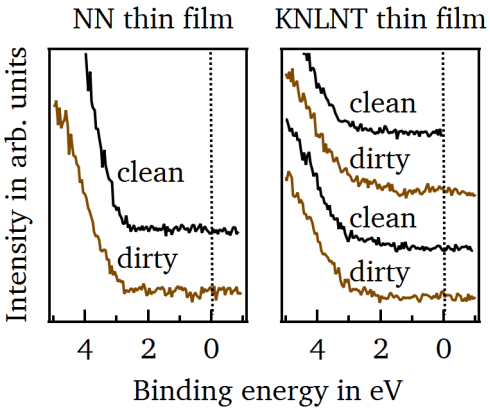

Figure 6.15.: Magnified view of the valence band maximum of a $NaNbO_3$ and a KNLNT thin film.

The intensity of surface component II is for the most measurements relatively small and negligible. Only for the RuO_2 interface an increase relative to the bulk contribution is recognized. Such behavior is also obtained for undoped and Sr-doped $NaNbO_3$. Surprisingly, the Nb 3*d* peak develops in parallel to the Na 1*s* emission line an asymmetry on the lower binding energy side. Figure A.18 in the appendix illustrates the modification of the asymmetric peak shape. A shoulder at lower binding energies is usually an indication for the element partially transforming to a state with a smaller valence. RuO_2 is a high work function material and is pushing the Fermi level at the surface of the investigated material closer to the valence band as revealed by the parallel binding energy shift to lower energies of all core levels shown in Fig. 6.10. The emerging of an oxidized species would be expected rather than a reduced one. Therefore, a changed oxidation state can be ruled out as an explanation.

The development of an asymmetric peak shape has already been observed for the Ti $2p_{3/2}$ core level line of a $BaTiO_3$ single crystal during an interface formation to NiO in this working group [276]. Similar to RuO_2, NiO is a high work function material leading to a downward band bending of the bands of $BaTiO_3$ at the interface, which would result in a higher oxidation state of titanium and not a lower one. No reasonable interpretation of the observations could be established so far except for a higher Fermi level shift occurring at the surface due to a very high band bending and a very narrow space charge region. The width of this space charge region would then be smaller than the detection limit of the XPS system and would allow for the measurement of photoelectrons excited from the

bulk and the surface region. Due to the high band bending at the surface, a lower Fermi level is measured. This in turn, leads to a smaller measured binding energy of the photoelectrons from this region. As result from the overlapping bulk and surface emission lines, a peak broadening towards lower binding energies is detected. However, this explanation could not be confirmed, yet.
Both, increase of surface component II of the alkali emission lines and the asymmetry of the Nb 3*d* peak, are not detected for $KNbO_3$ with RuO_2 on top. The Nb 3*d* core level lines of a $KNbO_3$ ceramic are plotted for comparison in Fig. A.18. Highly symmetric peak shapes are maintained while depositing RuO_2.

In literature surface components on the higher binding energy side of the Na 1*s* peak are reported, too. They are mainly attributed to secondary phases formed on the surface such as Na_2CO_3 or NaOH [247, 262, 263]. Surface contamination can be excluded for this work because after the cleaning procedure no carbon traces are detected any more (see Fig. 6.1).

6.4.3. Summary

In summary, two surface components are visible in the K 2*p* and the Na 1*s* peak. The origins are not completely clear though. Surface component I might be explained for both elements with some oxide species formed on the samples' surfaces. Finding an explanation for the appearance of surface component II is even more difficult. For potassium it could be influenced by the surrounding, e.g. changed bonding distances due to other A-site atoms such as sodium and lithium. Another origin could be substrate orientations. Final state effects, e.g. plasmon interactions and screening effects, could cause an increased intensity on the higher binding energy side as well because the emitted photoelectron loses kinetic energy on its way out. In contrast, these explanations do not seem reasonable for surface component II of the Na 1*s* peak because it is located on the lower binding energy side, which would imply an increased kinetic energy of the photoelectron. Hence, no clear explanations for surface component II of the K 2*p* and the Na 1*s* emission line can be given at them moment.
Surface components have been observed and analyzed quite extensively in $BaTiO_3$-based samples. Given explanations are surface contamination in form of carbonates or hydroxides [277], A-site rich oxide layers including Ruddlesden-Popper phases [278–280], undercoordinated A-site atoms at the surface [281, 282], relaxation effects [283, 284] or dipoles occurring on the surface [285, 286]. From these potential origins only carbonates and hydroxides can be quite certainly excluded.
In any way, it is clear that an easy interpretation of observed surface components in core level spectra of A-site atoms in perovskites does not exist. Hence, further investigations are necessary. However, in this work it could be shown that both, Na 1*s* and K 2*p* peaks, are composed of not only two but three components, one from the bulk material and two surface sensitive. Furthermore, one surface

component can very likely be attributed to a second phase established on the surface, which is most likely an oxide.

6.5. Fermi level positions

In this section the influence of different oxidizing and reducing treatments, including the interface analysis described in Section 6.3, on the Fermi level positions in $NaNbO_3$ and $KNbO_3$ are discussed and put in relation to the nominal band gaps determined in Section 6.2. At the end of this section a model for the band structures according to the XPS results is proposed, which is validated in the subsequent section.
For these investigations, the determined Na 1*s*, K 2*p*, Nb 3*d*, and O 1*s* core level binding energies, the core-level-to-VBM-distances illustrated in Section 6.3, and the mean nominal band gap values examined in Section 6.2 are required.

As mentioned in Section 6.3, interface experiments are performed in order to analyze the maximum and minimum accessible Fermi level within $NaNbO_3$ and $KNbO_3$. The shift in the Fermi level position can be determined by the shift of the VBM and the core levels as explained in Section 3.8. For this purpose, the core-level-to-VBM-distance of the clean samples is needed in order to subtract it from the binding energy of the corresponding peaks after each deposition step. In Fig. 6.9 an average value of the core-level-to-VBM-distance for each emission line extracted from all measured clean samples is marked for $Na_{0.99}Sr_{0.01}NbO_3$. Slightly different values are identified for $NaNbO_3$ and $Na_{0.99}Ca_{0.01}NbO_3$, which are given in Table 6.1. Table 6.1 includes also the corresponding values of $KNbO_3$.

Table 6.1.: Mean values of the core-level-to-VBM-distances determined from all clean samples for undoped, Ca- and Sr-doped $NaNbO_3$, and $KNbO_3$. For the Na 1*s* and K 2*p* peaks, values for bulk and both surface components are included.

	Na 1*s*-VBM-distance in eV			O 1*s*-VBM-distance	Nb 3*d*-VBM-distance
	bulk	surface I	surface II	in eV	in eV
$NaNbO_3$	1068.7	1069.6	1067.8	527.3	204.3
$Na_{0.99}Ca_{0.01}NbO_3$	1068.4	1069.4	1067.0	527.0	204.3
$Na_{0.99}Sr_{0.01}NbO_3$	1068.4	1069.4	1067.1	527.1	204.2
	K 2*p*-VBM-distance in eV			O 1*s*-VBM-distance	Nb 3*d*-VBM-distance
	bulk	surface I	surface II	in eV	in eV
$KNbO_3$	288.9	290.8	289.2	527.1	204.2

Subtracting the core-level-to-VBM-distances from the core level binding energies, reveals how much the Fermi level is shifted further away or closer to the VBM after each deposition step of ITO or RuO_2. Fig. 6.16 shows the development of the Fermi energy with increasing ITO (yellow) and RuO_2 film thickness (green) for undoped, Ca- and Sr-doped $NaNbO_3$, and $KNbO_3$. Here, the Fermi level is obtained from the Na 1*s* or K 2*p* bulk component and the Nb 3*d* peak. The O 1*s* emission line and the VBM cannot be taken as a measure for the Fermi level position as they are superimposed by the spectra of the deposited thin film. The green shaded areas represent the valence and conduction band. The nominal VBM is set to 0 eV. According to the nominal band gap detected by the EELS signal, the

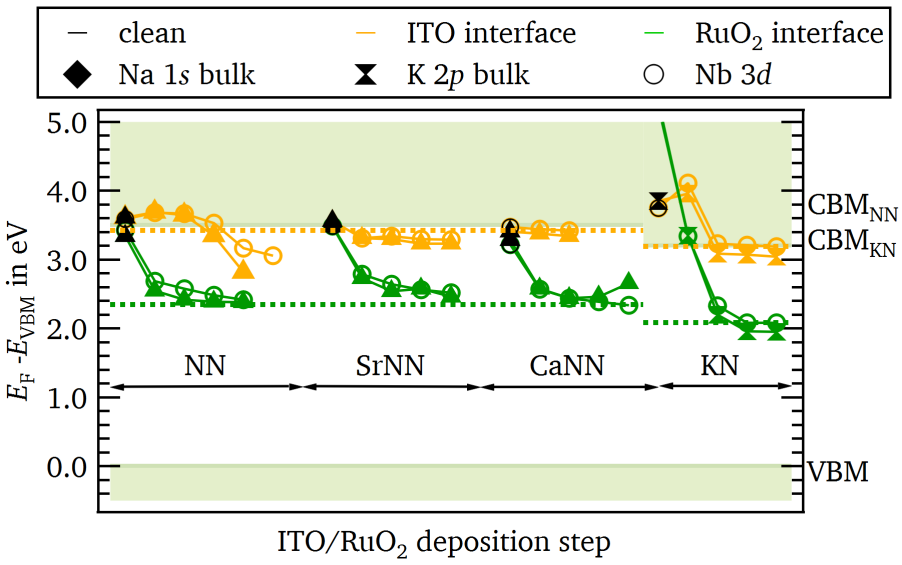

Figure 6.16.: Fermi level positions at interfaces of $NaNbO_3$, $Na_{0.99}Ca_{0.01}NbO_3$, $Na_{0.99}Sr_{0.01}NbO_3$, and $KNbO_3$ to ITO (yellow) and RuO_2 (green) as a function of deposition steps of the corresponding electrode material. For ITO the total deposition time per step was 0 s, 10 s, 20 s, 40 s, 80 s, and 160 s with a deposition rate of $5\,nm\,s^{-1}$, while for RuO_2 the total deposition time per step was 0 s, 20 s, 40 s, 80 s, 160 s with a deposition rate of $3\,nm\,s^{-1}$. The Fermi levels are extracted from the core level lines by subtracting the corresponding core-level-to-VBM-distance given in Table 6.1. The initial Fermi level positions are affected by charging, due to the low conductivity of the samples. Yellow and green dashed lines mark the highest and lowest obtained Fermi levels, respectively. Green shaded areas indicate the valence and conduction band.

nominal CBM is located 3.5 eV above the nominal VBM of $NaNbO_3$. For $KNbO_3$ the nominal CBM is 3.2 eV higher in energy than the nominal VBM in accordance with the band gap determined by an average value from literature [121, 126, 127, 164–167]. As the nominal VBM is positioned at 0 eV, the measured difference in energy between the Fermi level and the nominal VBM $E_F - E_{VBM}$ represents the energetically position of the Fermi level. $E_F - E_{VBM}$ is in turn determined by the

subtraction of the core-level-to-VBM-distances from the corresponding binding energies of Na 1*s* or K 2*p* bulk component and the Nb 3*d* peak.
From Fig. 6.16 it can be seen that the Fermi level of the clean samples (black data points) is located slightly above the nominal CBM for the $NaNbO_3$-based materials and within the conduction band for the $KNbO_3$ ceramics. However, as it has been already discussed in Section 6.1, these data points are compromised by charging of the clean samples during the XPS experiments, which shifts the whole XP-spectrum to higher binding energies. Therefore, this high Fermi energy can be explained by these charging effects. After depositing a 2 nm conductive film on top (after approximately two deposition steps), the charging effect is eliminated. Consequently, the last deposition step of each interface experiment is free of any charging and can be used to determine the Fermi level position. Considering these last deposition steps, an accessible Fermi level range close to the nominal conduction band for the $NaNbO_3$-containing samples is derived. In case of ITO a maximum Fermi energy of 3.4 eV above the nominal VBM is found indicated by the yellow dashed line in Fig. 6.16. With RuO_2 the Fermi level can be pushed down to 2.3 eV above the nominal VBM shown by the green dashed line. Hence, the Fermi level can be varied in a range of about 1.1 eV reaching the nominal CBM in the case of ITO deposition.

In $KNbO_3$ a maximum and minimum Fermi energy of 3.2 eV and 2.1 eV is reached with ITO and RuO_2, respectively. This corresponds as well to an accessible Fermi level variation of 1.1 eV. As for $NaNbO_3$, the Fermi level energy reaches the nominal CBM position at the $KNbO_3$/ITO interface.

Fig. 6.17 illustrates the Fermi level positions in relation to the nominal VBM and CBM found in the as-prepared $NaNbO_3$ and $K_{0.5}Na_{0.5}NbO_3$-based thin films (brown) and after different surface treatments such as heating in a low-pressure oxygen atmosphere (black) or in vacuum (green) at 400 °C, exposure to water (red) or to an oxygen plasma (blue). Heating in vacuum and exposing the sample to water are reducing treatments, which should lead to an upward-shift of the Fermi level. Heating in oxygen and treating the sample in an oxygen plasma are more oxidizing and should have a lowering effect on the Fermi level. For the thin films the Fermi level can be extracted from all core levels as no additional layer is deposited onto the samples' surface, which could interfere with the O 1*s* peak. Furthermore, charging effects are avoided because the samples are either prepared on a conductive substrate or a conductive intermediate film is used. This allows for charges to flow fast enough to the sample surface counterbalancing the positive charges created by the emission of the photoelectrons.

The green shaded areas in Fig. 6.17 represent the nominal valence and conduction band. For $NaNbO_3$ the nominal band gap of 3.5 eV measured by EELS is used while for the $K_{0.5}Na_{0.5}NbO_3$-based thin films an average band gap of literature values of 3.2 eV is considered. For both, $NaNbO_3$ and $K_{0.5}Na_{0.5}NbO_3$ films, an overall Fermi level range close to or even slightly above the nominal CBM is observed. The maximum and minimum achieved Fermi level is marked in black dashed lines. The reducing and oxidizing treatments do not have a pronounced effect on the Fermi level position, which is in contrast

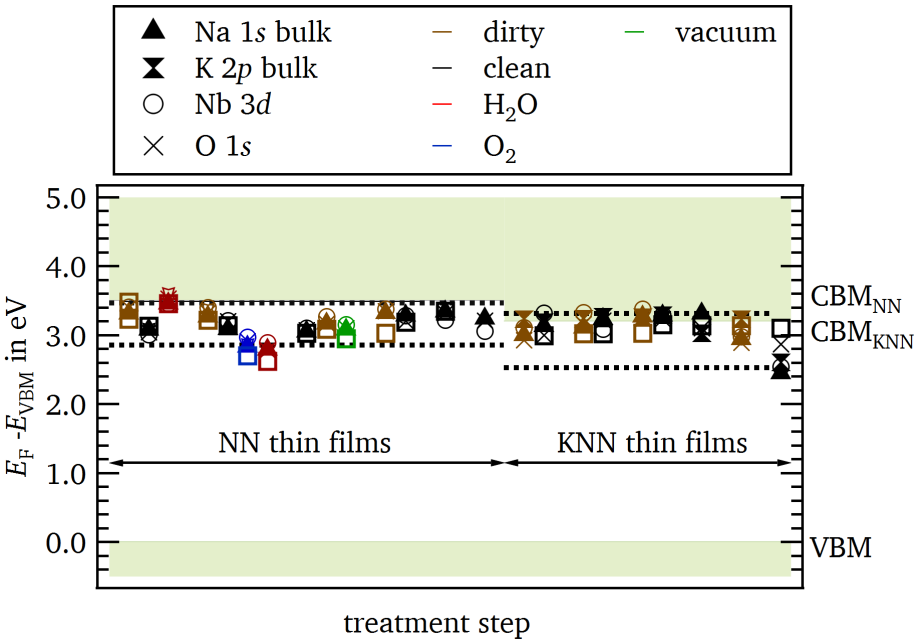

Figure 6.17.: Fermi level positions of $NaNbO_3$ and $K_{0.5}Na_{0.5}NbO_3$-based thin films before (dirty in brown) and after different surface treatments such as heating in a low oxygen pressure atmosphere at $400\,°C$ (black), heating in vacuum at $400\,°C$ (green), exposure to water (red), and treating in an oxygen plasma (blue). The Fermi levels are extracted from the core level lines by subtracting the corresponding core-level-to-VBM-distance given in Table 6.1. Black dashed lines mark the highest and lowest obtained Fermi levels, respectively. Green shaded areas indicate the valence and conduction band.

to what was already seen in the research group for other material systems [39, 80, 241]. For instance, in $BiFeO_3$ a $1.2\,eV$ higher Fermi level position is derived by water exposure compared to an oxygen plasma treatment [39]. In case of $BiVO_4$ a difference of $0.5\,eV$ is obtained [241].

So far, the sample composition, the band gap, and the maximum and minimum Fermi level positions of $NaNbO_3$- and $KNbO_3$-based samples have been investigated. In both material systems the Fermi level can be shifted within an energy range of $1.1\,eV$ with a lower limitation of $2.3\,eV$ and $2.1\,eV$ above the nominal VBM for $NaNbO_3$ and $KNbO_3$, respectively. Considering a nominal band gap of $3.5\,eV$ for $NaNbO_3$ and $3.2\,eV$ for $KNbO_3$, the Fermi level can be shifted close to the nominal CBM. With this information from the XPS measurements, a preliminary band structure can be established for the two material systems, which is shown in Fig. 6.18.
These band structures are verified in the next section by taking the room temperature conductivity results presented in Section 5.5 into account. In addition, the knowledge gained from the well studied oxide perovskite material $BaTiO_3$ is included in the discussion as a reference material.

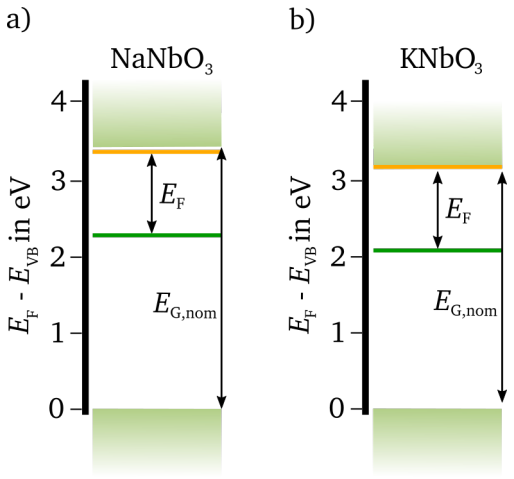

Figure 6.18.: Preliminary band structure of $NaNbO_3$ in a) and $KNbO_3$ in b) with nominal band gap $E_{G,nom}$ and the accessible Fermi level range. Upper (yellow line) and lower Fermi level limit (green line) are extracted from the ITO and RuO_2 interface, respectively.

6.6. First proposed band structure of sodium and potassium niobate

In this section, the preliminary band structure of $NaNbO_3$ and $KNbO_3$ presented in the previous section is validated by taking the room temperature electrical conductivity examined in Section 5.5 into account. Furthermore, it is compared to the band structure of the well known oxide perovskite material $BaTiO_3$. Possible discrepancies are analyzed and an extended band structure model for the two systems under investigation is introduced.

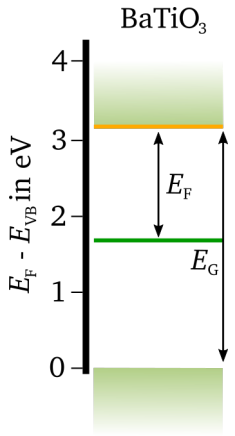

Figure 6.19.: Band structure of $BaTiO_3$ with band gap E_G and the accessible Fermi level range. Upper (yellow line) and lower Fermi level limit (green line) are extracted from the ITO and RuO_2 interface, respectively.

Let us first consider the band structure of $BaTiO_3$. $BaTiO_3$ is a ferroelectric perovskite material with a band gap of $3.2\,\text{eV}$ [287]. In addition, the maximum and minimum detected Fermi level is positioned at $3.2\,\text{eV}$ [288] and $1.7\,\text{eV}$ [278] above the VBM, respectively. Hence, the Fermi level can be shifted close to the CBM within a range of $1.5\,\text{eV}$. The corresponding band structure of $BaTiO_3$ is illustrated in Fig. 6.19. The VBM is mainly composed of O $2p$ states, while the CBM is mostly formed by O $2p$ and Ti $3d$ orbitals. This is similar to the band structure of $NaNbO_3$ and $KNbO_3$.

Here, the VBM is dominated by O p states as well and the CBM is mainly composed of Nb d orbitals. Hence, the band structure of $BaTiO_3$ is similar to the preliminary one of $NaNbO_3$ and $KNbO_3$ shown in Fig. 6.18. In all three materials a Fermi level range close to the nominal band gap is observed. When $BaTiO_3$ is donor doped the Fermi level is shifted to the upper limit close to the CBM. A high concentration of free (non-trapped) charges is introduced into the conduction band due to these donors. This in turn leads to a high conductivity of $\sim 1\,\mathrm{S\,cm^{-1}}$ [22, 37, 289]. Calcium and strontium act as donors on the Na-site in $NaNbO_3$. These donor doped $NaNbO_3$ samples exhibit a Fermi level close to the conduction band minimum as shown in Fig. 6.16. It might be that the first data point of the cleaned $Na_{0.99}Ca_{0.01}NbO_3$ and $Na_{0.99}Sr_{0.01}NbO_3$ ceramics is still affected by charging, hence, the actual Fermi level could be slightly lower. However, it should be still significantly higher as for undoped $NaNbO_3$. Therefore, a high concentration of free charges introduced by the donors can be assumed, which should result in a high conductivity as in $BaTiO_3$. Therefore, the following hypothesis can be proposed.

Hypothesis

- → $NaNbO_3$ and $KNbO_3$ have a similar band structure as $BaTiO_3$ with a comparable nominal band gap and a Fermi level range close to the nominal CBM.
- → Donor doping leads to an upward shift of the Fermi level in energy reaching the nominal CBM.
- → A high concentration of free charges is introduced into the conduction band leading to a high room temperature conductivity in the range of $1\,\mathrm{S\,cm^{-1}}$ as for $BaTiO_3$.

In order to check this hypothesis, the room temperature DC-conductivity analyzed in Section 5.5 is taken under consideration. A conductivity below $5 \times 10^{-10}\,\mathrm{S\,cm^{-1}}$ for electric fields up to $4\,\mathrm{kV\,mm^{-1}}$ is observed in Fig. 5.11 for both donor doped samples, $Na_{0.99}Ca_{0.01}NbO_3$ and $Na_{0.99}Sr_{0.01}NbO_3$. This is much lower than the expected $1\,\mathrm{S\,cm^{-1}}$. Hence, the question is why donor doped $NaNbO_3$ does not show a high conductivity as donor doped $BaTiO_3$.

A common situation in polycrystalline ceramics is the appearance of insulating grain boundaries [21, 253, 254, 290, 291]. Grain boundaries can act as sinks for defects due to a lower formation energy, which leads to an accumulation of theses. Vacancies are known to concentrate here leading to an upward or downward shift of the band edges at the grain boundaries depending on the type of specie. This can result in a potential barrier for the majority charges hindering them from moving freely through the sample causing a measured low total DC-conductivity. The grains themselves, however, exhibit still a high conductivity due to the donor doping. Such a scenario with insulating grain boundaries and highly conductive grains could explain the observed high Fermi level position in donor doped $NaNbO_3$ with a low measured total DC-conductivity.

Grain boundary contributions are also observed in $BaTiO_3$. For low doping concentrations a high conductivity is obtained whereas for increasing donor concentration the conductivity decreases again [22, 37, 38, 292, 293]. With La-doping, for example, a low resistivity of $1\,\Omega\,\mathrm{cm}$ is achieved by adding $0.10\,\mathrm{mol\,\%}$ to $0.25\,\mathrm{mol\,\%}$ lanthanum. Below $0.1\,\mathrm{mol\,\%}$ the dopants are compensated by electrons. With increasing doping concentration, however, the dopants are compensated by intrinsic defects such as barium vacancy (V''_{Ba}) or titanium vacancy (V''''_{Ti}). These cation vacancies can segregate to the grain boundaries during sintering and form potential barriers hindering the electrons from moving [37, 38, 293]. Fig. 6.20 illustrates the different situations for low and high doping concentrations in $BaTiO_3$.

Such a grain boundary effect is also used in varistors [21]. Varistors show a low conductivity until a certain threshold field at which the potential barriers at the grain boundaries are reduced enough in order to allow for electrons to flow. A sudden increase in conductivity appears as a consequence. For $Na_{0.99}Ca_{0.01}NbO_3$ and $Na_{0.99}Sr_{0.01}NbO_3$ such a varistor effect is not observed (see Fig. 5.11 in Section 5.5). The question is, if the applied electric field was high enough to lower the potential barriers at the grain boundaries and allow for a high electron flow. This can be verified by calculating the voltage applied at each grain boundary. With highly conductive grains and insulating grain boundaries it can be assumed that the voltage drops only across the grain boundaries. Then the voltage built up at the grain boundaries V_{GB} can be calculated by the maximum electric field applied before break down E_{max} and the grain size d_{grain}:

$$V_{GB} = E_{max} \cdot d_{grain} \tag{6.1}$$

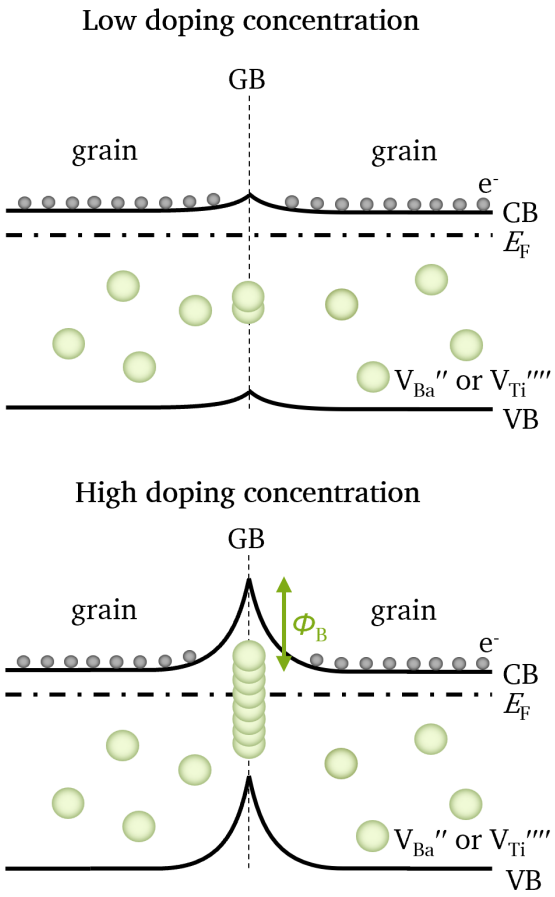

Figure 6.20.: Band diagram at a grain boundary (GB) for a low (top) and a high donor doping concentration (bottom).

In case of $Na_{0.99}Ca_{0.01}NbO_3$ and $Na_{0.99}Sr_{0.01}NbO_3$, a voltage of $6\,\mathrm{V}$ per grain boundary is reached during the conductivity measurements. The threshold voltage at which a significant conductivity increase is observed, is $0.1\,\mathrm{V}$ to $1.0\,\mathrm{V}$ per grain boundary in $BaTiO_3$ or $(Ba,Sr)TiO_3$ [294, 295].

Commercial available ZnO varistors exhibit a breakdown voltage of 3 V per grain boundary [21, 84]. Therefore, it is assumed that the threshold voltage for a varistor effect should have been reached in donor-doped $NaNbO_3$. Consequently, the mismatch between a low electrical conductivity and a high Fermi level located close to the conduction band cannot be explained by grain boundary contributions and a varistor effect.

The low measured conductivity implies that the Fermi level cannot be located close to the nominal conduction band. Hence, the fundamental electrical band gap $E_{G,el}$ of $NaNbO_3$ must be larger than the nominal band gap $E_{G,nom}$ determined by EELS and other optical methods. The lower nominal band gap might be a measure for the distance between the VBM and another in-gap trap state. Figure 6.21a) shows the the difference in the band structure of $NaNbO_3$ by taking $E_{G,nom}$ or $E_{G,el}$ as the real band gap value. From this picture it is clear that the measured Fermi level is most likely further away from the CBM and pinned by a trapping state, which results in a low electrical conductivity.

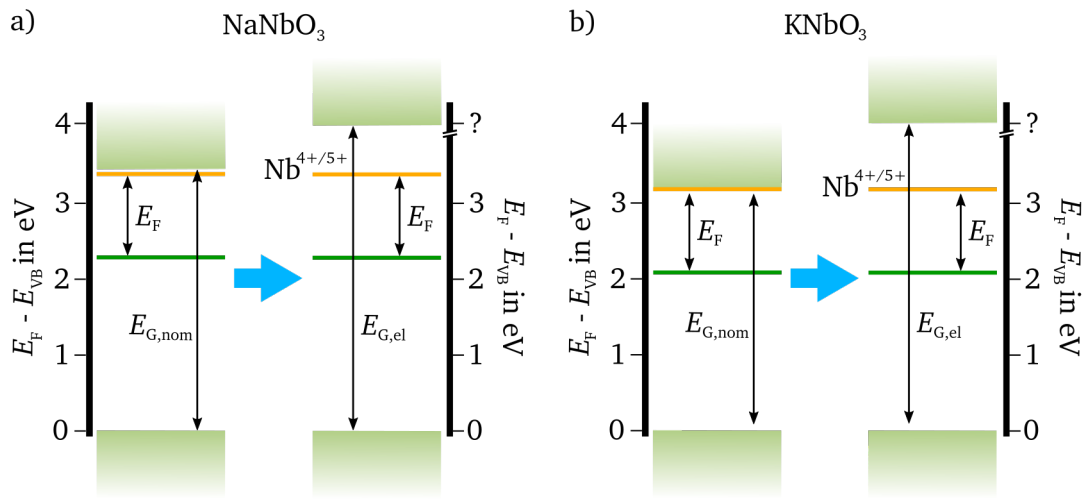

Figure 6.21.: Preliminary and new proposed band structure of $NaNbO_3$ in a) and $KNbO_3$ in b) with nominal band gap $E_{G,nom}$ determined by optical measurements and electrical band gap $E_{G,el}$, respectively. The accessible Fermi level range and the $Nb^{4+/5+}$ polaron state are marked as well.

A similar situation applies for $LiNbO_3$ in which the fundamental band gap, the difference between occupied valence and empty conduction band, is 1 eV larger than the band gap measured by optical spectroscopy. This conclusion is derived from Green's function G and dynamical screened interaction W (GW) calculations and explained by quasiparticle properties [296, 297]. During optical measurements an electron is excited from the valence to the conduction band and creates an electron hole in the valence band. These two charges can interact with each other because of their Coulomb

forces by forming a so-called exciton. The exciton formation lowers the energy of the excited electron leading to a smaller measured band gap. Consequently, methods which determine the band gap of a material by electron excitation, e.g. optical spectroscopy, XPS, or EELS measurements, do not properly evaluate the band gap of $LiNbO_3$ due to these strong electron-hole-interactions. In this thesis it is assumed that a similar consideration for $NaNbO_3$ can be made. This would be quite reasonable as $LiNbO_3$ and $NaNbO_3$ have a similar electronic structure. Both materials exhibit highly localized Nb $4d$-states at the conduction band minimum [296, 298]. Therefore, the creation of a polaron on the Nb-site has to be taken into account as well. Instead of an exciton, a polaron such as $Nb^{4+/5+}$ could trap the excited electron. Hence, the nominal band gap would reflect the energetic distance of the $Nb^{4+/5+}$ charge transition level to the VBM. This consideration is quite legitimate as a reduction of Nb^{5+} to Nb^{4+} has already been observed for Nb_2O_5 [299–302] and is also detected in $NaNbO_3$ in this thesis, which is shown in Fig. A.23 in the appendix and is further discussed in Section 8. Thus, a polaron formation on the Nb-site is assumed to pin the upper Fermi level limit here, which is indicated in Fig. 6.21a).
Nevertheless, we should not neglect that with some of the oxidizing and reducing methods including the interfaces to RuO_2 and ITO the maximum or minimum accessible Fermi level might not be reached because the maximal possible band bending has already been employed. This means that, for example at the ITO and/or RuO_2 interface the Fermi level cannot be shifted further, hence, is not representing the real Fermi level limitations. Whether or not this is true can be checked by using a more reducing or oxidizing method. Heating in forming gas might lead to a higher reduction of the sample, but this can only be done ex-situ in our laboratories so far. An interface formation to CoO_x or NiO can introduce a higher band bending, hence, shifting the Fermi level closer to the VBM, which was shown for $BiVO_4$ [241] and Fe_2O_3 [80]. Therefore, it could be verified by an interface experiment to one of these two materials if the Fermi level is pinned due to an trapping state at 2.3 eV or if it can be shifted further, which would mean that the maximal achievable Fermi level shift is reached with RuO_2 at 2.3 eV. However, these considerations do not affect the hypothesis that the fundamental band gap in $NaNbO_3$ must be larger than the measured nominal one.

Unfortunately, no doped $KNbO_3$ samples were prepared in this work, hence, it is not clear whether donor doped $KNbO_3$ exhibits a low or a high electrical conductivity. However, a larger fundamental band gap of 3.63 eV compared to the nominal band gap of 3.2 eV [121, 126, 127, 164–167] was determined by GW calculations [163]. These calculations of Schmidt et al. [163] show that the optical band gap is significantly reduced by a trapping state located 0.4 eV below the CBM. Therefore, we can assume that a similar picture as for $NaNbO_3$ can be applied. Figure 6.21b) illustrates the transition from a band structure with $E_{G,nom}$ determined by optical spectroscopy to the one with $E_{G,el}$ representing the fundamental band gap. The trapping state limiting the maximum reachable Fermi level could be either an exciton or a polaron on the Nb-site. In this thesis, a $Nb^{4+/5+}$ polaron state is assumed to be the trapping state as for $NaNbO_3$. Hence, the same considerations as for $NaNbO_3$

apply then for $KNbO_3$.

6.7. Electronic structure - Summary

In this chapter, the electronic structure of $NaNbO_3$- and $KNbO_3$-based materials have been mainly investigated by means of XPS analysis. Sample composition, contamination, band gap, surface effects, interface experiments, and Fermi level limitations have been evaluated in order to propose a possible band structure. Important observations, results, and conclusions are summarized in the following.

Table 6.2.: Main results of the electronic structure of $NaNbO_3$ and $KNbO_3$ including surface composition, contamination level, nominal and electrical band gap, and Fermi level limitations.

	pure $NaNbO_3$	**changes induced by Ca- and Sr-doping**	**pure $KNbO_3$**
surface composition	sodium deficient $NaNbO_3$ surface with possible overlaying sodium oxide layer	reduction of sodium deficiency but detectable calcium segregation towards the surface	enriched potassium $KNbO_3$ surface with possible overlaying potassium oxide layer
contamination	small traces of iron, potassium, and silicon	additional calcium segregation in $Na_{0.99}Sr_{0.01}NbO_3$	small traces of silicon
nominal band gap measured by optical spectroscopy	3.5 eV	none	3.2 eV [121, 126, 127, 164–167]
electrical band gap determined by GW calculations	?	?	3.63 eV [163]
Fermi level limitations	maximum and minimum Fermi level limit of 3.4 eV and 2.3 eV		maximum and minimum Fermi level limit of 3.2 eV and 2.1 eV

A high Fermi level range close to the CBM is also observed for $BaTiO_3$. Donor doped $BaTiO_3$ with a low doping concentration shows a high conductivity of $1\,S\,cm^{-1}$ and a Fermi level around the CBM. Hence, a similar situation is expected for $NaNbO_3$. However, for donor doped $NaNbO_3$ a low conductivity below $5 \times 10^{-10}\,S\,cm^{-1}$ is detected. A varistor effect with insulating grain boundaries and highly conductive grains can be excluded. One possible reason for this discrepancy could be that the electrical band gap is much larger than the nominal band gap determined by optical methods. The nominal band gap could be smaller due to a polaron formation trapping the excited electrons. Therefore, the nominal band gap represents the distance between VBM and electron polaron state, which could be located on the Nb-site. Similar conclusions are made for $LiNbO_3$ [296, 297] and $KNbO_3$ [163] by means of GW calculations. A $1.0\,eV$ and $0.5\,eV$ smaller optical band gap compared to the electrical band gap is found in $LiNbO_3$ and $KNbO_3$, respectively. With these considerations following hypothesis for the band structure of $NaNbO_3$ and $KNbO_3$ can be formulated.

Hypothesis

- → The electrical band gap of $NaNbO_3$- and $KNbO_3$-based materials is much larger than the nominal band gap determined by optical spectroscopy
- → The nominal band gap is reduced due to an electron polaron state on the Nb-site, which results in a reduction of the niobium ion from Nb^{5+} to Nb^{4+}

In the next chapter the transport properties and resistance degradation of $NaNbO_3$ and $KNbO_3$ are analyzed. On the ground of these results, the proposed hypothesis of the band structures is validated and elaborated in chapter 8.

7. Transport properties and degradation

Within this chapter important results of electrical AC- and DC-conductivity measurements as well as XPS-experiments combined with electrical conductivity and temperature analysis are described and examined for the further investigation of transport properties and electrical degradation behavior. In this part, the results are mainly presented. However, the discussion and integration of the observations into the band structure model introduced in the previous chapter is done in chapter 8. Hence, the aim of this chapter can be summarized as following.

This chapter has the aim to ...

- ... describe and analyze the results of the electrical conductivity experiments in dependence of frequency, temperature, atmosphere, electric field, and time.
- ... show the difference between AC- and DC-measurements.
- ... illustrate differences in the electrical conductivity of undoped and doped $NaNbO_3$ as well as $NaNbO_3$ and $KNbO_3$ samples.
- ... identify possible mobile charge carriers responsible for the observations.

For this purpose, DC- and AC-conductivity results at different temperatures and oxygen partial pressures are shown. Obtained activation energies are presented. Afterwards, differences between DC- and AC-experiments are worked out.
The degradation behavior meaning the combined influence of temperature and electric field on the conduction mechanism is analyzed by means of DC-measurements. These analyses are complemented by XPS investigations of a $Na_{0.99}Ca_{0.01}NbO_3$ sample with an ITO-electrode either as anode or cathode while applying an electric field and heating within the XPS-chamber.
In order to identify possible ionic diffusion processes, post-annealing experiments in a low pressure oxygen atmosphere and vacuum after ITO deposition are described. Furthermore, with these measurements the stability of sample and electrode material is examined.

7.1. DC-conductivity

In this section the measured DC-conductivity of all different ceramic sample types is analyzed. First, the dependence on temperature is examined followed by the influence of the gas atmosphere. Finally, relaxation experiments are investigated.

7.1.1. Influence of temperature

As illustrated in Section 4.11.2 the conductivity was measured at constant voltage of $0.1\,\mathrm{V}$ and $1.0\,\mathrm{V}$ by turning the temperature up to at least $500\,^{\circ}\mathrm{C}$ with a heating rate of $1\,\mathrm{K\,min^{-1}}$ in dry air for $NaNbO_3$- and $KNbO_3$-based ceramic samples, respectively. Figure 7.1 shows all conductivity cycles in air for pure $NaNbO_3$ (blue), Ca- (yellow) and Sr-doped $NaNbO_3$ (red), and $KNbO_3$ (green). All different phases appearing in the examined temperature range are illustrated at the top of each graph. The transition temperatures extracted from the permittivity data in Fig. 5.12 and 5.13 are indicated by gray dotted lines. Some transitions as the P-R-phase transition for $NaNbO_3$ or the O-T-phase transition for $KNbO_3$ exhibit different transition temperatures for the heating and cooling cycle. Therefore, a transition regime is marked in these cases. The R-S-phase transition cannot be determined by the permittivity curves in case of $Na_{0.99}Sr_{0.01}NbO_3$. Hence, the corresponding transition temperature is labeled with a question mark. For $Na_{0.99}Ca_{0.01}NbO_3$ conductivity values extracted from relaxation experiments, which will be analyzed in Section 7.1.2, are plotted for comparison as well. These data fit quite nicely with the measured loops indicating that there is no need for waiting until the conductivity is relaxed in order to determine activation energies.

At low temperatures the measured data points get very noisy, which can be explained by small currents below $1 \times 10^{-12}\,\mathrm{A}$ reaching the limit of the picoamperemeter. In the case of undoped $NaNbO_3$, the signal noise stays until $250\,^{\circ}\mathrm{C}$. The reason is the larger thickness of this sample compared to the other samples resulting in lower currents.
All samples show a higher conductivity within the first loop. From the second cycle on the conductivity seems to be relaxed and reproducible for all following loops. Only for undoped $NaNbO_3$ and $KNbO_3$ a small decrease in conductivity with cycle number can be observed, which will be analyzed in more detail in Section 7.1.2. In addition, the $NaNbO_3$-based samples exhibit a minimum at around $300\,^{\circ}\mathrm{C}$ to $350\,^{\circ}\mathrm{C}$. This is close to the temperature where the transition from P- to R-phase appears. This minimum comes along with a change in slope meaning a change in activation energy. All activation energies are investigated in Section 7.3 and compared to the values obtained by the AC-measurements. Furthermore, it can be noticed that pure $NaNbO_3$ has the highest conductivity of around $5.0 \times 10^{-6}\,\mathrm{S\,cm^{-1}}$ at $500\,^{\circ}\mathrm{C}$ followed by $Na_{0.99}Ca_{0.01}NbO_3$ with $2.5 \times 10^{-7}\,\mathrm{S\,cm^{-1}}$ and $Na_{0.99}Sr_{0.01}NbO_3$ with $1.0 \times 10^{-7}\,\mathrm{S\,cm^{-1}}$. $KNbO_3$ exhibits a slightly lower value of $1.0 \times 10^{-6}\,\mathrm{S\,cm^{-1}}$ than $NaNbO_3$. It is interesting that undoped $NaNbO_3$ has the highest conductivity at $500\,^{\circ}\mathrm{C}$ while at

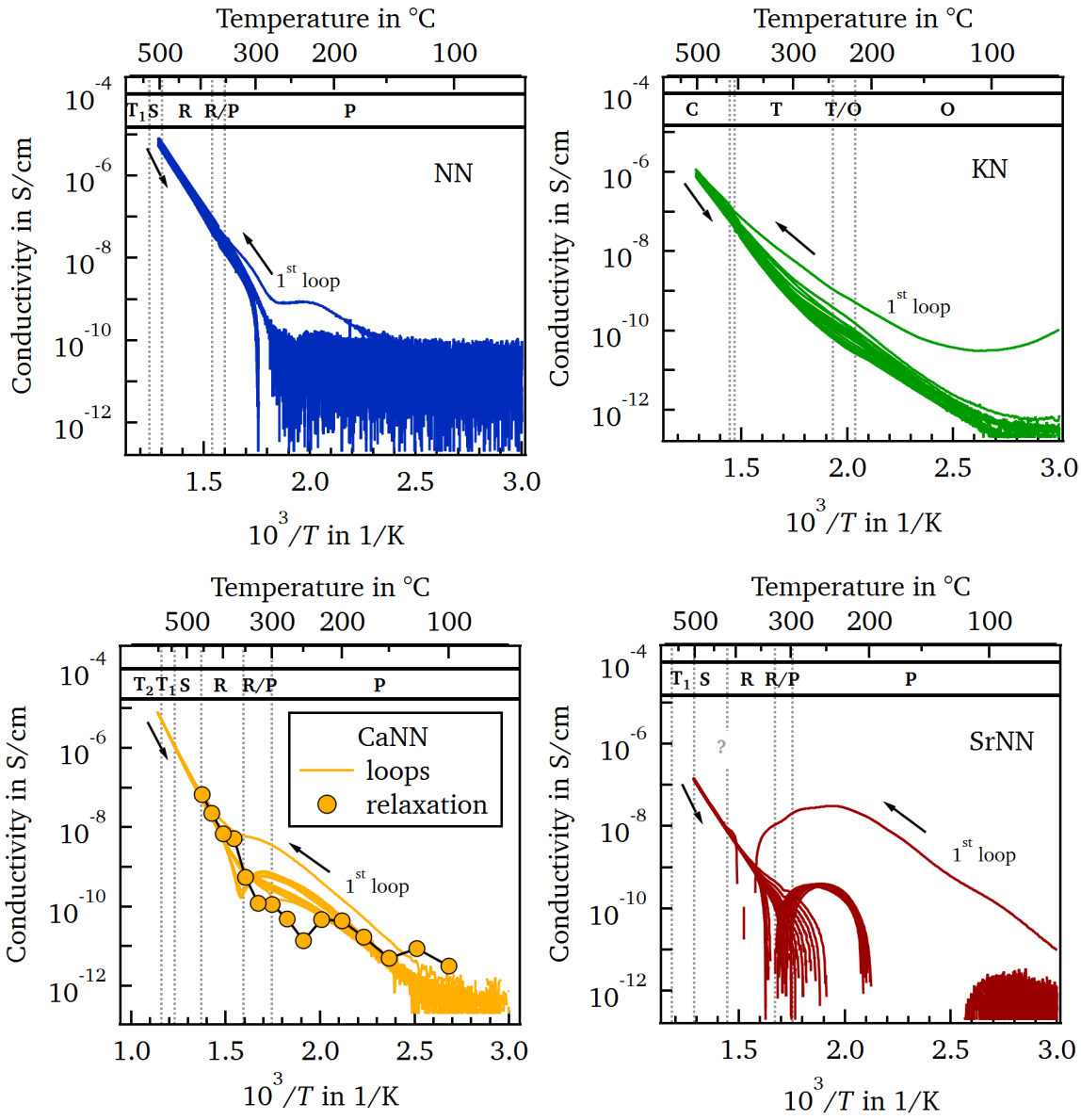

Figure 7.1.: Conductivity-vs-temperature-loops measured in dry air for pure $NaNbO_3$ (blue) and $KNbO_3$ (green), $Na_{0.99}Ca_{0.01}NbO_3$ (yellow), and $Na_{0.99}Sr_{0.01}NbO_3$ (red). All phases appearing in the investigated temperature range are included. The corresponding transition temperatures (gray dotted lines) are determined from the permittivity data for each material shown in Fig. 5.12 and 5.13. The R-S-transition temperature for $Na_{0.99}Sr_{0.01}NbO_3$ could not be identified and is marked with a question mark. Arrows indicate the heating and cooling direction of the first loop. For $Na_{0.99}Ca_{0.01}NbO_3$ additional data points extracted from relaxation experiments are included.

room temperature it shows the lowest (see Section 5.5). The values are listed in Table 7.1 for later comparison.

7.1.2. Influence of atmosphere

After measuring five to ten conductivity loops as a function of temperature in air, the atmosphere was changed to pure nitrogen, which led to a reduction of the oxygen partial pressure to 0.8×10^{-5} bar as described in Section 4.11.2. Both cycles recorded in air (dark blue) and nitrogen (orange), are displayed in the top row of Fig. 7.2 for all four different samples. It is observed that the conductivity at high temperatures is decreasing in nitrogen for the undoped $NaNbO_3$ and $KNbO_3$ sample while for the doped $NaNbO_3$ materials it is increasing. This is a first indication that, without doping, the samples exhibit a p-type behavior whereas with donor doping the conduction mechanism changes to n-type. In nitrogen the conductivity of the undoped samples is continually decreasing with cycle number, while for $Na_{0.99}Ca_{0.01}NbO_3$ it is continuously rising, which is shown by small arrows in Fig. 7.2. By having a closer look at the $Na_{0.99}Sr_{0.01}NbO_3$ sample it can be noticed that the conductivity is first increasing and then lowering again from cycle to cycle when the atmosphere is changed from air to nitrogen, which is marked by the arrow.

After a few cycles in nitrogen the atmosphere was changed back to dry air. The corresponding conductivity loops are shown in light blue in the top row of Fig. 7.2. The doped $NaNbO_3$ samples reach more or less directly the original conductivity in air at high temperatures as measured before. In contrast, at temperatures below $400\,°C$ a larger deviation to the loops recorded in air before the nitrogen treatment is observed. For the undoped materials the conductivity value at maximum temperature is not reached again indicating a possible change in the defect concentration of the sample. This behavior is more pronounced for $NaNbO_3$ than for $KNbO_3$.

In the bottom row of Fig. 7.2 the last recorded loop of each measurement is illustrated. Here, it can be seen more clearly that for $Na_{0.99}Ca_{0.01}NbO_3$ and $Na_{0.99}Sr_{0.01}NbO_3$ the conductivity examined in air before and after the nitrogen treatment are almost the same while for pure $NaNbO_3$ it is different. Furthermore, arrows elucidate the heating and cooling direction of the loops. Although the behavior with increasing cycle number is different, all samples show a hysteresis in air as well as in nitrogen, which is more pronounced for some cycles than for others. Thereby, the cooling cycle is always higher in conductivity than the heating cycle.

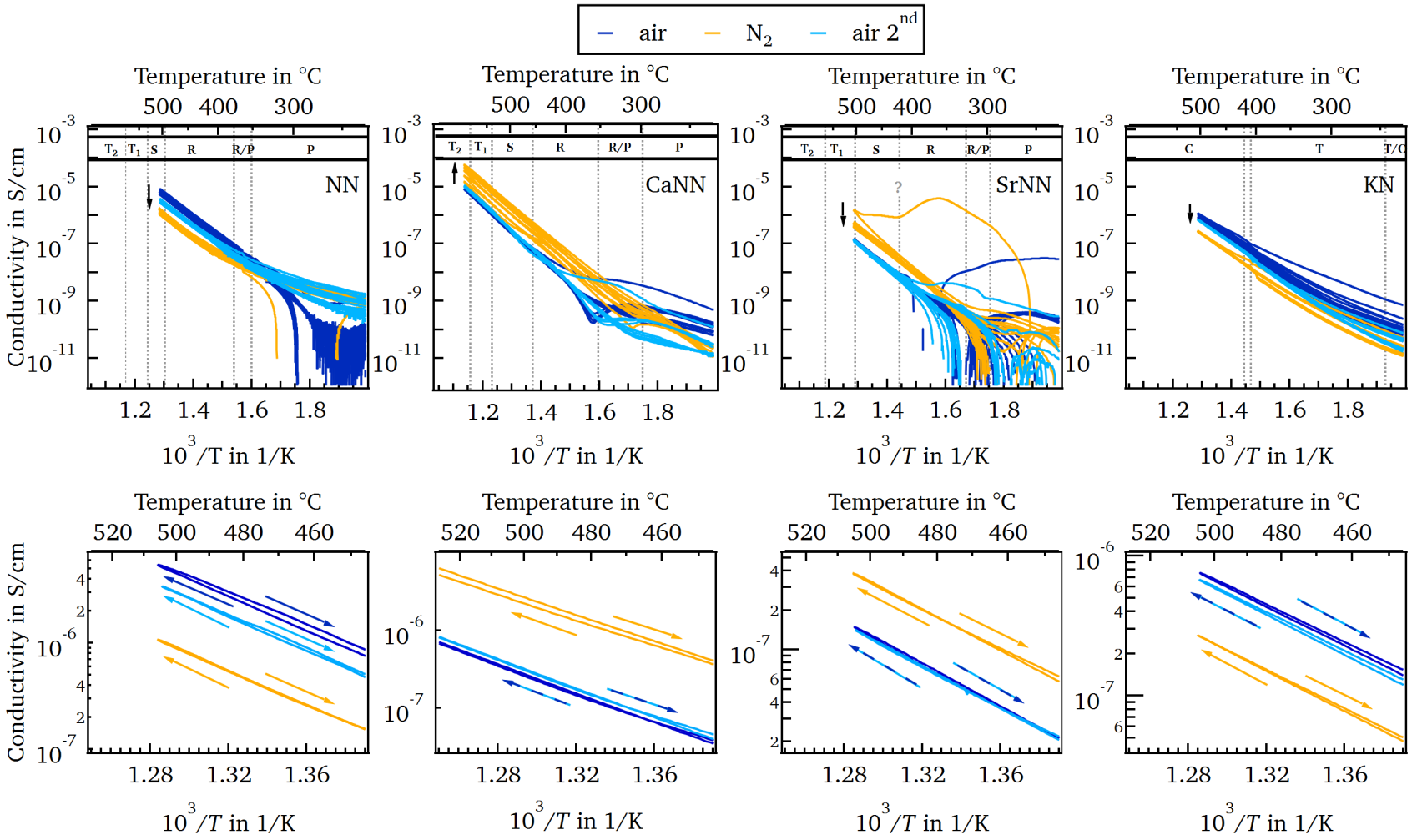

Figure 7.2.: Conductivity-vs-temperature-loops in dry air (blue) and nitrogen atmosphere (orange). Top: All measured cycles are illustrated. All phases appearing in the investigated temperature range are included as explained in the caption of Fig. 7.1. Arrows indicate the direction of conductivity with increasing cycle number. Bottom: The last cycle for the different atmospheres are shown. Arrows indicate heating/cooling directions of the small temperature hystereses.

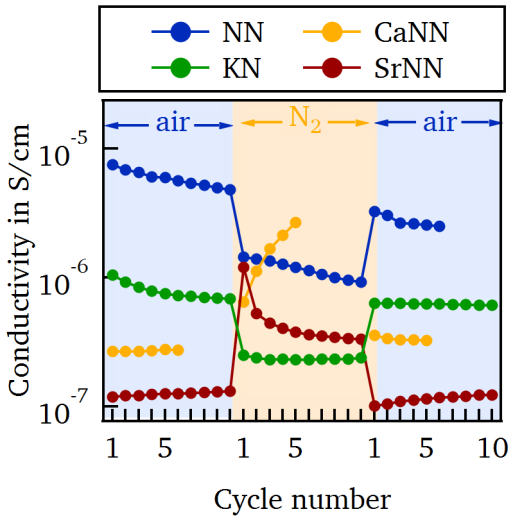

Figure 7.3.: Conductivity at 500 °C in dependence of the cycle number in air (blue) and nitrogen atmosphere (orange).

The development of the conductivity with cycle number can be seen more clearly in Fig. 7.3. For undoped $NaNbO_3$ the conductivity is decreasing with cycle number in both air and nitrogen. In contrast, for donor doped $NaNbO_3$, the conductivity in dry air is not changing much with time. In case of $Na_{0.99}Sr_{0.01}NbO_3$ it is even slightly increasing. The relaxation behavior in nitrogen seems to be different for $Na_{0.99}Ca_{0.01}NbO_3$ compared to $Na_{0.99}Sr_{0.01}NbO_3$. Here, the conductivity is increasing and has not reached its equilibrium after five cycles. On the contrary, $Na_{0.99}Sr_{0.01}NbO_3$ shows a lowering of the conductivity and has come to an equilibrium value after ten loops. For $KNbO_3$ there is no clear change in conductivity with the cycle number, except for the first measurement set in air exhibiting a small decrease in conductivity. Furthermore, Fig. 7.3 illustrates clearly the p- and n-type character of pure and donor doped samples, respectively.

7.1.3. Influence of time - Relaxation experiments

Finally, the relaxation behavior in dry air and in nitrogen is examined. The experiments were performed as described in Section 4.11.3 with a small voltage signal ranging from 0.05 V to 0.3 V in order to avoid any possible degradation of the sample. As the time until an equilibrium value is reached can take quite long (sometimes several days), it was only possible to investigate one material in this work, which is $Na_{0.99}Ca_{0.01}NbO_3$.

The relaxation behavior was recorded for temperatures ranging from 100 °C to 560 °C. However, for the sake of clarity, six different temperatures are chosen for representation. Figure 7.4 illustrates relaxation curves at 350 °C, 400 °C, 460 °C, 470 °C, 540 °C, and 560 °C. The parts measured in air and nitrogen are colored in blue and orange, respectively. For better analysis, the curves are plotted in three different graphs with different conductivity ranges and time axis scaling. Between temperatures 350 °C and 400 °C, 400 °C and 460 °C, and 470 °C and 540 °C more relaxation steps were performed. The relaxation experiments at 460 °C and 470 °C, and 540 °C and 560 °C were conducted consecutively. It should be mentioned that the measurements were examined on two different samples. Sample NB153 was analyzed at 350 °C and 400 °C while the other temperature ranges were investigated on sample NB136. Furthermore, the flow rate was kept constant at 5 sccm and the oxygen partial pressure was set to 5×10^{-3} bar in nitrogen atmosphere for sample NB136 whereas

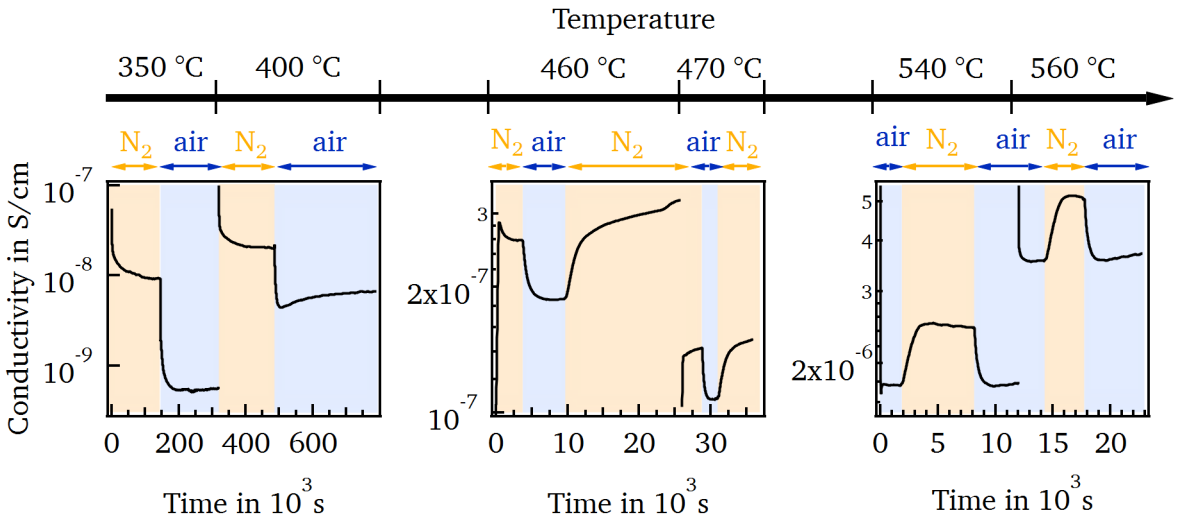

Figure 7.4.: Relaxation experiments of two $Na_{0.99}Ca_{0.01}NbO_3$ samples. Regions measured in dry air and nitrogen are colored in blue and orange, respectively. The temperature line indicates the temperature at which the relaxation curves were performed. Measurements at $350\,°C$ and $400\,°C$ were conducted on sample NB153. All other experiments were executed on sample NB136.

in case of sample NB153 the flow was increased to 50 sccm while the oxygen partial pressure was lowered to 8×10^{-6} bar. The reason for these different used oxygen partial pressures is that it was not sure how the samples would react under reducing conditions. Hence, the first experiments in nitrogen atmosphere were performed at higher oxygen partial pressure (sample NB136). Later the oxygen partial pressure was lowered to the minimum accessible oxygen content by the measurement setup (sample NB153).

From Fig. 7.4 it can be seen that the conductivity is subsequently increasing with temperature, except for the set measured at $470\,°C$. It is not clear why this is the case. For every temperature, the conductivity is always higher in nitrogen than in air and it is subsequently decreasing/increasing when changing the atmosphere from nitrogen to air/air to nitrogen. Furthermore, it seems that equilibrium is much faster obtained in air than in nitrogen indicating that oxygen incorporation is faster than oxygen excorporation. These observations match with the ones made in the previous section (see Fig. 7.3).

Having a closer look at the parts performed in air it is noticeable that, at some temperatures, the conductivity is increasing again after reaching a minimum value. This phenomenon can be observed best at $400\,°C$ and $560\,°C$. A more detailed view is shown in Fig. 7.5.

At $400\,°C$ four different regimes can be identified. On the left side of Fig. 7.5 a magnified view of the first $2000\,s$ is presented. Here, a rapid increase can be seen indicated by (0) followed by a fast decay in conductivity marked by (1). Afterwards, the conductivity drops with a different slope indicated by

(2). On the whole measured time scale illustrated on the right side of Fig. 7.5, a fourth mechanism dominates the conduction behavior, which is labeled with (3).

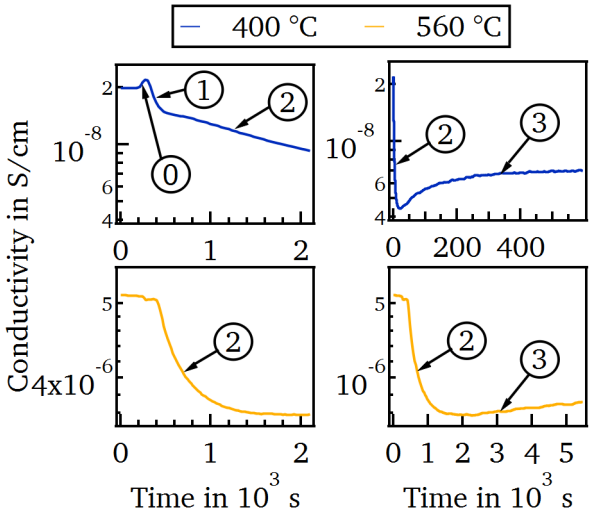

Figure 7.5.: Relaxation curves in dry air changing the atmosphere from nitrogen. The numbers mark different mechanisms appearing during the measurement. Left: magnified view. Right: complete measurement.

At 560 °C mechanisms (0) and (1) are not observed. Furthermore, mechanism (2) is decaying more rapidly and contribution (3) establishes on a shorter time scale. One difference between these two measurements is the lower oxygen partial pressure of 8×10^{-6} bar and the higher flow of 50 sccm used in nitrogen at 400 °C prior to the curve recorded in dry air. The relaxation experiments from 460 °C to 560 °C are measured all with a constant flow rate of 5 sccm in air and nitrogen and a higher oxygen partial pressure of 5×10^{-3} bar when measuring in nitrogen. None of these curves exhibit mechanism (0) and (1). Therefore, it seems that the higher nitrogen flow and the lower oxygen partial pressure are responsible for the appearance of contribution (0) and (1). However, it should be kept in mind that two different $Na_{0.99}Ca_{0.01}NbO_3$ samples were examined.

Contribution (2) and (3) are visible at all temperatures and can most likely be attributed to two different diffusing species such as oxygen and sodium. Oxygen is a well known mobile species in oxide materials, which can diffuse already at very low temperatures down to 100 °C [303]. In addition, it will be shown in Section 7.4.3 that sodium is diffusing at temperatures above 300 °C.

A similar temporal development of the conductivity as in this thesis was observed for ITO [304]. The authors explain the non-monotonic decrease of the carrier concentration with overlapping contributions from oxygen and tin diffusion. An other possible explanation for mechanism (2) and (3) would be the simultaneous diffusion of oxygen in the bulk and along grain boundaries, which exhibit different diffusion coefficients. However, due to the above mentioned observations indicating two diffusing species, it is assumed that a coincident transport of oxygen and sodium ions is appearing in sodium niobate.

Diffusion coefficients in air are extracted for mechanism (2) from the corresponding curves in Fig. 7.4 as explained in Section A.3.1 in the appendix. Contribution (3) is not easily seen at all temperatures,

hence, no diffusion coefficient is calculated. In order to evaluate it, longer measurement times are necessary. The diffusion coefficients of mechanism (2) are shown as well in Section A.3.1 in the appendix. Here, the diffusion coefficients obtained from the AC-experiments are illustrated, too. However, DC- and AC-methods determine different type of diffusion coefficients, which cannot be really compared with each other. Nevertheless, the diffusion coefficients are shown for completeness in the appendix of this thesis. In addition, the reason why the DC- and AC-investigations elucidate different diffusion behaviors is explained in more detail in the appendix.

7.2. AC-conductivity

Impedance measurements are described and analyzed in this section. First, impedance data illustrated as Nyquist plots are evaluated. Afterwards, the extracted conductivity values from the Nyquist plots are investigated in dependence of temperature.

The impedance of undoped, Ca- and Sr-doped $NaNbO_3$, and $KNbO_3$ was measured within a temperature range of $125\,°C$ to $600\,°C$ in air. Figure 7.6 shows the Nyquist plots of all samples at $250\,°C$, $425\,°C$, and $500\,°C$. At $250\,°C$ one semicircle is observed for all samples. For $NaNbO_3$ and $Na_{0.99}Ca_{0.01}NbO_3$ this semicircle is very symmetric. At lower frequencies a small tail indicating a second contribution is emerging for both samples. $Na_{0.99}Sr_{0.01}NbO_3$ and $KNbO_3$ do not show such a tail. However, the semicircle is more asymmetric towards lower frequencies, which is more pronounced for $Na_{0.99}Sr_{0.01}NbO_3$. With increasing temperature the tail in the impedance plot of undoped $NaNbO_3$ has further increased. This is not the case for $Na_{0.99}Ca_{0.01}NbO_3$ but a third contribution at medium frequencies develops at $425\,°C$. The semicircle of $Na_{0.99}Sr_{0.01}NbO_3$ gets more symmetric with temperature. In addition, a second contribution at low frequencies appears.
At $500\,°C$ one half of the semicircle of the second contribution of the $NaNbO_3$ ceramic sample can be observed. In case of $Na_{0.99}Ca_{0.01}NbO_3$, the third component is clearly visible. Therefore, $Na_{0.99}Ca_{0.01}NbO_3$ showing three contributions seems to be quite different compared to the other samples. In contrast, the Nyquist plot of $Na_{0.99}Sr_{0.01}NbO_3$ and $KNbO_3$ are not much changed from $425\,°C$ to $500\,°C$.

All samples exhibit at least two contributions, which are more pronounced in case of $NaNbO_3$ and $Na_{0.99}Ca_{0.01}NbO_3$. For the $NaNbO_3$-based samples this second contribution appears as a tail at low frequencies while for $KNbO_3$ it is present in the asymmetry of the semicircle. $Na_{0.99}Ca_{0.01}NbO_3$ is the only sample showing a third component.
The intercept of a semicircle with the Z'-axis corresponds to the resistance of this process. From Fig. 7.6 it can be seen that this value is decreasing with temperature for all samples meaning a lowering in resistance of the main component for all samples.

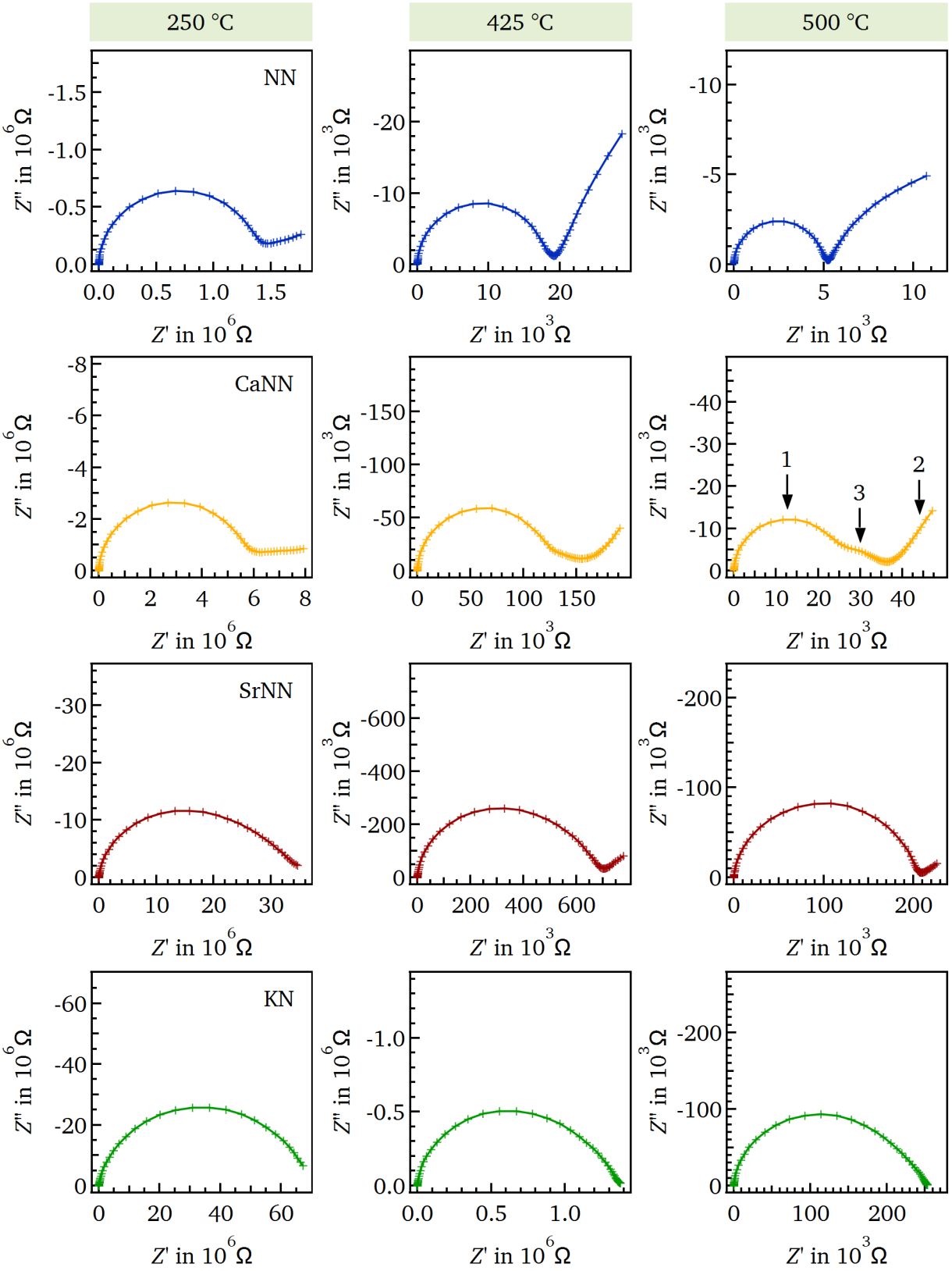

Figure 7.6.: Nyquist plots for pure $NaNbO_3$ (blue) and $KNbO_3$ (green), $Na_{0.99}Ca_{0.01}NbO_3$ (yellow), and $Na_{0.99}Sr_{0.01}NbO_3$ (red) at $250\,°C$, $425\,°C$, and $500\,°C$.

Figure A.19 in the appendix displays the frequency dependence of Z'' and M'' for the corresponding Nyquist plots in Fig. 7.6. All samples exhibit one clear maximum for both, Z'' and M''. The maxima are located at the same frequency for each temperature. In addition, they are shifting towards higher frequencies and are decreasing in height with increasing temperature. In case of the $NaNbO_3$-based samples the onset of a second maximum develops at low frequencies and higher temperatures in the Z''-plot. This cannot be observed for $KNbO_3$.
At $500\,°C$ a shoulder appears on the lower frequency side of the Z'' maximum for $Na_{0.99}Ca_{0.01}NbO_3$. This can most likely be attributed to the third contribution seen in the Nyquist plot.
The height of the Z''-maximum is proportional to the resistance of the corresponding process. As it is decreasing with temperature, the resistance gets smaller with temperature. This observation agrees with the reduced radius of the main contributions in the Nyquist plots with increasing temperature. Furthermore, the overlap of the Z'' and M'' maxima in frequency might be an indication that the samples are dominated by a long range conduction process [46].

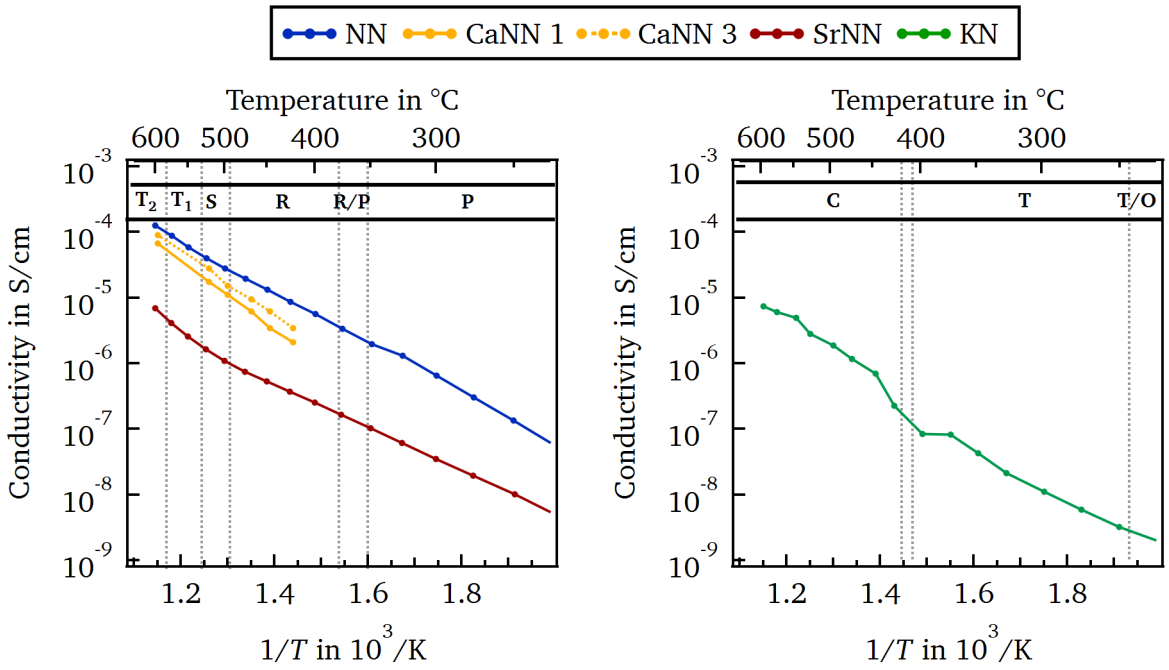

Figure 7.7.: Conductivity determined by the impedance data as a function of temperature. For $Na_{0.99}Ca_{0.01}NbO_3$ conductivity values of the main and the third component are plotted. All relevant phases are included as explained in the caption of Fig. 7.1.

Conductivity values are calculated by means of the resistances determined by the intercept of the semicircle with the Z'-axis in the Nyquist plots and by Eq. 3.10. Figure 7.7 illustrates these conductivity values as a function of temperature for the $NaNbO_3$-based samples on the left side and for $KNbO_3$ on the right side. All relevant phases are drawn in the corresponding graph. For $Na_{0.99}Ca_{0.01}NbO_3$ the conductivity of the third component is shown as well. As this contribution is appearing from

425 °C on, it is only possible to determine the conductivity from this temperature on.
The conductivity of undoped $NaNbO_3$ is the highest over the whole temperature range from 225 °C to 600 °C followed by $Na_{0.99}Ca_{0.01}NbO_3$ and $Na_{0.99}Sr_{0.01}NbO_3$. Values at 500 °C are listed in Table 7.1 for later comparison of AC- and DC-results. The slopes seem to be quite similar and are changing at the R-to-S-phase transition, hence, all samples exhibit similar activation energies. The activation energies will be shown in Section 7.3 and compared with the values obtained from the DC-experiments. The third component of $Na_{0.99}Ca_{0.01}NbO_3$ is slightly higher in conductivity than the main contribution. Furthermore, it has the same slope and activation energy. $KNbO_3$ exhibits a much lower AC conductivity than $NaNbO_3$ similar to the one of $Na_{0.99}Sr_{0.01}NbO_3$. The slope of the curve is also changing at the phase transition from tetragonal to cubic between 407 °C and 417 °C.

7.3. Comparison of DC- and AC-conductivity

In this section the results of DC- and AC-experiments are compared with each other. Subjects of the analysis are conductivity in dependence of temperature and activation energies.

In the two previous sections DC and AC conductivity-vs.-temperature-plots are shown illustrating that in both cases pure $NaNbO_3$ has the highest conductivity followed by $Na_{0.99}Ca_{0.01}NbO_3$ and $Na_{0.99}Sr_{0.01}NbO_3$. However, comparing conductivity values measured at 500 °C (see Table 7.1), it is noticeable that the conductivity examined by impedance are at least one order of magnitude higher than the ones determined by the DC-experiments for the $NaNbO_3$-based ceramics. In contrast, $KNbO_3$ exhibits approximately the same conductivity value at 500 °C for both, AC- and DC-measurements. In order to compare the activation energies, the conductivity multiplied by the temperature as function of temperature is illustrated in Fig. 7.8. DC- and AC-conductivity are represented by solid and dotted lines, respectively. For the DC-experiments, the last measured loop before changing the atmosphere is illustrated. The blue curves correspond to the cycles examined in air while the orange curve is the cycle performed in nitrogen.

Having a look at the DC-results, two regions with different activation energies are observed for $NaNbO_3$ and $KNbO_3$. $Na_{0.99}Sr_{0.01}NbO_3$ most likely exhibits a second part as well, however, at low temperatures no activation energies can be evaluated due to negative conductivity values. This is probably caused by a contact problem during the experiments resulting from the expansion and contraction of the sample while heating and cooling. $Na_{0.99}Ca_{0.01}NbO_3$ is the only material showing three activation energy regimes.

Table 7.1.: Conductivity values at room temperature and 500 °C in air for DC- and AC-experiments.

	$NaNbO_3$	$Na_{0.99}Ca_{0.01}NbO_3$	$Na_{0.99}Sr_{0.01}NbO_3$	$KNbO_3$
$\sigma_{RT,DC}$ in S cm^{-1}	$4.4 \cdot 10^{-14} - 3.3 \cdot 10^{-13}$	$1.6 \cdot 10^{-12} - 4.1 \cdot 10^{-10}$	$7.6 \cdot 10^{-13} - 2.9 \cdot 10^{-11}$	–
$\sigma_{500\,°C,DC}$ in S cm^{-1}	$5.0 \cdot 10^{-6}$	$2.5 \cdot 10^{-7}$	$1.0 \cdot 10^{-7}$	$1.0 \cdot 10^{-6}$
$\sigma_{500\,°C,AC}$ in S cm^{-1}	$2.8 \cdot 10^{-5}$	$1.1 \cdot 10^{-5}$	$1.1 \cdot 10^{-6}$	$1.9 \cdot 10^{-6}$

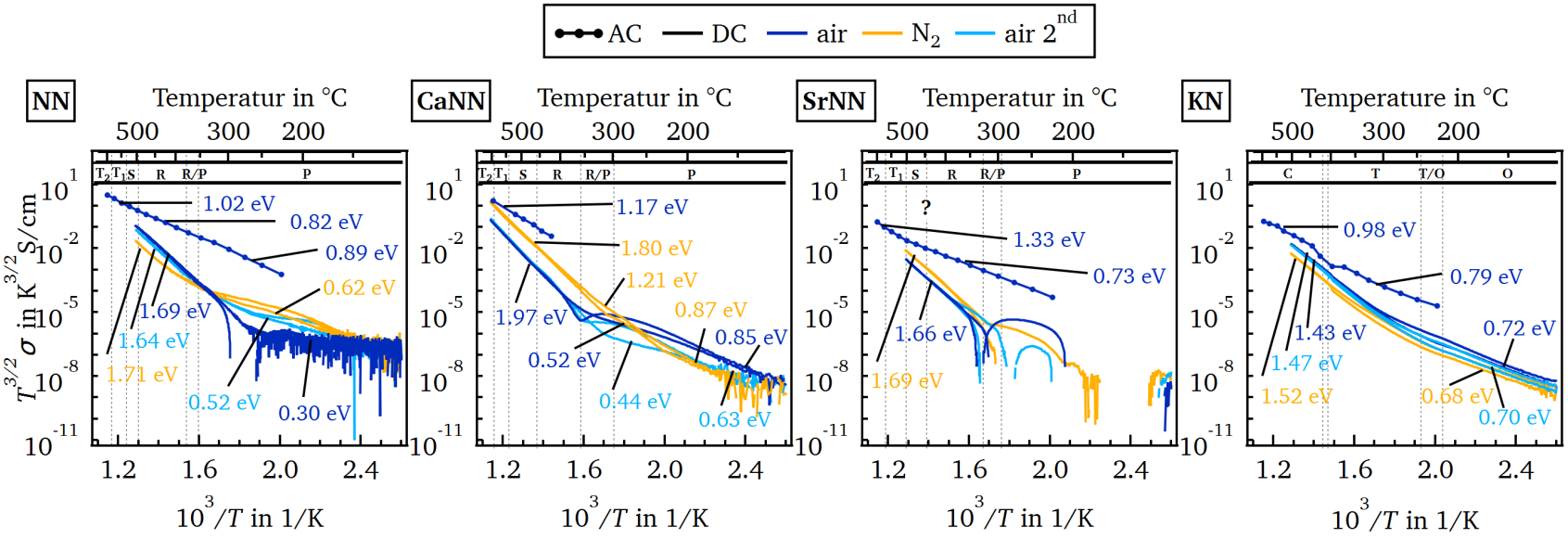

Figure 7.8.: Conductivity multiplied with $T^{3/2}$ as a function of temperature. The graphs include AC (dotted line) and DC results (solid line) measured in air (blue) and nitrogen (orange). Activation energies and phases are indicated for the corresponding temperature regimes.

At high temperatures in dry air atmosphere, the activation energies of $NaNbO_3$ and $Na_{0.99}Sr_{0.01}NbO_3$ are very similar with 1.69 eV and 1.66 eV whereas $Na_{0.99}Ca_{0.01}NbO_3$ exhibits a higher one of 1.97 eV. Changing the atmosphere to nitrogen has only a small effect on the activation energy of $NaNbO_3$ and $Na_{0.99}Sr_{0.01}NbO_3$, which is increasing to 1.71 eV and 1.69 eV, respectively. In contrast, it is decreasing from 1.97 eV to 1.80 eV in $Na_{0.99}Ca_{0.01}NbO_3$.
Below the P-R-phase transition the activation energies are reduced for the $NaNbO_3$-based samples. The values in dry air are again higher for $Na_{0.99}Ca_{0.01}NbO_3$ (0.52 eV) than for $NaNbO_3$ (0.30 eV). In nitrogen the activation energies are more than doubled. Changing the atmosphere back to dry air does not result in the same values as before.
Furthermore, it is very interesting that the conductivity curves are very different after annealing in nitrogen indicating an irreversible modification of the defect concentrations in the samples. Equally striking is the change from p- to n-type behavior for $NaNbO_3$ when cooling through the P-R-transition. As mentioned above, the activation energy of $Na_{0.99}Ca_{0.01}NbO_3$ is altered again below $200\,°C$. Here, the values are increased from 0.52 eV to 0.85 eV in dry air. In nitrogen the activation energies are gradually decreasing from 1.80 eV over 1.21 eV down to 0.87 eV over the whole temperature range.
It is concluded that these changes in activation energies are real alterations in the conduction mechanism and not due to a non-equilibrium state. Charging of the sample's capacitance can be excluded from the permittivity data described in Section 5.6. From these data the temperature dependent capacitance can be calculated. Combined with the temperature dependent DC-resistance a RC-value of 0.04 s, 0.50 s, and 1.3 s is determined at $300\,°C$, $150\,°C$, and $30\,°C$ for undoped $NaNbO_3$, respectively. Hence, charging of the capacitor should be fast enough and not affecting the temperature dependent conductivity measurements with a heating and cooling rate of $1\,K\,min^{-1}$. Therefore, the change in activation energy is not resulting from charging the capacitor but from a modification in the conduction mechanism.

$KNbO_3$ seems to be simpler in the course of conduction processes. The material exhibits a high and a low temperature region with activation energies of around 1.5 eV and 0.7 eV. In both temperature regimes a change in atmosphere does not alter these values. Nevertheless, the nitrogen atmosphere seems to modify the sample in some way as the conductivity in air does not reach the starting values again after treatment in nitrogen. In contrast to $NaNbO_3$, the p-type behavior is maintained over the whole measured temperature range.

In general, it is noticed that the conductivity is higher and the activation energies are much lower for the AC-measurements compared to the DC-experiments. Nevertheless, they also exhibit at least two regimes with different activation energies. It should be noted that the change in the activation energy appears at the R-to-S-phase transition and not at the P-to-R-phase transition as for the DC-data. Another similarity is the higher activation energies at higher temperatures. In contrast to the DC-experiments, $NaNbO_3$ and not $Na_{0.99}Ca_{0.01}NbO_3$ shows a second change in the activation energy at the P-R-phase transition below which it is again slightly higher.

In case of the $NaNbO_3$-based samples, $Na_{0.99}Sr_{0.01}NbO_3$ has the highest activation energy with $1.33\,eV$ and $NaNbO_3$ the lowest with $1.02\,eV$ in the high temperature regime. In contrast, within the low temperature part $Na_{0.99}Sr_{0.01}NbO_3$ posses the lowest activation energy with $0.73\,eV$ while $NaNbO_3$ shows the highest one with $0.89\,eV$.
Finally, it can be said that $KNbO_3$ has a similar activation energy of around $1\,eV$ like $NaNbO_3$ at high temperatures, which is decreasing to $0.79\,eV$ below the T-C-phase transition.

For the AC-measurements, the activation energies have been determined by plotting the conductivity values of the higher frequency component of the impedance Nyquist plot (see Fig. 7.6). However, at $500\,°C$ one half of a second semicircle is clearly visible in the case of $NaNbO_3$. It might be that this second contribution is corresponding to the DC-conductivity explaining the discrepancy between AC- and DC-measurements. An extrapolation of the second semicircle is carried out in order to determine the total resistance value as shown in Fig. 7.9. It should be mentioned that this value is the intercept with the Z'-axis including the diameter of both semicircles. The Nyquist plot of the admittance is illustrated as well, which indicates more clearly the presence of the second component resulting in a lowered conductivity value.

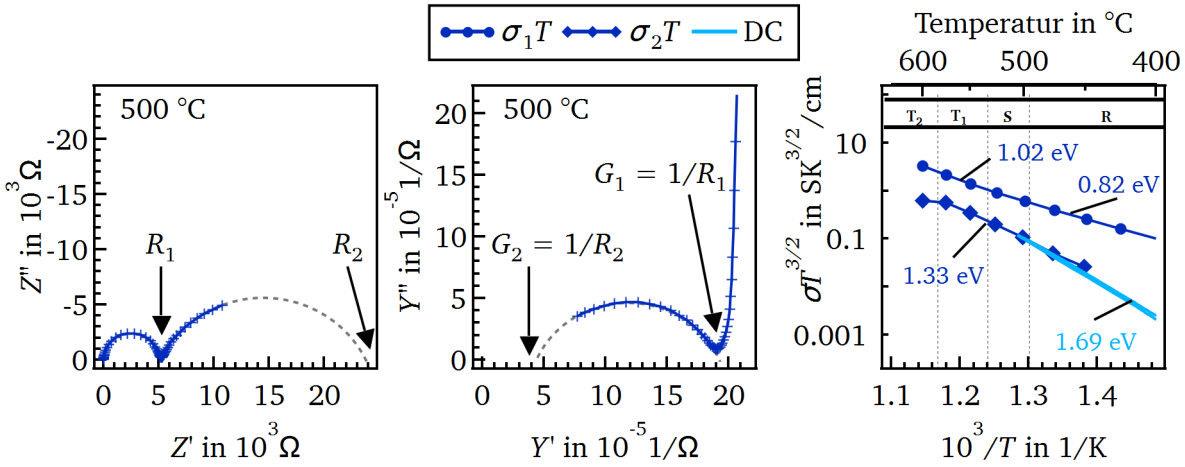

Figure 7.9.: Impedance and admittance Nyquist plots for $NaNbO_3$ at $500\,°C$ are shown. An extrapolation of the second component is illustrated in both graphs. R_1, R_2, G_1, and G_2 are the resistance and conductance of the corresponding parts. On the right side, conductivity multiplied by $T^{3/2}$ values of both AC-resistances and DC-results are plotted as function of temperature. Activation energies are marked in the relevant temperature regions.

Extrapolations are only done for the measurements at higher temperatures because the measured fraction of the second component gets less with decreasing temperature. In general, these values have to be considered with caution due to larger errors of the extrapolations. Nevertheless, the recalculated AC-conductivity values multiplied with temperature are illustrated as a function of temperature

on the right side of Fig. 7.9. For comparison, the DC-conductivity and the AC-conductivity, which corresponds to the first semicircle, are plotted. Indeed, the total AC- and DC-conductivity fit very well with each other. Still, the activation energies are different. The activation energy determined by AC has significantly increased from $1.02\,\mathrm{eV}$ to $1.33\,\mathrm{eV}$ but it is still lower than the one extracted from the DC-data of $1.69\,\mathrm{eV}$. As mentioned before, the extrapolation of the second semicircle is highly uncertain, which could result in an incorrect activation energy. Hence, it is very likely that with DC the total resistance of the AC-experiments meaning the process including first and second semicircle is measured. Probably the same can be applied to $Na_{0.99}Ca_{0.01}NbO_3$ and $Na_{0.99}Sr_{0.01}NbO_3$. However, the second semicircle is not well developed within the investigated frequency range, which is consistent with the lower DC conductivity in air of these samples. An extrapolation would result in uncertain results.

So far, the results of the DC- and AC-experiments have been illustrated, analyzed, and compared with each other. In the following the most important observations are summarized.

Table 7.2.: Main results of the DC- and AC-conductivity measurements of $NaNbO_3$ and $KNbO_3$ including temperature, atmosphere, and time dependency.

	pure $NaNbO_3$	**changes induced by Ca- and Sr-doping**	**pure $KNbO_3$**
DC-measurements			
temperature dependency	change in E_A close to P-to-R-phase transition	additional change in E_A below ca. $200\,^\circ\mathrm{C}$ for $Na_{0.99}Ca_{0.01}NbO_3$	change in E_A close to T-to-C-phase transition
conductivity at RT	low conductivity of $4.4 \times 10^{-14}\,\mathrm{S\,cm^{-1}}$ to $3.3 \times 10^{-13}\,\mathrm{S\,cm^{-1}}$	slightly increased conductivity of $7.6 \times 10^{-13}\,\mathrm{S\,cm^{-1}}$ to $4.1 \times 10^{-11}\,\mathrm{S\,cm^{-1}}$	
conductivity at $500\,^\circ\mathrm{C}$	still low conductivity of $5.0 \times 10^{-6}\,\mathrm{S\,cm^{-1}}$	decreased conductivity of $1.0 \times 10^{-7}\,\mathrm{S\,cm^{-1}}$ to $2.5 \times 10^{-7}\,\mathrm{S\,cm^{-1}}$	low conductivity of $1.0 \times 10^{-6}\,\mathrm{S\,cm^{-1}}$
atmosphere dependency	p-type below $300\,^\circ\mathrm{C}$, n-type above $300\,^\circ\mathrm{C}$	n-type over whole temperature region	p-type over whole temperature region
time dependency	?	at least two different diffusion mechanisms, which relax faster in air than in N_2	?

AC-measurements			
temperature dependency	two conductivity contributions appearing as two semicircles in the Nyquist plot	development of third conductivity contribution above $425\,°C$ for $Na_{0.99}Ca_{0.01}NbO_3$	two conductivity contributions identified by the asymmetry of the semicircle appearing in the Nyquist plot
	change in E_A close to R-to-S-phase transition		change in E_A close to T-to-C-phase transition
conductivity at $500\,°C$	higher conductivity of $2.8 \times 10^{-5}\,S\,cm^{-1}$ than for DC	decreased conductivity of $1.1 \times 10^{-6}\,S\,cm^{-1}$ to $1.1 \times 10^{-5}\,S\,cm^{-1}$ but still higher than for DC	almost the same low conductivity of $1.9 \times 10^{-6}\,S\,cm^{-1}$ as for DC

We can notice that with AC- and DC-experiments different conduction mechanisms with different activation energies are measured. In general, the main contribution of the AC-experiments exhibits a higher conductivity than the conductivity recorded by the DC-measurements. In order to measure the whole second semicircle observed in the AC-experiments, lower frequencies must be examined. This second conductivity contribution is most likely dominating the DC-conductivity. Nevertheless, both measurement techniques reveal a low conductivity of all samples. This agrees with the proposed band structure in Section 6.6 and the idea that the electrical band gap is larger than the one measured by optical methods The optically determined band gap is probably confined by a trapping state, e.g. polarons such as Nb^{4+}. Therefore, polaron conduction could affect the examined AC- and/or DC-results. Furthermore, ionic conduction of sodium and/or oxygen ions could be relevant. At least it is assumed that two different species are dominating the relaxation process investigated by means of the DC-setup in different atmospheres.

7.4. Degradation

In this section the experimental results of the degradation behavior of $NaNbO_3$- and $KNbO_3$-based materials as well as of ITO electrodes are described and analyzed. First, the degradation behavior of $NaNbO_3$, $Na_{0.99}Ca_{0.01}NbO_3$, $Na_{0.99}Sr_{0.01}NbO_3$, and $KNbO_3$ ceramics is investigated under the influence of temperature and electric field. Then, $Na_{0.99}Ca_{0.01}NbO_3$ in contact with an ITO electrode as both, cathode and anode, is examined with a XP-spectrometer while applying an electric field and heating up to $300\,°C$. Finally, a $NaNbO_3$ and $K_{0.5}Na_{0.5}NbO_3$ thin film covered with a thick ITO layer are heated in oxygen and vacuum at $300\,°C$ in order to identify possible diffusion processes.

7.4.1. Degradation behavior depending on temperature and electric field

The degradation behavior of a material can be analyzed by measuring the electrical conductivity while heating and applying a high electric field. In order to investigate at which combination of electric field and temperature a degradation mechanism develops, the samples were heated to a constant temperature while the electric field was increased step-wise every ten minutes. This measurement was then performed at several temperatures. Fig. 7.10 illustrates the conductivity performance of an undoped $NaNbO_3$ sample at room temperature up to $500\,°C$ in $100\,°C$-steps. The electric field profile is shown at the top of the figure. After each electric field cycle the sample was grounded for a few seconds in order to discharge it and remove any surface charges, which could influence the following measurements.

First, the room temperature conductivity is examined (black solid curve RT_1). At low electric fields no reliable conductivity values are obtained because the current is below the resolution limit of the picoamperemeter. Above $60\,V\,mm^{-1}$ the current is high enough in order to measure a reasonable conductivity. When the electric field is increased, the conductivity initially jumps to a higher value due to charging of the sample's capacitance followed by an exponential decay. As the calculated time constant for charging at $30\,°C$ is $1.3\,s$ as mentioned in Section 7.3, this exponential decay cannot be related to this charging. A closer look on the first view seconds of each electric field step reveals two exponential decays. One dominating for the first second and the other one from the second second on. A magnified view of the first five seconds of one electric field step is shown in Fig. A.22 in the appendix. However, it seems that at such low temperatures ten minutes are not long enough for the sample to establish an equilibrium state concerning the second decaying process. Nevertheless, a value of $5 \times 10^{-13}\,S\,cm^{-1}$ close to the ones in Section 5.5 is obtained. When the electric field is decreased again, the conductivity falls to a lower value as a result of decharging of the sample. Afterwards, the conductivity is again increasing exponentially until almost an equilibrium state is reached.

A second electric field profile is applied once again (black dashed curve RT_2) directly after the first one. No differences in the conductivity performance are observed. In order to transform the sample into its original state, it is heated at $500\,°C$ for $1\,h$. The same electric field profile as before is employed again (gray solid curve RT_3). As expected no differences to the conductivity measured before can be identified.

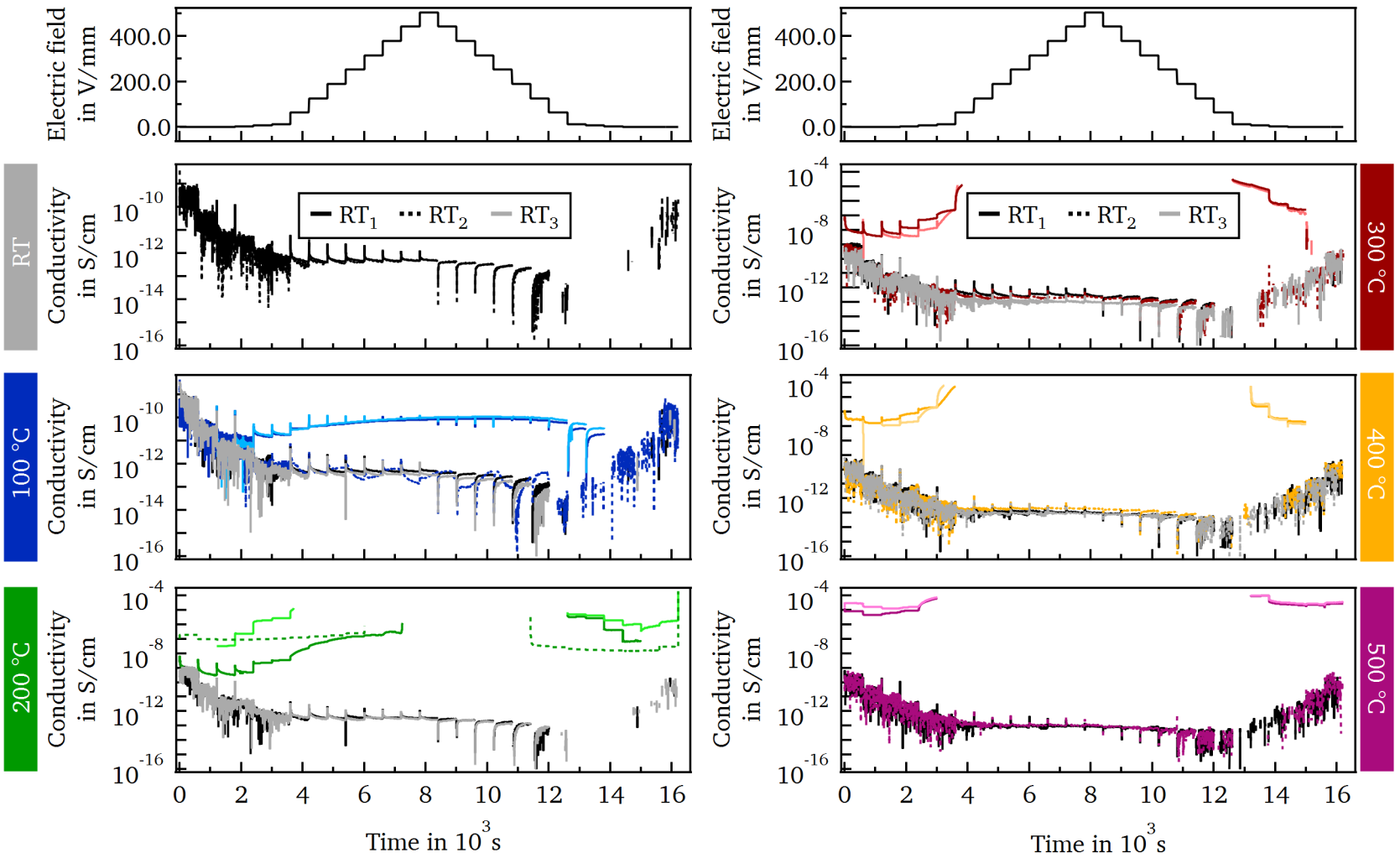

Figure 7.10.: Conductivity measured at different temperatures as a function of time in dependence of an electric field profile shown on the top. The colored solid lines show the curves at the corresponding temperature where the darker one represents the first and the lighter one the second measurement. Room temperature conductivity are examined before (black solid line) and after (colored dashed line) a temperature experiment as well as after a post-annealing step at $500\,^{\circ}\mathrm{C}$ for $1\,\mathrm{h}$ (gray solid line).

The field cycles at elevated temperatures have been recorded in the following sequence and are shown with the following colored and patterned lines in Fig. 7.10:

1. field cycle at room temperature (solid black line)
2. 1st field cycle at high temperature (solid dark colored line)
3. 2nd field cycle at high temperature (solid light colored line)
4. field cycle at room temperature after cooling down to room temperature (dashed dark colored line)
5. 2nd field cycle at room temperature after cooling down to room temperature (dashed light colored line)
6. field cycle at room temperature after heating to $500\,^{\circ}\mathrm{C}$ for $1\,\mathrm{h}$ without field to recover the initial state of the sample and cooling down to room temperature (solid gray line)

At $100\,^{\circ}\mathrm{C}$ a higher conductivity with a maximum equilibrium value of $1.1 \times 10^{-10}\,\mathrm{S\,cm^{-1}}$ is obtained. The conductivity of the sample cannot be measured at very low fields due to the low current resulting in a noisy output signal. With increasing electric field one relaxation mechanism is observed besides the charging peak as for the room temperature experiments. At electric fields higher than $60\,\mathrm{V\,mm^{-1}}$ the conductivity is rising again after the exponential decay, which indicates the overlap of a second relaxation process. These two contributions can most likely be attributed to the two different diffusion species (2) and (3), which have been already identified in Section 7.1.3 for the relaxation experiments and can be probably attributed to oxygen and sodium ions.

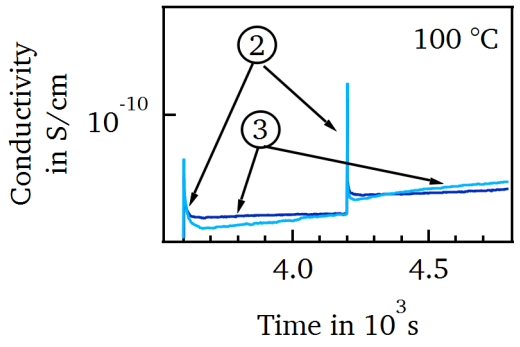

Figure 7.11.: Magnified view of two electric field steps at $100\,^{\circ}\mathrm{C}$ measured with $63.3\,\mathrm{V\,mm^{-1}}$ and $129.5\,\mathrm{V\,mm^{-1}}$ illustrating the different diffusion mechanism.

For better visibility, two electric field steps measured with $63.3\,\mathrm{V\,mm^{-1}}$ and $129.5\,\mathrm{V\,mm^{-1}}$ are shown in more detail in Fig. 7.11. Similar when the electric field is lowered again the conductivity first increases after the decharging peak, however, above $60\,\mathrm{V\,mm^{-1}}$ this increase is followed by a falling conductivity caused by the second diffusion process. Below $60\,\mathrm{V\,mm^{-1}}$ only one diffusion mechanism can be seen.

The second measurement at $100\,^{\circ}\mathrm{C}$ is approximately aligned with the first one. Small deviations from the first room temperature experiment (black solid line) are noticeable when examining the room temperature conductivity directly after the $100\,^{\circ}\mathrm{C}$-measurements (blue dashed line). These discrepancies are removed after heating at $500\,^{\circ}\mathrm{C}$ for $1\,\mathrm{h}$ (gray solid line).

Having a closer look at the conductivity recorded at $200\,°C$, a maximum equilibrium value of around $2.0 \times 10^{-7}\,S\,cm^{-1}$ is detected. The second relaxation mechanism occurs already at an electric field larger than $6\,V\,mm^{-1}$. At $440\,V\,mm^{-1}$ the current, and therefore, the conductivity jumps to a very high value, which is above the current limit of the picoamperemeter meaning a value higher than $1.6 \times 10^{-4}\,S\,cm^{-1}$. This increase of several orders of magnitude can be regarded as degradation process. When the electric field is decreased again, the conductivity is higher compared to before, which suggests a change in the defect concentration of the sample due to degradation. The modification of the sample has an impact on the second measurement done at $200\,°C$. Much higher conductivity are obtained throughout the whole electric field range. Furthermore, the degradation process develops at lower electric fields of $60\,V\,mm^{-1}$. In addition, the room temperature profile performed subsequently (green dashed line) deviates substantially from the one measured beforehand (black solid line) what can be explained by the change in defect concentration. However, this modification can be removed by a post-annealing step at $500\,°C$ for $1\,h$ demonstrated in the room temperature measurement (gray solid line), which is identical to the initial one.
As for the $200\,°C$-measurements, the relaxation process of the second diffusing species starts to dominate above $6\,V\,mm^{-1}$ at $300\,°C$. In contrast, a jump in conductivity revealing a degradation behavior occurs already at $60\,V\,mm^{-1}$. Moreover, the second measurement at $300\,°C$ does not differ that much from the first one. The room temperature conductivity examined before (solid black line) and after (red dashed line) the curves performed at $300\,°C$ as well as the one recorded after the post-annealing are more or less identical. Hence, heating at $300\,°C$ seems to be sufficient to remove the degradation effects. This can be also observed during the measurements conducted at $400\,°C$ and $500\,°C$.

All room temperature experiments exhibit the same conductivity. In addition, at higher temperatures the differences between first and second cycle are negligible. The second diffusion species influences the conductivity at electric fields above $0.6\,V\,mm^{-1}$ while degradation appears above $13\,V\,mm^{-1}$ at both, $400\,°C$ and $500\,°C$.

In summary, the degradation measurements indicate two different diffusion mechanisms, which could already be recognized in Section 7.1.3 during the relaxation experiments. The faster diffusing species can be identified at all temperatures while the slower species is only mobile at higher temperatures and electric fields. Furthermore, a degradation effect is observed at $200\,°C$ to $500\,°C$. The critical electric field necessary for both, degradation and detectable influence of the second diffusing species, decreases with temperature. Finally, it seems that heating at $300\,°C$ is sufficient to remove all effects of degradation on the conductivity.

Table 7.3.: Critical electric fields $E_{2^{nd},diff}$ and E_{deg} at which the second diffusion mechanism is clearly visible and at which degradation appears for all investigated ceramics, respectively.

	$E_{2^{nd},diff}$ in V mm^{-1}					E_{deg} in V mm^{-1}				
	100 °C	200 °C	300 °C	400 °C	500 °C	100 °C	200 °C	300 °C	400 °C	500 °C
$NaNbO_3$	60	6	6	0.6	0.6	–	440	60	13	6
$Na_{0.99}Ca_{0.01}NbO_3$	75	7.5	75	0.75	0.75	75	75	75	15	0.75
$Na_{0.99}Sr_{0.01}NbO_3$	150	75	7.5	7.5	–	?	75	15	7.5	–
$KNbO_3$	–	310	210	–	–	–	–	–	–	–

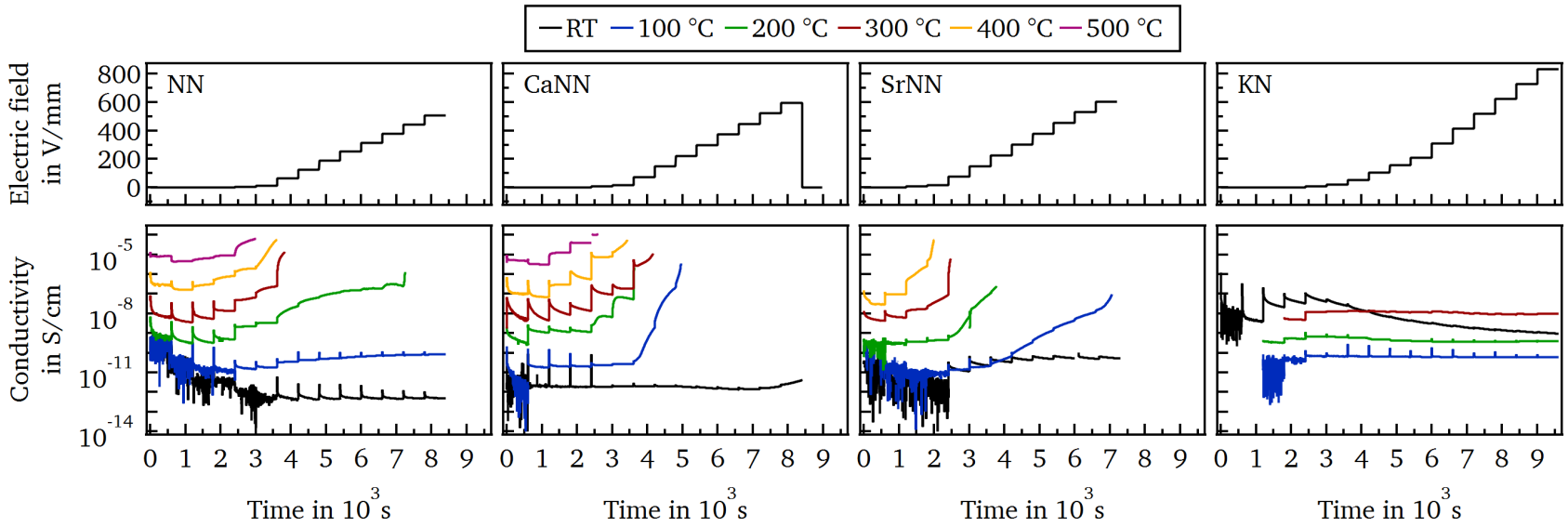

Figure 7.12.: Conductivity measured at different temperatures as a function of time in dependence of an electric field profile shown on the top for pure $NaNbO_3$ and $KNbO_3$ as well as doped $NaNbO_3$.

Similar electric field profiles as for pure $NaNbO_3$ were performed on $Na_{0.99}Ca_{0.01}NbO_3$, $Na_{0.99}Sr_{0.01}NbO_3$, and $KNbO_3$ at temperatures ranging from room temperature to $500\,°C$. However, only increasing electric fields were applied due to time limitations. In addition, no second measurement at higher temperatures nor subsequent room temperature conductivity were examined. Moreover, the samples were post-annealed at $500\,°C$ for $1\,h$ after each measurement but grounding of the samples' electrodes was not performed after each electric field profile.

Figure 7.12 illustrates the conductivity of all investigated ceramics at room temperature up to $500\,°C$ as a function of time. The applied electric field profile is shown above the conductivity diagrams for each material. For the doped samples an equilibrium state for the faster diffusion mechanism is established on a shorter time scale compared to undoped $NaNbO_3$, except at $300\,°C$ for $Na_{0.99}Ca_{0.01}NbO_3$. In case of $Na_{0.99}Ca_{0.01}NbO_3$, the second diffusion process starts to dominate the conductivity from the same electric field on as for pure $NaNbO_3$, although, the measurement at $300\,°C$ is again an exceptional case. Here, the slower diffusion mechanism appears at $75\,V\,mm^{-1}$. In contrast, higher electric fields are necessary for $Na_{0.99}Sr_{0.01}NbO_3$ in order to identify a clear influence of the second contribution on the conductivity. The electric fields required for the second process being evidently visible are listed in Table 7.3 for all $NaNbO_3$-based samples from room temperature up to $500\,°C$.

It is very striking that for the doped samples below $300\,°C$ degradation appears at much lower fields compared to the pure sample. At $300\,°C$ and above, however, all $NaNbO_3$-based ceramics exhibit a degradation behavior from the same electric field step on. The electric fields at which degradation emerges are shown for comparison in Table 7.3 for all samples and relevant temperatures. Furthermore, $Na_{0.99}Ca_{0.01}NbO_3$ shows already at room temperature an increase in conductivity at high fields, which cannot be observed for undoped $NaNbO_3$. The room temperature conductivity of $Na_{0.99}Sr_{0.01}NbO_3$ is higher and does not establish an equilibrium state within the ten minutes per step. This might be caused by the absence of post-annealing after grinding and polishing of this particular sample.

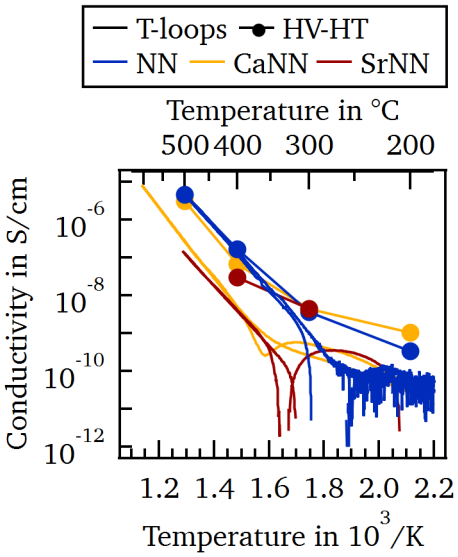

Figure 7.13.: Comparison of conductivity measured by T-loops and HV-HT-measurements at $0.1\,V\,mm^{-1}$ for $NaNbO_3$, $Na_{0.99}Ca_{0.01}NbO_3$, and $Na_{0.99}Sr_{0.01}NbO_3$.

Comparing the absolute conductivity values at $0.1\,V\,mm^{-1}$ as a function of temperature, it is noticeable that at $200\,°C$ and $300\,°C$ the conductivity of $NaNbO_3$ is the lowest while at $400\,°C$ and $500\,°C$ it is the highest. This can be seen more

clearly in Fig. 7.13, which includes as well the T-loop measurements discussed in Section 7.1 for comparison. Both experiments, degradation and T-loops, are measured with an electric field of $0.1\,\mathrm{V\,mm^{-1}}$ and show that between $250\,^{\circ}\mathrm{C}$ and $350\,^{\circ}\mathrm{C}$ a crossing point exists at which the material with the highest conductivity changes from $Na_{0.99}Ca_{0.01}NbO_3$ to pure $NaNbO_3$. Interestingly, in this temperature range the conductivity of $NaNbO_3$ switches from n- to p-type behavior. Moreover, the conductivity measured in the T-loop and degradation experiments match above $350\,^{\circ}\mathrm{C}$ for undoped $NaNbO_3$. This is not the case for Ca- and Sr-doped $NaNbO_3$. Here, the conductivity conducted within the T-loop measurements is always lower than the conductivity examined during the degradation experiments.

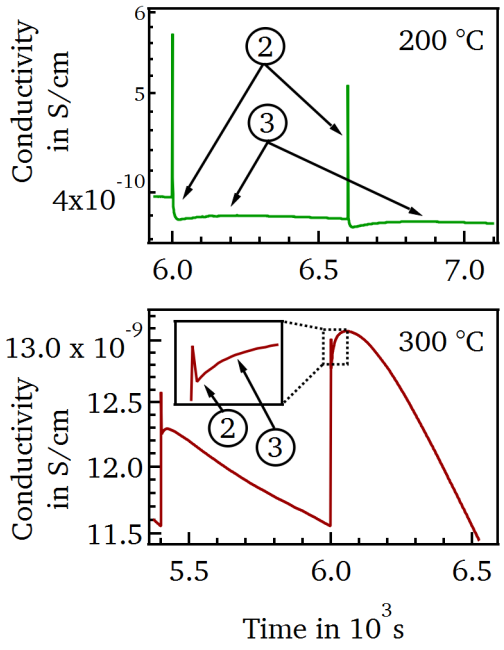

Figure 7.14.: Magnified view of two electric field steps at $200\,^{\circ}\mathrm{C}$ (green) and $300\,^{\circ}\mathrm{C}$ (red). A more detailed section of the first view seconds of the second step at $300\,^{\circ}\mathrm{C}$ is illustrated, too.

It is very interesting that $KNbO_3$ does not show a degradation process within the investigated temperature and electric field range as $NaNbO_3$. Although, it should be mentioned that no measurements could be conducted at $400\,^{\circ}\mathrm{C}$ and above because the sample broke down. Therefore, it would be interesting to know if this is caused by a changed conduction mechanism related to the tetragonal-to-cubic phase transition at around $400\,^{\circ}\mathrm{C}$ accompanied by a fast degradation process or if $KNbO_3$ is more resistant against degradation compared to $NaNbO_3$. Furthermore, after changing the electric field, an equilibrium state is much faster established for $KNbO_3$. Having a closer look at the conductivity at $200\,^{\circ}\mathrm{C}$ and $300\,^{\circ}\mathrm{C}$ for a ceramic $KNbO_3$ sample, at least two different conduction processes can be identified. Figure 7.14 illustrates the conductivity for an electric field of $300\,\mathrm{V\,mm^{-1}}$ and $400\,\mathrm{V\,mm^{-1}}$ at $200\,^{\circ}\mathrm{C}$ as well as of $200\,\mathrm{V\,mm^{-1}}$ and $300\,\mathrm{V\,mm^{-1}}$ at $300\,^{\circ}\mathrm{C}$. At $300\,^{\circ}\mathrm{C}$ an additional magnified view of the first few seconds of the $300\,\mathrm{V\,mm^{-1}}$-step is shown. It is obvious that the conductivity curve includes at least one more and one less mobile diffusing species which are, however, both much faster as the two contributions in $NaNbO_3$ and can most likely be attributed to oxygen and potassium ions. These two different diffusion processes are indicated by (2) and (3) as the two diffusion contributions observed for the $NaNbO_3$ samples. For $KNbO_3$, the second process gets more dominant at higher temperatures, which can be clearly seen in Fig. 7.14 for the conductivity measured at $300\,^{\circ}\mathrm{C}$. Here,

the first diffusion mechanism (2) is only observable for one second before diffusion process (3) is overlaying the first process. Furthermore, the second diffusion mechanism is not observed at $100\,°C$ as for $NaNbO_3$.

In summary, resistance degradation starts to develop at high electric fields and temperatures for the $NaNbO_3$-based ceramics. The effects of degradation on the conductivity can be eliminated by heating above $300\,°C$ for at least $1\,h$. In contrast, such degradation behavior is not obtained for $KNbO_3$. However, measurements above $300\,°C$ could not be conducted due to electric breakdown of the sample. In addition, two different diffusion processes are observed for all samples, a faster and a slower one, which can be most likely linked to oxygen and alkaline ions. The less mobile species starts to dominate the conduction behavior at higher temperatures and electric fields. In $KNbO_3$ both diffusion species are much more mobile than in $NaNbO_3$ as an equilibrium state of the conductivity establishes much faster. For the $NaNbO_3$-based ceramics both critical electric fields for a significant influence of the slower diffusion process and for the appearance of resistance degradation, decrease with increasing temperature.

7.4.2. Electrode degradation of ITO

In this section the sample-electrode interface of a $Na_{0.99}Ca_{0.01}NbO_3$ ceramic is examined. Furthermore, ITO is tested as suitable electrode material for $NaNbO_3$-based samples and checked for electrode degradation phenomena.
In order to investigate the behavior of $NaNbO_3$ in contact with such an ITO electrode, XPS interface analysis were conducted. ITO was used as a thin top electrode with $3\,nm$ thickness, which is sufficient to have a conductive enough electrode while still being able to measure a signal of the $NaNbO_3$ sample. As described in Section 4.13 a Pt-contact was used as the bottom electrode. ITO was probed as both, cathode and anode. After depositing the thin ITO-electrode, the sample had to be removed from the ultrahigh-vacuum system to mount the sample on a special sample holder, which allows for heating of the sample and applying a voltage while measuring XPS. As a consequence, a small amount of carbon could be detected on the surface visible in the survey spectra in Fig. A.24 in the appendix.
Figure 7.15 illustrates the core level lines of an ITO-electrode on top of a $Na_{0.99}Ca_{0.01}NbO_3$ sample. In a) ITO served as cathode while in b) it was used as anode. First, XP-spectra were recorded at room temperature (black curves). For $Na_{0.99}Ca_{0.01}NbO_3$ the Na 1*s*, Nb 3*d*, and the O 1*s* peak was measured, however, the O $1s$ emission line consists of an overlap of $Na_{0.99}Ca_{0.01}NbO_3$ and ITO contribution. Additionally, In 3*d* and Sn 3*d* core levels were examined. The intensity of the $Na_{0.99}Ca_{0.01}NbO_3$ signals is attenuated due to the ITO electrode. Besides a shoulder on the higher binding energy side of the O 1*s* peak caused by adsorbed carbonates and hydroxides, all spectra show typical binding energies and shapes for the investigated materials.

Next, the sample is heated up to 100 °C. In Fig. 7.15b) the core level spectra at 100 °C are plotted in dark blue. No significant changes are observed, except for a small shift of the emission lines towards lower binding energies, which can be explained by measuring at elevated temperatures having a reducing effect on the band gap. This in turn has an impact on the position of the Fermi level relative to the valence band maximum.

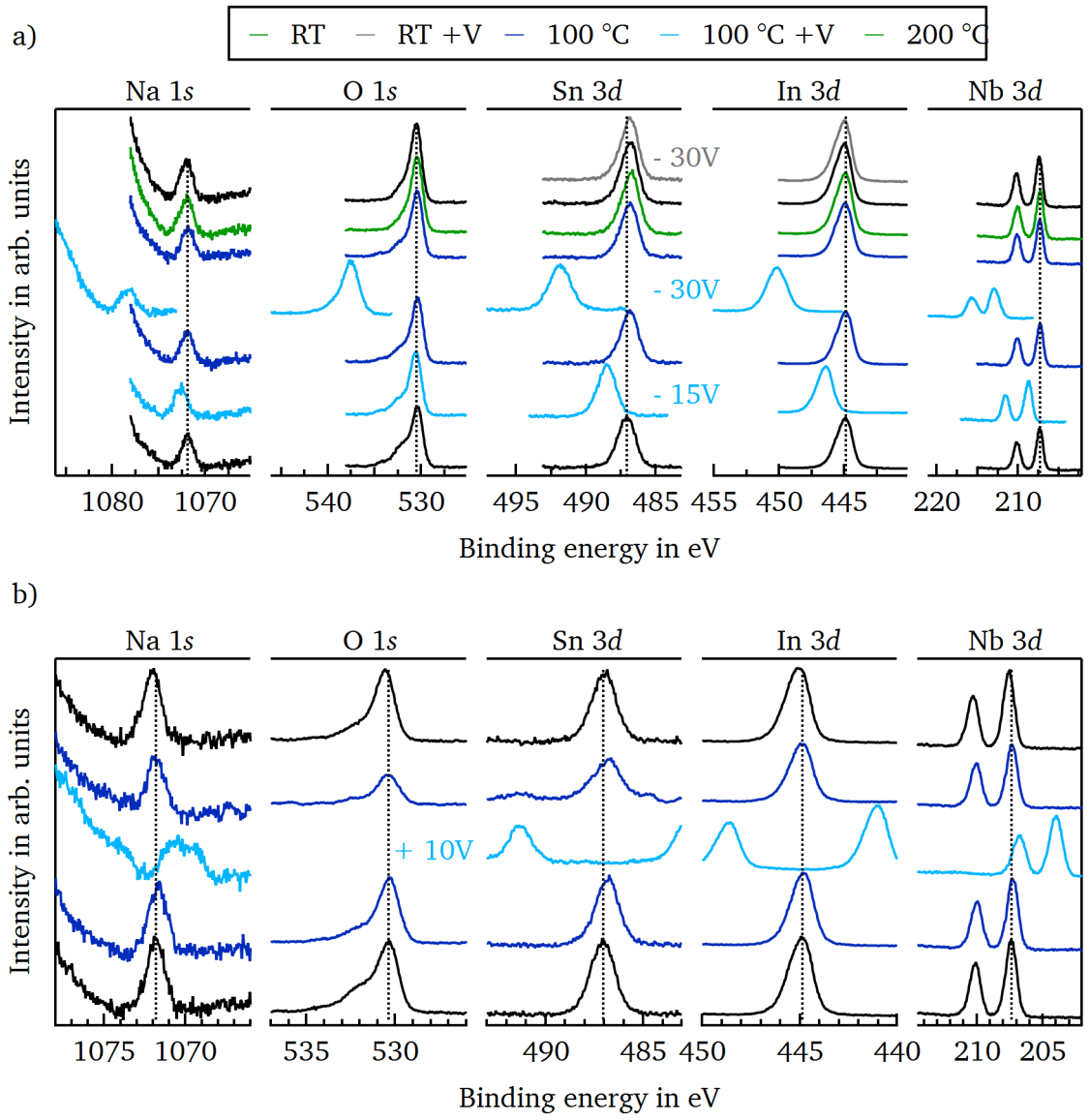

Figure 7.15.: Core level emission lines of a $Na_{0.99}Ca_{0.01}NbO_3$ samples with an ITO-electrode acting as cathode in a) and as anode in b). Dashed lines indicate the original peak position at room temperature.

Applying a voltage leads to a shift of all peaks to higher and lower binding energies when ITO acts as

cathode or anode, respectively. Furthermore, the peak shape is broadened, which can be seen the best in the Na 1*s* emission line in Fig. 7.15b). The core levels are not shifted by the same energy, e.g. the In 3*d* peak is shifted more in energy compared to the Na 1*s* line for both experiments. Considering the measuring order of the emission lines and the conductivity curve during the measuring time, a clear trend in the binding energy shift is noticed.

Figure 7.16 displays the conductivity on the left axis and the binding energy difference between 100 °C with applied voltage and room temperature on the right axis as a function of time for ITO as cathode in a) and as anode in b). Arrows mark the respective peak, which is examined during a certain time period. In both cases, the conductivity increases with time, which is accompanied by a rising shift in the absolute binding energy difference. If ITO is acting as cathode a positive binding energy shift is recognized, which means a shift towards higher binding energies while as anode a negative binding energy shift is identified due to the lowered binding energy by applying a voltage.
The shift in peak position as well as the changed peak shape while applying a voltage at 100 °C indicate charging of the sample-electrode-system during XPS-measurement. This would agree with the increasing peak shift with measuring time because of charge accumulation over time.

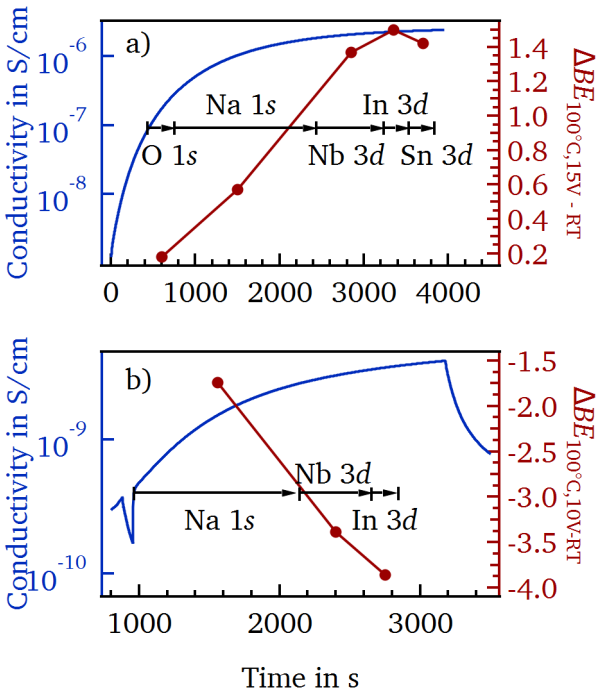

Figure 7.16.: Conductivity on the left axis and binding energy difference of the core level lines between 100 °C with applied voltage and room temperature on the right axis as a function of time for ITO as cathode in a) and as anode in b). Arrows mark the time period of each examined peak.

When the electric field is removed the emission lines switch back to their original positions. In case of ITO being the anode, a different peak shape with additional peaks at higher and lower binding energies appear in the Sn 3*d* core level line. In addition, the shoulders on the higher binding energy side of the O 1*s* peak are more pronounced in relation to the intensity of the main line. This intensification and the appearance of the additional component on the higher binding energy side of the Sn 3*d* peak can be explained by charging of at least some parts of the ITO film. The shoulder located at around 484.7 eV on the lower

binding energy side of the Sn 3*d* emission line could indicate the formation of metallic Sn [305, 306]. This would suggest that the ITO film is decomposing. However, these changes are vanishing after cooling down slowly to room temperature. Here, all spectra are shifted slightly to higher binding energies compared to the first room temperature measurement. Except for the O 1*s* emission line, all peaks exhibit the same peak shape as before. In case of oxygen, the shoulder at higher binding energies is reduced in intensity, which can be explained by the evaporation of carbon oxide and hydroxide species and agrees with the smaller C $1s$ peak in the survey spectra of Fig. A.24.

When ITO is acting as the cathode, no different peak shapes and positions are seen after removing the electric field at $100\,°$C. Applying a higher voltage of $-30\,$V leads to an even larger shift in binding energy of all spectra, which is again linked to the measuring order and the conductivity profile. The corresponding graph illustrating this relation is shown in Fig. A.25 in the appendix. After removing the electric field again, the spectra shift back to their original location. Hence, no residual charging or decomposition of the ITO film occurs as for the ITO-anode.
Besides a lowered intensity of the shoulder in the O 1*s* peak due to the evaporation of adsorbents, heating up to $200\,°$C does not further modify the core level spectra. Comparing the room temperature measurements before and after heating, no differences in peak position and shape are observed. The gray Sn 3*d* and In 3*d* spectra are measured at room temperature while applying a voltage of $-30\,$V. Surprisingly, neither peak shape nor position are modified. Hence, only simultaneous heating induces these changes. The question is why ITO is charging as cathode and anode when applying a voltage at $100\,°$C but not at room temperature.

When ITO is the anode it is positively polarized. Therefore, negatively charged species, e.g. O^{2-}, from the sample are attracted. This could lead to an oxidation of the ITO-electrode due to incorporation of oxygen from the $NaNbO_3$ substrate. In ITO the Fermi level is close to or within the conduction band leading to a high conductivity due to the donor doping. Oxidation leads to a downward shift of the Fermi level within the band gap causing a lower conductivity. Consequently, the ITO-electrode is most likely not conductive enough anymore to maintain a fast enough electron flow to the surface, which would balance the positive charges created by the emission of the photoelectrons during XPS analysis. A similar observation was done in a former work by Baris Öcal [307] within the working group. In this work, the effect of an ITO-anode on the resistance degradation of $BaTiO_3$ is investigated. This was done by examining the conductivity of $BaTiO_3$ and simultaneously monitoring the conductivity of the ITO-electrode by a 4-point-measurement while heating at $200\,°$C. From these results it is very clear when degradation starts to develop that the conductivity of ITO is decreasing correspondingly. Both, degradation of $BaTiO_3$ and the larger resistivity of ITO, can be explained by the migration of O^{2-} to the ITO-anode. However, it is very interesting that the measurements in this work show that oxygen seems to migrate already at $100\,°$C.
In contrast, when ITO is used as cathode it is negatively polarized. Hence, not negatively but positively charged species are attracted, e.g. oxygen vacancies $V_O^{\cdot\cdot}$. This would lead to a reduction of

the ITO-electrode meaning that ITO exhibits the same or even higher conductivity. Therefore, the question remains why the sample-electrode-system seems to be charging while measuring XPS at $100\,°C$. Interestingly, no charging phenomenon is observed when applying the same voltage of $-30\,V$ at room temperature.

Figure 7.17 illustrates the applied electric field and the conductivity of $Na_{0.99}Ca_{0.01}NbO_3$ measured at room temperature (left side) and at $100\,°C$ (right side) in vacuum in the XPS chamber and in air. It should be mentioned that the experiment in air was conducted with two Pt electrodes. First, it is noticeable that the conductivity recorded in vacuum is at least one order of magnitude higher. Furthermore, at $100\,°C$ the degradation increase is much faster in vacuum than in air, although, a higher electric field is applied in air. Considering the sample thickness of $0.5\,mm$ results in a measuring current of $>1\times10^{-7}\,A$. The same current flows through the sample and the ITO-electrode. However, the contact area of the ITO-layer to the mask of the sample holder, A_{ITO}, is much smaller as the contact area between ITO-electrode and $Na_{0.99}Ca_{0.01}NbO_3$ sample, A_{CaNN}, as shown in the drawing of Fig. 7.18. Taking Eq. 7.1 and the contact areas A_{ITO} and A_{CaNN} into account, reveals an one order of magnitude higher current density at the ITO-mask-contact j_{ITO} compared to the ITO-$Na_{0.99}Ca_{0.01}NbO_3$-contact j_{CaNN}.

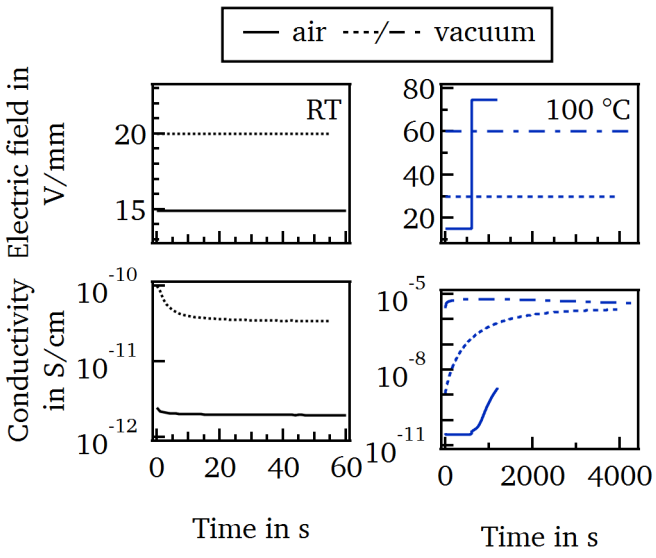

Figure 7.17.: Applied electric field and conductivity of $Na_{0.99}Ca_{0.01}NbO_3$ with ITO cathode and Pt cathode measured at room temperature (left) and $100\,°C$ (right) in air and vacuum.

$$
\begin{gathered}
j_{CaNN} = \frac{I}{A_{CaNN}} \qquad j_{ITO} = \frac{I}{A_{ITO}} \\
A_{CaNN} = \pi r_{CaNN}^2 \qquad A_{ITO} = \pi\left(r_{ITO,out}^2 - r_{ITO,in}^2\right) \\
\text{with} \quad I = 1\cdot10^{-7}\,A; \quad r_{CaNN} = 3\,mm; \quad r_{ITO,out} = 2.0\,mm; \quad r_{ITO,in} = 1.5\,mm \\
j_{CaNN} = 3.5\cdot10^{-7}\,\frac{A}{cm^2} \qquad j_{ITO} = 1.8\cdot10^{-6}\,\frac{A}{cm^2} \qquad \Rightarrow j_{ITO} > j_{CaNN}
\end{gathered}
\tag{7.1}
$$

With constant applied voltage and increasing current density, the conductivity of ITO might not be high enough to counterbalance the additional positive charges created by the photoelectrons.

Consequently, an additional bias evolves responsible for the charging of the sample and the shifted peak positions during XPS analysis. This charging phenomenon of the ITO electrode is also observed with other materials such as $BaTiO_3$ and $Na_{0.5}Bi_{0.5}TiO_3$ in our working group. It seems that currents higher than 1×10^{-7} A to 1×10^{-6} A lead to a charging of the sample-electrode-system and shifted peak positions.

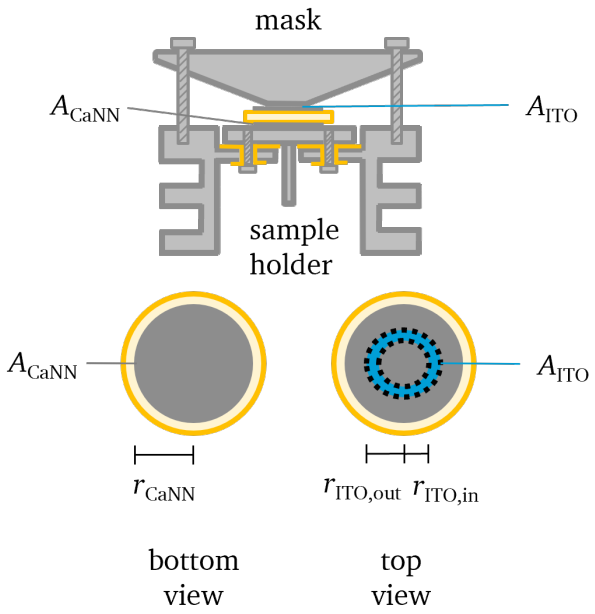

Figure 7.18.: Profile view of the $Na_{0.99}Ca_{0.01}NbO_3$ sample mounted on the sample holder as well as bottom and top view to indicate the relevant contact areas.

As mentioned before, degradation appears on a much shorter time scale in vacuum than in air. Except for the charging effects, no significant influence on peak positions or shapes are observed. However, the carbon adsorbents overlaying the whole spectra, make it more difficult to investigate small differences in the peak shape, which could be related to the appearance of, e.g. the shoulder in the Na 1*s* peak analyzed in Section 6.1.1.

In summary, it can be observed that ITO is not a good electrode material for materials, which are not highly insulating. For highly insulating materials, e.g. PZT, ITO can be used as cathode, which has been shown in this working group by Binxiang Huang [308]. However, if the conductivity of the investigated materials is getting too high and the contact area is very small, the conductivity of ITO is not sufficient to conduct the current. As anode ITO cannot be used at temperatures of 100 °C or higher in combination with an oxide material as substrate due to oxygen migration and incorporation of oxygen into the ITO layer. This leads to the increase of the ITO resistivity.

7.4.3. Heating in oxidizing and reducing atmospheres with a thick ITO layer

The influence of oxidizing and reducing conditions on the ITO-electrode-sample-system were investigated in order to analyze possible ionic diffusion processes. As ITO is an oxygen containing material, only the suggested sodium and potassium diffusion (Section 7.1.3 and 7.4.1) can be checked.
For this purpose, thin films instead of ceramics were analyzed in order to prevent charging effects during the XPS-measurements. A 100 nm thick ITO layer was deposited at room temperature on top

of the sample. Afterwards, the sample was first annealed for 3 h at 300 °C in a low pressure oxygen atmosphere of 0.5 Pa with an oxygen flow of 5 sccm in the Ox II-chamber, followed by a reducing annealing step at 300 °C in vacuum in the XPS-chamber with a pressure of around 1×10^{-6} Pa for additional 3 h. A survey and detailed spectra of the sample and electrode core levels and valence bands were measured before and after ITO-deposition as well as after each heating step. Figure 7.19 illustrates the Na 1*s*, O 1*s*, Sn 3*d*, In 3*d*, and Nb 3*d* emission lines and the valence band of a $NaNbO_3$ thin film with a 100 nm thick ITO-layer on top.

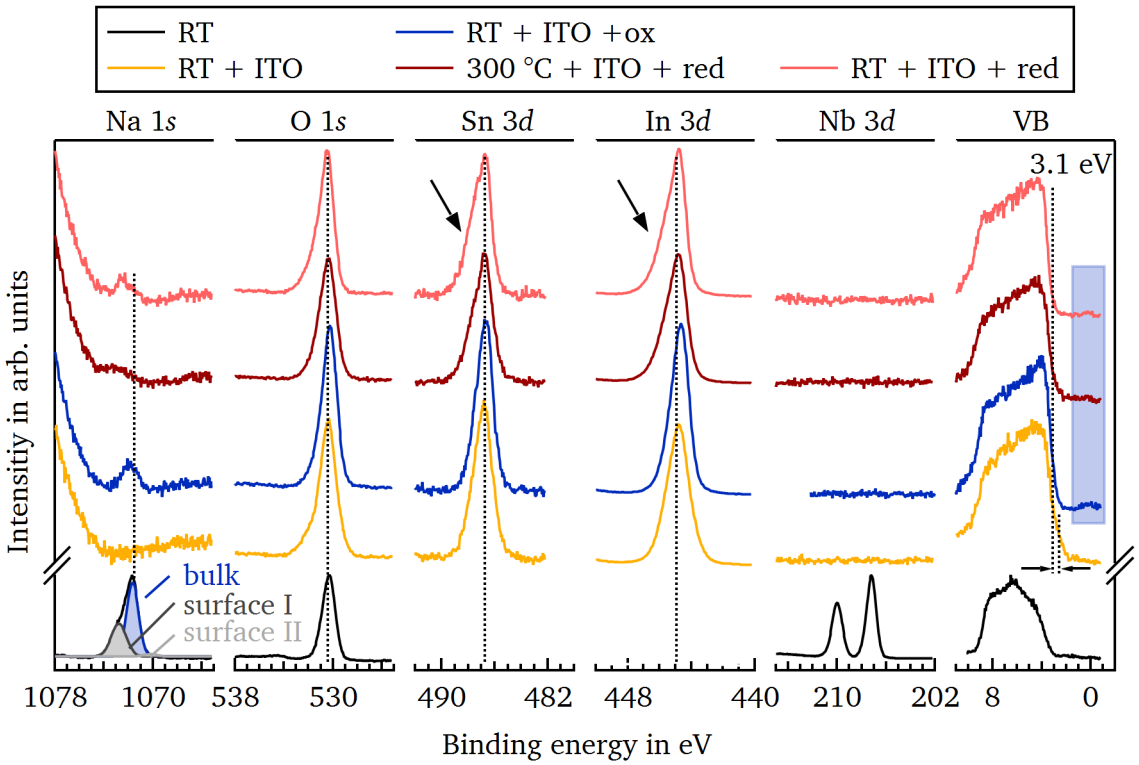

Figure 7.19.: Core level and valence band XP-spectra of a clean $NaNbO_3$ thin film (black), after deposition of 100 nm thick ITO layer (yellow), followed by an oxidizing (blue) and reducing treatment (red) both at 300 °C. The dark red curves were measured during heating whereas the light red spectra were recorded at room temperature after heating. Dashed lines mark the core level binding energies of the clean $NaNbO_3$ and ITO film. In the Na 1s emission line, bulk and both surface components are illustrated.

Before the ITO-deposition (black spectra) typical core level peaks of undoped $NaNbO_3$ were measured, which have been already analyzed in Section 6.1.1. No signal of the sample elements is detected anymore after the deposition of the thick ITO layer (yellow spectra). After annealing the sample at 300 °C in an oxidizing atmosphere, a clear peak appears in the Na 1*s* spectrum with a slightly higher binding energy of 1072.0 eV as the Na 1*s* bulk component (1071.7 eV). In contrast, no Nb 3*d* peak has developed. Niobium has a higher cross-section and a higher escape depth compared to sodium.

Hence, the formation of holes in the ITO film can be excluded. Instead, sodium must have been diffused through the ITO layer towards the surface. The emerging Na 1*s* line is accompanied by the appearance of new states at the valence band maximum highlighted by a blue box in Fig. 7.19. All other spectra are shifted slightly to lower binding energies. Heating at 300 °C in vacuum decreases the peak intensity of the Na 1*s* emission line. In addition, the peak width is broader and it is shifted to higher binding energies. When measuring at room temperature after cooling down over night, the peak can be seen more clearly again. Nevertheless, it has an asymmetric peak shape and is still shifted towards higher binding energies. However, due to the overlapping In MNN Auger line on the higher binding energy side, it is difficult to make any clear statements about peak shape and intensity. Therefore, the measured spectra of the Na 1*s* region after ITO deposition has been subtracted as baseline from the other Na 1*s* emission lines. The resulting peaks are presented in Fig. 7.20. No differences between oxidized and reduced emission lines examined at room temperature are recognized. Furthermore, the peak recorded at 300 °C deviates not that extremely anymore. The remaining differences could result from a stronger overlap with the In MNN Auger line making the subtraction more difficult. In any way, the intensity of the Na 1*s* emission line measured at 300 °C exhibit a lower intensity compared to the corresponding peak recorded at room temperature, which applies for all other core levels. The smaller measured intensities at 300 °C can be explained by the sample being slightly out of focus because of small thermal expansions of sample and sample holder.

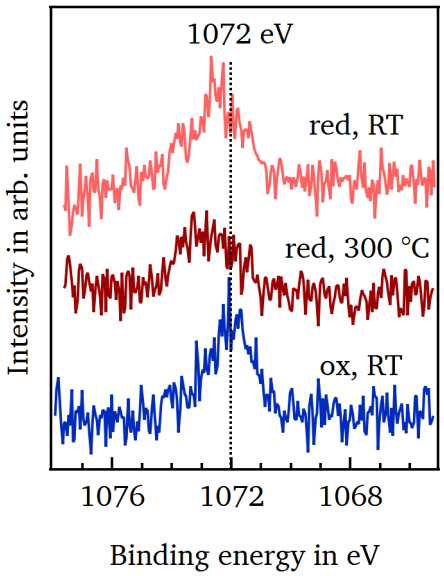

Figure 7.20.: Na 1s peak with subtracted In *MNN* Auger line.

Both, Sn 3*d* and In 3*d* peak are getting more asymmetric and develop a shoulder on the higher binding energy side when heating in vacuum, which is indicated by arrows in Fig. 7.19. This can be explained by a reduction of the ITO film while heating in vacuum, which is accompanied by an increase in charge carrier concentration. The electrons can have a screening effect on the core hole left behind by the formed photoelectron, which exhibits a lower binding and a higher kinetic energy due to the screening [309–311]. The reduction effect is also observable in the shift of the valence band maximum towards higher binding energies when comparing it's position after deposition and after heating in vacuum, which can be set in relation with a Fermi level closer to the conduction band. The two valence band maxima are indicated by dashed lines in Fig. 7.19.

A KNLNT thin film was mounted on the same sample holder as the $NaNbO_3$ sample discussed above. Hence, the same treatments and XPS analysis were performed on this sample. Figure 7.21 shows the corresponding core level and valence band spectra before and after ITO deposition and after each annealing step. In addition, the K 2*p* emission line is included. For the clean KNLNT film (black curves) all elements can be identified with regular peak position and shape, which are discussed in Section 6.1.2. Unfortunately, the Nb 3*d* peak of the uncovered surface was not saved during the measurement which is why it cannot be shown here. The room temperature deposition of the thick ITO layer prevents the detection of the KNLNT sample (yellow curves). Similar to the $NaNbO_3$ thin film a small Na 1*s* peak appears after annealing in an oxidizing atmosphere while no Nb 3*d* peak is observed. In addition, a K 2*p* emission line emerges at $293.5\,\text{eV}$ with a much higher intensity compared to the Na 1*s* peak. This core level line can be fitted with the same parameters as surface component I but has a $0.3\,\text{eV}$ lower binding energy. Interestingly, the new states appearing at the valence band maximum after heating in oxygen for the $NaNbO_3$ sample are not observed for KNLNT. Heating in vacuum leads to reduced peak intensities because of the sample being slightly out of focus as explained above. This effect is reversed after cooling down to room temperature (light red curves). Although the valence band maximum as well as the O 1*s*, Sn 3*d*, and In 3*d* emission line are shifted to higher binding energies, no clear shoulder is visible in the Sn 3*d* and In 3*d* peaks, which would indicate a reduction of the ITO film. This is in line with the valence band maximum position of $2.9\,\text{eV}$, which is lower than the valence band maximum measured at room temperature after heating in vacuum of $3.1\,\text{eV}$ in case of the $NaNbO_3$ thin film. Therefore, the ITO layer on the $K_{0.5}Na_{0.5}NbO_3$ sample was less reduced as on the $NaNbO_3$ sample after vacuum annealing.
The same observations were done for a $K_{0.5}Na_{0.5}NbO_3$ ceramic in the advanced research lab internship of Sabrina Kahse [312]. She investigated the interaction of a $100\,\text{nm}$ thick ITO-electrode on a $K_{0.5}Na_{0.5}NbO_3$ ceramic sample by heating in vacuum at $100\,^\circ\text{C}$, $200\,^\circ\text{C}$, and $300\,^\circ\text{C}$. In addition, she applied a voltage of $-1\,\text{V}$ and $-3\,\text{V}$ with ITO acting as cathode while heating at $300\,^\circ\text{C}$. For convenience only, the relevant Na 1*s*, O 1*s*, K 2*p*, and Nb 3*d* spectra of the XPS measurements are illustrated in Fig. A.26 in the appendix. These experiments show that the applied voltage increases the amount of alkali metals on the surface even more indicating a diffusion of the Na^+ and K^+ cations to the surface. Surprisingly, very small potassium traces are already noticed at room temperature after breaking the vacuum and exposing the sample to air while mounting the sample on a special sample holder in order to apply the voltage in the XPS system.

For both, $NaNbO_3$ and $K_{0.5}Na_{0.5}NbO_3$ thin film samples, traces of the alkali metals are observed on the surface of the ITO-electrode after annealing at $300\,^\circ\text{C}$ in an oxidizing atmosphere. Heating in vacuum does not further increase nor reduce the intensity of the alkali metal peaks. This is clear evidence that sodium and potassium diffuse from the substrate through the ITO layer to the surface. Interestingly, the diffusion of potassium seems to be much faster since a higher concentration of potassium is detected on the surface, which is quite surprising because of potassium being larger

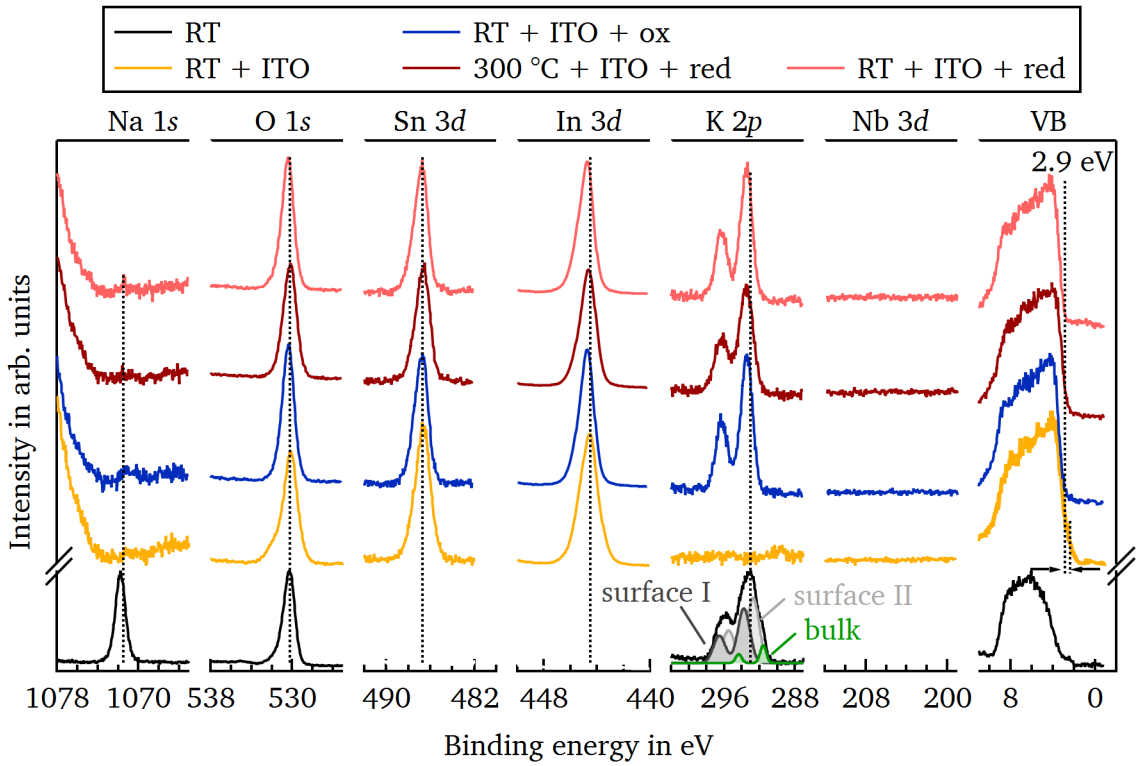

Figure 7.21.: Core level and valence band XP-spectra of a clean $K_{0.5}Na_{0.5}NbO_3$ thin film (black), after deposition of 100 nm thick ITO layer (yellow), followed by a oxidizing (blue) and reducing treatment (red) both at 300 °C. The dark red curves were measured during heating whereas the light red spectra were recorded at room temperature after heating. Dashed lines mark the core level binding energies of the clean $K_{0.5}Na_{0.5}NbO_3$ and ITO film. In the Na 1*s* and K 2*p* emission lines, bulk and both surface components are illustrated.

than sodium. Furthermore, it is shown in literature that sodium is moving faster than potassium during processing of $K_{0.5}Na_{0.5}NbO_3$ ceramics [191, 202].

In case of potassium, the binding energy of K 2*p* peak is in good agreement with binding energies found in literature for K_2O and K_2O_2 [269, 273]. The formation of potassium peroxide seems to be questionable when heating in a low pressure oxygen atmosphere or even in vacuum. However, in Section 6.4 it has been discussed that the formation of K_2O_2 could be preferred because it seems to be more stable due to a more negative formation enthalpy compared to K_2O. Furthermore, the absence of a O 1*s* emission line at around 527.2 eV to 528.3 eV corresponding to K_2O supports the formation of K_2O_2. Nevertheless, K_2O cannot completely be excluded as possible oxide species.

Metallic sodium and sodium oxide exhibit Na 1*s* peaks with binding energies of 1070.8 eV to 1071.8 eV [274, 275] and 1072.0 eV [275], respectively. Therefore, it is not clear whether metallic sodium or oxide sodium is formed at the surface. The simultaneous appearance of the new state at the

valence band maximum of the ITO-film on $NaNbO_3$, however, could be an indication for pure sodium. Metallic sodium has a Fermi edge as all metals do, which would explain the additional state at the valence band maximum. In contrast, no Fermi edge is observed during the experiments on the KNLNT thin film. This is in line with the hypothesis that a potassium oxide species is formed on the surface, since for metallic potassium a Fermi edge should be visible as well [273, 313]. However, in KNLNT not only potassium but sodium is diffusing towards the surface as well, which could stay in the metallic form as for the $NaNbO_3$ thin film. In this case, a Fermi edge should be created, too. The detected amount of sodium is much smaller on the KNLNT than on the $NaNbO_3$ layer, which means that measured sodium intensity is highly reduced. Therefore, the amount of sodium might just be not high enough to detect a significant Fermi edge. Scanning the valence band with more than 100 sweeps could resolve this issue revealing a Fermi edge formed by metallic sodium.
The formation of a Fermi edge due to a highly reduced ITO-layer can be excluded because after the oxidizing step the Fermi level is located at 2.7 eV for ITO on $NaNbO_3$ and at 2.9 eV for ITO on KNLNT. Consequently, if highly reduced ITO is responsible for the observed Fermi edge it should also be seen for ITO on KNLNT. Instead, it is only visible for ITO on $NaNbO_3$. Furthermore, the Sn 3*d* and In 3*d* peaks are almost symmetric, which suggests a more oxidized ITO layer rather than a reduced one.

In this section, the diffusion of sodium and potassium through a 100 nm thick ITO film has been observed after oxidation in a low pressure oxygen atmosphere at $300\,^{\circ}$C for 3 h. Potassium is most likely forming K_2O_2 on the surface as it is the most stable oxide form and the K $2p_{3/2}$ binding energy of 293.5 eV fits to K_2O_2. In contrast, sodium is very likely staying in it's metallic form because of the simultaneous appearance of a Fermi edge. Highly reduced ITO cannot be responsible for the observed Fermi edge as the Fermi level of 2.7 eV is too low and Sn 3*d* and In 3*d* core level are too symmetric. Annealing in vacuum at $300\,^{\circ}$C does not change anything on the potassium and sodium compounds on the ITO film. However, ITO itself is reduced on the $NaNbO_3$ layer but not on the KNLNT film. This can be identified by the very asymmetric shape of the Sn 3*d* and In 3*d* peak of the ITO film on $NaNbO_3$ after vacuum annealing, while on the KNLNT sample they stay more symmetric.

7.4.4. Degradation - Summary

Resistance degradation of $NaNbO_3$- and $KNbO_3$-based samples have been analyzed within this section. High temperatures and electric fields have been applied. In addition, degradation of the material-electrode-system has been investigated by combination of heating, applied electric field, and XPS measurements. The interaction between substrate and electrode have been further examined by post-annealing experiments in oxygen and vacuum. In the following, the main observations are summarized.

Important observations

- Sodium and potassium are mobile in $NaNbO_3$- and $KNbO_3$-based material when heating at temperatures of $300\,°C$ and higher.
- For both sample types one slow and one fast diffusion mechanism is observed, which can be most likely be attributed to oxygen and sodium or potassium ions.
- The less mobile species dominates the conduction behavior at higher temperatures.
- In $KNbO_3$ both species are much more mobile than in $NaNbO_3$.
- For $NaNbO_3$-based ceramics resistance degradation develops at high electric fields and temperatures - it's effects can be removed by heating above $300\,°C$ for at least $1\,h$.
- No resistance degradation is observed for $KNbO_3$.
- Below $300\,°C$ the conductivity of undoped $NaNbO_3$ is lower than of donor doped $NaNbO_3$.
- Above $300\,°C$ the conductivity of undoped $NaNbO_3$ is higher than of donor doped $NaNbO_3$
- ITO is not a good electrode material for materials which are not highly insulating.

All degradation experiments confirm the ionic conduction of two species as concluded from the relaxation measurements in Section 7.1.3. The assignment of alkaline ions to one of these two diffusion processes is further verified by the clear segregation of sodium and potassium ions on the surface, when heating above $300\,°C$. Hence, not only electronic but also ionic conduction plays a role in niobate materials.

Taking all observations of AC- and DC-measurements and degradation experiments into account, it is clear that electronic and ionic movement must be considered when analyzing the conductivity results and the band structure of $NaNbO_3$ and $KNbO_3$. Band and polaron conduction of electrons and holes as well as oxygen, sodium, and potassium diffusion are important for the following discussion.

8. Discussion

In the last Section 7 all results of electrical AC- and DC-conductivity and degradation measurements have been presented and analyzed. The main observations and conclusions can be summarized as:

Main observations and conclusions

- All samples show a low AC- and DC-conductivity.
- Two contributions are observed within the AC-conductivity for all samples.
- The AC-conductivity extracted from the first semicircle of the impedance Nyquist plots is higher than the DC-conductivity.
- The AC-conductivity corresponding to the extrapolated resistance including both semicircles equals the DC-conductivity.
- At temperatures above $350\,°C$ $NaNbO_3$ exhibits a higher conductivity than donor doped $NaNbO_3$.
- At temperatures below $350\,°C$ $NaNbO_3$ has a lower conductivity than donor doped $NaNbO_3$.
- $E_{A,AC}$ values are lower than $E_{A,DC}$ values for all samples.
- Between $300\,°C$ and $350\,°C$ a change in $E_{A,DC}$ is observed for the $NaNbO_3$-based samples.
- Undoped $NaNbO_3$ shows a change from n- to p-type behavior at around $340\,°C$ while $KNbO_3$ is p-type over the whole temperature range.
- Two diffusing species most likely oxygen and alkaline atoms can be identified for all samples.
- Degradation is only observable for $NaNbO_3$-based samples but not for $KNbO_3$.

The purpose of this chapter is to draw a connection between these observations and to find the origin for them.

This chapter has the aim to ...

... explain the electrical transport mechanisms in $NaNbO_3$ and $KNbO_3$.

... explain the differences between AC- and DC-conductivity.

... explain the change from n- to p-type behavior with increasing temperature in $NaNbO_3$.

... explain the p-type behavior of $KNbO_3$.

To reach this goal, two different possible scenarios are discussed. The first scenario is including a microstructural point of view while the second scenario is taking different conduction mechanisms into account. However, the main focus is put on the second scenario as it is the more promising approach. In addition, two different cases are analyzed for the second scenario considering different transport mechanisms. First, only the $NaNbO_3$-based samples are discussed. Afterwards, the most promising model found for $NaNbO_3$ is adopted to $KNbO_3$.

Let us first consider the undoped $NaNbO_3$ material. Looking at Fig. 7.9, which is presented in Fig. 8.1 again for convenience, two overall questions can be formulated:

1. What are the electrical transport mechanisms in $NaNbO_3$?
2. What is determining the electrical conductivity measured with AC and DC?

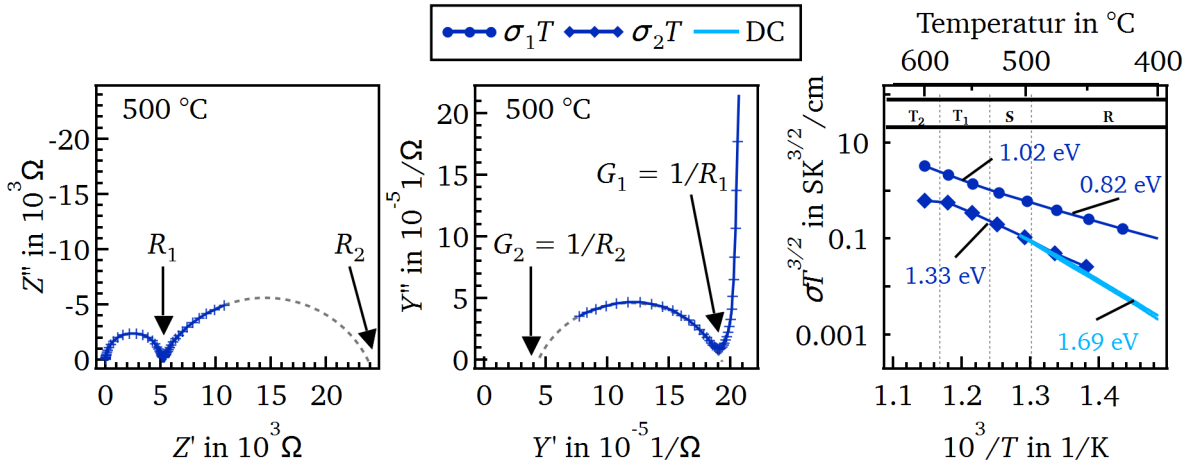

Figure 8.1.: Impedance and admittance Nyquist plots for $NaNbO_3$ at $500\,°C$ are shown. An extrapolation of the second component is illustrated in both graphs. R_1, R_2, G_1, and G_2 are the resistance and conductance of the corresponding parts. On the right side, conductivity multiplied by $T^{3/2}$ values of both AC-resistances and DC-results are plotted as function of temperature. Activation energies are marked in the relevant temperature regions.

As examined in Section 7.3 one full and one third semicircle can be observe in the Nyquist plot of the impedance data. Furthermore, the total AC-conductivity represented by the conductance G_2 in the middle of Fig. 8.1 is approximately the same as the measured DC-conductivity. Hence, the question is what the different origins of these two contributions are. In the following two different scenarios, which could explain these observations, are compared.

8.1. Different scenarios explaining the electrical transport in sodium niobate

Impedance measurements examine the frequency dependent conductivity. Therefore, it is possible to separate mechanisms appearing in different frequency ranges. Fast processes are dominating the high frequency region while slow processes are appearing at low frequencies because they cannot follow the electric field at high frequencies any more. In polycrystalline samples, grain boundaries can hinder the movement of electronic and ionic charge carriers due to potential barriers at the grain boundaries leading to a higher resistance. This could lead to an additional RC-element and a second semicircle appearing in the impedance Nyquist plot as shown in scenario 1 of Fig. 8.2 [290, 314, 315].

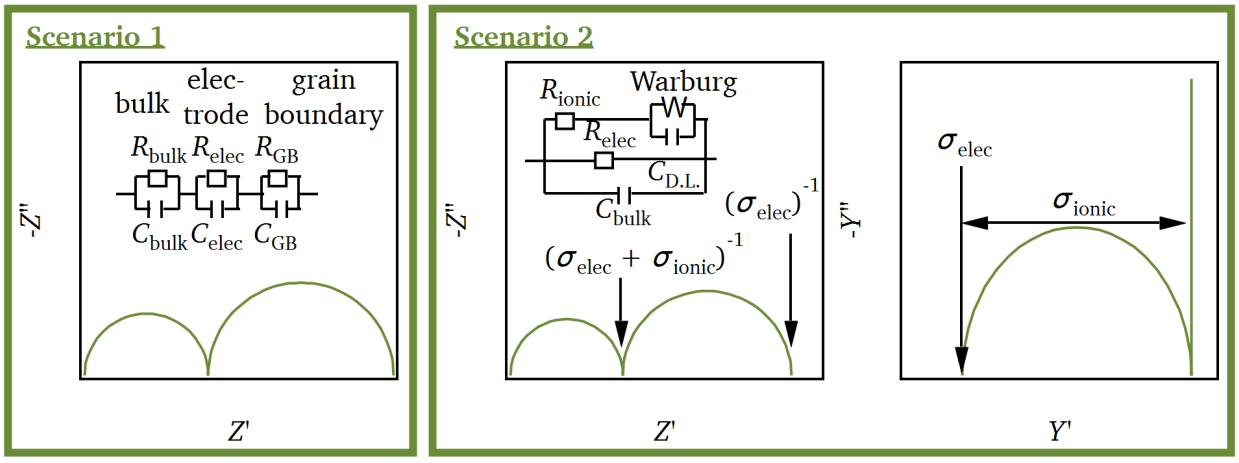

Figure 8.2.: Scenario 1: Impedance Nyquist plot with equivalent circuit for a bulk, electrode, and grain boundary process in series. Scenario 2: Impedance Nyquist plot and equivalent circuit of mixed electronic and ionic conduction on the left side. Corresponding admittance plot with electronic σ_{elec} and ionic conductivity σ_{ionic} on the right side. Adapted from [316].

However, ionic or electronic transport could also appear along the grain boundaries, which could, e.g. be faster than the bulk process resulting in an additional element with lower resistance [317]. Furthermore, a high resistance step at the electrode can cause a second semicircle within the impedance Nyquist plot [290, 314]. For example the oxygen incorporation at the electrode could be slow dominating the low frequency part [314].
If we apply this microstructural picture to the measured conductivity results, it would mean that the first semicircle is representing the bulk conductivity while the emerging second semicircle is caused by a high resistance process at the grain boundaries or the electrode. For $NaNbO_3$-containing samples, a second low frequency contribution has been mainly attributed to grain boundary effects in literature [138, 143, 150, 213].
In Section 7.1.2 and 7.4 ion diffusion is observed. At least two different species can be identified, which are most likely sodium and oxygen. Hence, the bulk conductivity is either purely ionic or a mixture of ionic and electronic conductivity. In literature, the bulk conductivity is related to oxygen vacancy migration [138, 213] or small polaron hopping [150].
This model implies that DC-conductivity is measuring both, bulk and grain boundary or electrode conductivity, but is mainly dominated by the higher resistant grain boundary or electrode part. Grain boundary barriers could hinder both electronic and ionic charges from moving. In this case, the second semicircle could represent the grain boundary resistance and the first one the bulk resistance, which is about one order of magnitude lower. As the bulk would not be highly conductive, no varistor effect would be expected. Indeed, no varistor was observed during high-voltage measurements at room temperature, which was shown in Fig. 5.11 in Section 5.5. A varistor effect can be seen in materials with highly conductive grains in the range of $1\,\Omega$ cm with highly insulating grain boundaries as in ZnO [21]. Therefore, the interpretation of the two semicircles as bulk and grain boundary contributions cannot be ruled out. In order to clarify whether grain boundaries play a role in the observed conduction behavior, single crystals should be examined to probe only the bulk conductivity. However, the single crystals prepared within the FLAME project were too small to conduct conductivity experiments.
In addition, oxygen incorporation at the electrode could be a reason for the observed high resistance. In order to analyze and discuss such electrode effects causing the second semicircle in more detail and to exclude them as possible origins, impedance measurements with different electrode materials should be conducted in future [290]. If an electrode effect is responsible for the appearance of the second semicircle, its resistance value should change with the electrode material. If the second semicircle stays unaffected, then its origin cannot be explained by an electrode effect. Various electron conducting electrodes, e.g. platinum, silver, and gold could be used to analyze this effect [290]. In addition, oxygen or sodium exchange at the electrode can be investigated by applying purely oxygen or sodium conducting electrodes. Here, the most important part is that the electrodes are conducting only one ionic species and no electronic charge carriers. This is not trivial. In order to examine oxygen ion contributions oxygen ion conductors such as Y-stabilized ZrO_2, $La_{0.9}Sr_{0.1}Ga_{0.8}Mg_{0.2}O_{2.85}$,

$Ce_{0.9}Gd_{0.1}O_{2.85}$, or $Bi_2V_{1.9}Cu_{0.1}O_{5.35}$ can be applied as electrode [236]. Good sodium ion conductors are β''-alumina and NASICON (NAtrium Super Ion CONductor)-type materials, e.g. $Na_3Zr_2Si_2PO_{12}$ or $Na_{3.35}La_{0.35}Zr_{1.65}Si_2PO_{12}$, which can be used as electrode for investigating sodium ion conduction [318–320].

Another approach explaining the two contributions examined in the impedance experiments is the consideration of different transport mechanisms, i.e. electronic and ionic conductivity. Scenario 2 of Figure 8.2 shows the impedance Nyquist plot with equivalent circuit on the left side and the corresponding admittance plot on the right side [316].
In the equivalent circuit R_{ionic} and R_{elec} represent the resistance of the ionic and electronic conduction process, respectively, which are in parallel with the total bulk capacitance. The Warburg impedance describes the diffusion-controlled charge transfer at the electrode whereas the double layer capacitance $C_{\text{D.L.}}$ represents the polarization of the electrode. These parallel elements are in series with the ionic resistance [316, 321]. With this equivalent circuit the resistance including both semicircles can be expressed by the electronic conductivity ($^1/_{\sigma_{\text{elec}}}$) whereas the first semicircle is caused by a mixture of electronic and ionic conductivity ($^1/_{(\sigma_{\text{elec}}+\sigma_{\text{ionic}})}$). Applying this scenario to the measured impedance data would mean that the resistance R_2 in Fig. 8.1 is a measure for the electronic conductivity and resistance R_1 is a mixture of electronic and ionic conductivity. Hence, by means of DC-experiments only the electronic conductivity is measured. The AC-conductivity extracted from the first semicircle is at least one order of magnitude higher than the DC-conductivity. This implies that the first contribution is mainly determined by the ionic conductivity. Hence, the following hypothesis can be established:

Hypothesis

- → DC experiments are measuring the electronic conductivity.
- → AC measurements are examining electronic and ionic conductivity but are dominated by the ionic conductivity in the present case.
- → Ionic conductivity is higher than electronic conductivity in the present case.

As the first microstructural scenario needs more experimental investigations with different electrode materials and single crystals to figure out whether the second semicircle is caused by an electrode or grain boundary effect or not, we try to explain the observed conductivity measurements with the second scenario. This scenario includes the different transport mechanisms via electronic or ionic conduction, which can be revisited for the start by some simple calculations and considerations. In the following sections, band transport via electrons and holes and polaron transport via electron and hole polarons on the niobium ($Nb^{4+/5+}$) and oxygen site ($O^{2-/-}$) are examined, respectively.

8.2. Explanation of the electrical transport mechanism by ionic and electronic conductivity

As explained in the previous section, we assume that the AC-measurements are examining mainly the ionic conductivity while the DC-experiments are dominated by electronic conduction. In addition, it was shown that oxygen, sodium, and potassium are mobile in $NaNbO_3$ and $KNbO_3$. Hence, the conductivity of the impedance measurements is the sum of oxygen and alkaline ion movement. This means that the activation energies include both contributions as well. The activation energies of all investigated samples is ranging between $0.7\,\text{eV}$ and $1.3\,\text{eV}$. Oxygen migration exhibits in the most oxide perovskite materials an activation energy within this range [303]. Hence, we could assume that the ionic conductivity is dominated by oxygen migration. However, in order to determine the exact activation energy of oxygen and sodium ions, AC-measurements with electrodes conducting only oxygen or sodium ions are required as already suggested in the previous section. Such experiments could not be conducted within this work due to time limitations. Therefore, in the next sections only the DC-conductivity is analyzed in more detail because simple calculations and considerations can be done for first estimations.

8.2.1. Analysis of DC-conductivity of undoped sodium niobate

In this section a model explaining the observed DC-conductivity of undoped $NaNbO_3$ with electronic transport is derived. Two cases are investigated, the first one including band conduction and the second one considering polaron conduction.
Figure 8.3 a) illustrates the temperature dependent conductivity of undoped $NaNbO_3$ recorded in nitrogen (orange curve) and in air after the measurement in nitrogen (blue curve), which has been analyzed in more detail in Section 7.1.2. The product of conductivity and $T^{3/2}$ as a function of temperature for both curves is shown in Fig. 8.3 b). Here, the activation energies extracted from the cooling curves at low and high temperatures are marked. In both diagrams, the different polymorphs are indicated as well. As reported in Section 7.3, the activation energies above $340\,^{\circ}\text{C}$ are much larger than below this temperature. Above $340\,^{\circ}\text{C}$ the activation energy in nitrogen is $1.71\,\text{eV}$ while in air it is $1.64\,\text{eV}$. Below $340\,^{\circ}\text{C}$ the activation energy is $0.62\,\text{eV}$ and $0.52\,\text{eV}$ in nitrogen and air, respectively.

Investigating these two graphs, the following questions can be outlined:

1. Why is the conductivity p-type above $340\,^{\circ}\text{C}$ and n-type below $340\,^{\circ}\text{C}$?
2. What are the transport mechanisms in the two temperature regimes?
3. Why do we have a change in activation energy between $300\,^{\circ}\text{C}$ and $350\,^{\circ}\text{C}$?
4. What is the cause for the different activation energies in nitrogen and air?

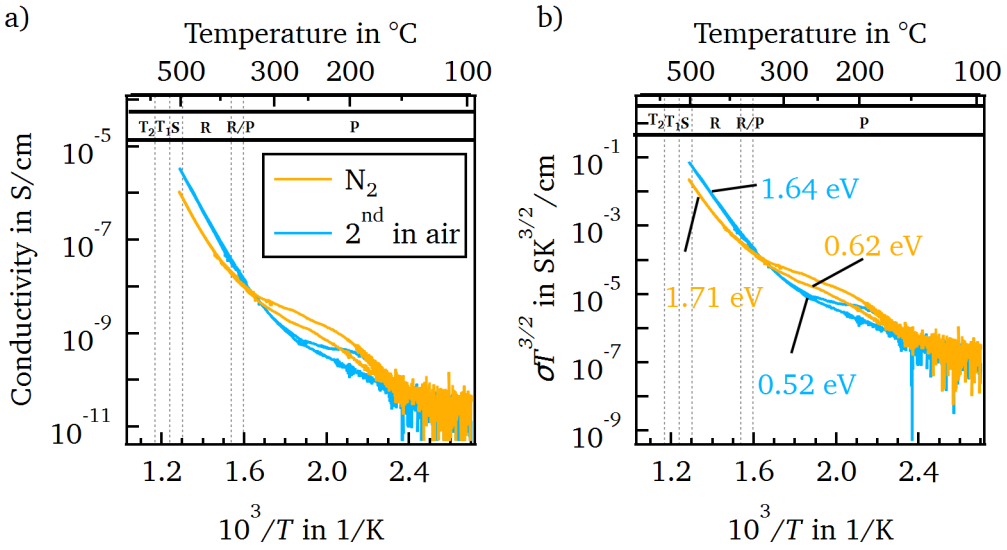

Figure 8.3.: Temperature dependent conductivity in nitrogen and in air for undoped $NaNbO_3$ in a) and the product of the conductivity and $T^{3/2}$ as function of temperature for both curves in b). The activation energies for both measurements are extracted from the cooling curves and indicated below and above $340\,°C$.

Case 1: Band conduction

In the following band conduction is considered as the main transport mechanism observed by applying an DC-field. Hence, the idea is that:

Hypothesis

→ At high temperatures (above $340\,°C$) only intrinsic band conductivity is measured.

→ The band conductivity of holes (p-type) is dominating.

Although p-type conductivity is dominating above $340\,°C$ it is assumed that the charge carrier concentrations of holes and electrons are in the same range due to the change from p- to n-type behavior at $340\,°C$ ($p \approx n$). For intrinsic conductivity Eq. 2.12 is valid, which implies that the activation energy for intrinsic band conduction is half the band gap. Assuming that the band gap value of $3.5\,eV$ extracted from the EELS spectrum analyzed in Section 6.2.2 is valid, we obtain an activation energy of $1.75\,eV$, which is close to the determined $1.64\,eV$ to $1.71\,eV$ above $340\,°C$. If we further estimate that p-type conductivity is dominant Eq. 2.19 can be reduced to the following term.

$$\sigma = q\mu_p p \tag{8.1}$$

At $500\,°C$ a conductivity of $5 \times 10^{-6}\,S\,cm^{-1}$ is evaluated. By means of Eq. 2.12, a band gap of $3.5\,eV$,

and density of states in conduction and valence band of $N_{\mathrm{CB}} = N_{\mathrm{VB}} = 10^{20}\,\frac{1}{\mathrm{cm}}$ the concentration of holes can be calculated at $500\,^{\circ}\mathrm{C}$.

$$p = \sqrt{N_{\mathrm{CB}} N_{\mathrm{VB}}} \exp\left(-\frac{E_{\mathrm{G}}}{2 k_{\mathrm{B}} T}\right) \tag{8.2}$$

$$= \sqrt{10^{20}\,\frac{1}{\mathrm{cm}^3} \cdot 10^{20}\,\frac{1}{\mathrm{cm}^3}} \exp\left(-\frac{3.5\,\mathrm{eV}}{2 \cdot 8.617 \cdot 10^{-5}\,\frac{\mathrm{K}}{\mathrm{eV}} \cdot 773\,\mathrm{K}}\right) \tag{8.3}$$

$$= 3.9 \cdot 10^{8}\,\frac{1}{\mathrm{cm}^3} \tag{8.4}$$

Consequently, the mobility of the holes can be determined as follows:

$$\mu_p = \frac{\sigma}{q p} \tag{8.5}$$

$$= \frac{5 \cdot 10^{-6}\,\frac{\mathrm{S}}{\mathrm{cm}}}{1.6 \cdot 10^{-19}\,\mathrm{C} \cdot 3.9 \cdot 10^{8}\,\frac{1}{\mathrm{cm}^3}} \tag{8.6}$$

$$= 8 \cdot 10^{4}\,\frac{\mathrm{cm}^2}{\mathrm{Vs}} \tag{8.7}$$

This hole mobility of $8 \times 10^4\,\mathrm{cm^2\,V^{-1}\,s^{-1}}$ is too high for hole band conduction. In literature, a hole mobility of $0.1\,\mathrm{cm^2\,V^{-1}\,s^{-1}}$ and $1.0\,\mathrm{cm^2\,V^{-1}\,s^{-1}}$ at $950\,^{\circ}\mathrm{C}$ and room temperature is reported for SrTiO3, respectively [322]. These values are three to four orders of magnitudes lower than the one calculated here.

In Section 6.6 it has been already proposed that the electrical band gap is much larger than the optical band gap measured with EELS or optical spectroscopy. It was postulated that due to an exciton or an electron polaron formation the optical band gap is reduced in comparison to the electrical one. Hence, instead of electron band conduction, we can also consider electron polaron conduction on the Nb-site, which leads to a reduction of $\mathrm{Nb^{5+}}$ to $\mathrm{Nb^{4+}}$. Therefore, in Eq. 2.12 instead of the density of states in the conduction band the number of niobium atoms has to be taken into account. In $\mathrm{NaNbO_3}$ the concentration of niobium atoms is $1.6 \times 10^{22}\,\mathrm{cm^{-3}}$. With this value a hole concentration of $5 \times 10^9\,\mathrm{cm^{-3}}$ and a new hole mobility of $6 \times 10^3\,\mathrm{cm^2\,V^{-1}\,s^{-1}}$ is established. Although this number is one order of magnitude lower than the one calculated with electron band conduction, it is still too high for realistic hole mobility. Therefore, we can conclude that hole band conduction with an activation energy of half the band gap or half the energy distance between valence band and $\mathrm{Nb^{4+/5+}}$-level cannot explain the p-type conduction behavior above $340\,^{\circ}\mathrm{C}$.

Case 2: Polaron conduction

Instead of band conduction, electron and hole polaron conduction is taken into account as the responsible transport mechanism for the observed DC-process, now. In Section 2.4.3 the appearance of extrinsic and intrinsic conductivity regimes has been explained by Schottky defect pairs. However,

the polaron concentration can also be determined extrinsically by other defects or dopants in a lower temperature range while at high temperatures intrinsic polaron conduction can dominate. Hence, at low temperatures the activation energy would be governed by half of the polaron binding energy whereas at high temperatures it would be given by the sum of formation and half of the binding energy of the polarons. However, in the following sections we will see that the formation energy is different for hole and electron polarons as the Fermi level is not located in the mid-gap between hole and polaron state. Hence, the formation energy is determined by the Fermi level location, which is defined by the extrinsic defects. This means that the intrinsic conductivity part of the polaron model cannot be taken as intrinsic band conductivity, which is why in the following the "intrinsic" polaron conduction is set in quotation marks. As all conductivity measurements are conducted at room temperature and above, it is assumed that small polaron hopping in the diabatic regime is valid. Tunneling of polarons from one site to the other is expected to take place in the adiabatic regime, which appears at temperatures below room temperature [59].
In literature small polaron hopping is suggested by the majority of the publications investigating the electronic conductivity in $NaNbO_3$ as reason for the observed conduction curves [144, 145, 149, 150, 152]. However, it is never mentioned what kind of polarons could be responsible. In other niobium containing perovskite materials, e.g. $LiNbO_3$, the appearance of the reduced Nb^{4+} form has been investigated as well [74–76]. In addition, hole polarons on the O-site are considered as well in $LiNbO_3$. In general, hole polarons are mainly assumed to be located on the O-site in oxide materials [74, 76, 323]. Hence, possible small polaron candidates are $Nb^{4+/5+}$ and $O^{2-/-}$. With this knowledge following hypothesis can be formulated:

Hypothesis

- → The electronic conductivity is determined by polaron transport.
- → Electron polarons are trapped on the Nb-site leading to a reduction of Nb^{5+} to Nb^{4+}.
- → Hole polarons are trapped on the O-site leading to an oxidation of O^{2-} to O^{-}.
- → Above $340\,°C$ hole polarons are dominating the process and "intrinsic" hole polaron conductivity (p-type) is measured.
- → Below $340\,°C$ electron polarons are dominating the process, which concentration is fixed extrinsically by oxygen vacancies, hence, extrinsic electron polaron conductivity (n-type) is measured.

In order to establish a model explaining the DC-conductivity by small polaron hopping, the charge equilibrium must be considered. Besides electron and hole polarons, oxygen and sodium vacancies are most likely present in $NaNbO_3$. These ionic defects are assumed to be responsible for the higher

conductivity observed in the impedance measurements as well as for the degradation and relaxation behavior conducted by the DC-experiments with changing electric field and oxygen partial pressure, respectively. The following equation for charge neutrality can be formulated as:

$$[\mathrm{O}_{\mathrm{O}}^{\cdot}] + 2[\mathrm{V}_{\mathrm{O}}^{\cdot\cdot}] = [\mathrm{V}_{\mathrm{Na}}^{\prime}] + [\mathrm{Nb}_{\mathrm{Nb}}^{\prime}] \tag{8.8}$$

The concentration of sodium vacancies $[\mathrm{V}_{\mathrm{Na}}^{\prime}]$ is assumed to be fixed by the amount of sodium evaporating during sintering. In contrast, the concentration of oxygen vacancies $[\mathrm{V}_{\mathrm{O}}^{\cdot\cdot}]$ can change at elevated temperatures when annealing in different atmospheres. Furthermore, we assume that the defect concentration of the vacancies is much larger than the electron and hole polaron concentration. Hence, following relation applies:

$$[\mathrm{V}_{\mathrm{Na}}^{\prime}] \gg [\mathrm{Nb}_{\mathrm{Nb}}^{\prime}] \qquad \text{and} \qquad 2[\mathrm{V}_{\mathrm{O}}^{\cdot\cdot}] \gg [\mathrm{O}_{\mathrm{O}}^{\cdot}] \tag{8.9}$$

It is further assumed that more $\mathrm{V}_{\mathrm{O}}^{\cdot\cdot}$ than half of $\mathrm{V}_{\mathrm{Na}}^{\prime}$ are created during sintering and/or post-annealing. The higher number of $\mathrm{V}_{\mathrm{O}}^{\cdot\cdot}$ is then compensated by electron polarons. Consequently, the concentration of hole polarons can be neglected and the concentration of electron polarons is fixed extrinsically by the concentration of $\mathrm{V}_{\mathrm{O}}^{\cdot\cdot}$ at low temperatures.

$$2[\mathrm{V}_{\mathrm{O}}^{\cdot\cdot}] > [\mathrm{V}_{\mathrm{Na}}^{\prime}] \qquad \rightarrow \qquad 2[\mathrm{V}_{\mathrm{O}}^{\cdot\cdot}] - [\mathrm{V}_{\mathrm{Na}}^{\prime}] = \mathrm{Nb}_{\mathrm{Nb}}^{\prime} \tag{8.10}$$

We can now apply these assumptions to the polaron model introduced in Section 2.4.1. Figure 8.4 illustrates the extrinsic and "intrinsic" regime with polaron formation energy E_{Pf} and binding energy E_{PB} of the measured conductivity multiplied by $T^{3/2}$ in dependence of the temperature on the left side. On the right side the polaron formation and binding energies are put in perspective to the relevant energy bands.

In the extrinsic regime ($T < 340\,^{\circ}\mathrm{C}$) the electron polaron concentration is fixed by the $\mathrm{V}_{\mathrm{O}}^{\cdot\cdot}$ concentration:

$$c_{\mathrm{Nb}^{4+}} = 2[\mathrm{V}_{\mathrm{O}}^{\cdot\cdot}] - [\mathrm{V}_{\mathrm{Na}}^{\prime}] = [\mathrm{Nb}_{\mathrm{Nb}}^{\prime}]_{\mathrm{ext}} = \text{constant} \tag{8.11}$$

Hence, in this region the conductivity is determined by polaron migration on the Nb-site and can be written as in Eq. 8.12, which shows that the activation energy only depends on the electron polaron binding energy $E_{\mathrm{PB}}^{\mathrm{e}}$.

$$\begin{aligned} \sigma_{\mathrm{ext}} &= c_{\mathrm{Nb}^{4+}} \cdot \mu_{\mathrm{Nb}^{4+}} \cdot q \\ &= [\mathrm{Nb}_{\mathrm{Nb}}^{\prime}]_{\mathrm{ext}} \cdot \frac{\mu_{\mathrm{Nb}^{4+},0}}{T^{3/2}} \exp\left(-\frac{E_{\mathrm{PB}}^{\mathrm{e}}/2}{k_{\mathrm{B}}T}\right) \cdot q \end{aligned} \tag{8.12}$$

In the "intrinsic" regime the polaron concentration is not fixed by the vacancy concentration any more. Here, the intrinsically formed polaron concentration determines the overall polaron concentration. Assuming a higher mobility of the hole polarons then explains why the hole polaron conductivity is

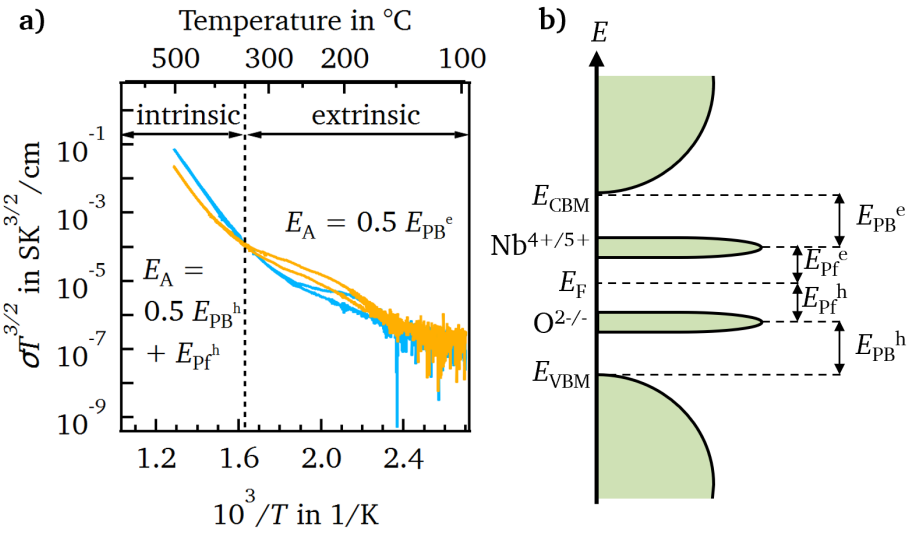

Figure 8.4.: a): "intrinsic" and extrinsic regime with corresponding activation energies. b): Polaron formation and binding energies in perspective to the relevant energy bands.

larger than the electron polaron conductivity. Therefore, the activation energy is not only determined by the hole polaron binding energy but also by the hole polaron formation energy.

$$\begin{aligned}\sigma_{\text{int}} &= c_{\text{O}^-} \cdot \mu_{\text{O}^-} \cdot q \\ &= N_{\text{O}} \exp\left(-\frac{E_{\text{Pf}}^{\text{h}}}{k_{\text{B}}T}\right) \cdot \frac{\mu_{\text{O}^-,0}}{T^{3/2}} \exp\left(-\frac{E_{\text{PB}}^{\text{h}}/2}{k_{\text{B}}T}\right) \cdot q\end{aligned} \tag{8.13}$$

By means of this model the above formulated questions can be answered. The first two questions concerning the change from n- to p-type behavior at $340\,^{\circ}\text{C}$ and the transport mechanisms in the two temperature regimes can be explained by the change in the dominating transport species. At low temperatures the migration of electron polarons on the Nb-site are dominant because of their higher concentration fixed extrinsically by $V_{\text{O}}^{\cdot\cdot}$. With rising temperature the concentration of hole polarons is increasing leading to a change of the dominating transport species at around $340\,^{\circ}\text{C}$. Hence, at high temperatures small polaron hopping on the O-site is dominating the electronic conductivity.
The third question regarding the difference in activation energy between the low and high temperature region can be answered by the combination of changing from extrinsic to "intrinsic" region and from electron polaron to hole polaron conduction. Therefore, the activation energy below $340\,^{\circ}\text{C}$ is lower because it is only determined by the migration of the electron polarons meaning half of the polaron binding energy. Above $340\,^{\circ}\text{C}$ the activation energy is much higher because it is given by the sum of the hole polaron formation energy and half of the hole polaron binding energy.
The last question concerning the change in activation energy at high temperatures when heating in nitrogen instead of dry air can be explained by the variation of the Fermi level. As the polaron formation energy is the energy difference between polaron band and Fermi level, its value depends

on the position of the Fermi level. Consequently, when the Fermi level is increased by heating in nitrogen, $E_{\mathrm{Pf}}^{\mathrm{h}}$ is increasing, which results in a higher activation energy.

8.2.2. Analysis of DC-conductivity of donor doped sodium niobate

In this section the DC-conductivity of donor doped $NaNbO_3$ is analyzed. However, $Na_{0.99}Ca_{0.01}NbO_3$ is mainly in focus because for $Na_{0.99}Sr_{0.01}NbO_3$ the low temperature data is missing due to a contact problem during the measurement. Furthermore, as band conduction could be excluded already by the examination of the undoped material, only the polaron model is taken into account within this section.

Figure 8.5 a) shows the conductivity of $Na_{0.99}Ca_{0.01}NbO_3$ as function of the temperature measured in nitrogen and examined in dry air after the measurement in nitrogen. In Fig. 8.5 b) the product of conductivity and $T^{3/2}$ is plotted in dependence of the temperature. The activation energies above and below $312\,^{\circ}$C and $220\,^{\circ}$C are marked. In addition, the different polymorphs stable within different temperature windows are indicated on top. Compared to undoped $NaNbO_3$ the activation energies above $312\,^{\circ}$C are both, in nitrogen ($1.80\,$eV) and air ($1.97\,$eV), higher in $Na_{0.99}Ca_{0.01}NbO_3$. Below $312\,^{\circ}$C the value in nitrogen ($1.21\,$eV) is higher as in undoped $NaNbO_3$ whereas the activation energy in air ($0.44\,$eV) is in the same range. Interestingly, below $220\,^{\circ}$C the activation energy is changing again. By analyzing and comparing these two graphs further with the ones shown in Fig. 8.3, following questions can be outlined:

1. Why is the conductivity n-type over the whole temperature range?
2. What are the transport mechanisms in the three temperature regions?
3. Why do we have a change in activation energy around $312\,^{\circ}$C and again around $220\,^{\circ}$C?
4. Why are the activation energies higher for $Na_{0.99}Ca_{0.01}NbO_3$ than for $NaNbO_3$?
5. Why is the activation energy above $312\,^{\circ}$C higher in air than in nitrogen?

Calcium is acting as donor on the sodium side, hence, n-type conductivity should be supported. Indeed, a n-type behavior is observed over the whole temperature range when comparing the conductivity measurements in nitrogen and air. Here, the measured conductivity is higher in nitrogen than in air. Applying the polaron model developed in the previous section for undoped $NaNbO_3$ to Ca-doped $NaNbO_3$ would mean that electron polaron conduction dominates the complete examined temperature range. Nevertheless, a change in activation energy can still be detected at around $312\,^{\circ}$C, which suggests that at low temperatures the conductivity is determined by extrinsic defects and at high temperatures ”intrinsic” conductivity is dominant. Hence, the following hypothesis can be stated:

Hypothesis

→ The electronic conductivity is determined by electron polaron transport on the Nb-site leading to a reduction of Nb^{5+} to Nb^{4+}.

→ Above 312 °C "intrinsic" electron polaron conductivity is measured.

→ Below 312 °C the concentration of electron polarons is fixed extrinsically by oxygen vacancies and calcium dopants, hence, extrinsic electron polaron conductivity is measured.

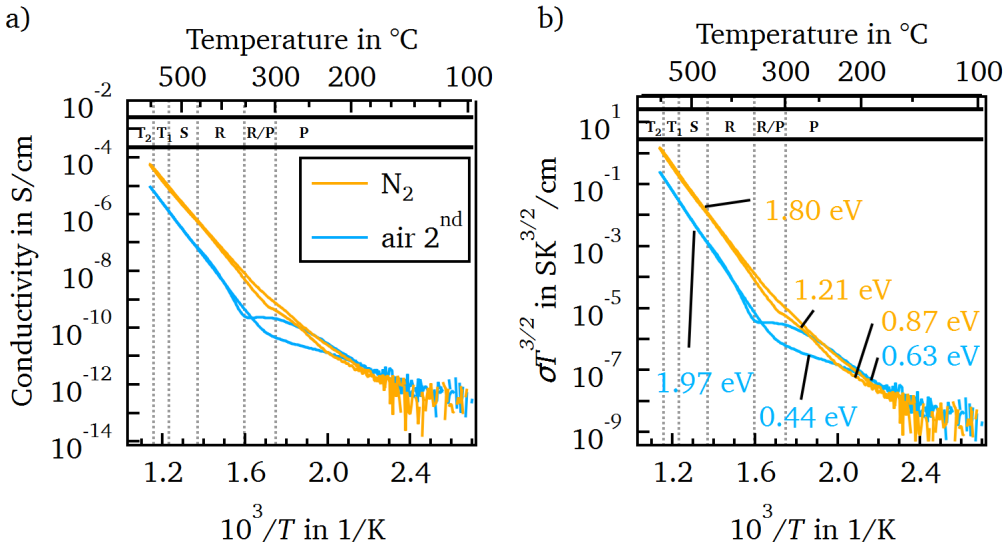

Figure 8.5.: Temperature dependent conductivity in nitrogen and in air for Ca-doped $NaNbO_3$ in a) and the product of the conductivity and $T^{3/2}$ as function of temperature for both curves in b). The activation energies for both measurements are extracted from the cooling curve. At around 220 °C and 312 °C a change in activation energy occurs.

Similar to the considerations made for undoped $NaNbO_3$, the charge equilibrium should be examined first. Besides electron and hole polarons, and oxygen and sodium vacancies, calcium dopants must be included in the charge neutrality equation.

$$[O_O^{\cdot}] + 2[V_O^{\cdot\cdot}] + [Ca_{Na}^{\cdot}] = [V_{Na}^{\prime}] + [Nb_{Nb}^{\prime}] \tag{8.14}$$

The concentration of the sodium vacancies $[V_{Na}^{\prime}]$ is fixed by the amount of evaporated sodium during sintering while the concentration of oxygen vacancies $[V_O^{\cdot\cdot}]$ can still be adjusted when heating at elevated temperatures during post-annealing or the conductivity measurements itself. Here, we also assume that the defect concentration of the vacancies is much larger than the concentration of the polarons:

$$[V_{Na}^{\prime}] \gg [Nb_{Nb}^{\prime}] \qquad \text{and} \qquad 2[V_O^{\cdot\cdot}] + [Ca_{Na}^{\cdot}] \gg [O_O^{\cdot}] \tag{8.15}$$

However, the concentration of the electron polarons on the Nb-site are not only determined extrinsically by the concentration of $V_O^{\cdot\cdot}$ but also by the doping concentration at low temperatures.

$$2[V_O^{\cdot\cdot}] + [Ca_{Na}^{\cdot}] > [V_{Na}^{\prime}] \quad \rightarrow \quad 2[V_O^{\cdot\cdot}] + [Ca_{Na}^{\cdot}] - [V_{Na}^{\prime}] = [Nb_{Nb}^{\prime}] \tag{8.16}$$

All these assumptions can be applied again to the polaron model. Figure 8.6 a) illustrates the "intrinsic" and extrinsic regime in the $\sigma T^{3/2}$–$^1/_T$-plot. Note here that the activation energies are only controlled by the formation and binding energy of the electron polarons. In Fig. 8.6 b) these energies are put in relation to the electron and hole polaron bands as well to the conduction and valence band.

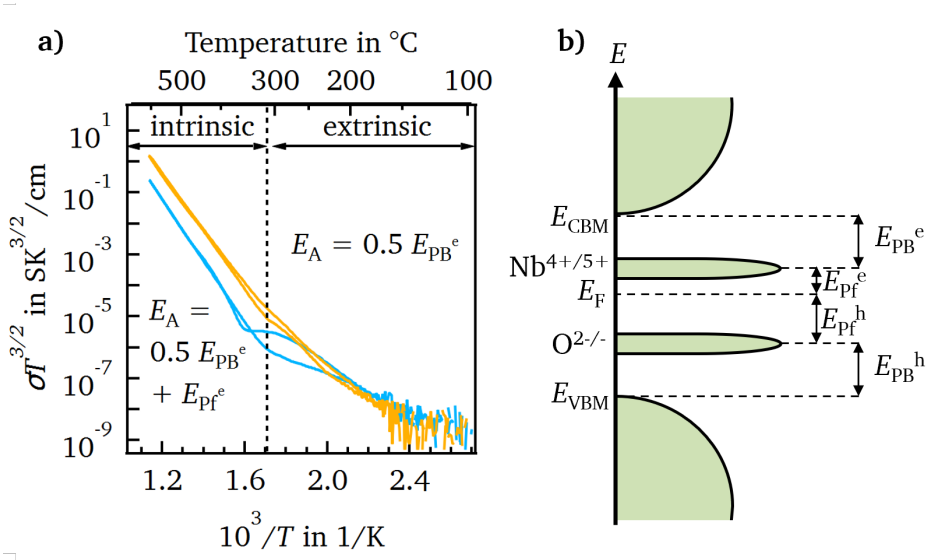

Figure 8.6.: a): "intrinsic" and extrinsic regime with corresponding activation energies of a $Na_{0.99}Ca_{0.01}NbO_3$ sample. b): Polaron formation and binding energies in perspective to the relevant energy bands.

Keeping in mind that the electron polaron concentration at low temperatures is fixed by the doping and $V_O^{\cdot\cdot}$ concentration, we can formulate the conductivity in the extrinsic and "intrinsic" part as follows:

$$\sigma_{ext} = c_{Nb^{4+}} \cdot \mu_{Nb^{4+}} \cdot q \tag{8.17}$$

$$= [Nb_{Nb}^{\prime}]_{ext} \cdot \frac{\mu_{Nb^{4+},0}}{T^{3/2}} \exp\left(-\frac{E_{PB}^{e}/2}{k_B T}\right) \cdot q \tag{8.18}$$

$$\sigma_{int} = c_{Nb^{4+}} \cdot \mu_{Nb^{4+}} \cdot q \tag{8.19}$$

$$= N_{Nb} \exp\left(-\frac{E_{Pf}^{e}}{k_B T}\right) \cdot \frac{\mu_{Nb^{4+},0}}{T^{3/2}} \exp\left(-\frac{E_{PB}^{e}/2}{k_B T}\right) \cdot q \tag{8.20}$$

Hence, the total conductivity for Ca-doped $NaNbO_3$ can be written as:

$$\sigma_{\text{tot}} = c_{\text{Nb}^{4+}} \cdot \mu_{\text{Nb}^{4+}} \cdot q \tag{8.21}$$

$$= \left[[\text{Nb}'_{\text{Nb}}]_{\text{ext}} + N_{\text{Nb}} \exp\left(-\frac{E^{\text{e}}_{\text{Pf}}}{k_{\text{B}} T} \right) \right] \cdot \frac{\mu_{\text{Nb}^{4+},0}}{T^{3/2}} \exp\left(-\frac{E^{\text{e}}_{\text{PB}}/2}{k_{\text{B}} T} \right) \cdot q \tag{8.22}$$

On the basis of this model the majority of the questions above can be answered. The first two questions can be explained by small polaron hopping of electron polarons on the Nb-site. Due to the calcium doping, the Fermi level is located closer to the $Nb^{4+/5+}$-state than to the $O^{2-/-}$-state, hence, the formation energy of the electron polarons is smaller than for the hole polarons compared to values in $NaNbO_3$. This leads to a higher concentration of electron polarons in the "intrinsic" region. Consequently, they dominate the conduction process not only in the extrinsic region but also in the "intrinsic" part.

The third question addressing the activation energy change at around $312\,^{\circ}$C and $220\,^{\circ}$C can only be partially explained. At $312\,^{\circ}$C the conductivity changes from being extrinsically determined to being intrinsically defined. Below $312\,^{\circ}$C the concentration of the electron polarons is fixed by the calcium dopant and $V_{\text{O}}^{\cdot\cdot}$ concentration, which means that the activation energy is only influenced by half of the polaron binding energy. Above $312\,^{\circ}$C the electron polaron concentration is defined by the "intrinsic" electron and hole polaron formation, which implies that the activation energy equals the sum of half of the binding energy and the formation energy of the electron polarons. However, it is not clear why the activation energy is modified again below $220\,^{\circ}$C.

The reason explaining the fourth question concerning the higher activation energy in $Na_{0.99}Ca_{0.01}NbO_3$ compared to $NaNbO_3$ are the different transport mechanisms in the "intrinsic" region. Hole and electron polarons have different binding and formation energies leading to the differences observed in the activation energies. In the extrinsic regime, the activation energy in air are similar in Ca-doped and undoped $NaNbO_3$, which agrees with hopping transport of electron polarons dominating the conductivity in both materials. Small differences of $\pm$ 200 meV can occur due to inaccuracy of the measurements and errors done during the extraction of the activation energies. However, it is not clear why the activation energy of $Na_{0.99}Ca_{0.01}NbO_3$ in the extrinsic region in nitrogen is more than double of the value in air.

The last question addressing the higher activation energy in nitrogen than in air at temperatures above $312\,^{\circ}$C can be answered by the fact that the formation energy of the electron polarons is higher in air than in nitrogen. Annealing in air leads to a shift in the Fermi level closer to the valence band, which means that the energetic distance between the $Nb^{4+/5+}$-state and Fermi level is rising, hence, the electron polaron formation energy is larger in air.

8.2.3. Applying the polaron model to undoped and donor doped sodium niobate

After analyzing and discussing the polaron model for undoped and donor doped $NaNbO_3$, we want to fit the measured data with concrete values for the electron and hole polaron binding and formation energy, their mobility, and their fixed concentration in the extrinsic regime by the $V_O^{\cdot\cdot}$ and dopant concentration. For this investigation, the assumptions of the polaron model captured so far are summarized once again.

Assumptions of the polaron model

- → The extrinsic regime is governed in both materials by small polaron hopping of electron polarons on the Nb-site, which means that $E_{A,ext} = {}^1/_2 E_{PB}^e$.
- → The electron polaron concentration within the extrinsic part in undoped $NaNbO_3$ is determined by the $V_O^{\cdot\cdot}$ concentration while in Ca-doped $NaNbO_3$ it is defined by the dopant and $V_O^{\cdot\cdot}$ concentration.
- → The "intrinsic" region of undoped $NaNbO_3$ is dominated by hole polarons, which means that $E_{A,int} = {}^1/_2 E_{PB}^h + E_{Pf}^h$.
- → The "intrinsic" region of $Na_{0.99}Ca_{0.01}NbO_3$ is dominated by electron polarons, which means that $E_{A,int} = {}^1/_2 E_{PB}^e + E_{Pf}^e$.

First, we consider the extrinsic regime, which is governed by small polaron hopping of electron polarons on the Nb-site in both, undoped and Ca-doped $NaNbO_3$. The activation energies in this region are $0.52\,\text{eV}$ and $0.44\,\text{eV}$ measured in air and $0.62\,\text{eV}$ and $1.21\,\text{eV}$ examined in nitrogen for $NaNbO_3$ and $Na_{0.99}Ca_{0.01}NbO_3$, respectively. It is unclear why the activation energy in nitrogen of $Na_{0.99}Ca_{0.01}NbO_3$ is more than double the value in air, hence, we will exclude this value from the next considerations. The other activation energies are within the same range, which is why we assume an electron polaron binding energy of $1.00\,\text{eV}$ for the sake of simplicity. This means that the extrinsic activation energy has a value of $0.50\,\text{eV}$. The second main influencing factor in this region is the electron polaron concentration, which is fixed extrinsically. It is adjusted in a way that the fitted extrinsic conductivity equals the measured one. Therefore, $[Nb'_{Nb}]_{ext}$ is set to $1.5 \times 10^{11}\,\text{cm}^{-3}$ and to $6 \times 10^{9}\,\text{cm}^{-3}$ for $NaNbO_3$ and $Na_{0.99}Ca_{0.01}NbO_3$ in air, respectively. In nitrogen the value is increased to $3.5 \times 10^{11}\,\text{cm}^{-3}$ in case of $NaNbO_3$ while for $Na_{0.99}Ca_{0.01}NbO_3$ $[Nb'_{Nb}]_{ext}$ remains the same. This is an indication that $[Nb'_{Nb}]_{ext}$ is mainly determined by the dopant concentration in $Na_{0.99}Ca_{0.01}NbO_3$ while in $NaNbO_3$ it is adjusted by the formation of $V_O^{\cdot\cdot}$.

In the "intrinsic" regime the activation energy is not only governed by the polaron binding energy but additionally by the polaron formation energy. Hence, in case of the Ca-doped sample E_{Pf}^e can be

calculated by the difference of the measured activation energy and half of the electron polaron binding energy, which equals $1.47\,\text{eV}$ in air ($1.97\,\text{eV}$ - $0.50\,\text{eV}$ = $1.47\,\text{eV}$) and $1.30\,\text{eV}$ in nitrogen ($1.80\,\text{eV}$ - $0.50\,\text{eV} = 1.30\,\text{eV}$). The number of niobium atoms in the $NaNbO_3$ lattice is $N_{\text{Nb}} = 1.6 \times 10^{22}\,\text{cm}^{-3}$ and the elementary charge of an electron representing q is $1.6 \times 10^{-19}\,\text{C}$. Taking Eq. 8.22 into account, the only undefined parameter left is the pre-factor of the electron polaron mobility $\mu_{\text{Nb}^{4+},0}$. This value is adjusted until the fitted "intrinsic" conductivity matches with the measured one. Hence, $\mu_{\text{Nb}^{4+},0}$ is set to $1.65 \times 10^7\,\text{K}^{3/2}\,\text{cm}^2\,\text{V}^{-1}\,\text{s}^{-1}$.

In the same way we can determine the pre-factor of the hole polaron mobility $\mu_{\text{O}^-,0}$ in case of undoped $NaNbO_3$. $\mu_{\text{O}^-,0}$ is modified until the "intrinsic" conductivity equals the measured one, resulting in a value of $4 \times 10^5\,\text{K}^{3/2}\,\text{cm}^2\,\text{V}^{-1}\,\text{s}^{-1}$. The perovskite lattice contains more oxygen than niobium atoms, hence, the number of oxygen atoms is $N_{\text{O}} = 4.8 \times 10^{22}\,\text{cm}^{-3}$. It is a little bit more complicated to figure out reasonable fitting parameters for the activation energy within the "intrinsic" regime of $NaNbO_3$. Here, the activation energy is the sum of the polaron formation energy and half of the polaron binding energy of the hole polarons. As we cannot determine the hole polaron binding energy from the extrinsic part as for the electron polarons, it is not clear whether the $\text{O}^{2-/-}$ trap state is a shallow state close to the valence band or a deep state positioned more in the middle of the band gap. The formation energy, in turn, is larger or smaller depending on the position of the $\text{O}^{2-/-}$ state. However, we do know that the "intrinsic" conductivity is dominated by the hole polaron transport for undoped $NaNbO_3$ while for $Na_{0.99}Ca_{0.01}NbO_3$ the transport of the electron polarons is larger. Hence, the polaron binding and formation energy of the hole polarons must be adapted in a way that the "intrinsic" hole conductivity is lower than the "intrinsic" electron conductivity in $Na_{0.99}Ca_{0.01}NbO_3$. Figure 8.7 illustrates the measured (blue curve) and fitted conductivity (black curve) of $Na_{0.99}Ca_{0.01}NbO_3$ in air for a shallow and a deep hole polaron trap state in a) and b), respectively. The contribution of the electron polarons is indicated in gray while the one of the hole polarons is colored in red. All relevant energies are marked in the conductivity plots as well as in the energy band diagrams. It is clear that the $\text{O}^{2-/-}$ trap state must be a shallow state because otherwise the hole polaron conduction overtakes the electron polaron conduction. Further fitting procedures reveal that E_{PB}^{h} cannot be larger than $0.2\,\text{eV}$ to fulfill these requirements. Now, E_{Pf}^{h} can be derived by the difference of the measured activation energy and half of the hole polaron binding energy. Hence, in air E_{Pf}^{h} is $1.54\,\text{eV}$ ($1.64\,\text{eV}$ - $0.10\,\text{eV} = 1.54\,\text{eV}$) and in nitrogen it is $1.60\,\text{eV}$ ($1.70\,\text{eV}$ - $0.10\,\text{eV} = 1.60\,\text{eV}$).

Figure 8.8 shows the measured and fitted conductivity including all relevant energies as well as the corresponding energy band diagram in air and nitrogen for $NaNbO_3$ on the left and for $Na_{0.99}Ca_{0.01}NbO_3$ on the right side. It can be seen that the model fits well to both material systems and describes the measured curves quite accurate in air and nitrogen. Furthermore, the polaron model suggests that the measured optical band gap of $3.5\,\text{eV}$ is the distance between VBM and the $\text{Nb}^{4+/5+}$-state and that the electrical band gap is $1.0\,\text{eV}$ higher.

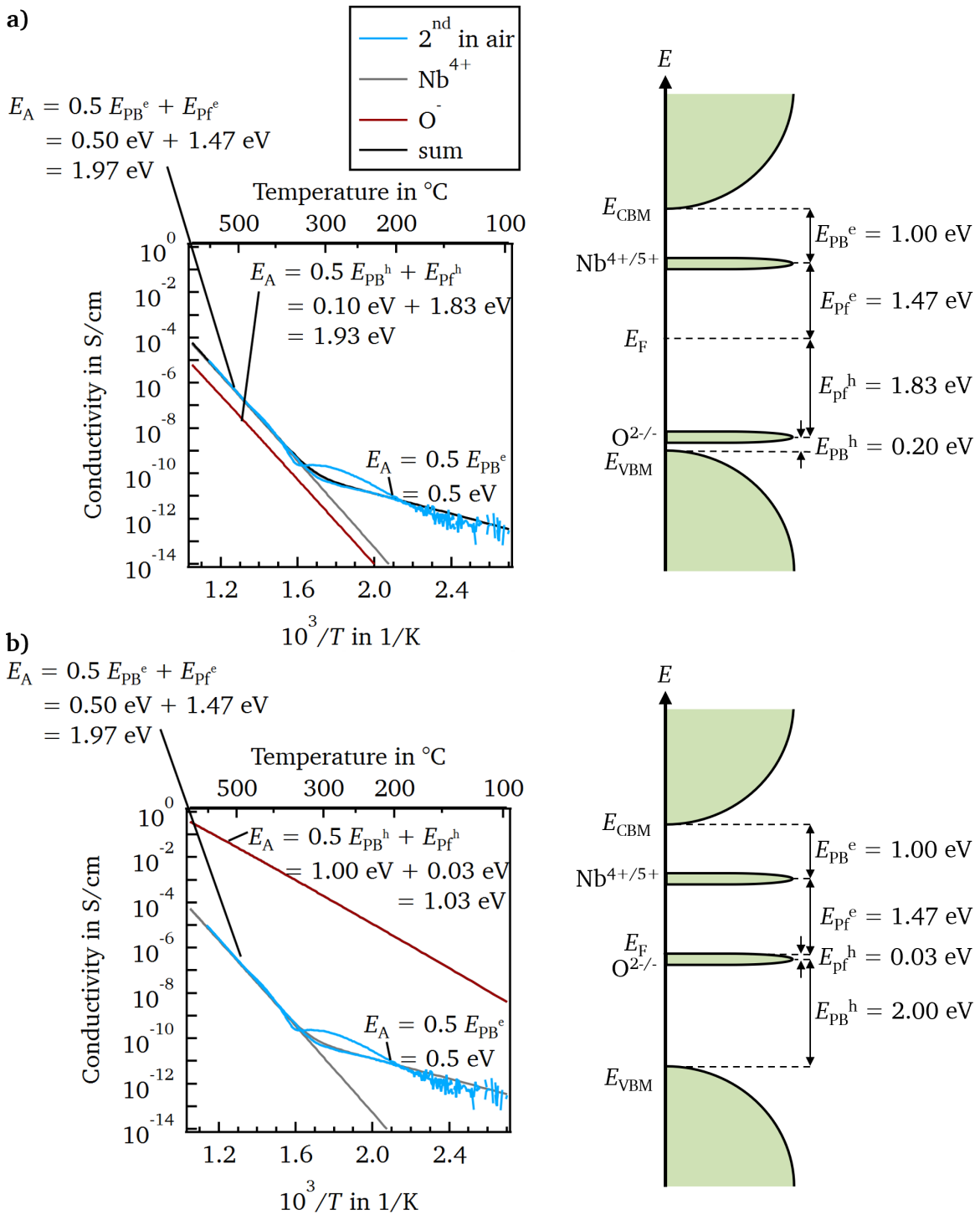

Figure 8.7.: Measured and fitted conductivity of $Na_{0.99}Ca_{0.01}NbO_3$ in air including all relevant energies and the corresponding band diagram for a shallow and a deep hole polaron trap state in a) and b), respectively.

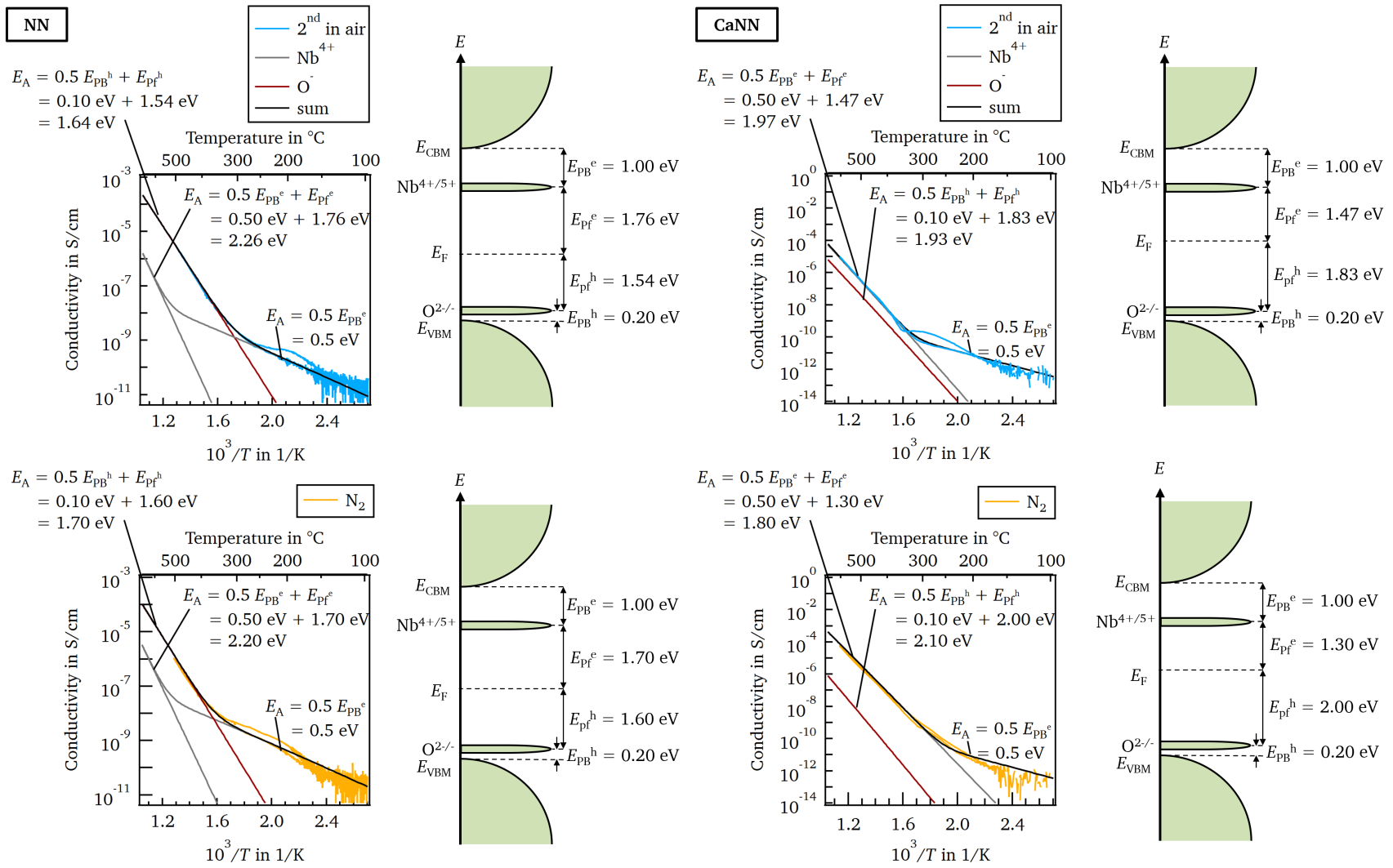

Figure 8.8.: Measured and fitted conductivity of $NaNbO_3$ on the left and of $Na_{0.99}Ca_{0.01}NbO_3$ on the right side in air (top) and nitrogen (bottom) including all relevant energies and the corresponding band diagrams.

Table 8.1 lists the hole and electron polaron concentration and mobility at $500\,°C$ in air and nitrogen for undoped and Ca-doped $NaNbO_3$. Both, the charge carrier concentrations as well as the mobility are within an acceptable range. Especially, the calculated mobility is much smaller for the polaron transport than for band transport examined in Section 8.2.1. This is a further indication that the measured conductivity can be described with the introduced polaron model.

After analyzing the conductivity examined in nitrogen and in air, which was conducted after the nitrogen experiment, with the polaron model, we can apply it to the first conductivity measurements in air before exposing the samples to nitrogen. Here, the same fitting values as before are used. Figure 8.9 shows the measured and fitted conductivity of $NaNbO_3$ in a) and of $Na_{0.99}Ca_{0.01}NbO_3$ in b) in air before exposing the samples to nitrogen including all relevant energies and the corresponding band diagrams. For undoped $NaNbO_3$ the extrinsic regime cannot be observed, at least, within the resolution limit of the picoamperemeter. Hence, only intrinsically formed polarons are contributing to the measured conductivity and hole polarons are the dominating species. $E_{\mathrm{Pf}}^{\mathrm{h}}$ equals $1.505\,\mathrm{eV}$, which is lower than the value examined for the second measurement in air of $1.540\,\mathrm{eV}$. This explains the higher conductivity of the first air measurement compared to the second one. After nitrogen annealing the extrinsic regime appears, which indicates that this step introduces $V_O^{\cdot\cdot}$ into the $NaNbO_3$ lattice. Heating in dry air once again does not annihilate all the $V_O^{\cdot\cdot}$, which implies that the formation of $V_O^{\cdot\cdot}$ is not entirely reversible.
In contrast, $Na_{0.99}Ca_{0.01}NbO_3$ exhibits an extrinsic part for the first measurement in air due to the dopants fixing the electron polaron concentration from the beginning. $E_{\mathrm{Pf}}^{\mathrm{h}}$ is the same for the experiments conducted in air both, before and after annealing in nitrogen. Hence, the formation of $V_O^{\cdot\cdot}$ is reversible in case of $Na_{0.99}Ca_{0.01}NbO_3$. This in turn supports the idea that the extrinsic electron polaron concentration $[Nb'_{Nb}]_{ext}$ is mainly determined by the Ca-dopant concentration.
In addition, this result resolves the question why the conductivity of $Na_{0.99}Ca_{0.01}NbO_3$ is higher at room temperature and lower above $350\,°C$ than the conductivity of $NaNbO_3$ when measuring the first time in air. For $Na_{0.99}Ca_{0.01}NbO_3$ the dopant concentration leads to a larger number of electron polarons and a higher conductivity in the extrinsic part from the beginning. In $NaNbO_3$ the extrinsically determined electron polarons only appear due the formation of $V_O^{\cdot\cdot}$ as result of a reducing step (nitrogen annealing). Consequently, only after this reducing procedure the conductivity of $NaNbO_3$ is also higher below $350\,°C$ than the one in $Na_{0.99}Ca_{0.01}NbO_3$.

However, without a reducing annealing no $V_O^{\cdot\cdot}$ are formed in $NaNbO_3$, hence, the extrinsic electron polaron concentration stays low. As a result the room temperature conductivity is lower in $NaNbO_3$ than in $Na_{0.99}Ca_{0.01}NbO_3$. Above $350\,°C$ the ”intrinsic” part is overtaking the extrinsic part. As the hole polarons exhibit a higher mobility than the electron polarons, the conductivity in $NaNbO_3$ is larger than in $Na_{0.99}Ca_{0.01}NbO_3$ within this region.

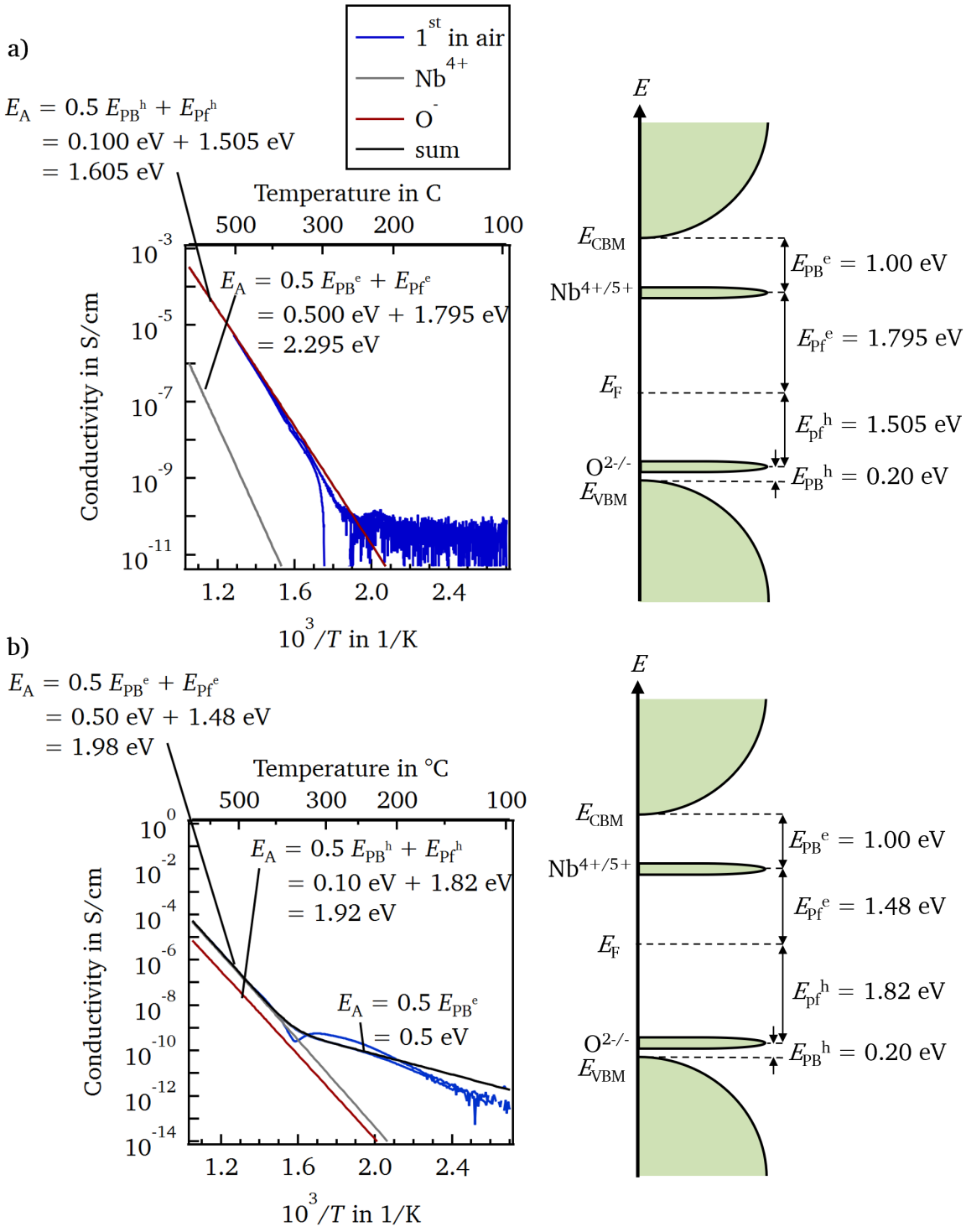

Figure 8.9.: Measured and fitted conductivity of $NaNbO_3$ and $Na_{0.99}Ca_{0.01}NbO_3$ in air before exposing the samples to nitrogen including all relevant energies and the corresponding band diagram in a) and b), respectively.

This polaron model has also been applied to the conductivity of $Na_{0.99}Sr_{0.01}NbO_3$. The results are shown in Fig. A.27 in the appendix. The extrinsic part cannot be fitted very well because of the missing data points in this regime. However, an activation energy of 0.5 eV as for the other $NaNbO_3$-based samples is assumed. Taking the same hole polaron binding energy of 0.2 eV and the same values for $\mu_{Nb^{4+},0}$ and $\mu_{O^-,0}$ into account does not result in a good fit. Furthermore, it is very confusing that the measured conductivity increases when heating in nitrogen suggesting electron polaron hopping (n-type) but the activation energy is higher when measuring in nitrogen. This in turn hints more to hole polaron transport (p-type). In Fig. A.27 the conductivity is calculated assuming hole polaron transport dominating the ”intrinsic” region because the deviation from the measured curve is less when taking hole polarons instead of electron polarons as the major transport. Nevertheless, fitted and measured conductivity differ significantly.

In summary, the hypothesized polaron model can explain the observed conductivity results of $NaNbO_3$ and $Na_{0.99}Ca_{0.01}NbO_3$. The conductivity can be divided into a high and a low temperature part, which are characterized by ”intrinsic” and extrinsic polaron concentrations. Hole and electron polarons are dominating the ”intrinsic” region for $NaNbO_3$ and $Na_{0.99}Ca_{0.01}NbO_3$ with a polaron binding energy of 0.2 eV and 1.0 eV, respectively. This means that the $O^{2-/-}$ state is a shallow trapping state located 0.2 eV above the VBM whereas the $Nb^{4+/5+}$ state is a deep trapping state positioned 1.0 eV below the CBM. The total electrical band gap is then 4.5 eV, which is 1.0 eV larger than the measured optical band gap. However, the Fermi level is not located in the middle of the two polaron states, which leads to different formation energies for the hole and electron polarons. Hence, the ”intrinsic” part cannot be understood as intrinsic band conduction because the Fermi level position is still determined by the extrinsic defects. This is the reason why the ”intrinsic” polaron conduction is set in quotation marks. For both materials, the extrinsic regime is dominated by the hopping transport of the electron polarons on the Nb-site. Their concentration is fixed by the amount of $V_O^{\cdot\cdot}$ and dopants, which are not compensated by V'_{Na}, in case of $NaNbO_3$ and $Na_{0.99}Ca_{0.01}NbO_3$, respectively. The additional dopants in $Na_{0.99}Ca_{0.01}NbO_3$ are the reason why the extrinsic region is observable when measuring in air and nitrogen. In contrast, $NaNbO_3$ shows only two regimes after annealing in nitrogen, when enough additional $V_O^{\cdot\cdot}$ are generated.
In general, by means of the polaron model the transport mechanism of $NaNbO_3$-based samples including the different activation energies can be described and the change from n- to p-type conductivity for $NaNbO_3$ is resolved.

Nevertheless, there are still open questions. The activation energies and the polaron model are adapted to the cooling curves. However, in the extrinsic regime the conductivity measured while heating is higher and has a different activation energy than during cool down. It is not clear what is causing these differences.
In contrast, in the ”intrinsic” regime the conductivity is lower during heating than during cooling for all materials in both, air and nitrogen, which is shown in more detail in Fig. 7.2 in Section 7.1.2.

For $NaNbO_3$ this phenomena could be explained by a longer time for incorporation of oxygen while heating in air decreasing the Fermi level position, hence, rising the hole polaron conductivity. In the same way the higher conductivity examined in nitrogen in case of $Na_{0.99}Ca_{0.01}NbO_3$ could be caused by a longer time for oxygen removal resulting in a higher Fermi level and an increased electron polaron conductivity. However, it is not clear why the conductivity is also higher during cool down in nitrogen and air for $NaNbO_3$ and $Na_{0.99}Ca_{0.01}NbO_3$ as here it should be lower according to this explanation, respectively.
Furthermore, it is not clear why the activation energy is changing again below $220\,°C$ in case of the Ca-doped sample. Having a closer look on the conductivity performed in nitrogen for $NaNbO_3$ a similar change in activation energy is observed at around $235\,°C$. It might be that this change in activation energy is not detected in air because the conductivity is lower and reaches the resolution limit of the picoamperemeter. Hence, it could be that this features is a general process appearing in $NaNbO_3$. Transition temperatures ranging from $225\,°C$ to $300\,°C$ were reported in literature and shown in Fig. 2.13 for the Q-to-R phase transition [114–117]. In addition, an anomaly at $150\,°C$ was detected in $NaNbO_3$-based materials [112, 114, 116, 136]. This anomaly is not fully understood but often explained by incommensurate phases [114, 136] or the appearance of ferroelectric nanodomains within an antiferroelectric matrix [112, 116]. Such an anomaly was also observed in the temperature dependent permittivity curves of $Na_{0.99}Ca_{0.01}NbO_3$ shown in Fig. 5.12 in Section 5.6. Both explanations do not match $100\,\%$ the temperature window of the activation energy change at $220\,°C$ for $Na_{0.99}Ca_{0.01}NbO_3$. Hence, the origin remains unknown so far.
Finally, we must point out that all the calculations are done with a constant Fermi level over the whole temperature range. However, the Fermi level should decrease with temperature as the band gap is reduced with temperature as well. A changing Fermi level would mean that the polaron and hole formation energy is changing with temperature, too. This would result in a continuously modifying activation energy in the ”intrinsic” part. Only very small variations of the ”intrinsic” activation energy can be observed with temperature, which are not affecting much the overall activation energy. Therefore, further considerations must be taken into account in future to revisit and verify the proposed polaron model.

8.2.4. Applying the polaron model to undoped potassium niobate

For $KNbO_3$ only undoped samples were prepared to compare the electronic structure of a ferroelectric material with $NaNbO_3$ as an antiferroelectric material. However, no doped samples were synthesized. Therefore, applying the polaron model to $KNbO_3$ is more difficult. In Section 7.1.2 it was shown that $KNbO_3$ exhibits a p-type behavior over the whole temperature range with two activation energy regimes. Hence, the conduction process behaves different to $NaNbO_3$, which shows a change from n- to p-type conductivity at around $340\,°C$. Nevertheless, we could assume an extrinsic regime below

270 °C and an ”intrinsic” region above 270 °C in $KNbO_3$ leading to the following hypothesis.

Hypothesis

→ The electronic conductivity is determined by hole polaron transport on the O-site leading to an oxidation of O^{2-} to O^{-}.

→ Above 270 °C ”intrinsic” hole polaron conductivity is measured.

→ Below 270 °C the concentration of hole polarons is fixed extrinsically by potassium vacancies, hence, extrinsic hole polaron conductivity is measured.

According to this hypothesis, both parts are p-type and the extrinsic regime is dominated by hole polarons, which would mean that the concentration of V'_K must be larger than twice the concentration of $V^{\cdot\cdot}_O$. Hence, the concentration of V'_K is determining the concentration of hole polarons in the extrinsic regime.

$$[O^{\cdot}_O] + 2[V^{\cdot\cdot}_O] = [V'_K] + [Nb'_{Nb}] \tag{8.23}$$

$$2[V^{\cdot\cdot}_O] < [V'_K] \qquad \rightarrow \qquad [V'_K] - 2[V^{\cdot\cdot}_O] = [O^{\cdot}_O] \tag{8.24}$$

Consequently, the activation energy in the extrinsic regime equals half of the hole polaron binding energy E^{h}_{PB}. The activation energy of the ”intrinsic” part is then the sum of the hole polaron formation energy E^{h}_{Pf} and half of E^{h}_{PB}, which leads to a total conductivity of:

$$\begin{aligned}\sigma_{tot} &= c_{O^-} \cdot \mu_{O^-} \cdot q \\ &= \left[[O^{\cdot}_O]_{ext} + N_O \exp\left(\frac{E^{h}_{Pf}}{k_B T}\right)\right] \cdot \frac{\mu_{O^-,0}}{T^{3/2}} \exp\left(\frac{E^{h}_{PB}/2}{k_B T}\right) \cdot q\end{aligned} \tag{8.25}$$

Figure 8.10 illustrates the measured and fitted conductivity of $KNbO_3$ in air (left), nitrogen (center), and air again (right) on the top including all relevant energies. On the bottom the corresponding energy band diagrams are shown. Let us first consider the extrinsic region. Here, the extrinsically fixed hole polaron concentration $[O^{\cdot}_O]$ is set to 4.25×10^{15} cm^{-3}, 1.50×10^{15} cm^{-3}, and 2.30×10^{15} cm^{-3} for the first measurement in air, the curve in nitrogen, and the second experiment in air, respectively. These values are much higher compared to $[Nb'_{Nb}]_{ext}$ ranging from 1.5×10^{11} cm^{-3} to 3.5×10^{11} cm^{-3} defined for $NaNbO_3$. Hence, a high amount of V'_K must be present in the $KNbO_3$ material. This is not surprising as in Section 5.1, 5.2, and 6.1.2 a high potassium deficiency in the prepared samples has already been suggested, which results from evaporation of potassium during sintering. As potassium is more volatile than sodium [177, 187] a higher amount of V'_K in $KNbO_3$ than V'_{Na} in $NaNbO_3$ can be expected. When annealing in nitrogen, however, $[O^{\cdot}_O]$ is decreasing because more oxygen vacancies are formed compensating the amount of V'_K. Heating in air again decreases the number of $V^{\cdot\cdot}_O$ by oxygen incorporation, which in turn increases the concentration of the hole polarons compensating the remaining V'_K.

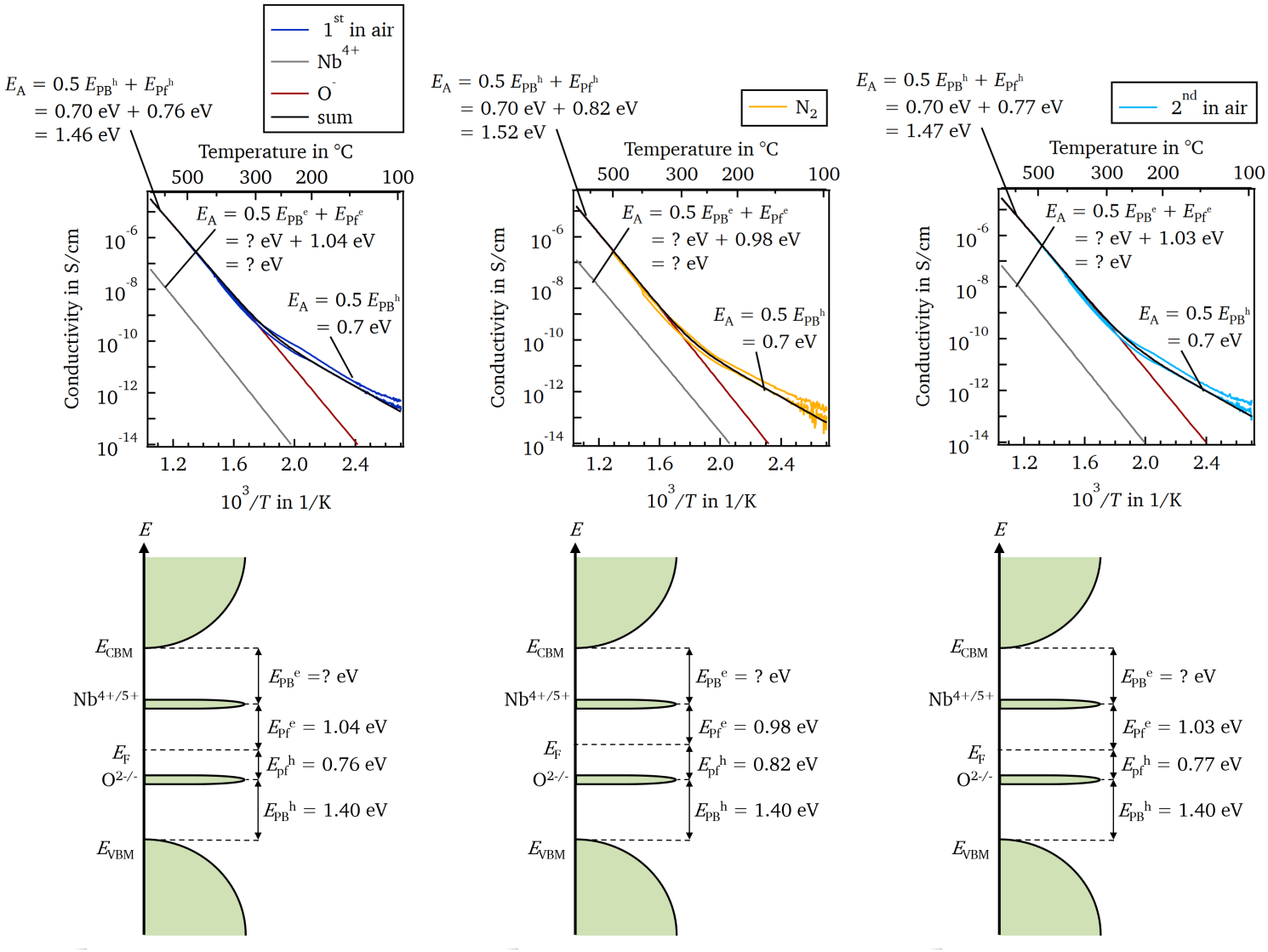

Figure 8.10.: Measured and fitted conductivity of $KNbO_3$ in air (left), nitrogen (middle), and air (right) again including all relevant energies (top) and the corresponding band diagrams (bottom).

The activation energy in the extrinsic part is 0.7 eV, which means that the hole polaron binding energy, hence, the distance between VBM and $O^{2-/-}$ state is 1.4 eV. This would imply that the $O^{2-/-}$ state is a deep trapping state. In literature hole polarons on the O-site are usually assigned to be very shallow states located close to the VBM with binding energies ranging from 0.01 eV to 0.25 eV [324, 325]. However, hole polarons can be bound to acceptor states, which increases the binding energy significantly. For acceptor-bound hole polarons binding energies between 0.5 eV and 1.4 eV [326, 327] can be found in literature. Hence, it could be that the hole polarons in $KNbO_3$ are bound to the potassium vacancies, which is not that unrealistic as the V'_K concentration is assumed to be high. In addition, a hole polaron binding energy of 1.22 eV was already reported in literature for $KNbO_3$ [328]. However, it is very unclear if the transport mechanism under a DC-field can be explained by acceptor-bound polarons. Nevertheless, such acceptor-bound polarons of $O^{\cdot}$-V'_K might cause the aged P-E-loops observed in Section 5.4. However, this whole mechanism needs further experimental and simulated investigations. In addition, it remains an open question why the hole polarons in $NaNbO_3$ have a much lower binding energy, hence, seem not to be bound to an acceptor such as V'_{Na}. Consequently, further investigations are required, why acceptor-bound polarons seem to appear in $KNbO_3$ but no in $NaNbO_3$.
According to the polaron model, the "intrinsic" regime would be also dominated by small polaron hopping of holes. The formation energy E_{Pf}^{h} in air and nitrogen is 0.76 eV and 0.82 eV, which explains the slight decrease of the conductivity in nitrogen. In Section 6.6 it was suggested that the band gap is underestimated as well by the optical spectroscopy due to an exciton formation or the trapping of the electron on the Nb-site. Assuming that the measured band gap of about 3.2 eV is in reality the distance between VBM and the $Nb^{4+/5+}$-state, the formation energy of the electron polaron can be calculated. Here, E_{Pf}^{e} has a value of 1.04 eV and 0.98 eV in air and nitrogen, respectively. The electron polaron binding energy cannot be determined because only the hole polaron hopping process is measured. Hence, it is not clear what the distance between the $Nb^{4+/5+}$-state and the CBM is and, therefore, it is also not clear what the real band gap might be. For the sake of completeness, it should be mentioned that $\mu_{O^-,0}$ and $\mu_{Nb4+,0}$ are set to $6.5 \times 10^3\,K^{3/2}\,cm^2\,V^{-1}\,s^{-1}$ and $1 \times 10^2\,K^{3/2}\,cm^2\,V^{-1}\,s^{-1}$ that the calculated conductivity fits the measured one in the "intrinsic" regime, respectively. Furthermore, a E_{PB}^{e} of 1.0 eV as in $NaNbO_3$ is assumed for the calculations.

Table 8.1 shows the hole and electron polaron concentrations and mobility in $KNbO_3$ at $500\,°C$ in comparison to undoped and Ca-doped $NaNbO_3$ assuming a E_{PB}^{e} of 1.0 eV. The polaron concentrations are much higher in $KNbO_3$ than in $NaNbO_3$ while the mobility is much lower. This can be explained by the deep in gap $O^{2-/-}$-state resulting in a higher polaron binding and therefore a higher migration energy and a lower polaron formation energy facilitating the creation of charge carriers. However, it is questionable if the $O^{2-/-}$-state is located in reality that deep in the energy gap. Acceptor-bound hole polarons to the potassium vacancies could be an explanation. More experiments with denser and less potassium deficient samples might give more insights into this problem. Furthermore, differently

doped materials could help to identify any changes in the transport mechanism.

Table 8.1.: Hole and electron polaron concentration and mobility at $500\,^{\circ}\mathrm{C}$ in air and nitrogen for undoped and Ca-doped $NaNbO_3$ and undoped $KNbO_3$.

	atmosphere	c_{O^-} in cm^{-2}	μ_{O^-} in $cm^2\,V^{-1}\,s^{-1}$	$c_{Nb^{4+}}$ in cm^{-2}	$\mu_{Nb^{4+}}$ in $cm^2\,V^{-1}\,s^{-1}$
$NaNbO_3$	air	$4.24 \cdot 10^{12}$	4.15	$2.02 \cdot 10^{11}$	0.42
$Na_{0.99}Ca_{0.01}NbO_3$		$5.42 \cdot 10^{10}$	4.15	$4.05 \cdot 10^{12}$	0.42
$KNbO_3$		$4.53 \cdot 10^{17}$	$8.16 \cdot 10^{-6}$	$3.02 \cdot 10^{15}$	$2.54 \cdot 10^{-6}$
$NaNbO_3$	nitrogen	$1.72 \cdot 10^{12}$	4.15	$4.78 \cdot 10^{11}$	0.42
$Na_{0.99}Ca_{0.01}NbO_3$		$4.21 \cdot 10^{9}$	4.15	$5.21 \cdot 10^{13}$	0.42
$KNbO_3$		$2.14 \cdot 10^{17}$	$8.16 \cdot 10^{-6}$	$6.40 \cdot 10^{15}$	$2.54 \cdot 10^{-6}$

9. Conclusion of the proposed band structure model for sodium and potassium niobate

Within this thesis a band structure model based on a high electrical band gap with polaron trapping states lowering the optical band gap is proposed for sodium and potassium niobate. This model is established on basis of the determined sample composition, surface, and interface characterization to the electrode materials ITO and RuO_2 including annealing experiments in oxidizing and reducing atmospheres, and examined Fermi level limitations analyzed via XPS, as well as the temperature, atmosphere, time, and electric field dependent conductivity probed with AC- and DC-signals. A schematic of the proposed band structure is illustrated in Fig. 9.1 a) for $NaNbO_3$ and b) for $KNbO_3$.

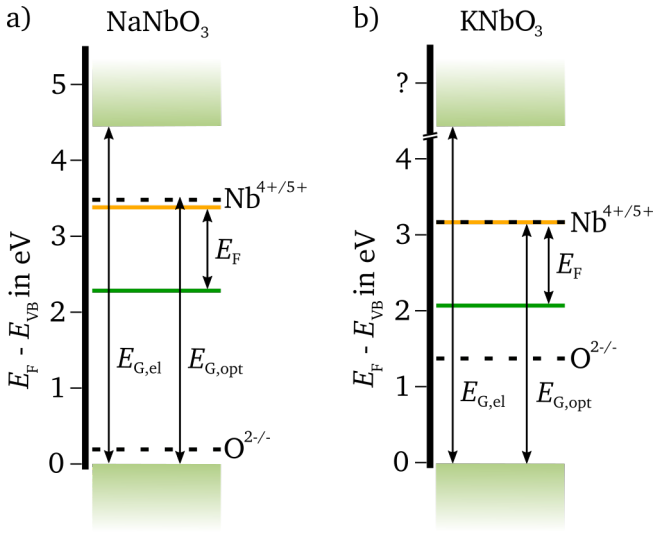

Figure 9.1.: New proposed band structure of $NaNbO_3$ in a) and $KNbO_3$ in b) with nominal band gap $E_{G,opt}$ determined by optical measurements and electrical band gap $E_{G,el}$, respectively. The accessible Fermi level range and the $Nb^{4+/5+}$ and $O^{2-/-}$ polaron states are marked as well. Upper (yellow line) and lower Fermi level limit (green line) are extracted from the ITO and RuO_2 interface, respectively.

For $NaNbO_3$ an electrical band gap of $4.5\,\text{eV}$ is identified. The $Nb^{4+/5+}$ and $O^{2-/-}$ polaron states are located at $3.5\,\text{eV}$ and $0.2\,\text{eV}$ above the VBM, respectively. Hence, optical spectroscopy measurements

are measuring the distance between VBM or the $O^{2-/-}$ state and the $Nb^{4+/5+}$ level by exciting an electron, which is trapped on the Nb-site.
By means of an interface experiment to ITO an upper Fermi level limit of 3.4 eV is determined, which is close to the $Nb^{4+/5+}$ polaron state. Therefore, we can conclude that the Fermi level is pinned at the $Nb^{4+/5+}$ level and cannot be pushed closer to the CBM. If the Fermi level is exceeding the $Nb^{4+/5+}$ state, the sample would decompose because of the reduction of all niobium ions from Nb^{5+} to Nb^{4+}. A lower Fermi level limit of 2.3 eV is identified with a RuO_2 interface. This is much higher in energy than the calculated $O^{2-/-}$ polaron state. Hence, it cannot be explained by a Fermi level pinning at the $O^{2-/-}$ level. This means that either the Fermi level minimum cannot be measured by means of a RuO_2 interface because the maximum band bending, which can be introduced, is reached or that at least one other trapping state is present in the band gap of $NaNbO_3$. If the Fermi level can be shifted closer to the VBM, could be evaluated by a more oxidizing treatment, e.g. an interface experiment with NiO or CoO_x [80, 241]. However, both materials are less conductive than RuO_2, which could lead to charging effects influencing the Fermi level determination on highly insulating $NaNbO_3$ samples. Therefore, $NaNbO_3$ thin films on a conductive substrate would be required for these experiments. If the Fermi level can be shifted closer to the VBM with NiO or CoO_x, it would be clear that the 2.3 eV measured with RuO_2 is not a fundamental limitation of the Fermi level. However, the same minimal Fermi level of 2.3 eV measured with NiO and CoO_x, would reveal another trapping state in the band gap pinning the Fermi level.

The polaron states confining the Fermi level and the large electrical band gap of 4.5 eV explain the low electronic conductivity measured with the DC-experiments. In addition, the proposed polaron model assumes a high concentration of sodium and oxygen vacancies, which determine the charge equilibrium. As the concentration of V'_{Na} is fixed during sintering, the $V_O^{\cdot\cdot}$ concentration is the more crucial parameter influencing the extrinsic polaron concentrations. Consequently, annealing in atmospheres with different oxygen partial pressures modifies the extrinsic part of the DC-conductivity. Donor doping determines the electron polaron concentration already during sintering and, therefore, the change in $V_O^{\cdot\cdot}$ concentration does not significantly influence the extrinsic part anymore. The high electron polaron concentration fixed by the donors explains the higher conductivity of donor doped $NaNbO_3$ at low temperatures. As-prepared undoped $NaNbO_3$ has a low electron polaron concentration meaning a lower electronic conductivity. It is only increasing when heating in a reducing atmosphere, which creates the necessary amount of additional $V_O^{\cdot\cdot}$. This means that the extrinsically determined conductivity is increasing with higher donor or $V_O^{\cdot\cdot}$ concentration.
In contrast, at high temperatures undoped $NaNbO_3$ has the higher conductivity as hole polaron hopping is faster than electron polaron hopping. Hence, the ”intrinsic” conductivity is decreasing with increasing $V_O^{\cdot\cdot}$ concentration because of a lower amount of hole polarons. The hole polaron concentration is decreasing due to a higher formation energy as a result of the raised Fermi level. The same would probably apply for a very low donor concentration.

If the donor or $V_O^{\cdot\cdot}$ concentration is much higher than the V'_{Na} concentration, the "intrinsic" conductivity is again rising as the electron polaron number is getting larger because of the higher Fermi level position and lower electron polaron formation energy. Consequently, the "intrinsic" electron polaron conductivity is overtaking the "intrinsic" hole polaron conductivity.
Hence, the conductivity of $NaNbO_3$ can be divided into three regimes, in which either hole or electron polaron hopping is dominating the extrinsic and/or "intrinsic" part depending on the extrinsic defect concentrations of acceptors $c_{A'}$, sodium vacancies $c_{V'_{Na}}$, donors $c_{D^{\cdot}}$, and oxygen vacancies $c_{V_O^{\cdot\cdot}}$:

1. $c_{A'} + c_{V'_{Na}} \gg c_{D^{\cdot}} + c_{V_O^{\cdot\cdot}}$
2. $c_{A'} + c_{V'_{Na}} < c_{D^{\cdot}} + c_{V_O^{\cdot\cdot}}$
3. $c_{A'} + c_{V'_{Na}} \ll c_{D^{\cdot}} + c_{V_O^{\cdot\cdot}}$

Figure 9.2 illustrates these three scenarios including the behavior for further increasing defect concentration of the dominating defect species.
In this regard, it would be interesting to see, if heating in different sodium containing atmospheres is changing the conductivity behavior in the opposite way. With this approach it might be possible to induce an extrinsic p-type region. In this context, acceptor doping of $NaNbO_3$ would be also interesting to analyze. This behavior is illustrated in Fig. 9.2 as well for the sake of completeness.

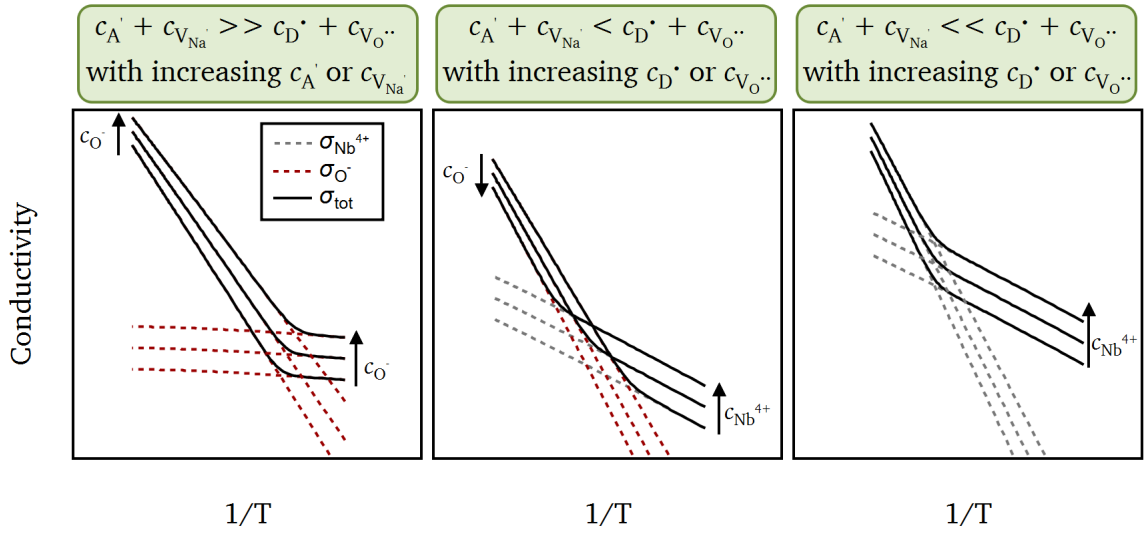

Figure 9.2.: Temperature dependent conductivity of $NaNbO_3$ for different acceptor $c_{A'}$, donor $c_{D^{\cdot}}$, sodium vacancy $c_{V'_{Na}}$, and oxygen vacancy $c_{V_O^{\cdot\cdot}}$ concentrations.

Besides polaron conduction, ionic migration of sodium and oxygen takes place in $NaNbO_3$. However, based on the proposed model their contribution can only be directly elucidated by AC-signals, where the ions can freely move. With DC-experiments the movement of ions and vacancies can only be indirectly examined when the atmosphere is changed (relaxation experiments) or high electric

fields and temperatures are employed (degradation experiments). Otherwise they are hindered by potential barriers at the grain boundaries and by impermeable electrodes. In relaxation and degradation experiments, however, these potential barriers are lowered by means of the external conditions and can be resolved in terms of time (Section 7.1.3 and 7.4.1). Although ionic movement was detected, the two different contributions present in the samples cannot be clearly assigned to oxygen or sodium migration. In this regard, it would be interesting to repeat the relaxation experiments as well as the impedance measurements with electrodes conducting only oxygen ions such as Y-stabilized ZrO_2 [236], or sodium ions such as β''-alumina or NASICON-materials [318–320]. Then, these two diffusion processes could potentially be separated from each other.
In order to investigate the frequency and temperature dependent permittivity as well as polarization hysteresis loops, AC-fields are applied. As shown in Sections 5.4 and 5.6, high leakage currents are influencing both measurements, which is why either high frequencies or low electric fields had to be used. According to the proposed model, ionic conduction is higher than electronic conduction. Hence, the leakage current in the polarization loops are most likely caused by ionic conductivity of oxygen and sodium ions/vacancies. In order to reduce the leakage current, the $V_O^{\cdot\cdot}$ and V'_{Na} concentration must be as low as possible to avoid any ionic diffusion. This can be realized by embedding the samples in some $NaNbO_3$ powder during sintering and all post-annealing steps above $300\,°C$ to avoid any oxygen or sodium loss.

For $KNbO_3$ it is not possible to propose a clear band structure model as for $NaNbO_3$ because only undoped $KNbO_3$ was investigated. Donor doped material would probably give more insides into electron polaron conduction. Therefore, we cannot derive the electrical band gap from the present conductivity results. The $Nb^{4+/5+}$ and $O^{2-/-}$ states are located at $3.2\,eV$ and $1.4\,eV$ above the VBM, respectively. This high $O^{2-/-}$ level is questionable as oxygen polaron states have only been found close to the VBM in other oxide materials, so far [324, 325]. However, hole polarons with a binding energy of $1.22\,eV$ were reported in literature [328]. Acceptor-bound hole polarons can be an explanation for such a deep trapping state [326, 327]. These acceptor-bound polarons of $O^{\cdot}$-V'_K could as well be responsible for the aged P-E-loops observed in Section 5.4. Hence, it is necessary to measure different types of $KNbO_3$ samples (donor and acceptor doped material) in the future to validate this polaronic state.

An upper Fermi level of $3.2\,eV$ is measured by means of an ITO interface. According to the model the Fermi level is pinned at this energy by the $Nb^{4+/5+}$ state. The same considerations as for $NaNbO_3$ apply here, meaning that a Fermi level above the $Nb^{4+/5+}$ state would lead to decomposition of the sample.
The lower Fermi level limit is identified by a RuO_2 interface to be located at $2.1\,eV$. Although the $O^{2-/-}$ state is positioned much higher in energy than the one in $NaNbO_3$, it is still $0.7\,eV$ below the lower Fermi level limit and cannot be responsible for the pinned Fermi level at $2.1\,eV$. Similar to $NaNbO_3$, either the maximum band bending achievable with RuO_2 is reached or another trapping

state exists in the band gap pinning the Fermi level. This issue can be clarified in future by interface experiments with NiO and CoO_x as mentioned above.

The same considerations for the AC- and DC-experiments made for $NaNbO_3$ apply for $KNbO_3$. With a DC-field only polaron conduction is measured because the ions are hindered by the potential barriers at the grain boundaries. Furthermore, the low electronic conductivity can be explained by the proposed polaron model with a high electrical band gap. The high potassium and oxygen vacancy concentration compared to the amount of electron and hole polarons defines the charge equilibrium. Potassium is more volatile than sodium [177, 187], hence, more V'_K are formed during sintering. Interestingly, the amount of V'_K after sintering and stress-release-annealing is more than twice the number of $V^{\cdot\cdot}_O$, which leads to a compensation by hole polarons. This results in an extrinsic hole polaron conductivity at low temperatures from the first measurement on. In contrast, in $NaNbO_3$ the amount of V'_{Na} seems to be compensated by $V^{\cdot\cdot}_O$ after sintering and stress-release-annealing and, therefore, the extrinsic part is not detected from the first measurement on (see Fig. 8.9). Similar as in $NaNbO_3$ the "intrinsic" conductivity is dominated by hole polaron hopping in $KNbO_3$, which leads to an overall p-type conductivity over the whole temperature range.
The high concentration of V'_K can be confirmed by the sintering curve shown in Section 5.1, which exhibits a typical behavior for Nb-rich (K-deficient) samples with an increased temperature range of shrinkage. In addition, potassium deficiency leads to a smaller grain size and a reduced relative density [204], which is the case for the prepared samples in this work as illustrated in Section 5.2. Moreover, the XPS experiments show that potassium is diffusing to the surface leading to a potassium enriched surface and probably to a potassium deficient bulk. The potassium at the surface is forming an oxide. This in turn explains the possibility of a changed V'_K concentration in the extrinsic regime of the hole polaron conductivity when heating in different atmospheres. The changed oxygen partial pressure leads to an incorporation or removal of potassium and oxygen available from the potassium oxide phase at the surface.
During the degradation experiments at high voltages and high temperatures, two diffusion processes are identified, which can most likely be attributed to oxygen and potassium ions/vacancies. However, the contributions cannot directly pinpoint to one of the species. Relaxation experiments and impedance measurements with different electrode materials conducting either only oxygen ions as Y-stabilized ZrO_2 [236] or only potassium ions as potassium-ion-conducting β-alumina, $K_3Sb_4O_{10}$ (BO_3), $K_2Fe_4O_7$ [329], or $0.35Gd_2O_3$–$0.3KNO_2$ solution [330] are necessary in order to separate the two processes. It is interesting that no degradation is observed for the undoped $KNbO_3$ material, which indicates that the potential barriers for oxygen and potassium diffusion hampering the degradation mechanism are higher than in $NaNbO_3$. Measurements with holding times longer than the 10 min used in this work, could give more insight into this issue.
How far the ionic conductivity is compromising experiments using AC-signals cannot be stated in this work because polarization hysteresis loops have only been conducted at high frequencies. At least

from the frequency and temperature dependent permittivity measurements, it can be concluded that the influence is less than in undoped $NaNbO_3$, however, frequency dispersion is still an issue suggesting an effect of leakage current.

In general, the proposed band structure and polaron model in this work can explain quite a lot of the measured material properties in regard of band gap and electrical conductivity. However, there are still some open questions, which cannot be clarified.

1. Scenario 1 interpreting the AC- and DC-results in terms of bulk, grain boundary, and electrode contributions must be excluded as possible explanation in order to verify the discussed polaron model. Electrode effects could be ruled out by conducting impedance experiments with different electrode materials, e.g. platinum, silver, and gold. If with all electrodes the same conductivity behavior is observed, an electrode effect can be excluded. A grain boundary contribution can be probed by measuring a single crystal with impedance spectroscopy, which is free of any grain boundary effect. However, the $NaNbO_3$ single crystals produced in the FLAME project are too small for any conductivity measurements. Hence, further development in crystal growth must be done.

2. The proposed electronic structure and transport mechanism is based on the assumption that the samples contain a high sodium or potassium and oxygen vacancy concentration. These vacancies/ions are considered to be very mobile and responsible for the two different contributions observed in the degradation and relaxation experiments. Although the behavior looks similar to observations done for ITO [304], two different diffusion mechanisms, e.g. diffusion of oxygen in the bulk and along grain boundaries, cannot be completely ruled out as potential explanation. In order to analyze this issue, conductivity measurements with different electrode materials, which are either oxygen (Y-stabilized ZrO_2 [236]), sodium (beta-sodium alumina [319, 320]) or potassium ion conductors (beta-potassium alumina[329]), should be examined. If still both diffusion processes are detected, different diffusing species cannot be responsible for the observations. In addition, SIMS measurements with oxygen, sodium, and potassium isotopes could resolve whether all ions are mobile and how they diffuse, e.g. through the bulk and/or along the grain boundaries.

3. The high and low frequency semicircles in the Nyquist plot in Section 7.2 are interpreted as mainly ionic and electronic conductivity in the presented model. However, for $Na_{0.99}Ca_{0.01}NbO_3$ a third semicircle at medium frequencies exists, which develops at elevated temperatures. It is not clear what effect is responsible for this contribution. Further impedance experiments with different doping concentrations, doping atoms, and electrode materials might give more insights into this effect.

4. The activation energies of the extrinsic and ”intrinsic” region of the DC-conductivity are determined from the cooling curves. However, the heating cycles deviate from the cooling

curves in the extrinsic regime. The presented model cannot give an answer to that. Further conduction experiments are necessary to resolve these variations.

5. The model considers the ionic conduction process to be dominant in experiments using AC-signals. Therefore, ionic conductivity is presumed to be the main origin for the leakage current compromising the permittivity measurements and polarization hysteresis loops at low frequencies. In this regard, it is also unclear why the doped $NaNbO_3$ samples exhibit a higher leakage current in the polarization experiments resulting in balloon-shaped loops while the permittivity of undoped $NaNbO_3$ is influenced more by the leakage current at low frequencies and temperatures above $200\,°C$. It would be interesting to measure polarization loops above $200\,°C$ to see whether the undoped $NaNbO_3$ samples get more leaky than the doped material. In addition, samples with different oxygen and sodium vacancy concentrations could confirm if the nature of the leakage current is really ionic. Samples post-annealed in different atmospheres might be suitable for such experiments.

6. No temperature dependency of the Fermi level is considered within the proposed model. However, the Fermi level should decrease with temperature along with the band gap due to phonon excitation with increasing temperature. A decreasing Fermi level and reduced band gap should have an impact on the activation energies, especially in the ”intrinsic” region. This issue needs further experimental and simulated investigations and discussions.

In the end, the proposed band structure and polaron model gives a first idea of the electronic structure of sodium and potassium niobate. However, a connection between electronic structure and antiferroelectric or ferroelectric properties cannot be drawn. In order to elucidate a potential linkage in more detail, the leakage current compromising the measurements must be reduced. Hence, according to this work, samples with a low $V_O^{\cdot\cdot}$, V_{Na}', and V_K' concentration must be prepared by e.g. sintering and post-annealing the samples in $NaNbO_3$- and $KNbO_3$-based powders. In a second step, samples with different donor and acceptor dopants in varying concentrations can be produced to change the electron and hole polaron concentration in order to examine if polarons play a role in the (anti)ferroelectric character of a material. In this regard, it is interesting to verify if the polaron model is valid or if another process describes the conduction behavior more accurately.

10. Summary and outlook

In this work, the antiferroelectric material $NaNbO_3$ and the ferroelectric material $KNbO_3$ were investigated. The main focus was laid on the electronic structure and the differences between these two systems. However, the aim of finding a connection between electronic structure and (anti)ferroelectric properties could not be achieved. Nevertheless, first hypotheses about the transport mechanisms in $NaNbO_3$ and $KNbO_3$ could be established.

For this purpose, ceramic samples were prepared by a common solid state synthesis and sintering method. Here, the best calcination and sintering temperatures for the individual powders were evaluated by an optical dilatometer. The resulting microstructure of the samples was elucidated by SEM measurements revealing large abnormal grown grains of 90 µm in diameter with pore inclusions and a relative density of 94.5 % in undoped $NaNbO_3$. Doping led to a decreased grain size of about 0.9 µm to 1.5 µm but an increased relative density of 96.0 %. In contrast, undoped $KNbO_3$ exhibited small grains of about 1.0 µm and a low relative density of 88.7 %. No secondary phases were identified. The composition and the crystal structure was examined by means of XRD. All $NaNbO_3$-based samples crystallized mainly in the AFE P phase while small traces of the FE Q phase could be observed. For $KNbO_3$ the orthorhombic FE crystal structure with Amm2 space group was identified.
By means of polarization hysteresis loops the polarization behavior was examined. Irreversible AFE polarization loops were recorded in case of undoped and doped $NaNbO_3$. However, high frequencies were required for the measurements due to the high leakage currents of the doped samples. In contrast, ferroelectric polarization loops were detected for $KNbO_3$, which were highly influenced by aging. Defect complexes are most probable causing the aging effects. However, it is not clear what kind of defect complexes, e.g. $(V'_K\text{-}V^{\cdot\cdot}_O)^{\cdot}$, $(V'_K\text{-}V^{\cdot\cdot}_O\text{-}V'_K)^{x}$, or $(O^{\cdot}\text{-}V'_K)^{x}$ are the origin.
In the end, phase pure samples were prepared, which were used for the investigation of the electronic structure of antiferroelectric $NaNbO_3$ and ferroelectric $KNbO_3$.

The electronic structure including band gap, accessible Fermi level positions, and trapping states was mainly analyzed by XPS measurements. It was found that the optical band gap cannot be identified easily with XPS because of other states, e.g. surface oxide layers and Auger lines, compromising the distance between main oxygen peak and the onset of the loss spectrum. Hence, EELS conducted with a TEM was used to measure the optical band gap of 3.5 eV for $NaNbO_3$. Unfortunately, no $KNbO_3$

samples were examined by TEM.
By means of interface experiments with the low work function material ITO and the high work function material RuO_2, the accessible Fermi level range was investigated. For both, $NaNbO_3$ and $KNbO_3$, a Fermi level range of 1.1 eV located close to the optical band gap was revealed. Further oxidizing and reducing treatments conducted on $NaNbO_3$ and KNLNT thin films could not give any more details.
Besides the analysis of the electronic structure, the surface composition was examined in more detail with XPS. For undoped $NaNbO_3$ a sodium deficient surface was identified. In addition, it was proposed that some sodium oxide species are detected on the samples' surfaces. Doping reduced the sodium deficiency, however, calcium segregation was observed, which could result from a facilitated diffusion along dislocations at elevated temperatures during stress-release annealing after grinding. These dislocations were observed in TEM. Calcium segregation was measured for both, Ca- and Sr-doped samples. The origin for calcium in the $Na_{0.99}Sr_{0.01}NbO_3$ ceramics was suspected to be a powder contamination of the $SrCO_3$ precursor powder. For $KNbO_3$ the surface was highly enriched with potassium. In addition, a potassium oxide layer was covering the surface of the samples.

The electrical transport mechanism was investigated by AC- and DC-experiments. DC-measurements were conducted in dependence of temperature, atmosphere, and time, while impedance spectra were only recorded with changing temperature.
In general, a low conductivity for all samples was detected at room temperature as well as at high temperatures. However, the AC-conductivity was higher compared to the DC-conductivity. In addition, the activation energies were different measuring under an AC- and a DC-field.
For the DC-experiments the activation energies of $NaNbO_3$-based and $KNbO_3$ samples were changing around the P-to-R- and the T-to-C-phase transition, respectively. Undoped $NaNbO_3$ was the only material, which was changing from a n-type behavior below $300\,°C$ to a p-type behavior above this temperature. Interestingly, undoped $NaNbO_3$ exhibited a lower conductivity than the Ca- and Sr-doped sample below $300\,°C$ and a higher one above $300\,°C$. Donor doping led to a n-type conductivity over the whole temperature range. In, contrast $KNbO_3$ was behaving like a p-type material in the whole measured temperature regime.
Two conduction contributions were resolved by means of impedance spectroscopy for all ceramics. In addition, a third semicircle developed above $425\,°C$ in the Nyquist plot for $Na_{0.99}Ca_{0.01}NbO_3$.

Degradation experiments were conducted to examine the behavior of the materials under harsh conditions at high temperatures and electric fields. After charging of the ceramic capacitors, two relaxation mechanisms were observed, which can most likely be attributed to oxygen and alkaline ion diffusion. This would mean that sodium and potassium are mobile above $300\,°C$ and are dominating the conduction mechanism at high temperatures. Heating experiments in oxygen and vacuum of a $NaNbO_3$ and a KNLNT thin film within the XPS system confirmed the diffusion of sodium and potassium above $300\,°C$. For the $NaNbO_3$-based samples a degradation behavior was observed at

elevated temperatures and electric fields. This effect could be removed when heating above $300\,^{\circ}\mathrm{C}$ for $1\,\mathrm{h}$. In contrast, no degradation was detected for $KNbO_3$ under the investigated temperature-electric-field-combinations.
The same conductivity curves were recorded within the XPS system by using an ITO top electrode and a Pt bottom electrode to detect possible changes during the degradation process. For both, cathode and anode, ITO was not a good option because the resistivity was not low enough when the current flow through the sample was above a critical value.

Based on these observations a model was developed explaining the transport mechanism in $NaNbO_3$ and $KNbO_3$. This model assumes that with an AC-signal mainly ionic conductivity is measured, which is much higher than electronic conductivity. DC-experiments can only detect electronic conductivity as the ions are hindered by the electrodes when measuring at low applied voltages. Hence, the impedance measurements were dominated by oxygen, sodium, and potassium diffusion. The DC-conductivity was explained by polaron hopping of hole and electron polarons located on the oxygen and niobium site, respectively. Band conduction was excluded because of a too high mobility even for free band charge carriers.
This model explains the observed change in conductivity in all samples by a transition from an extrinsic to an ”intrinsic” conduction process. In the extrinsic regime, extrinsic defects such as oxygen and alkaline vacancies as well as other donor and acceptor states fix the electron or hole polaron concentration. Hence, the activation energy is only depending on the migration barrier, which corresponds to half of the polaron binding energy. Within the ”intrinsic” region hole and electron polarons can be formed by exciting an electron from the oxygen site to the niobium site. Therefore, the activation energy depends on the migration and formation energy of the polarons. The formation energy is depending on the Fermi level position, which is again fixed by the ionic defects. Hence, the concentration of ionic defects determines whether the conductivity is n- or p-type. At very high donor or oxygen vacancy concentrations the samples are n-type, which was the case for $Na_{0.99}Ca_{0.01}NbO_3$ and $Na_{0.99}Sr_{0.01}NbO_3$. When the donors and oxygen vacancies have a slightly higher concentration than acceptors and alkaline vacancies, n-type conductivity is dominant in the extrinsic part while a p-type behavior can be observed in the ”intrinsic” regime. This situation applies to the undoped $NaNbO_3$ samples. In case acceptors and alkaline vacancies are higher in concentration than donors and oxygen vacancies, p-type conduction is obtained for both regions. Such a behavior was most likely observed in $KNbO_3$ because the samples exhibit a high V'_K concentration.

This model explains the discrepancy between detected Fermi levels close to the optical band gap and a low conductivity. The optical band gap is a measure for the energetic distance between VBM and the electron polaron trapped on the niobium site ($Nb^{4+/5+}$). Hence, the electrical band gap between VBM and CBM is much larger.
For $NaNbO_3$ the proposed model predicts an electrical band gap of $4.5\,\mathrm{eV}$ with an electron trapping state on the niobium site ($Nb^{4+/5+}$) and a hole trapping state on the oxygen site ($O^{2-/-}$). The

$Nb^{4+/5+}$ and $O^{2-/-}$ state is located at $4.5\,\text{eV}$ and $0.2\,\text{eV}$ above the VBM, respectively. In case of $KNbO_3$ the $Nb^{4+/5+}$ level is positioned at $3.2\,\text{eV}$ while the $O^{2-/-}$ polaron is located at $1.4\,\text{eV}$ with respect to the VBM. The electrical band gap of $KNbO_3$ could not be determined. Donor doped samples would be needed to examine this value. The $O^{2-/-}$ is a deep trapping state in $KNbO_3$. It is unclear if such a trapping state is very likely as $O^{2-/-}$ polarons are usually shallow states [324, 325]. However, acceptor-bound polarons to the potassium vacancies could increase the hole polaron binding energy significantly leading to a deep trapping state [326, 327].

Another origin for the observed two contributions in the Nyquist plot of the impedance measurements could be the presence of insulating grain boundaries and slightly more conductive grains, which would result in the two observed semicircles. In order to exclude grain boundary effects the conductivity of single crystals should be examined. Furthermore, electrode effects could cause the higher resistive part, which would then dominate the DC-conductivity. In order to rule out this explanation, experiments with different electrodes, e.g. Au, Ag, and Pt, must be conducted in the future. Therefore, a model explaining the two contributions observed with impedance spectroscopy with bulk and grain boundary or electrode contributions cannot be excluded. As further experiments would be required to rule out these possible interpretations, some basic calculations based on the polaron model were carried out. These calculations fit well with the measured DC-conductivity results supporting the proposed polaron model in this work.

In general, a lot of questions remain open, e.g. the possibility of electrode effects, the diffusion of oxygen and alkaline ions, the formation of acceptor-bound polarons, and the temperature dependence of the Fermi level. Consequently, further investigations of both material systems are necessary.
In order to confirm oxygen and alkaline ion diffusion, experiments with electrodes conducting only oxygen, sodium, or potassium would be very informative. For example, Y-stabilized ZrO_2 [236], β-sodium-alumina [319, 320], and β-potassium-alumina [329] could be used as oxygen, sodium, and potassium conductors, respectively.
Donor doped $KNbO_3$ samples could help to verify the polaron model of $KNbO_3$. It would be interesting to see whether or not the acceptor-bound polaron state disappears due to a low acceptor concentration and if instead a shallow hole polaron level appears. In this regard, it would be very informative to find a method to reduce the potassium vacancy concentration. This could be done by heating in potassium containing powder during sintering and all other post-annealing steps above $300\,^\circ\text{C}$.
In general, doping $NaNbO_3$ and $KNbO_3$ with different dopant elements and in different concentration would be helpful to validate the polaron model. Furthermore, detailed computational simulations and calculations could give more insights into the electronic structure especially on the dependence of the defect type and concentration. In addition, the temperature dependence of the Fermi level could be elucidated in more detail, which might result in corrections of the proposed polaron model.

In summary, no connection between electronic structure and (anti)ferroelectric behavior could be drawn. Oxygen, sodium, and potassium vacancies as well as niobium and oxygen polarons influence

the electrical properties. Hence, it is very complex to pinpoint individual properties such as the appearance of (anti)ferroelectricity to one or several contributions. In this regard, more experiments with different defect concentrations should be conducted. Comparing the electrical conduction behavior, the polarization hysteresis, and permittivity curves of samples with different V'_{Na}, V'_{K}, and $V_O^{\cdot\cdot}$ concentrations could resolve this issue. This could be realized by post-annealing steps at different temperatures and for a variation of dwelling times in sodium- or potassium-rich powder.
The problem of high leakage currents in $K_{0.5}Na_{0.5}NbO_3$-based materials can most likely be explained with a high ionic conductivity of oxygen and alkaline ions. Therefore, it would be important to validate the proposed model and to verify that AC-measurements are highly influenced by ionic conductivity. The suggested post-annealing steps to create different vacancy concentrations would help to understand the origin of the leakage currents in future.

In the end, $K_{0.5}Na_{0.5}NbO_3$-based systems are very complicated but fascinating to study. On the one hand, the further investigation of $NaNbO_3$ and $KNbO_3$ could be very helpful to understand the influence of mobile charge carriers on the antiferroelectricity and ferroelectricity because these two material systems differ only in the A-site atom. On the other hand, $NaNbO_3$ is not the perfect AFE material due to the irreversible AFE-to-FE transition upon poling [133, 134]. PZT-based materials show a more clear and reproducible AFE behavior [11, 25, 331, 332]. In addition, they do not suffer from high leakage currents [333], which makes the analysis and interpretation of the electrical properties more easy. Life cycle assessment (LCA) studies have shown that the production of $K_{0.5}Na_{0.5}NbO_3$-based devices could have an even more severe effect on the environment and human health than the PZT production [334]. This fact should not be neglected completely from an application-oriented point of view when investigating PZT- and $K_{0.5}Na_{0.5}NbO_3$-based systems in research.

Bibliography

[1] Roberta Quadrelli and Sierra Peterson. “The energy-climate challenge: Recent trends in CO2 emissions from fuel combustion”. In: *Energy Policy* 35.11 (2007), pp. 5938–5952.

[2] *Enerdata*. URL: https://yearbook.enerdata.net/ (visited on 04/04/2023).

[3] Steven J. Davis et al. “Net-zero emissions energy systems”. In: *Science* 360.6396 (2018).

[4] “High-power wind energy conversion systems: State-of-the-art and emerging technologies”. In: *Proceedings of the IEEE*. Vol. 103. 5. IEEE, 2015, pp. 740–788.

[5] Szymon Piasecki et al. “Analysis of AC/DC/DC Converter Modules for Direct Current Fast-Charging Applications”. In: *Energies* 14 (2021), p. 6369.

[6] Peter Matthews. *Looking Closer at DC Link Capacitors in Electric Vehicles*. June 2022. URL: https://blog.knowlescapacitors.com/blog/looking-closer-at-dc-link-capacitors-in-electric-vehicles (visited on 11/01/2023).

[7] Huai Wang and Frede Blaabjerg. “Reliability of capacitors for DC-link applications in power electronic converters - An overview”. In: *IEEE Transactions on Industry Applications* 50.5 (2014), pp. 3569–3578.

[8] Xihong Hao. “A review on the dielectric materials for high energy-storage application”. In: *Journal of Advanced Dielectrics* 3.1 (2013), p. 1330001.

[9] Aditya Chauhan et al. “Anti-ferroelectric ceramics for high energy density capacitors”. In: *Materials* 8.12 (2015), pp. 8009–8031.

[10] Zhen Liu et al. “Antiferroelectrics for Energy Storage Applications: a Review”. In: *Advanced Materials Technologies* 3.9 (2018), pp. 1–21.

[11] Clive A. Randall et al. “Antiferroelectrics: History, fundamentals, crystal chemistry, crystal structures, size effects, and applications”. In: *Journal of the American Ceramic Society* 104.8 (2021), pp. 3775–3810.

[12] TDK Electronics AG. *CeraLink Capacitors - For Automotive and Industrial Applications*. 2018.

[13] Xihong Hao et al. “A comprehensive review on the progress of lead zirconate-based antiferroelectric materials”. In: *Progress in Materials Science* 63 (2014), pp. 1–57.

[14] *DIRECTIVE 2011/65/EU OF THE EUROPEAN PARLIAMENT AND OF THE COUNCIL of 8 June 2011 on the restriction of the use of certain hazardous substances in electrical and electronic equipment*. 2011. URL: http://data.europa.eu/eli/dir/2011/65/2023-03-01.

[15] Jurij Koruza et al. “Requirements for the transfer of lead-free piezoceramics into application”. In: *Journal of Materiomics* 4.1 (2018), pp. 13–26.

[16] Jing Feng Li et al. “(K, Na)NbO_3-Based Lead-Free Piezoceramics: Fundamental Aspects, Processing Technologies, and Remaining Challenges”. In: *Journal of the American Ceramic Society* 96.12 (2013), pp. 3677–3696.

[17] Jiagang Wu, Dingquan Xiao, and Jianguo Zhu. “Potassium–Sodium Niobate Lead-Free Piezoelectric Materials: Past, Present, and Future of Phase Boundaries”. In: *Chemical Reviews* 115.7 (2015), pp. 2559–2595.

[18] David R. Lide. *CRC Handbook of Chemistry and Physics*. Boca Raton, FL: CRC Press, 2005.

[19] Jürgen Rödel et al. “Perspective on the Development of Lead-free Piezoceramics”. In: *Journal of the American Ceramic Society* 92.6 (2009), pp. 1153–1177.

[20] Tudor Baiatu, Rainer Waser, and Karl-Heinz Härdtl. “dc Electrical Degradation of Perovskite-Type Titanates: III, A Model of the Mechanism”. In: *Journal of the American Ceramic Society* 73.6 (1990), pp. 1663–1673.

[21] Kazuo Eda. “Zinc Oxide Varistors”. In: *IEEE Electr. Insul. Mag.* 5.6 (1989), pp. 28–41.

[22] W. Heywang. “Semiconducting Barium Titanate”. In: *J. Mater. Sci.* 6.9 (1971), pp. 1214–1224.

[23] G. V. Lewis, C. R.A. Catlow, and R. E.W. Casselton. “PTCR Effect in $BaTiO_3$”. In: *Journal of the American Ceramic Society* 68.10 (1985), pp. 555–558.

[24] Jurij Koruza et al. “Grain-size-induced ferroelectricity in $NaNbO_3$”. In: *Acta Materialia* 126.57 (2017), pp. 77–85.

[25] Gen Shirane. “Ferroelectricity and Antiferroelectricity in Ceramic $PbZrO_3$ Containing Ba or Sr*”. In: *Physical Review* 86 (2 1952).

[26] Hiroyuki Shimizu et al. “Lead-free antiferroelectric: x$CaZrO_3$-(1 - x)$NaNbO_3$ system ($0 \leq x \leq 0.10$)”. In: *Dalton Transactions* 44.23 (2015), pp. 10763–10772.

[27] Mao Hua Zhang et al. “Design of Lead-Free Antiferroelectric (1-x)$NaNbO_3$- x$SrSnO_3$ Compositions Guided by First-Principles Calculations”. In: *Chemistry of Materials* 33.1 (2021), pp. 266–274.

[28] K. Carl and K. H. Hardtl. “Electrical After-Effects In Pb(Ti, Zr)O_3 Ceramics”. In: *Ferroelectrics* 17.1 (1977), pp. 473–486.

[29] P. V. Lambeck and G. H. Jonker. “The Nature of Domain Stabilization in Ferroelectric”. In: *J. Phys. Chem. Solids* 47.5 (1986), pp. 453–461.

[30] Lixue Zhang and Xiaobing Ren. “Aging behavior in single-domain Mn-doped $BaTiO_3$ crystals: Implication for a unified microscopic explanation of ferroelectric aging”. In: *Physical Review B - Condensed Matter and Materials Physics* 73.9 (2006).

[31] Yuri A. Genenko et al. “Mechanisms of aging and fatigue in ferroelectrics”. In: *Materials Science and Engineering B: Solid-State Materials for Advanced Technology* 192 (C 2015), pp. 52–82.

[32] M. Acosta et al. *$BaTiO_3$-based piezoelectrics: Fundamentals, current status, and perspectives*. Dec. 2017.

[33] Binzhi Liu and Xiaoli Tan. “Structure, ferroelectric, and dielectric properties of $(Na_{1-2x}Ca_x)NbO_3$ ceramics”. In: *Journal of Materials Research* 36 (2021), pp. 1076–1085.

[34] Dabin Lin et al. “Influence of MnO_2 doping on the dielectric and piezoelectric properties and the domain structure in $(K_{0.5}Na_{0.5})NbO_3$ single crystals”. In: *Journal of the American Ceramic Society* 93 (4 Apr. 2010), pp. 941–944.

[35] Gurvinderjit Singh, V. S. Tiwari, and P. K. Gupta. “Role of oxygen vacancies on relaxation and conduction behavior of $KNbO_3$ ceramic”. In: *Journal of Applied Physics* 107.064103 (2010).

[36] Dan Xu et al. “Electrical properties of Li and Nb modified $BiFeO_3$ ceramics with reduced leakage current”. In: *Ceramics International* 47 (3 Feb. 2021), pp. 4217–4225.

[37] G. H. Jonker. “Some aspects of semiconducting barium titanate”. In: *Solid-State Electron.* 7 (1964), pp. 895–903.

[38] Cheng-Jien Peng and Hong-Yang Lu. “Compensation Effect in Semiconducting Barium Titanate”. In: *Journal of the American Ceramic Society* 71.1 (1988), pp. C-44–C-46.

[39] Nicole S. Bein et al. “Electrochemical Reduction of Undoped and Cobalt-Doped $BiFeO_3$ Induced by Water Exposure: Quantitative Determination of Reduction Potentials and Defect Energy Levels Using Photoelectron Spectroscopy”. In: *Journal of Physical Chemistry Letters* 10.22 (2019), pp. 7071–7076.

[40] Tadej Rojac et al. “Domain-wall conduction in ferroelectric $BiFeO_3$ controlled by accumulation of charged defects”. In: *Nature Materials* 16 (3 Mar. 2017), pp. 322–327.

[41] A. Molak. “The influence of reduction in valency of Nb ions on the antiferroelectric phase transition in $NaNbO_3$”. In: *Solid State Communications* 62.6 (1987), pp. 413–417.

[42] Issei Suzuki, Leonard G Gura, and Andreas Klein. “The energy level of the $Fe^{2+/3+}$-transition in $BaTiO_3$ and $SrTiO_3$ single crystals”. In: *Phys. Chem. Chem. Phys.* 21 (2019), pp. 6238–6246.

[43] R. Schafranek et al. “Barrier height at (Ba,Sr)TiO_3/Pt interfaces studied by photoemission”. In: *Physical Review B* 77 (19 2008), p. 195310.

[44] I. M. Hodge, M. D. Ingram, and A. R. West. “Impedance and modulus spectroscopy of polycrystalline solid electrolytes”. In: *Journal of Electroanalytical Chemistry* 74.2 (1976), pp. 125–143.

[45] A K Jonscher. “Review: A new understanding of the dielectric relaxation of solids”. In: *Journal of Materials Science* 16 (1981), pp. 2037–2060.

[46] R. Gerhardt. “Impedance and dielectric spectroscopy revisited: Distinguishing localized relaxation from long-range conductivity”. In: *Journal of Physics and Chemistry of Solids* 55.12 (1994), pp. 1491–1506.

[47] D. C. Sinclair and A. R. West. “Effect of atmosphere on the PTCR properties of $BaTiO_3$ ceramics”. In: *Journal of Materials Science* 29.23 (1994), pp. 6061–6068.

[48] Tudor Baiatu, Rainer Waser, and Karl-Heinz Härdtl. “dc Electrical Degradation of Perovskite-Type Titanates: III, A Model of the Mechanism”. In: *Journal of the American Ceramic Society* 73.6 (1990), pp. 1663–1673.

[49] Rainer Waser, Tudor Baiatu, and Karl-Heinz Härdtl. “dc Electrical Degradation of Perovskite-Type Titanates: II, Single Crystals”. In: *J. Am. Ceram. Soc.* 73.6 (1990), pp. 1654–1662.

[50] A.J. Moulson and J.M. Herbert. *Electroceramics*. 2nd. 2003.

[51] Kwan Chi Kao. *Dielectric Phenomena In Solids*. Elsevier Academic Press, 2004, pp. 1–581.

[52] C. Kittel. “Theory of antiferroelectric crystals”. In: *Physical Review* 82.5 (1951), pp. 729–732.

[53] V.M. Goldschmidt. “Die Gesetze der Krystallochemie”. In: 14 (1926), pp. 477–485.

[54] T. Schenk et al. “About the deformation of ferroelectric hystereses”. In: *Applied Physics Reviews* 1.4 (2014), pp. 1–14.

[55] A. Halliyal and T. R. Shrout. In: *Am. Ceram. Conf. (Regional)* (1986).

[56] S. M. Sze and Kwok K. Ng. *Physics of Semiconductor Devices*. 3rd ed. New Jersey: John Wiley & Sons, Inc., 2007.

[57] Siegfried Hunklinger. *Festkörperphysik*. 2002.

[58] Harry L. Tuller and Sean R. Bishop. “Point defects in oxides: Tailoring materials through defect engineering”. In: *Annual Review of Materials Research* 41 (Aug. 2011), pp. 369–398.

[59] I. G. Austin and N. F. Mott. “Polarons in crystalline and non-crystalline Materials”. In: *Advances in Physics* 18.71 (1969), pp. 41–102.

[60] David Emin. *Polarons*. Cambridge University Press, 2013, pp. 1–209.

[61] Michele Reticcioli et al. *Small Polarons in Transition Metal Oxides*. Jan. 2020.

[62] Cesare Franchini et al. “Polarons in materials”. In: *Nature Reviews Materials* 6 (2021), pp. 560–586.

[63] P K Basu. “Excitonic absorption”. In: *Theory of Optical Processes in Semiconductors: Bulk and Microstructures*. New York: Oxford University Press Inc., 2003. Chap. 6, pp. 124–152.

[64] Xihan Chen et al. “Excitonic Effects in Methylammonium Lead Halide Perovskites”. In: *Journal of Physical Chemistry Letters* 9.10 (2018), pp. 2595–2603.

[65] James H. Schulman and Dale W. Compton. *Color Centers in Solids*. Oxford Pergamon, 1962.

[66] Andreas Klein et al. “The Fermi energy as common parameter to describe charge compensation mechanisms: A path to Fermi level engineering of oxide electroceramics”. In: *Journal of Electroceramics* (2023).

[67] F. A. Kröger and N. H. Nachrtrieb. “The Chemistry of Imperfect Crystals”. In: *Physics Today* 17.10 (1964), pp. 66–69.

[68] Seshu B. Desu and David A. Payne. “Interfacial Segregation in Perovskites: II, Experimental Evidence”. In: *Journal of the American Ceramic Society* 73.11 (1990), pp. 3398–3406.

[69] Yet-Ming -M Chiang and Touichi Takagi. “Grain-Boundary Chemistry of Barium Titanate and Strontium Titanate: I, High-Temperature Equilibrium Space Charge”. In: *Journal of the American Ceramic Society* 73.11 (1990), pp. 3278–3285.

[70] Lorenzo Villa and Karsten Albe. “Role of doping and defect quenching in antiferroelectric NaNbO3 from first principles”. In: *Physical Review B* 106.13 (2022), pp. 1–12.

[71] Zuyong Feng and Xiaobing Ren. “Aging effect and large recoverable electrostrain in Mn-doped $KNbO_3$ -based ferroelectrics”. In: *Applied Physics Letters* 91.3 (2007), pp. 89–92.

[72] Xiaoli Tan et al. “Double hysteresis loops at room temperature in $NaNbO_3$-based lead-free antiferroelectric ceramics”. In: *Materials Research Letters* 6.3 (2018), pp. 159–164.

[73] Talal M. Kamel and G. de With. “Poling of hard ferroelectric PZT ceramics”. In: *Journal of the European Ceramic Society* 28.9 (2008), pp. 1827–1838.

[74] O. F. Schirmer and D. Von Der Linde. “Two-photon- and x-ray-induced Nb^{4+} and O^{-} small polarons in $LiNbO_3$”. In: *Applied Physics Letters* 33 (1 1978), pp. 35–38.

[75] K. L. Sweeney and L. E. Halliburton. “Oxygen vacancies in lithium niobate”. In: *Applied Physics Letters* 43 (4 1983), pp. 336–338.

[76] D. Conradi et al. “Influence of Mg doping on the behaviour of polaronic light-induced absorption in $LiNbO_3$”. In: *Physica Status Solidi - Rapid Research Letters* 2 (6 2008), pp. 284–286.

[77] Yu Jun Zhao et al. “Why can $CuInSe_2$ be readily equilibrium-doped n -type but the wider-gap $CuGaSe_2$ cannot?” In: *Applied Physics Letters* 85 (24 2004), pp. 5860–5862.

[78] Andreas Klein. “Transparent Conducting Oxides: Electronic Structure-Property Relationship from Photoelectron Spectroscopy with *in situ* Sample Preparation”. In: *Journal of the American Ceramic Society* 96 (2 2013), pp. 331–345.

[79] S. B. Zhang, Su Huai Wei, and Alex Zunger. “A phenomenological model for systematization and prediction of doping limits in II-VI and I-III-VI_2 compounds”. In: *Journal of Applied Physics* 83 (6 1998), pp. 3192–3196.

[80] Christian Lohaus. “The Fermi Level in Hematite”. PhD. Technical University Darmstadt, 2019.

[81] D. Hull and D. J. Bacon. *Introduction to disclocations*. fifth. Elsevier Ltd., 2011.

[82] Roger A. De Souza. “Transport properties of dislocations in $SrTiO_3$ and other perovskites”. In: *Current Opinion in Solid State and Materials Science* 25 (4 Aug. 2021).

[83] J. P. Hirth. “The Influence of Grain Boundaries on Mechanical Properties”. In: *Metallurgical transcations* 3 (1972), pp. 3047–3067.

[84] G. Blatter and F. Greuter. “Electrical breakdown at semiconductor grain boundaries”. In: *Phys. Rev. B* 34.12 (1986), pp. 8555–8572.

[85] R. Waser and R. Hagenbeck. “Grain boundaries in dielectric and mixed-conducting ceramics”. In: *Acta Materialia* 48.4 (2000), pp. 797–825.

[86] R. A. De Souza and E. C. Dickey. “The effect of space-charge formation on the grain-boundary energy of an ionic solid”. In: *Philosophical Transactions of the Royal Society A: Mathematical, Physical and Engineering Sciences* 377 (2152 2019).

[87] J. Seidel et al. “Conduction at domain walls in oxide multiferroics”. In: *Nature Materials* 8 (3 2009), pp. 229–234.

[88] Tadej Rojac et al. “Mobile Domain Walls as a Bridge between Nanoscale Conductivity and Macroscopic Electromechanical Response”. In: *Advanced Functional Materials* 25 (14 2015), pp. 2099–2108.

[89] Xian Kui Wei et al. “Ferroelectric translational antiphase boundaries in nonpolar materials”. In: *Nature Communications* 5 (2014).

[90] Xian Kui Wei et al. “Polarity of translation boundaries in antiferroelectric $PbZrO_3$”. In: *Materials Research Bulletin* 62 (2015), pp. 101–105.

[91] Hui Ding. “Domain Morphology and Atomic Structure of Antiferroelectric Perovskites”. Dr. rer. nat. Technische Universität Darmstadt, 2022, pp. 1–130.

[92] Georg Rupprecht. “Untersuchungen der elektrischen und lichtelektrischen Leitfähigkeit dünner Indiumoxydschichten”. In: *Zeitschrift für Physik* 139 (1954), pp. 504–509.

[93] H. Köstlin, R. Jost, and W. Lems. “Optical and electrical properties of doped In_2O_3 films”. In: *physica status solidi (a)* 29 (1 1975), pp. 87–93.

[94] S. P. S. Badwal. “Electrical conductivity of single crystal and polycrystalline yttria-stabilized zirconia”. In: *JOURNAL OF MATERIALS SCIENCE* 19 (1984), pp. 1767–1776.

[95] Harry Tuller. “Ionic conduction and applications”. In: *Handbook of Electronic and Photonic Materials*. Ed. by Safa Kasap and Peter Capper. 2nd ed. Springer Nature, 2017, pp. 247–266.

[96] Guoqing Wu and J. J. Neumeier. “Small polaron transport and pressure dependence of the electrical resistivity of $La_{2-x}Sr_xNiO_4$ ($0 \leq x \leq 1.2$)”. In: *Physical Review B - Condensed Matter and Materials Physics* 67 (2003), p. 125116.

[97] Yuriy Natanzon, Amram Azulay, and Yaron Amouyal. “Evaluation of Polaron Transport in Solids from First-principles”. In: *Israel Journal of Chemistry* 60 (2020), pp. 768–786.

[98] Roger A. De Souza. “The formation of equilibrium space-charge zones at grain boundaries in the perovskite oxide $SrTiO_3$”. In: *Physical Chemistry Chemical Physics* 11 (43 2009), pp. 9939–9969.

[99] B. T. Matthias. “New Ferroelectric Crystals”. In: *Physical Review* 75 (1949), p. 1771.

[100] P. Vousden. “The structure of ferroelectric sodium niobate at room temperature”. In: *Acta Crystallographica* 4.6 (1951), pp. 545–551.

[101] P. Vousden. “The non-polarity of sodium niobate”. In: *Acta Crystallographica* 5.5 (1952), pp. 690–690.

[102] H. D. Megaw and M. Wells. “The space group of NaNbO 3 and $(Na_{0.995}K_{0.005})NbO_3$”. In: *Acta Crystallographica* 11.12 (1958), pp. 858–862.

[103] G. Shirane, R. Newnham, and R. Pepinsky. “Dielectric properties and phase transitions of $NaNbO_3$ and (Na,K)NbO_3”. In: *Physical Review* 96.3 (1954), pp. 581–588.

[104] Helen D. Megaw. “The Seven Phases of Sodium Niobate”. In: *Ferroelectrics* 7.1 (1974), pp. 87–89.

[105] A. M. Glazer. “The classification of tilted octahedra in perovskites”. In: *Acta Crystallographica Section B Structural Crystallography and Crystal Chemistry* 28.11 (1972), pp. 3384–3392.

[106] A M Glazer and H D Megaw. “Studies of the Lattice Parameters and Domains in the Phase Transitions of $NaNbO_3$”. In: *Acta Crystallographica* A29 (1973), pp. 489–495.

[107] M Ahtee, A M Glazer, and H D Megaw. “The structures of sodium niobate between 480° and $575\,^\circ$C, and their relevance to soft-phonon modes”. In: *Philosophical Magazine* 26.4 (1972), pp. 995–1014.

[108] K. Sakowski-Cowley A. C.and Łukaszewicz and H. D. Megaw. “The Structure of Sodium Niobate at Room Temperature, and the Problem of Reliability in Pseudosymmetric Structures”. In: *Acta Crystallographica Section B* 25.5 (1969), pp. 851–865.

[109] V.A. Shuvaeva et al. “Crystal structure of the electric-field-induced ferroelectric phase of $NaNbO_3$”. In: *Ferroelectrics* 141.1 (1993), pp. 307–311.

[110] Mao Hua Zhang et al. “Revealing the mechanism of electric-field-induced phase transition in antiferroelectric $NaNbO_3$ by in situ high-energy x-ray diffraction”. In: *Applied Physics Letters* 118 (2021), p. 132903.

[111] O A Zhelnova and O E Fesenko. “Phase transitions and twinning in $NaNbO_3$ crystals”. In: *Ferroelectrics* 75 (1987), pp. 469–475.

[112] Hangfeng Zhang et al. “Isolation of a ferroelectric intermediate phase in antiferroelectric dense sodium niobate ceramics”. In: *Acta Materialia* 179 (2019), pp. 255–261.

[113] Takuya Mino et al. “Piezoelectric properties of epitaxial NaNbO3 thin films deposited on (001)$SrRuO_3$/Pt/MgO substrates”. In: *Japanese Journal of Applied Physics* 46.10 B (2007), pp. 6960–6963.

[114] L. A. Reznichenko et al. “Structural instabilities, incommensurate modulations and P and Q phases in sodium niobate in the temperature range 300-500 K”. In: *Crystallography Reports* 48.3 (2003), pp. 448–456.

[115] I. Lefkowitz, K. Lukaszewicz, and Helen D. Megaw. “The High-Temperature Phases of Sodium Niobate and the Nature of Transitions in Psendosymmetrie Structures”. In: *Acta Crystallographica* 20 (1966), pp. 670–683.

[116] J. Koruza J.and Tellier et al. “Phase transitions of sodium niobate powder and ceramics, prepared by solid state synthesis”. In: *Journal of Applied Physics* 108.11 (2010).

[117] R. A. Shakhovoy et al. “Ferroelectric Q and antiferroelectric P phases’ coexistence and local phase transitions in oxygen-deficient $NaNbO_3$ single crystal: Micro-Raman, dielectric and dilatometric studies”. In: *Journal of Raman Spectroscopy* 43.8 (2012), pp. 1141–1145.

[118] Guillaume Gouget et al. “Isolating the Two Room-Temperature Polymorphs of $NaNbO_3$: Structural Features, Optical Band Gap, and Reactivity”. In: *ACS Applied Electronic Materials* 1.4 (2019), pp. 513–522.

[119] Hideki Kato, Hisayoshi Kobayashi, and Akihiko Kudo. “Role of Ag^+ in the Band Structures and Photocatalytic Properties of $AgMO_3$ (M: Ta and Nb) with the Perovskite Structure”. In: *J. Phys. Chem. B* 106.48 (2002), pp. 12441–12447.

[120] Guoqiang Li et al. “Band structure and photoelectrochemical behavior of $AgNbO_3$-$NaNbO_3$ solid solution photoelectrodes”. In: *Electrochimica Acta* 55.24 (2010), pp. 7235–7239.

[121] Gh. H. Khorrami, A. Kompany, and A. Khorsand Zak. “Structural and optical properties of (K,Na)NbO_3 nanoparticles synthesized by a modified sol-gel method using starch media”. In: *Adv. Powder Technol.* 26.1 (2015), pp. 113–118.

[122] Jun Lv et al. “Synthesis and Photocatalytic Activities of $NaNbO_3$ Rods Modified by In_2O_3 Nanoparticles”. In: *J. Phys. Chem. C* 114.13 (2010), pp. 6157–6162.

[123] Huaiyong Zhu et al. “Structural Evolution in a Hydrothermal Reaction between Nb_2O_5 and NaOH Solution : From Nb_2O_5 Grains to Microporous $Na_2Nb_2O_6 \cdot \frac{2}{3} H_2O$ Fibers and $NaNbO_3$ Cubes”. In: *J. Am. Chem. Soc.* 128.8 (2006), pp. 2373–2384.

[124] Wei Chen, Yin Hu, and Mingwei Ba. “Surface interaction between cubic phase $NaNbO_3$ nanoflowers and Ru nanoparticles for enhancing visible-light driven photosensitized photocatalysis”. In: *Appl. Surf. Sci.* 435 (2018), pp. 483–493.

[125] Peng Li, Hideki Abe, and Jinhua Ye. “Band-Gap Engineering of $NaNbO_3$ for Photocatalytic H_2 Evolution with Visible Light”. In: *Int. J. Photoenergy* 2014 (2014).

[126] Sebastian Zlotnik et al. “Alkali Niobate and Tantalate Perovskites as Alternative Photocatalysts”. In: *ChemPhysChem* 17.21 (2016), pp. 3570–3575.

[127] Haifeng Shi and Zhigang Zou. “Photophysical and photocatalytic properties of $ANbO_3$ (A=Na, K) photocatalysts”. In: *Journal of Physics and Chemistry of Solids* 73.6 (2012), pp. 788–792.

[128] Lorenzo Villa. “Impact of doping conditions on the Fermi level in lead-free antiferroelectrics”. Materials Modelling, 2023, pp. 1–144.

[129] Guang Zhao Wang et al. “Hybrid Density Functional Study on Mono- and Codoped $NaNbO_3$ for Visible-Light Photocatalysis”. In: *ChemPhysChem* 17 (4 2016), pp. 489–499.

[130] Peng Li et al. “The effects of crystal structure and electronic structure on photocatalytic H_2 evolution and CO_2 reduction over two phases of perovskite-structured $NaNbO_3$”. In: *Journal of Physical Chemistry C* 116 (14 Apr. 2012), pp. 7621–7628.

[131] L.E. Cross and B.J. Nicholson. “The optical and electrical properties of single crystals of sodium niobate”. In: *The London, Edinburgh, and Dublin Philosophical Magazine and Journal of Science* 46.376 (1955), pp. 453–466.

[132] L.E. Cross. “Electric Double Hysteresis in $(K_xNa_{1-x})NbO_3$ Single Crystals”. In: *Nature* 181 (1958), pp. 178–179.

[133] Mao Hua Zhang et al. “Electric-field-induced antiferroelectric to ferroelectric phase transition in polycrystalline $NaNbO_3$”. In: *Acta Materialia* 200 (2020), pp. 127–135.

[134] He Qi et al. “Emerging antiferroelectric phases with fascinating dielectric, polarization and strain response in $NaNbO_3$ -$(Bi_{0.5}Na_{0.5})TiO_3$ lead-free binary system”. In: *Journal of the European Ceramic Society* 39.13 (2019), pp. 3703–3709.

[135] Hanzheng Guo et al. “Domain configuration changes under electric field-induced antiferroelectric-ferroelectric phase transitions in $NaNbO_3$-based ceramics”. In: *Journal of Applied Physics* 118.5 (2015), pp. 1–7.

[136] Hanzheng Guo, Hiroyuki Shimizu, and Clive A. Randall. “Direct evidence of an incommensurate phase in $NaNbO_3$ and its implication in $NaNbO_3$-based lead-free antiferroelectrics”. In: *Applied Physics Letters* 107.11 (2015).

[137] Lisheng Gao et al. “A perovskite lead-free antiferroelectric xCaHfO_3-(1-x)NaNbO_3 with induced double hysteresis loops at room temperature”. In: *Journal of Applied Physics* 120.20 (2016).

[138] He Qi et al. “Excellent energy-storage properties of NaNbO_3-based lead-free antiferroelectric orthorhombic P-phase (Pbma) ceramics with repeatable double polarization-field loops”. In: *Journal of the European Ceramic Society* 39.13 (2019), pp. 3703–3709.

[139] A. Torres-Pardo et al. “Room Temperature Ferroelectricity in $Na_{1-x}Sr_{x/2}\square_{x/2}NbO_3$ through the Introduction of Cationic Vacancies”. In: *Chem. Mater.* 20.22 (2008), pp. 6957–6964.

[140] Takahiro Arioka et al. “Ferroelectricity in NaNbO_3: Revisited”. In: *Ferroelectrics* 401.1 (2010), pp. 51–55.

[141] Mao-Hua Zhang. “Field-Induced Phase Transition of Lead-Free Antiferroelectric Niobates”. Dr. rer. nat. Technische Universität Darmstadt, 2022, pp. 1–124.

[142] J. Macutkevic, A. Molak, and J. Banys. “Dielectric properties of NaNbO_3 ceramics”. In: *Ferroelectrics* 479.1 (2015), pp. 48–55.

[143] Silvania Lanfredi, Laurent Dessemond, and Ana C.M. Rodrigues. “Effect of Porosity on the Electrical Properties of Polycrystalline Sodium Niobate: I, Electrical Conductivity”. In: *Journal of the American Ceramic Society* 86.2 (2003), pp. 291–298.

[144] W. Bak, C. Kus, and W. S. Ptak. “The transport properties of polycrystalline NaNbO_3 determined from immitance spectra at very low frequencies”. In: *Ferroelectrics* 115.1 (1991), pp. 105–111.

[145] M Pisarski. “Hydrostatic Pressure in Kinetic Phenomena in NaNbO_3 Single Crystals”. In: *Physica Status Solidi (B)* 101 (1980), pp. 635–644.

[146] T. Ruf et al. “The influence on sintering and properties of sodium niobate (NaNbO_3) ceramics by “non-stoichiometric” precursor compositions”. In: *Materials Chemistry and Physics* 229 (2019), pp. 437–447.

[147] Michal Pilch and Andrzej Molak. “Resistance switching in rejuvenated NaNbO_3:Mn crystals”. In: *Phase Transitions* 87.10-11 (2014), pp. 1114–1128.

[148] Fen Ye et al. “The effect of B-site acceptor doping on the microstructure and electric properties of NaNbO_3 ceramics”. In: *Journal of Materials Science: Materials in Electronics* 33 (2022), pp. 4497–4509.

[149] I. P. Raevski et al. “Study of intrinsic point defects in oxides of the perovskite family: II. Experiment”. In: *Journal of Physics Condensed Matter* 10.36 (1998), pp. 8015–8032.

[150] M. A.L. Nobre and S. Lanfredi. “Ferroelectric state analysis in grain boundary of $Na_{0.85}Li_{0.15}NbO_3$ ceramic”. In: *Journal of Applied Physics* 93.9 (2003), pp. 5557–5562.

[151] J. Tanaka et al. “The electrical conduction mechanism in the semiconducting sodium niobate”. In: *Solid State Communications* 34 (1980), pp. 221–224.

[152] K. Krzywanek et al. “Polaronic transport in $NaNbO_3$”. In: *Ferroelectrics* 126.1 (1992), pp. 173–178.

[153] E. A. Wood. “Polymorphism in potassium niobate, sodium niobate, and other ABO_3 compounds”. In: *Acta Crystallographica* 4.4 (1951), pp. 353–362.

[154] G. Shirane et al. “Phase transitions in ferroelectric $KNbO_3$”. In: *Physical Review* 93.4 (1954), pp. 672–673.

[155] R. M. Cotts and W. D. Knight. “Nuclear Resonance of Nb^{93} in $KNbO_3$”. In: *Physical Review* 96.5 (1954), pp. 1285–1293.

[156] A. W. Hewat. “Cubic-tetragonal-orthorhombic-rhombohedral ferroelectric transitions in perovskite potassium niobate: Neutron powder profile refinement of the structures”. In: *Journal of Physics C: Solid State Physics* 6.16 (1973), pp. 2559–2572.

[157] S. L. Skjærvo et al. “Thermal evolution of the crystal structure and phase transitions of $KNbO_3$”. In: *Royal Society Open Science* 5.6 (2018).

[158] L. Katz and H. D. Megaw. “The structure of potassium niobate at room temperature: the solution of a pseudosymmetric structure by Fourier methods”. In: *Acta Crystallographica* 22.5 (1967), pp. 639–648.

[159] Akio Shigemi and Takahiro Wada. “Evaluations of phases and vacancy formation energies in $KNbO_3$ by first-principles calculation”. In: *Japanese Journal of Applied Physics* 44.11 (2005), pp. 8048–8054.

[160] Koichi Momma and Fujio Izumi. *Visualization of Electronic and STructural Analysis*. Aug. 2022.

[161] Falko Schmidt et al. “Consistent atomic geometries and electronic structure of five phases of potassium niobate from density-functional theory”. In: *Advances in Materials Science and Engineering* (2017), pp. 1–13.

[162] Chung-gang Duan et al. “First-principles study on the optical properties of $KNbO_3$”. In: *Journal of Physics: Condensed Matter* 13 (2001), pp. 8189–8195.

[163] Falko Schmidt et al. “Quasiparticle and excitonic effects in the optical response of $KNbO_3$”. In: *Physical Review Materials* 3.5 (2019), p. 054401.

[164] Kenichi Kudo et al. “Characterization of $KNbO_3$ crystal by traveling solvent floating zone (TSFZ) method”. In: *Japanese Journal of Applied Physics* 42.9B (2003), pp. 6099–6101.

[165] Tiago Bender Wermuth et al. “GMicrowave-synthesized $KNbO_3$ perovskites: photocatalytic pathway on the degradation of rhodamine B”. In: *Ceramics International* 45.18 (2019), pp. 24137–24145.

[166] Cristina Pascual-Gonzalez, Giorgio Schileo, and Antonio Feteira. “Band gap narrowing in ferroelectric $KNbO_3$-Bi(Yb,Me)O_3 (Me=Fe or Mn) ceramics”. In: *Applied Physics Letters* 109.13 (2016).

[167] Tingting Zhang et al. “Photocatalytic water splitting for hydrogen generation on cubic, orthorhombic, and tetragonal $KNbO_3$ microcubes”. In: *Nanoscale* 5.18 (2013), pp. 8375–8383.

[168] R Resta, M Posternak, and A Baldereschi. “Towards a Quantum Theory of Polarization in Ferroelectrics: The Case of $KNbO_3$”. In: *Physical Review Letters* 70.7 (1993), pp. 1010–1013.

[169] S. Triebwasser. “Behavior of ferroelectric $KNbO_3$ in the vicinity of the cubic-tetragonal transition”. In: *Physical Review* 101.3 (1956), pp. 993–997.

[170] P Günter. “Spontaneous polarization and pyroelectric effect in $KNbO_3$”. In: *Journal of Applied Physics* 48 (1977), pp. 3475–3477.

[171] W. Kleemann, F. J. Schäfer, and M. D. Fontana. “Crystal optical studies of spontaneous and precursor polarization in $KNbO_3$”. In: *Physical Review B* 30.3 (1984), pp. 1148–1154.

[172] Ken Ichi Kakimoto, Izumi Masuda, and Hitoshi Ohsato. “Ferroelectric and piezoelectric properties of $KNbO_3$ ceramics containing small amounts of $LaFeO_3$”. In: *Japanese Journal of Applied Physics* 42.9B (2003), pp. 6102–6105.

[173] Dae Hyeon Kim et al. “Influence of sintering conditions on piezoelectric properties of $KNbO_3$ ceramics”. In: *Journal of the European Ceramic Society* 34 (2014), pp. 4193–4200.

[174] Xiang Lv et al. “New dielectric anomalies in the A-site highly deficient Na_xNbO_3 electroceramics”. In: *ACS Applied Materials and Interfaces* 8.44 (2016), pp. 30304–30311.

[175] U Flückiger and H Arend. “On the preparation of pure, doped and reduced $KNbO_3$ single crystals”. In: *Journal of Crystal Growth* 43 (1978), pp. 406–416.

[176] Kohei Kodaira et al. “Sintering and dielectric properties of $KNbO_3$”. In: *Journal of Materials Science Letters* 1.7 (1982), pp. 277–278.

[177] A. Popovič et al. “Vapour pressure and mixing thermodynamic properties of the $KNbO_3$-$NaNbO_3$ system”. In: *RSC Advances* 5.93 (2015), pp. 76249–76256.

[178] Jong Hyun Kim et al. “Effect of CuO on the ferroelectric and piezoelectric properties of lead-free $KNbO_3$ ceramics”. In: *Sensors and Actuators, A: Physical* 234 (2015), pp. 9–16.

[179] Kenji Matsumoto et al. “Piezoelectric properties of pure and Mn-doped potassium niobate ferroelectric ceramics”. In: *Japanese Journal of Applied Physics* 45.5 B (2006), pp. 4479–4483.

[180] Zuyong Feng and Siu Wing Or. “Aging-induced, defect-mediated double ferroelectric hysteresis loops and large recoverable electrostrains in Mn-doped orthorhombic $KNbO_3$-based ceramics”. In: *Journal of Alloys and Compounds* 480.2 (2009), pp. 29–32.

[181] Jigong Hao et al. “Electric Field Cycling Induced Large Electrostrain in Aged $(K_{0.5}Na_{0.5})NbO_3$-Cu Lead-Free Piezoelectric Ceramics”. In: *Journal of the American Ceramic Society* 99.2 (2016), pp. 402–405.

[182] Meng Jiang et al. “Double hysteresis loops induced by Mn doping in $Pb_{0.99}Nb_{0.02}(Zr_{0.95}Ti_{0.05})_{0.98}O_3$ ferroelectric ceramics”. In: *Current Applied Physics* 10.2 (2010), pp. 526–530.

[183] Chanku Lee et al. “Frequency dependence of AC conductivities of $KNb_{1-x}V_xO_3$ single crystals”. In: *Physica B: Condensed Matter* 239.3-4 (1997), pp. 316–321.

[184] J. Handerek et al. “The electric and thermoelectric singularities due to the small polaron hopping motion conductivity transition in $KNbO_3$ monocrystals”. In: *Ferroelectrics* 22.1 (1978), pp. 735–737.

[185] B. Sundarakannan, K. Kakimoto, and H. Ohsato. “Frequency and temperature dependent dielectric and conductivity behavior of $KNbO_3$ ceramics”. In: *Journal of Applied Physics* 94.8 (2003), pp. 5182–5187.

[186] A.E. Krumins and P. Guenter. “Photovoltaic Effect and Photoconductivity in Reduced Potassium Niobate Crystals”. In: *Physica Status Solidi (a)* 55 (1979), pp. 185–189.

[187] Yongli Wang et al. “High-temperature instability of Li- and Ta-modified (K,Na)NbO_3 piezoceramics”. In: *Journal of the American Ceramic Society* 91.6 (2008), pp. 1962–1970.

[188] Arnold Reisman et al. “Metastability in Niobate Systems”. In: (1959), pp. 1292–1295.

[189] Hansu Birol, Dragan Damjanovic, and Nava Setter. “Preparation and characterization of $KNbO_3$ ceramics”. In: *Journal of the American Ceramic Society* 88 (7 July 2005), pp. 1754–1759.

[190] Yuhua Zhen and Jing Feng Li. “Normal sintering of (K,Na)NbO_3-based ceramics: Influence of sintering temperature on densification, microstructure, and electrical properties”. In: *Journal of the American Ceramic Society* 89 (12 2006), pp. 3669–3675.

[191] Jitka Hrščeak et al. “The influence of different niobium pentoxide precursors on the solid-state synthesis of potassium sodium niobate”. In: *Journal of the European Ceramic Society* 33.15–16 (2013), pp. 3065–3075.

[192] Jurij Koruza and Barbara Malič. “Initial stage sintering mechanism of $NaNbO_3$ and implications regarding the densification of alkaline niobates”. In: *Journal of the European Ceramic Society* 34.8 (2014), pp. 1971–1979.

[193] Darja Jenko et al. “Electron microscopy studies of potassium sodium niobate ceramics”. In: *Microscopy and Microanalysis* 11 (6 Dec. 2005), pp. 572–580.

[194] Jurij Koruza, Barbara Malič, and Marija Kosec. “Microstructure evolution during sintering of sodium niobate”. In: *Journal of the American Ceramic Society* 94.12 (2011), pp. 4174–4178.

[195] Azar Nazeri-Eshghi, A. X. Kuang, and J. D. Mackenzie. “Preparation and properties of $KNbO_3$ via the sol-gel method”. In: *Journal of Materials Science* 25 (1990), pp. 3333–3337.

[196] Gregory K L Goh et al. “Hydrothermal synthesis of $KNbO_3$ and $NaNbO_3$ powders”. In: *Journal of Material Research* 18 (2003), pp. 338–345.

[197] Chung-Hsin Lu, Shih-Yen Lo, and Yueh-Lu Wang. “Glycothermal preparation of potassium niobate ceramic particles under supercritical conditions”. In: *Materials Letters* 55 (2002), pp. 121–125.

[198] Yosuke Shiratori et al. “Polymorphism in micro-, Submicro-, and nanocrystalline $NaNbO_3$”. In: *Journal of Physical Chemistry B* 109 (43 Nov. 2005), pp. 20122–20130.

[199] G. H. HAERTLING. “Properties of Hot-Pressed Ferroelectric Alkali Niobate Ceramics”. In: *Journal of the American Ceramic Society* 50 (6 1967), pp. 329–330.

[200] Takahiro Wada et al. “Ferroelectric $NaNbO_3$ ceramics fabricated by spark plasma sintering”. In: *Japanese Journal of Applied Physics, Part 1: Regular Papers and Short Notes and Review Papers* 42 (9 B 2003), pp. 6110–6114.

[201] Ruiping Wang et al. “Fabrication and characterization of potassium-sodium niobate piezoelectric ceramics by spark-plasma-sintering method”. In: *Materials Research Bulletin* 39 (11 Sept. 2004), pp. 1709–1715.

[202] Barbara Malič et al. “Synthesis of sodium potassium niobate: A diffusion couples study”. In: *Journal of the American Ceramic Society* 91.6 (2008), pp. 1916–1922.

[203] Barbara Malič et al. “Synthesis and Sintering of (K,Na)NbO_3 Based Ceramics”. In: *Materials Research Society* 755 (2003).

[204] Jérôme Acker, Hans Kungl, and Michael J. Hoffmann. “Sintering and microstructure of potassium niobate ceramics with stoichiometric composition and with potassium- or niobium excess”. In: *Journal of the European Ceramic Society* 33.11 (2013), pp. 2127–2139.

[205] Jernej Pavlič, Barbara Malič, and Tadej Rojac. “Microstructural, structural, dielectric and piezoelectric properties of potassium sodium niobate thick films”. In: *Journal of the European Ceramic Society* 34 (2 2014), pp. 285–295.

[206] Dunmin Lin, K. W. Kwok, and H. L.W. Chan. “Piezoelectric and ferroelectric properties of Cu-doped $K_{0.5}Na_{0.5}NbO_3$ lead-free ceramics”. In: *Journal of Physics D: Applied Physics* 41 (4 2008).

[207] Kepi Chen et al. “Screening sintering aids for $(K_{0.5}Na_{0.5})NbO_3$ ceramics”. In: *Journal of the American Ceramic Society* 98 (6 2015), pp. 1698–1701.

[208] Xuming Pang et al. “Effect of ZnO on the microstructure and electrical properties of $(K_{0.5}Na_{0.5})NbO_3$ lead-free piezoelectric ceramics”. In: *Journal of Materials Science: Materials in Electronics* 23 (5 2012), pp. 1083–1086.

[209] Dunmin Lin et al. “Dielectric and piezoelectric properties of MnO_2-doped $K_{0.5}Na_{0.5}Nb_{0.9}2Sb_{0.08}O_3$ lead-free ceramics”. In: *Journal of Materials Science: Materials in Electronics* 21 (7 2010), pp. 649–655.

[210] L. Ramajo et al. “Influence of MoO_3 on electrical and microstructural properties of $(K_{0.44}Na_{0.52}Li_{0.04})(Nb_{0.86}Ta_{0.10}Sb_{0.04})O_3$”. In: *Journal of Materials Science: Materials in Electronics* 24 (9 2013), pp. 3587–3593.

[211] Nader Marandian Hagh, Bahram Jadidian, and Ahmad Ashbahian Eric andSafari. “Lead-free piezoelectric ceramic transducer in the donor-doped $K_1/2Na_1/2NbO_3$ solid solution system”. In: *IEEE Transactions on Ultrasonics, Ferroelectrics, and Frequency Control* 55.1 (2008), pp. 214–224.

[212] J. Hrščeak et al. “Donor doping of $K_0.5Na_0.5NbO_3$ ceramics with strontium and its implications to grain size, phase composition and crystal structure”. In: *Journal of the European Ceramic Society* 37.5 (2017), pp. 2073–2082.

[213] Zhiyong Liu et al. “Energy storage properties of $NaNbO_3$-$CaZrO_3$ ceramics with coexistence of ferroelectric and antiferroelectric phases”. In: *Journal of the European Ceramic Society* 38 (2018), pp. 4939–4945.

[214] Marija Kosec et al. “KNN-Based Piezoelectric Ceramics”. In: *Piezoelectric and Acoustic Materials for Transducer Applications*. Ed. by Ahmad Safari and E. Koray Akdogan. Springer, 2008, pp. 81–102.

[215] Ajit Jillavenkatesa, Stanley J. Dapkunas, and Lin-Sien H. Lum. “Size Characterization by Laser Light Diffraction Techniques”. In: *Particle Size Characterization*. Washington, 2001. Chap. 6, pp. 93–124.

[216] Jurij Koruza. “Sintering and phase transition behaviour of sodium niobate”. Doctoral Dissertation. Jozef Stefan International Postgraduate School, 2013, p. 131.

[217] A. R. Boccaccini and B. Hamann. “In situ high-temperature optical microscopy”. In: *Journal of Materials Science* 34.22 (1999), pp. 5419–5436.

[218] Sudip Kundu et al. “On the density calculation of fabricated zirconia toughened alumina by unconventional method”. In: vol. 561. Institute of Physics Publishing, Nov. 2019.

[219] Anwar Ul-Hamid. *A Beginners’ Guide to Scanning Electron Microscopy*. Switzerland: Springer Nature Switzerland AG, 2018, p. 213.

[220] Lothar Spieß et al. *Moderne Röntgenbeugung*. 2nd ed. Vieweg+Teubner, 2009, pp. 1–557.

[221] C. B. Sawyer and C. H. Tower. “Rochelle salt as a dielectric”. In: *Physical Review* 35.3 (1930), pp. 269–273.

[222] S. Tiedke and T. Schmitz. “Electrical Characterization of Nanoscale Ferroelectric Structures”. In: *Nanoscale Characterisation of Ferroelectric Materials*. Ed. by Marin Alexe and Alexei Gruverman. Heidelberg: Springer, 2004. Chap. 3, pp. 87–114.

[223] Stefan Hüfner. *Photoelectron Spectroscopy - Principles and Applications*. 3rd. Springer, 2003.

[224] T. Koopmans. “Über die Zuordnung von Wellenfunktionen und Eigenwerten zu den Einzelnen Elektronen Eines Atoms”. In: *Physica* 1.1-6 (1934), pp. 104–113.

[225] W. F. Egelhoff. “Core-level binding-energy shifts at surfaces and in solids”. In: *Surface Science Reports* 6 (1987), pp. 253–415.

[226] Andreas Klein et al. “Photoelectron Spectroscopy in Materials Science and Physical Chemistry: Analysis of Composition, Chemical Bonding and Electronic Structure of Surfaces and Interfaces”. In: *Bunsen-Magazin* 10.4 (2008), pp. 124–139.

[227] D. A. Shirley. “High-resolution x-ray photoemission spectrum of the valence bands of gold”. In: *Physical Review B* 5.12 (1972), pp. 4709–4714.

[228] S. Miyazaki et al. “Structure and electronic states of ultrathin SiO_2 thermally grown on Si(100) and Si(111) surfaces”. In: *Appl. Surf. Sci.* 113-114 (1997), pp. 585–589.

[229] Stephan Hillmann et al. “Application of atomic layer deposited Al_2O_3 as charge injection layer for high-permittivity dielectrics”. In: *Semicond. Sci. Technol.* 30.2 (2015).

[230] Christian Lohaus, Andreas Klein, and Wolfram Jaegermann. “Limitation of Fermi level shifts by polaron defect states in hematite photoelectrodes”. In: *Nature Communications* 9 (1 2018), pp. 1–7.

[231] Yannick Hermans et al. “Energy-Band Alignment of $BiVO_4$ from Photoelectron Spectroscopy of Solid-State Interfaces”. In: *Journal of Physical Chemistry C* 122.36 (2018), pp. 20861–20870.

[232] Andreas Klein. “Interface Properties of Dielectric Oxides”. In: *Journal of the American Ceramic Society* 99 (2016), pp. 369–387.

[233] A. Klein et al. “Surface potentials of magnetron sputtered transparent conducting oxides”. In: *Thin Solid Films* 518.4 (2009), pp. 1197–1203.

[234] Shengtao Li. “Improvement of surface flashover in vacuum”. In: *High Voltage* 5 (2 Apr. 2020), pp. 122–133.

[235] Georg S. Ohm. *Die galvanische Kette*. Ed. by T. H. Riemann. 1827, pp. 1–245.

[236] Stephen J. Skinner and John A. Kilner. “Oxygen ion conductors”. In: *Materialstoday* 6 (3 2003), pp. 30–37.

[237] Keith J. Laidler. “The Development of the Arrhenius Equation”. In: *Journal of Chemical Education* 61.6 (1984), pp. 494–498.

[238] Hiroshi Kishi, Youichi Mizuno, and Hirokazu Chazono. “Base-metal electrode-multilayer ceramic capacitors: Past, present and future perspectives”. In: *Japanese Journal of Applied Physics, Part 1: Regular Papers and Short Notes and Review Papers* 42 (1 2003), pp. 1–5.

[239] Vadim F. Lvovich. *Impedance Spectroscopy: Applications to Electrochemical and Dielectric Phenomena*. New Jersey: John Wiley & Sons, Inc., 2012, p. 353.

[240] Evgenij Barsoukov and J. Ross Macdonald, eds. *Impedance Spectroscopy: Theory, Experiment, and Applications*. Third. New Jersey: John Wiley & Sons, Inc., 2018, p. 528.

[241] Yannick Hermans. “Interface analysis and development of $BiVO_4$ and $CuFeO_2$ heterostructures for photochemical water splitting”. PhD. Technical University of Darmstadt, 2019.

[242] Mareike Frischbier. “Die elektrischen Eigenschaften von Indiumoxid-Dünnschichten : in-situ Hall-Effekt-Messungen zur Aufklärung des Einflusses von Punktdefekten und Korngrenzen”. Dr.-Ing. Technische Universität Darmstadt, 2015, pp. 1–259.

[243] Barbara Malič et al. “Strontium doped $K_0.5Na_0.5NbO_3$ based piezoceramics”. In: *Ferroelectrics* 314 (2005), pp. 149–156.

[244] Shinjiro Tashiro and Keisuke Ishii. “Grain Size and Piezoelectric Properties of (Ba, K, Na)NbO_3 Lead-Free Ceramics”. In: *Journal of the Ceramic Society of Japan* 114.5 (2006), pp. 386–391.

[245] J. Lee and K. Hong. “Revisit to the Origin of Grain Growth Anomaly in Yttria-Doped Barium Titanate”. In: *J. Am. Ceram. Soc.* 84.8 (2001), pp. 1745–1749.

[246] Ming Hong Lin and Hong Yang Lu. “Site-occupancy of yttrium as a dopant in BaO-excess $BaTiO_3$”. In: *Mater. Sci. Engin. A* 335.15 (2002), pp. 101–108.

[247] I. López M. L.and Álvarez-Serrano et al. “New dielectric anomalies in the A-site highly deficient Na_xNbO_3 electroceramics”. In: *Ceramics International* 46.10 (2020), pp. 16770–16780.

[248] R. D. Shannon. “Revised effective ionic radii and systematic studies of interatomic distances in halides and chalcogenides”. In: *Acta Crystallographica Section A* 32.5 (1976), pp. 751–767.

[249] Hanzheng Guo et al. “Strategy for stabilization of the antiferroelectric phase (Pbma) over the metastable ferroelectric phase ($P2_1ma$) to establish double loop hysteresis in lead-free (1-x)$NaNbO_3$-x$SrZrO_3$ solid solution”. In: *Journal of Applied Physics* 117.21 (2015).

[250] Lisheng Gao et al. “Stabilized antiferroelectricity in x$BiScO_3$-(1-x)$NaNbO_3$ lead-free ceramics with established double hysteresis loops”. In: *Applied Physics Letters* 112.9 (2018).

[251] Min Chen et al. “Realizing room temperature double hysteresis loops in antiferroelectric $NaNbO_3$ based ceramics”. In: *Ceramics International* 47.15 (2021), pp. 21303–21309.

[252] Yuzhu Fan et al. “The effect of A-site nonstoichiometry on the microstructure, electric properties, and phase stability of $NaNbO_3$ polycrystalline ceramics”. In: *Journal of the European Ceramic Society* 39.15 (2019).

[253] R. Wernicke. “The Influence of Kinetic Processes on the Electrical Conductivity of Donor-Doped $BaTiO_3$ Ceramics”. In: *Physica Status Solidi (a)* 47.1 (1978), pp. 139–144.

[254] Yet-Ming -M Chiang and Touichi Takagi. “Grain-Boundary Chemistry of Barium Titanate and Strontium Titanate: II, Origin of Electrical Barriers in Positive-Temperature-Coefficient Thermistors”. In: *Journal of the American Ceramic Society* 73.11 (1990), pp. 3286–3291.

[255] Ken Ichi Kakimoto, Izumi Masuda, and Hitoshi Ohsato. “Lead-free $KNbO_3$ piezoceramics synthesized by pressure-less sintering”. In: *Journal of the European Ceramic Society* 25.12 SPEC. ISS. (2005), pp. 2719–2722.

[256] B. K. Yun et al. “Coexistence of piezoelectricity and electric conduction in oxygen-deficient $NaNbO_{3-\delta}$ sub-micron cubes”. In: *Materials Science and Engineering B: Solid-State Materials for Advanced Technology* 182.1 (2014), pp. 81–85.

[257] S. Lanfredi, M. H. Lente, and J. A. Eiras. “Phase transition at low temperature in $NaNbO_3$ ceramic”. In: *Applied Physics Letters* 80.15 (2002), pp. 2731–2733.

[258] A. Mansingh and A. Dhar. “The AC conductivity and dielectric constant of lithium niobate single crystals”. In: *Journal of Physics D: Applied Physics* 18.10 (1985), pp. 2059–2071.

[259] A K Jonscher. “Dielectric relaxation in solids”. In: *Journal of Physics D: Applied Physics* 32.14 (1999), R57–R70.

[260] Shengping Ding and Jiaqi Shen. “Microstructures and Dielectric Properties of Pure and Doped $KNbO_3$ Ceramics”. In: *Journal of the American Ceramic Society* 73.55 (1990), pp. 1449–1450.

[261] Fei Han et al. “Impedance Spectroscopy and Photovoltaic Effect of Oxygen Defect Engineering on $KNbO_3$ Ferroelectric Semiconductors”. In: *IEEE Transactions on Ultrasonics, Ferroelectrics, and Frequency Control* 49.10 (2020), pp. 6165–6174.

[262] Magdalena Kruczek, Ewa Talik, and Antoni Kania. “Electronic structure of $AgNbO_3$ and $NaNbO_3$ studied by X-ray photoelectron spectroscopy”. In: *Solid State Communications* 137.9 (2006), pp. 469–473.

[263] A. Molak et al. “Nano-scale chemical and structural segregation induced in surface layer of $NaNbO_3$ crystals with thermal treatment at oxidising conditions studied by XPS, AFM, XRD, and electric properties tests”. In: *Phase Transitions* 82.9 (2009), pp. 662–682.

[264] Amit Singh Vig et al. “Influence of Ca-doped $NaNbO_3$ and its heterojunction with g-C_3N_4 on the photoredox performance”. In: *Solar Energy* 185 (2019), pp. 469–479.

[265] K. Szot et al. “Surface defect segregation in the perovskite-type ferroelectric $KNbO_3$”. In: *Applied Physics Letters* 48.7 (1986), pp. 490–492.

[266] K. Szot et al. “Surface chemistry and molecular reactions on $KNbO_3$ single crystal surfaces”. In: *Surface Science* 280 (1993), pp. 179–184.

[267] Fabiano R. Praxedes et al. “Nanostructured $K_xNa_{1-x}NbO_3$ hollow spheres as potential materials for the photocatalytic treatment of polluted water”. In: *Applied Catalysis B: Environmental* 298 (2021).

[268] G. Pirug, O. Müller, and H.P. Bonzel. “The Alkali Metal Induced Oxidation of Si(1OO) Surfaces”. In: *Surface Science - Principles and Applications*. Ed. by R.F. Howe, R.N. Lamb, and K. Wandelt. 1st ed. Berlin: Springer, 1993. Chap. 3, pp. 145–154.

[269] B. Lamontagne, F. Semond, and D. Roy. “X-ray photoelectron spectroscopic study of Si(111) oxidation promoted by potassium multilayers under low O_2 pressures”. In: *Journal of Electron Spectroscopy and Related Phenomena* 73.1 (1993), pp. 81–88.

[270] B. Lamontagne, F. Semond, and D. Roy. “K overlayer oxidation studied by XPS: the effects of the adsorption and oxidation conditions”. In: *Surface Science* 327.3 (1995), pp. 371–378.

[271] Robert Schafranek. “Kathodenzerstäubte (Ba,Sr)TiO_3-Dünnschichten für steuerbare Mikrowellenkomponenten”. Dr.-Ing. Technische Universität Darmstadt, 2009, pp. 107–124.

[272] Karsten Rachut. “Zusammensetzung von dünnen Schichten im System $SrTiO_3$–$BaTiO_3$”. Dr.-Ing. Technische Universität Darmstadt, 2019, pp. 189–195.

[273] Carla Puglia et al. “A photoemission and XAS study of oxygen coadsorbed with a (2 × 2) layer of K on graphite”. In: *Surface Science* 383 (1997), pp. 149–161.

[274] P. Steiner, H. Höchst, and S. Hüfner. “XPS investigation of simple metals”. In: *Zeitschrift für Physik B Condensed Matter and Quanta* 30.2 (1978), pp. 129–143.

[275] A. Barrie and F. J. Street. “An auger and x-ray photoelectron spectroscopic study of sodium metal and sodium oxide”. In: *Journal of Electron Spectroscopy and Related Phenomena* 7 (1975), pp. 1–31.

[276] Daniel M. Long, Andreas Klein, and Elizabeth C. Dickey. “Barrier formation at $BaTiO_3$ interfaces with Ni and NiO”. In: *Applied Surface Science* 466 (2019), pp. 472–476.

[277] J. L. Wang et al. “Strain dependence of dissociative adsorption of H$_2$O on epitaxially strained, out-of-plane polarized, BaTiO$_3$(001) thin films”. In: *Thin Solid Films* 717 (2021).

[278] Katharina N.S. Schuldt et al. “Influence of Defects on the Schottky Barrier Height at $BaTiO_3$/RuO_2 Interfaces”. In: *Physica Status Solidi (A) Applications and Materials Science* 218.14 (2021), pp. 1–9.

[279] T. Al Morgan et al. “Self-assembled stoichiometric barium titanate thin films grown by molecular beam epitaxy”. In: *Journal of Crystal Growth* 493 (2018), pp. 15–19.

[280] Irena Spasojevic et al. “Oxidation processes at the surface of BaTiO$_3$ thin films under environmental conditions”. In: *Applied Surface Science* 565 (2021).

[281] L. T. Hudson, R. L. Kurtz, and S. W. Robey. “Surface core-level shifts of barium observed in photoemission of vacuum-fractured $BaTiO_3$ (100)”. In: *Physical Review B* 47.16 (1993), pp. 832–838.

[282] J. D. Baniecki et al. “Surface core-level shifts of strontium observed in photoemission of barium strontium titanate thin films”. In: *Applied Physics Letters* 89.16 (2006), pp. 89–91.

[283] X. L. Li et al. “Characteristics of the low electron density surface layer on $BaTiO_3$ thin films”. In: *Applied Physics Letters* 92.1 (2008), pp. 23–25.

[284] V. Craciun and R. K. Singh. “Characteristics of the surface layer of barium strontium titanate thin films deposited by laser ablation”. In: *Applied Physics Letters* 76.14 (2000), pp. 1932–1934.

[285] J. E. Rault et al. “Interface electronic structure in a metal/ferroelectric heterostructure under applied bias”. In: *Physical Review B* 87.15 (2013), pp. 1–8.

[286] Dana G. Popescu et al. “Influence of hole depletion and depolarizing field on the $BaTiO_3$/$La_{0.6}Sr_{0.4}MnO_3$ interface electronic structure revealed by photoelectron spectroscopy and first-principles calculations”. In: *Physical Review B* 92.23 (2015), pp. 1–11.

[287] Manuel Cardona. “Optical Properties and Band Structure of $SrTiO_3$ and $BaTiO_3$”. In: *Physical Review* 140.2 (1965), pp. 651–655.

[288] Shunyi Li et al. “Electrical properties of (Ba, Sr)TiO_3 thin films with Pt and ITO electrodes: Dielectric and rectifying behaviour”. In: *Journal of Physics Condensed Matter* 23.33 (2011), p. 334202.

[289] Donald M. Smyth. “The Defect Chemistry of Donor-Doped $BaTiO_3$: A Rebuttal”. In: *J. Electroceram.* 9.3 (2002), pp. 179–186.

[290] Ming Li, Derek C. Sinclair, and Anthony R. West. “Extrinsic origins of the apparent relaxorlike behavior in $CaCu_3Ti_4O_{12}$ ceramics at high temperatures: A cautionary tale”. In: *Journal of Applied Physics* 109.8 (2011).

[291] Giuliano Gregori, Rotraut Merkle, and Joachim Maier. “Ion conduction and redistribution at grain boundaries in oxide systems”. In: *Progress in Materials Science* 89 (2017), pp. 252–305.

[292] N.-H. Chan and D. M. Smyth. “Defect Chemistry of Donor-Doped $BaTiO_3$”. In: *J. Am. Ceram. Soc.* 67.4 (1984), pp. 285–288.

[293] J. Daniels, K. H. Haerdtl, and R. Wernicke. “The PTC effect of barium titanate”. In: *Philips Tech. Rev.* 38 (1979), p. 73.

[294] G. T. Mallick and P. R. Emtage. “Current-Voltage Characteristics of Semiconducting Barium Titanate Ceramic”. In: *J. Appl. Phys.* 39.7 (1968), pp. 3088–3094.

[295] T. Kolodiazhnyi, A. Petric, and G. P. Johari. “Models of the current-voltage dependence of $BaTiO_3$ with positive temperature coefficient of resistivity”. In: *J. Appl. Phys.* 89.7 (2001), pp. 3939–3946.

[296] W. G. Schmidt et al. “$LiNbO_3$ ground- and excited-state properties from first-principles calculations”. In: *Phys. Rev. B* 77.3 (2008), p. 035106.

[297] C. Thierfelder et al. “Do we know the band gap of lithium niobate?” In: *phys. stat. sol. (c)* 7.2 (2010), pp. 362–365.

[298] R. D. King-Smith and D. Vanderbilt. “First-principles investigation of ferroelectricity in perovskite compounds”. In: *Phys. Rev. B* 49.9 (1994), pp. 5828–5844.

[299] R. J. Cava et al. “Antiferromagnetism and metallic conductivity in $Nb_{12}O_{29}$”. In: *Nature* 350.6319 (1991), pp. 598–600.

[300] C. H. Rüscher. “The structural effect on the electrical properties of $NbO_{2.5-x}$ block-type compounds”. In: *Physica C: Superconductivity and its applications* 200 (1992), pp. 129–139.

[301] J. E.L. Waldron, M. A. Green, and D. A. Neumann. “Charge and spin ordering in monoclinic $Nb_{12}O_{29}$”. In: *Journal of the American Chemical Society* 123.24 (2001), pp. 5833–5834.

[302] Takeo Ohsawa et al. “An n-Type Transparent Conducting Oxide : $Nb_{12}O_{29}$”. In: *The Journal of Physical Chemistry C* 115 (2011), pp. 16625–16629.

[303] R. A. De Souza. “Oxygen Diffusion in $SrTiO_3$ and Related Perovskite Oxides”. In: *Advanced Functional Materials* 25 (40 2015), pp. 6326–6342.

[304] Mareike V. Hohmann, André Wachau, and Andreas Klein. “In situ Hall effect and conductivity measurements of ITO thin films”. In: *Solid State Ionics* 262 (2014), pp. 636–639.

[305] R. Cavicchi and S. Semancik. “Reactivity of Pd and Sn adsorbates on plasma and thermally oxidized SnO_2 (110)”. In: *Surface Science* 257.1-3 (1991), pp. 70–78.

[306] L. Kövér et al. “Electronic structure of tin oxides: High-resolution study of XPS and Auger spectra”. In: *Surface and Interface Analysis* 23.7-8 (1995), pp. 461–466.

[307] Baris Öcal. “Effect of ITO anode on resistance degradation of $BaTiO_3$”. Master of Science. Technical University of Darmstadt, 2019, p. 41.

[308] Binxiang Huang et al. “Electrostatic Boundary Conditions and (Electro)chemical Interface Stability”. In: *Advanced Materials Interfaces* 10 (2023), p. 2300332.

[309] Russ G. Egdell, T. J. Walker, and G. Beamson. “The screening response of a dilute electron gas in core level photoemission from Sb-doped SnO_2”. In: *Journal of Electron Spectroscopy and Related Phenomena* 128.1 (2003), pp. 59–66.

[310] Y. Gassenbauer et al. “Surface states, surface potentials, and segregation at surfaces of tin-doped In_2O_3”. In: *Physical Review B* 73.24 (2006), pp. 1–11.

[311] Yvonne Gassenbauer and Andreas Klein. “Electronic and chemical properties of tin-doped indium oxide (ITO) surfaces and ITO/ZnPc interfaces studied in-situ by photoelectron spectroscopy”. In: *Journal of Physical Chemistry B* 110.10 (2006), pp. 4793–4801.

[312] Sabrina Kahse. “Investigation of the Stability of the BTO|ITO and KNN|ITO Interface”. Advanced Research Lab. Technical University of Darmstadt, 2021.

[313] P. Bennich et al. “Photoemission study of K on graphite”. In: *Physical Review B - Condensed Matter and Materials Physics* 59.12 (1999), pp. 8292–8304.

[314] John T.S. Irvine, Derek C. Sinclair, and Anthony R. West. “Electroceramics: Characterization by Impedance Spectroscopy”. In: *Advanced Materials* 2.3 (1990), pp. 132–138.

[315] Anthony R. West, Derek C. Sinclair, and Naohiro Hirose. “Characterization of Electrical Materials, Especially Ferroelectrics, by Impedance Spectroscopy”. In: *Journal of Electroceramics* 1.1 (1997), pp. 65–71.

[316] Niall J. Donnelly and Clive A. Randall. “Mixed conduction and chemical diffusion in a $Pb(Zr_{0.53},Ti_{0.47})\ O_3$ buried capacitor structure”. In: *Applied Physics Letters* 96.5 (2010).

[317] Makoto Aoki et al. “Solute Segregation and Grain-Boundary Impedance in High-Purity Stabilized Zirconia”. In: *J. Am. Ceram. Soc.* 79.5 (1996), pp. 1169–1180.

[318] Brian L. Ellis and Linda F. Nazar. “Sodium and sodium-ion energy storage batteries”. In: *Current Opinion in Solid State and Materials Science* 16 (4 2012), pp. 168–177.

[319] Jung Joon Kim et al. “Progress in the Development of Sodium-Ion Solid Electrolytes”. In: *Small Methods* 1 (10 2017).

[320] Yumei Wang et al. “Development of solid-state electrolytes for sodium-ion battery–A short review”. In: *Nano Materials Science* 1 (2 2019), pp. 91–100.

[321] S. R. Taylor and E. Gileadi. “Physical interpretation of the Warburg impedance”. In: *Corrosion* 51.9 (1995), pp. 664–671.

[322] G M Choi, H L Tuller, and D Goldschmidt. “Electronic-transport behavior in single-crystalline $Ba_{0.03}Sr_{0.97}TiO_3$”. In: 34 (10 1986), pp. 6972–6979.

[323] T. Berger et al. “Light-induced charge separation in anatase TiO_2 particles”. In: *Journal of Physical Chemistry B* 6 (2005), pp. 2104–2112.

[324] Hungru Chen and Naoto Umezawa. “Hole localization, migration, and the formation of peroxide anion in perovskite $SrTiO_3$”. In: *Physical Review B - Condensed Matter and Materials Physics* 90 (3 2014).

[325] Anderson Janotti et al. “Vacancies and small polarons in $SrTiO_3$”. In: *Physical Review B - Condensed Matter and Materials Physics* 90 (8 Aug. 2014).

[326] O. F. Schirmer. “Holes bound as small polarons to acceptor defects in oxide materials: Why are their thermal ionization energies so high?” In: *Journal of Physics Condensed Matter* 23 (33 2011).

[327] L. P. Putilov and V. I. Tsidilkovski. “The role of deep acceptor centers in the oxidation of acceptor-doped wide-band-gap perovskites ABO_3”. In: *Journal of Solid State Chemistry* 247 (2017), pp. 147–155.

[328] R. I. Eglitis, E. A. Kotomin, and G. Borstel. “Semi-empirical calculations of hole polarons in MgO and $KNbO_3$ crystals”. In: *Physica Status Solidi (B) Basic Research* 208 (1 1998), pp. 15–20.

[329] Rakesh Verma et al. “Recent Progress in Electrolyte Development and Design Strategies for Next-Generation Potassium-Ion Batteries”. In: *Batteries and Supercaps* 4 (9 2021), pp. 1428–1450.

[330] Young Woon Kim, Atsushi Oda, and Nobuhito Imanaka. “Extraordinary high potassium ion conducting polycrystalline solids based on gadolinium oxide-potassium nitrite solid solution”. In: *Electrochemistry Communications* 5 (2003), pp. 94–97.

[331] G. Shirane, E. Sawaguchi, and Y. Takagi. “Dielectric Properties of Lead Zirconate”. In: *Physical Review* 84 (3 1951), pp. 476–483.

[332] W. Y. Pan et al. “Large displacement transducers based on electric field forced phase transitions in the tetragonal $(Pb_{0.97}La_{0.02})$ (Ti,Zr,Sn)O_3 family of ceramics”. In: *Journal of Applied Physics* 66 (12 1989), pp. 6014–6023.

[333] Xunhu Dai, A. Digiovanni, and Dwight Viehland. “Dielectric properties of tetragonal lanthanum modified lead zirconate titanate ceramics”. In: *Journal of Applied Physics* 74 (5 1993), pp. 3399–3405.

[334] T. Ibn-Mohammed et al. “Integrated hybrid life cycle assessment and supply chain environmental profile evaluations of lead-based (lead zirconate titanate): Versus lead-free (potassium sodium niobate) piezoelectric ceramics”. In: *Energy and Environmental Science* 9 (11 2016), pp. 3495–3520.

[335] Helmut Mehrer. “Solutions of the Diffusion Equation”. In: *Diffusion in Solids*. Ed. by Manuel Cardona et al. Springer, 2007. Chap. 3, pp. 47–53.

[336] Isamu Yasuda and Tomoji Hikita. “Precise Determination of the Chemical Diffusion Coefficient of Calcium-Doped Lanthanum Chromites by Means of Electrical Conductivity Relaxation”. In: *Journal of The Electrochemical Society* 141.5 (1994), pp. 1268–1273.

[337] P. K. Metselaar R. and Larsen. “Diffusion of oxygen vacancies in yttrium iron garnet investigated by dynamic conductivity measurements”. In: *Journal of Physics and Chemistry of Solids* 37.6 (1976), pp. 599–605.

[338] J. M. Mauvy F.and Bassat et al. “Chemical oxygen diffusion coefficient measurement by conductivity relaxation-correlation between tracer diffusion coefficient and chemical diffusion coefficient”. In: *Journal of the European Ceramic Society* 24.6 (2004), pp. 1265–1269.

List of Figures

List of Tables

A. Appendix

A.1. Sample preparation

A.1.1. Optical dilatometry

In Section 3.2 the basic principle of an optical dilatometer is described. While heating the pellet, pictures are taken periodically to analyze the shrinkage and expansion of the sample. Figure A.1 shows three pictures of a $KNbO_3$ pellet at $1070\,°C$, $1080\,°C$, and $1100\,°C$. It can be observed that at $1080\,°C$ the material starts to soften. At $1100\,°C$ the melting temperature of $KNbO_3$ is reached, which leads to a decreased measured sample diameter. This results in a sudden increase in the shrinkage curve illustrated in Fig. 5.2 in Section 5.1.

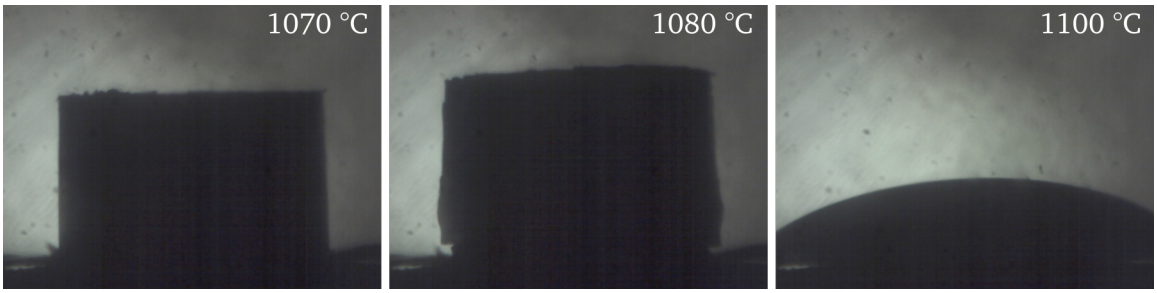

Figure A.1.: Profile of $KNbO_3$ pellet at three different temperatures while measuring the shrinkage curve.

A.1.2. X-ray diffraction

XRD was performed to determine the crystalline phases in the calcined and sintered powders, the appearance of possible secondary phases, and the effect of the dopants on the crystal lattice. In Fig. 5.4 in Section 5.3 the XRD results of undoped $NaNbO_3$ are shown and discussed. Figure A.2 and A.3 illustrate the recorded reflexes for $Na_{0.99}Ca_{0.01}NbO_3$ and $Na_{0.99}Sr_{0.01}NbO_3$ after first and second calcination and after sintering, respectively. For both materials only the ferroelectric Q phase can be

identified after calcination. When the samples are sintered the material crystallizes mainly in the antiferroelectric P phase. Only small traces of the Q phase can still be seen. No secondary phases appear in the diffraction pattern. For better differentiation between P and Q phase a magnified view of four 2θ-sections are shown. The colored frames refer to the same colored regions in the survey diffraction patterns. Reference reflexes for Q and P phase are plotted as bars. For the Q phase with space group $P2_1ma$ (grey) the powder diffraction file JCPDS 01-082-0606 [109] is used. In case of the P phase with space group Pbcm (red) the reference pattern was calculated by the program VESTA [160]. For better comparison, the measured patterns are aligned in position according to the (110)- and (101)-reflection located around $26.7°$ of the reference patterns of P and Q phase, respectively.

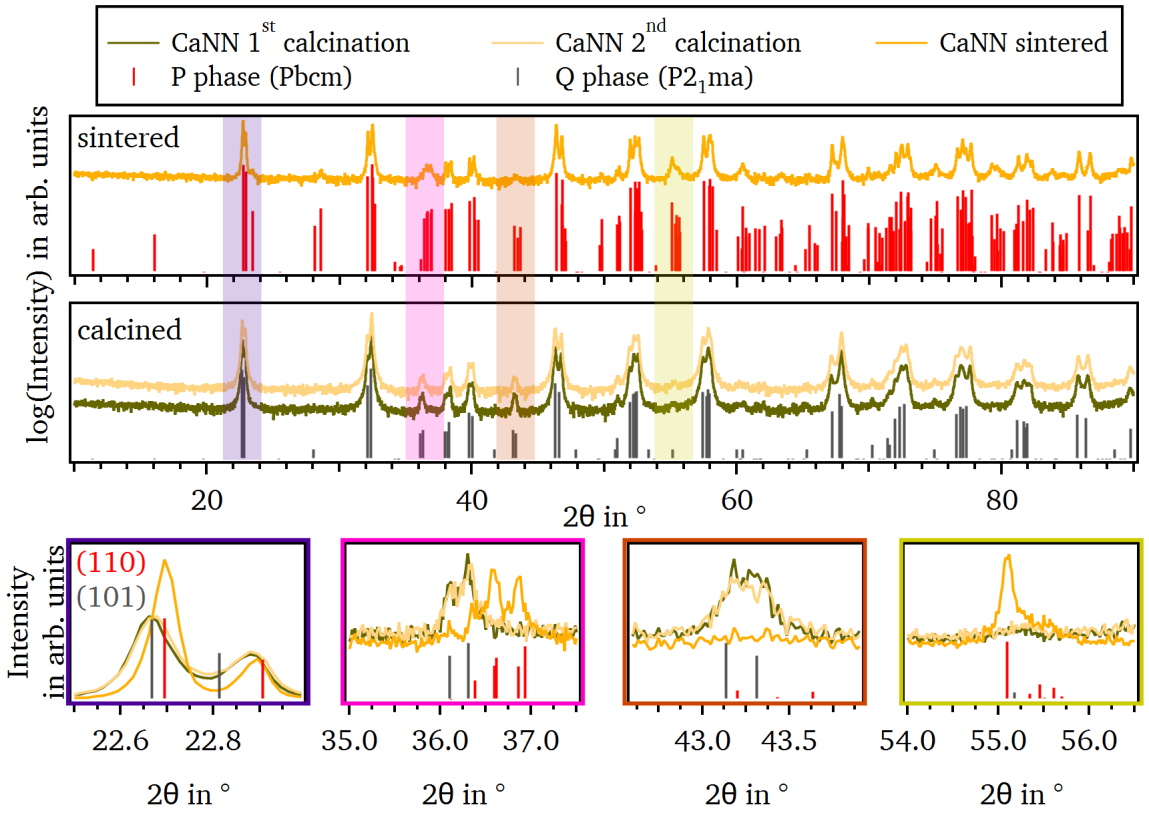

Figure A.2.: X-ray diffraction pattern of $Na_{0.99}Ca_{0.01}NbO_3$ after first and second calcination and after sintering. The reflections of the antiferroelectric P phase with space group Pbcm (red) was calculated by the program VESTA [160] while the lines of the ferroelectric Q phase with space group $P2_1ma$ (grey) correspond to the powder diffraction file JCPDS 01-082-0606 [109]. The measured patterns are aligned in position according to the (110)- and (101)-reflection located around $26.7°$ of the reference patterns of P and Q phase, respectively.

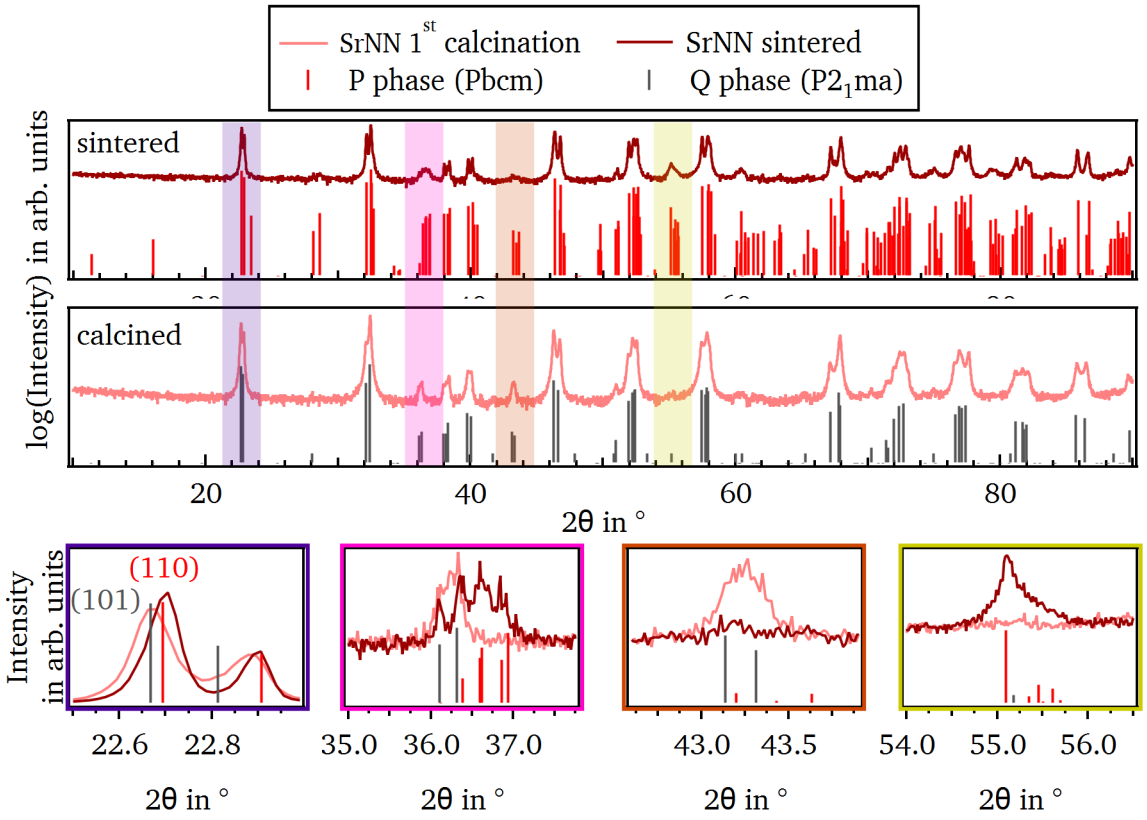

Figure A.3.: X-ray diffraction pattern of $Na_{0.99}Sr_{0.01}NbO_3$ after first and second calcination and after sintering. The reflections of the antiferroelectric P phase with space group Pbcm (red) was calculated by the program VESTA [160] while the lines of the ferroelectric Q phase with space group $P2_1ma$ (grey) correspond to the powder diffraction file JCPDS 01-082-0606 [109]. The measured patterns are aligned in position according to the (110)- and (101)-reflection located around $26.7°$ of the reference patterns of P and Q phase, respectively.

A.1.3. Polarization hysteresis loops

Polarization curves of undoped as well as Ca- and Sr-doped $NaNbO_3$ were conducted at a low frequency of 1 Hz and 0.3 Hz as described in Section 4.7, respectively. In Figure A.4 the corresponding *P*-*E*-loops are shown. For undoped $NaNbO_3$ the irreversible FE-to-AFE-transition is clearly visible, which is not the case for the doped samples. However, no complete loop could be obtained for the undoped material due to breakdown of the ceramic samples. In contrast, for donor doped $NaNbO_3$ a loop over the whole frequency range could be recorded but the conductivity of the samples is too high. Hence, the leakage current is overlaying the polarization current, which results in the balloon-like shaped loops. Consequently, polarization loops at higher frequencies were recorded as illustrated

and discussed in Section 5.4.

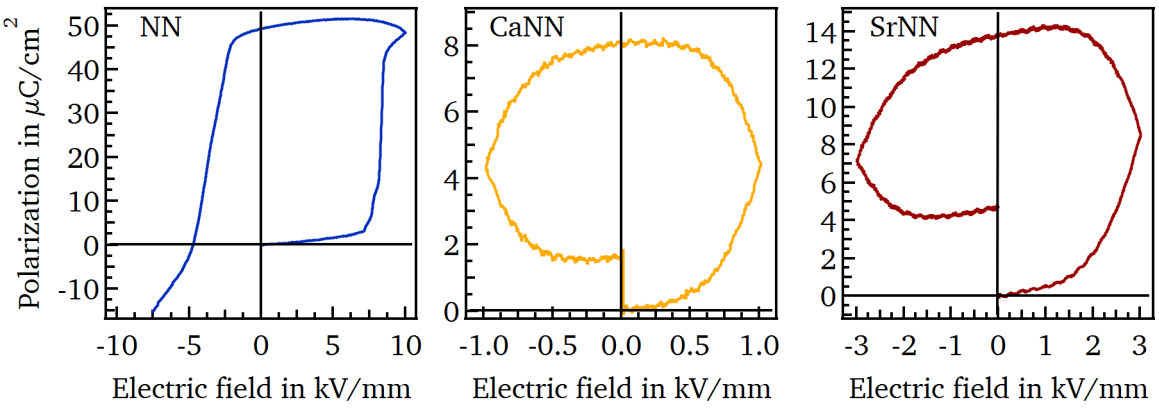

Figure A.4.: Polarization hysteresis loops of $NaNbO_3$ (blue), $Na_{0.99}Ca_{0.01}NbO_3$ (yellow), and $Na_{0.99}Sr_{0.01}NbO_3$ (red). The pure $NaNbO_3$ sample is measured at a frequency of $0.3\,\mathrm{Hz}$ whereas the doped samples are recorded at $1\,\mathrm{Hz}$.

In addition, aged and equilibrated samples were measured for all $NaNbO_3$-based and the $KNbO_3$ samples. While the aged samples were stored for one year in the lab, the equilibrated samples were freshly annealed at $600\,^{\circ}\mathrm{C}$ for $1\,\mathrm{h}$ directly before the polarization loop measurements. The corresponding polarization and currents in dependence of the electric field are shown in Fig. A.5. For all sample types a difference between aged and equilibrated samples is clearly observed. The $NaNbO_3$-based probes have a lower remanent and maximum polarization after aging. Aged Ca- and Sr-doped $NaNbO_3$ exhibit slanted loops whereas the undoped $NaNbO_3$ develops a pinched loop. In addition, all samples have a lower coercive field in positive than in negative field direction, which suggests the appearance of an internal bias field.
$KNbO_3$ has already a slanted polarization loop and broad current peaks after equilibration. However, the aged sample exhibits a highly pinched loop leading to four separate current peaks, which could be misinterpreted as an antiferroelectric polarization behavior. In addition, remanent and maximum polarization is decreased after aging as for the $NaNbO_3$-based samples. Furthermore, a small internal bias field can be observed as well.
The detailed discussion and interpretation of these observations is described in Section 5.4.

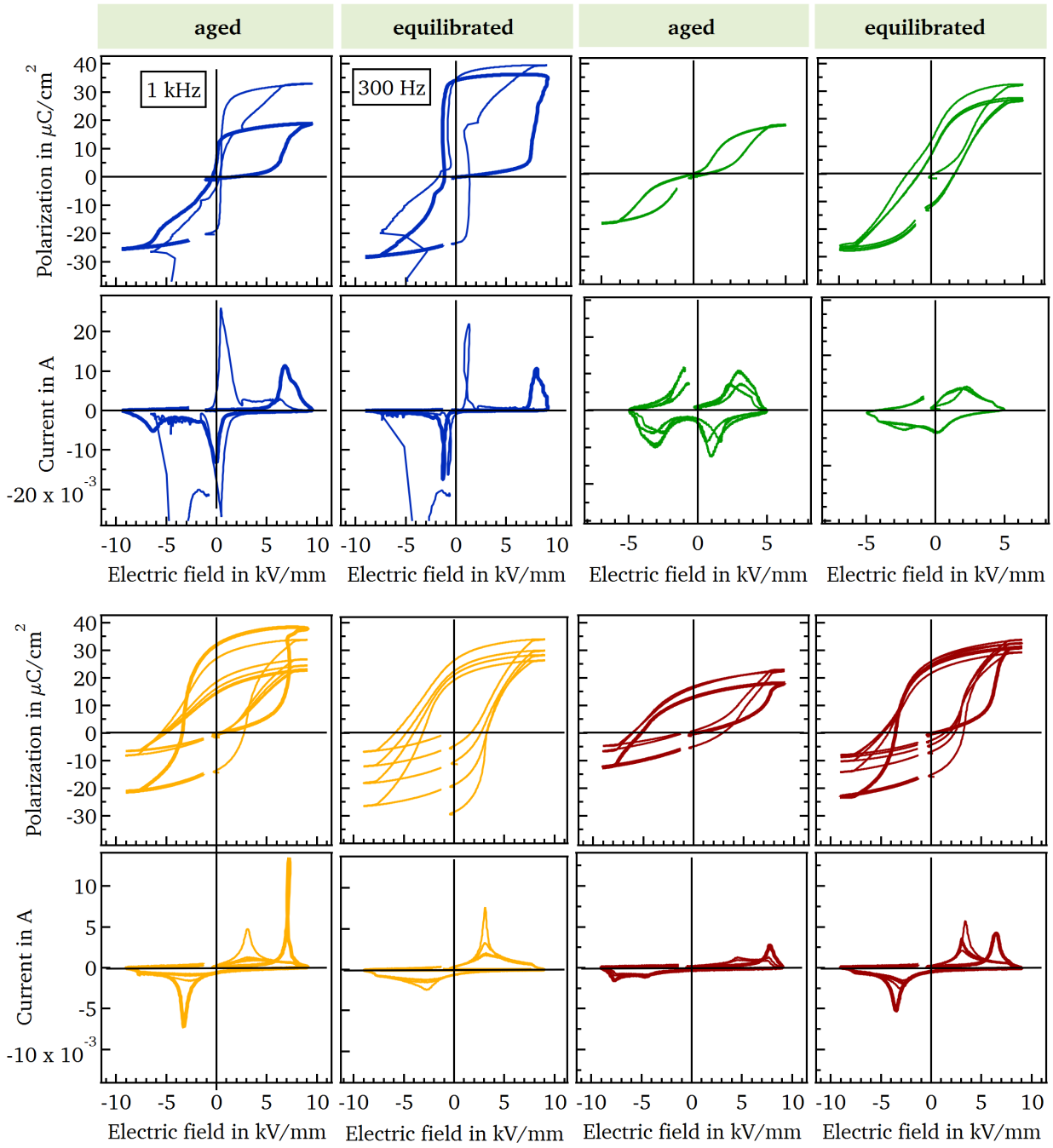

Figure A.5.: Polarization and current hysteresis loops of $NaNbO_3$ (blue), $KNbO_3$ (green), $Na_{0.99}Ca_{0.01}NbO_3$ (yellow), and $Na_{0.99}Sr_{0.01}NbO_3$ (red) for an aged and a freshly equilibrated sample. The aged undoped $NaNbO_3$ sample is measured at a frequency of $1\,\mathrm{kHz}$ whereas all other samples are examined at $300\,\mathrm{Hz}$.

A.1.4. Temperature and frequency dependent permittivity

The temperature dependent permittivity was probed at different frequencies for all investigated sample types as outlined in Section 4.8. For undoped $NaNbO_3$ a significant frequency dispersion can be observed at temperatures above 200 °C. Figure A.6 shows the permittivity as function of temperature for different frequencies on three different permittivity and temperature scales. The dashed rectangular boxes illustrate the range of the magnified views.

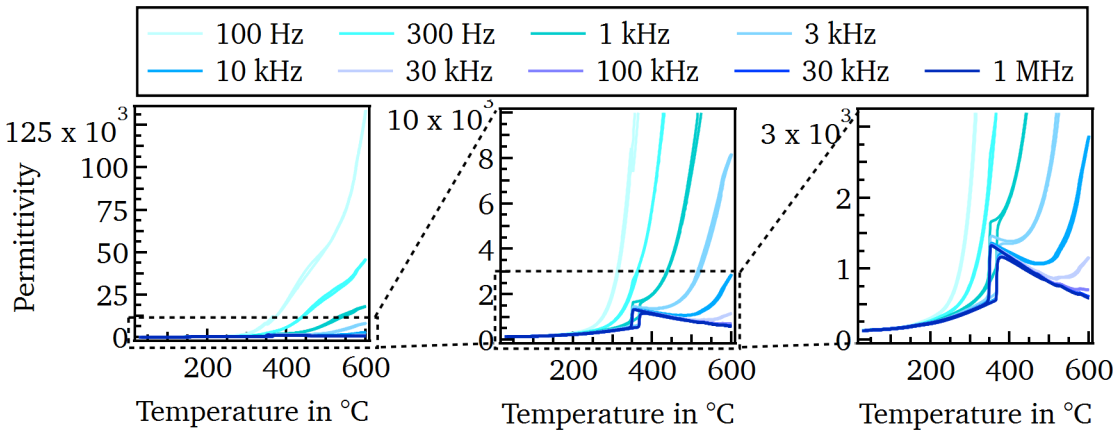

Figure A.6.: Permittivity vs. temperature curves for $NaNbO_3$ measured at different frequencies for different permittivity ranges.

A.1.5. Scanning transmission electron microscope

STEM measurements were conducted on $Na_{0.99}Ca_{0.01}NbO_3$ and $Na_{0.99}Sr_{0.01}NbO_3$ ceramic pellets. For sample preparation the samples were first mechanically polished and then prepared by ion beam milling for electron transparency. The STEM images and the energy-dispersive x-ray (EDX) spectra were taken by a Jeol ARM 200 CF (equipped with Jeol Centurio EDX system, Akishima, Tokyo, Japan), which was calibrated with a Cs-sample.

Figure A.7 shows the bright field image in (a), the detected EDX-spectrum for each element including a magnified view of the Ca K line in (b), and the recorded intensity of Na, Nb, and Ca in a mapping mode in (c), (d), and (e), respectively, for a Ca-doped sample. In case of $Na_{0.99}Sr_{0.01}NbO_3$, a magnified view of the Sr K peak is additionally illustrated in (b) and instead of the Ca distribution the Sr content is outlined in (e). It can be observed that both Ca and Sr are homogeneously distributed within the whole grains and do not segregate at the grain boundaries.

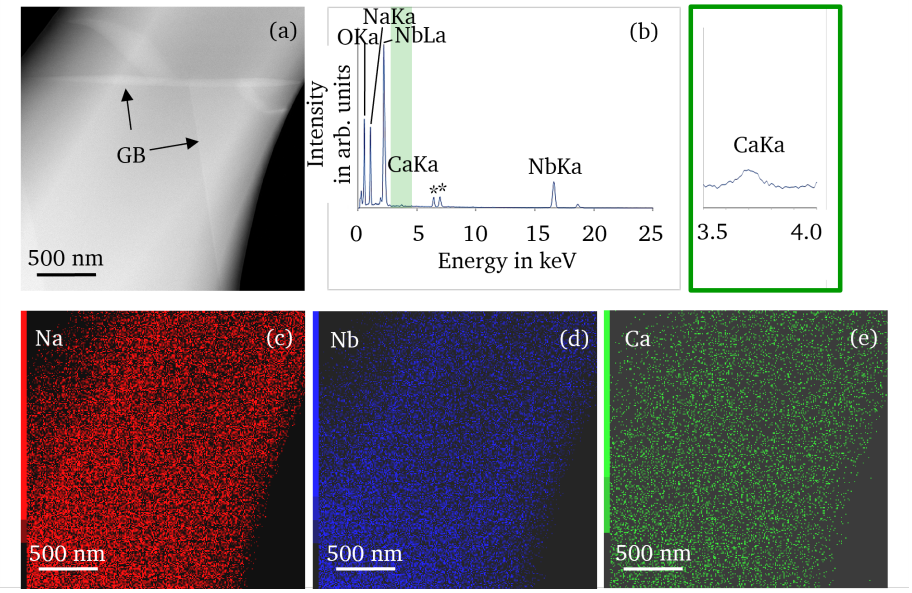

Figure A.7.: Bright field STEM image of two grain boundaries (GB) of a $Na_{0.99}Ca_{0.01}NbO_3$ sample taken by TEM in (a), with corresponding EDXS spectrum in (b), and intensity maps of Na K, Nb K, and Ca K lines in (c)-(e).

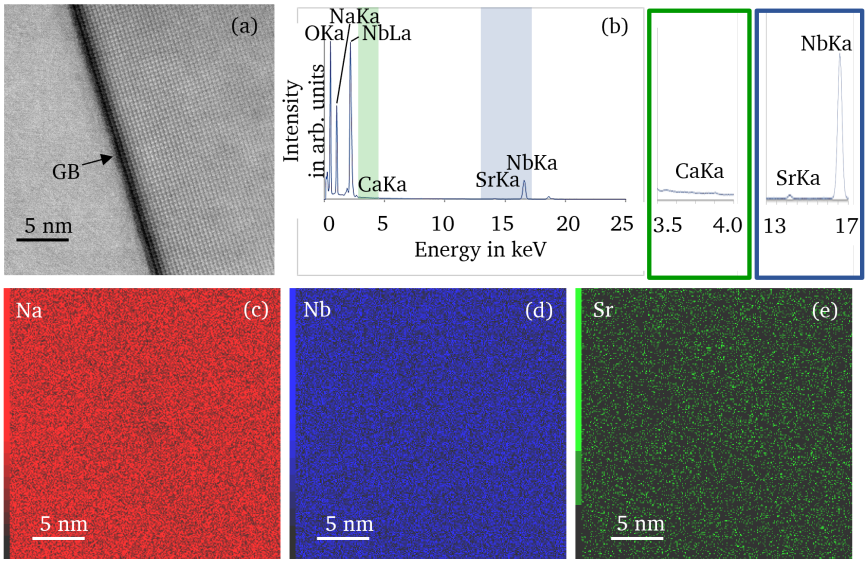

Figure A.8.: Bright field STEM image of two grain boundaries (GB) of a $Na_{0.99}Sr_{0.01}NbO_3$ sample taken by TEM in (a), with corresponding EDXS spectrum in (b), and intensity maps of Na K, Nb K, and Sr K lines in (c)-(e).

A closer inspection of the surface of the $Na_{0.99}Ca_{0.01}NbO_3$ samples reveals calcium segregation towards the surface, which is illustrated in Figure A.9. This explains why with XPS a higher concentration of $10\,\text{mol}\,\%$ to $20\,\text{mol}\,\%$ calcium was measured. In contrast, with STEM a lower bulk concentration of $0.5\,\text{mol}\,\%$ was identified. Hence, the samples exhibit a slightly smaller doping concentration as intended.

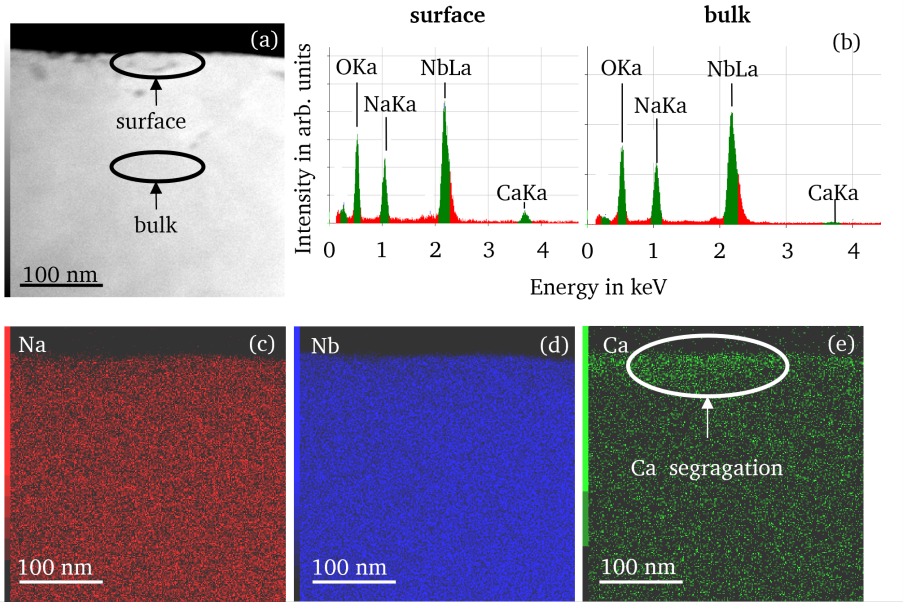

Figure A.9.: Bright field STEM image of the cross-section of a $Na_{0.99}Ca_{0.01}NbO_3$ sample taken by TEM in (a), with corresponding EDXS spectrum of surface and bulk in (b), and intensity maps of Na K, Nb K, and Ca K lines in (c)-(e).

A.2. Electronic structure

A.2.1. Fitting of Na 1*s* and K 2*p* peak

The measured Na 1*s* and K 2*p* emission lines are a superimposition of three components. The origin of the different contributions were discussed in Section 6.4. In order to analyze changes in the peak shape and differences in the binding energy distance and the intensity ratios of the individual peak components, the emission lines are fitted with Voigt functions. A Voigt function is a convolution between a Lorentzian and a Gaussian function. The fitting parameters required for these functions are the binding energy, the intensity, the Gaussian width, and the Gaussian-Lorentzian ratio. For fitting the Na 1*s* and K 2*p* lines a fixed Gaussian width and Gaussian-Lorentzian ratio was used. The values of the individual components are listed in Table A.1. In case of the Na 1*s* core level line three

Table A.1.: Fitting parameters of the single Voigt functions and Voigt-doublets required for the fit of the three components of Na 1*s* and K 2*p* emission line, respectively.

	Na 1*s*			K 2*p*		
	bulk	surface component I	surface component II	bulk	surface component I	surface component II
Gaussian width in eV	0.80	1.60	1.60	1.10	1.46	1.30
Gaussian-Lorentzian ratio	0	0	0	0	0	0
branching ratio	-	-	-	0.5	0.5	0.5
spin-orbit-splitting in eV	-	-	-	2.77	2.77	2.77

single Voigt functions representing bulk, surface I and surface II contribution are required. For the K 2*p* emission line three Voigt-doublets are needed because of the spin-orbit-splitting of the K 2*p* peak. Hence, two more parameters are used for fitting the K 2*p* line, the spin-orbit-splitting and the branching ratio giving the binding energy difference and the intensity ratio between the K $2p_{5/2}$ and K $2p_{3/2}$ line, respectively. These two values are fixed as well and shown in Table A.1. Hence, the only varying parameters are the binding energies and intensities of the individual fitted Voigt profiles. Figure A.10 illustrates a Na 1*s* and a K 2*p* emission line of a $NaNbO_3$ and a $KNbO_3$ clean ceramic sample. Bulk, surface I and surface II components are marked as well. By means of these fits the changes in the intensity ratio and binding energy distances between the different contributions can be determined to analyze the origin of these different components.

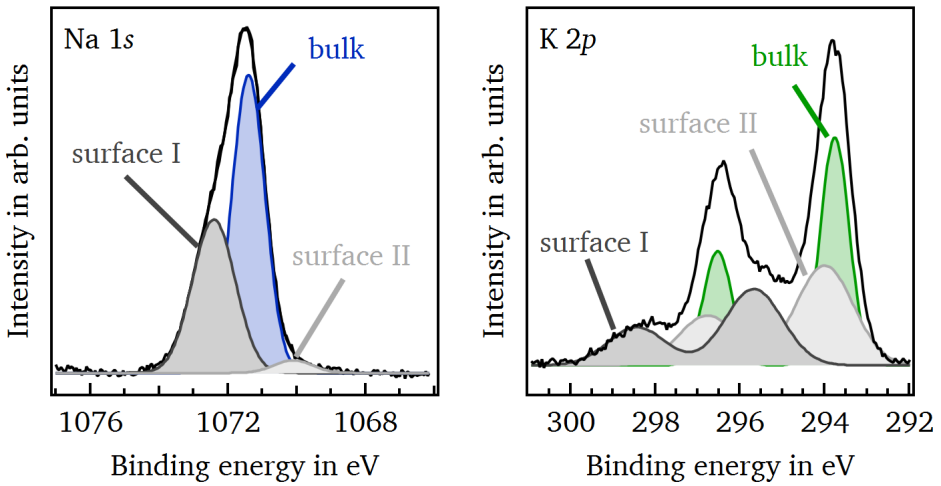

Figure A.10.: Na 1*s* and K 2*p* emission line of a clean $NaNbO_3$ and $KNbO_3$ ceramic sample with the three contributions bulk, surface I and surface II. For the Na 1*s* peak three single Voigt functions are used while for the K 2*p* line three Voigt-doublets are required.

A.2.2. Interface experiments

Interface experiments were conducted as described in Section 4.10.2 and discussed in Section 6.3. Figure A.11, A.12, and A.13 show the XP-spectra of the Na 1*s* or K 2*p*, O 1*s*, Sn 3*d*, In 3*d*, and Nb 3*d* core level and valence band spectra of an undoped $NaNbO_3$, a $Na_{0.99}Ca_{0.01}NbO_3$, and a $KNbO_3$ bulk ceramic sample after cleaning and step-wise ITO deposition, respectively.

For undoped $NaNbO_3$ the spectra of the as-prepared pellets are detected additionally. Furthermore, the fitted bulk (blue for sodium and green for potassium) and two surface components (surface component I in dark gray and surface component II in light gray) are plotted for the Na 1*s* and the K 2*p* emission line. For all samples a clear shift to lower binding energies with increasing ITO layer thickness is obtained, which would indicate a Fermi level shift closer to the VBM. However, the as-prepared and cleaned sample are too insulating, which results in charging of the sample's surface and a shift of the emission lines to higher binding energies. Hence, the Fermi level position cannot be extracted from the as-prepared and cleaned ceramic pellets because it is overestimated.

In Fig. A.14, A.15, and A.16 the corresponding XP-spectra of a $NaNbO_3$, $Na_{0.99}Sr_{0.01}NbO_3$, and $KNbO_3$ sample after cleaning and step-wise RuO_2 deposition are shown. For undoped $NaNbO_3$ the emission lines of the as-prepared (dirty) state are plotted as well. Moreover, the fitted bulk and surface components of the Na 1*s* and K 2*p* core levels are indicated in the corresponding spectra. All spectra shift to lower binding energies due to a Fermi level shift towards lower binding energies at the sample-RuO_2-interface. Nevertheless, the as-prepared and cleaned core level binding energies are again overestimated because of the surface charging.

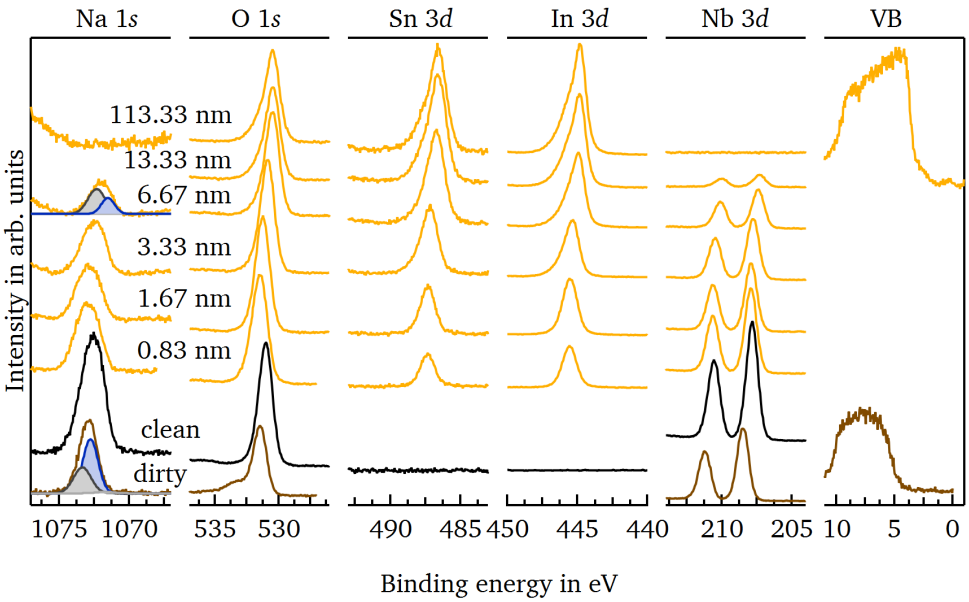

Figure A.11.: Na 1*s*, O 1*s*, Sn 3*d*, In 3*d*, and Nb 3*d* core level and valence band spectra of an undoped $NaNbO_3$ bulk ceramic sample in the course of ITO deposition. The brown and black lines belong to the as-prepared and cleaned sample, whereas the yellow spectra are measured after depositing a few nanometers of ITO on top. The bulk and surface components of the Na 1*s* emission line are colored in blue and grey in the as-prepared and the last but one XP-spectrum.

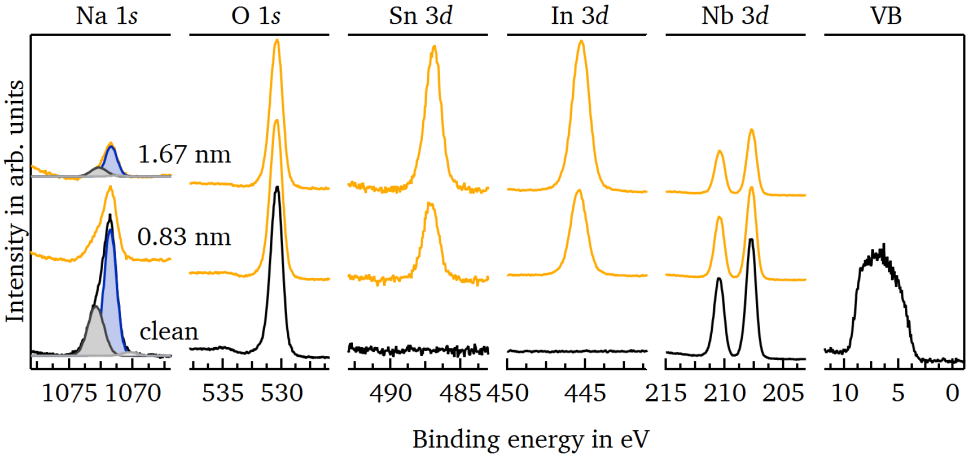

Figure A.12.: Na 1*s*, O 1*s*, Sn 3*d*, In 3*d*, and Nb 3*d* core level and valence band spectra of a Ca-doped $NaNbO_3$ bulk ceramic sample in the course of ITO deposition. The black lines belong to the cleaned sample, whereas the yellow spectra are measured after depositing a few nanometers of ITO on top. The bulk and surface components of the Na 1*s* emission line are colored in blue and grey in the clean and the last XP-spectrum.

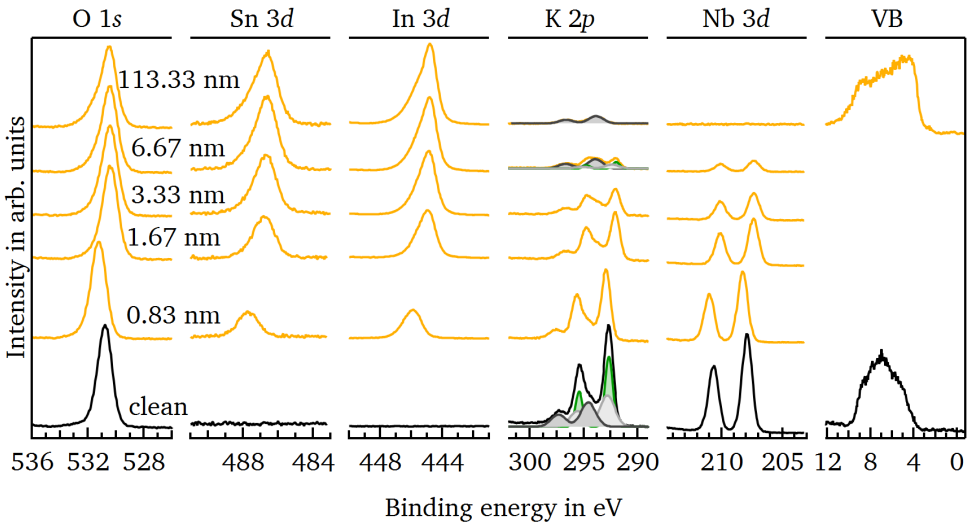

Figure A.13.: O 1s, K 2*p*, Sn 3*d*, In 3*d*, and Nb 3*d* core level and valence band spectra of $KNbO_3$ bulk ceramic sample in the course of ITO deposition. The black lines belong to the cleaned sample, whereas the yellow spectra are measured after depositing a few nanometers of ITO on top. The bulk and surface components of the K 2*p* emission line are colored in green and grey in the clean, the last but one, and the last XP-spectrum.

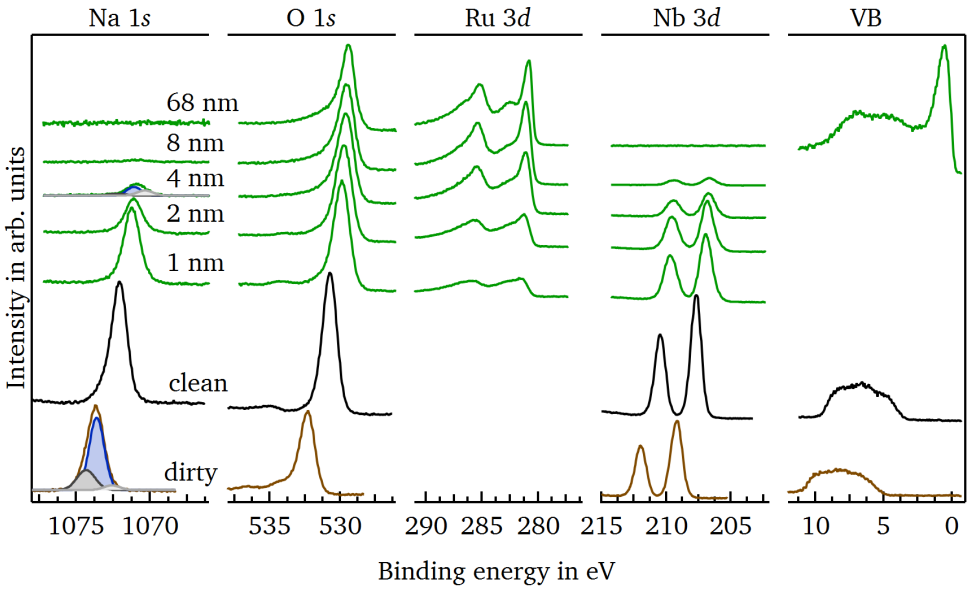

Figure A.14.: Na 1s, O 1s, Ru 3*d*, and Nb 3*d* core level and valence band spectra of an undoped $NaNbO_3$ bulk ceramic sample in the course of RuO_2 deposition. The brown and black lines belong to the as-prepared and cleaned sample, whereas the green spectra are measured after depositing a few nanometers of RuO_2 on top. The bulk and surface components of the Na 1s emission line are colored in blue and grey in the as-prepared and last but two XP-spectrum.

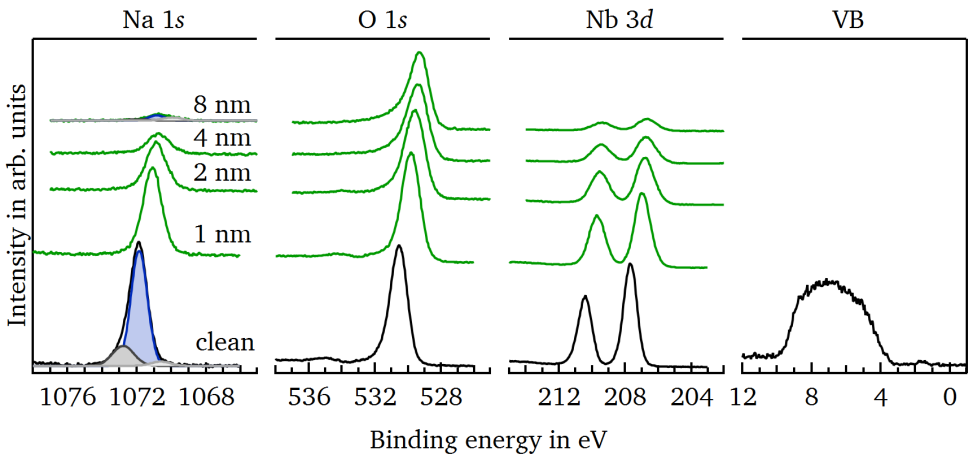

Figure A.15.: Na 1*s*, O 1*s*, and Nb 3*d* core level and valence band spectra of a $Na_{0.99}Sr_{0.01}NbO_3$ bulk ceramic sample in the course of RuO_2 deposition. The black lines belong to the cleaned sample, whereas the green spectra are measured after depositing a few nanometers of RuO_2 on top. The bulk and surface components of the Na 1*s* emission line are colored in blue and grey in the clean and the last XP-spectrum.

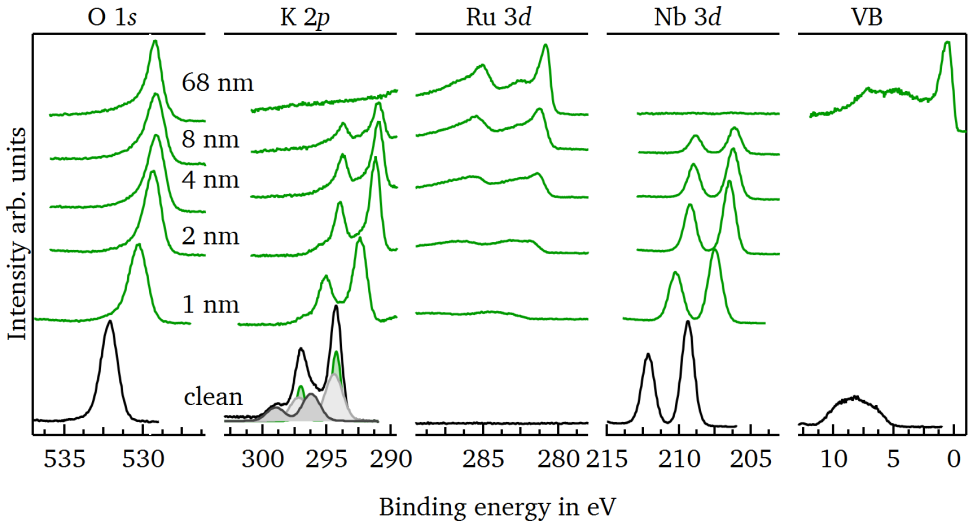

Figure A.16.: O 1*s*, K 2*p*, Ru 3*d*, and Nb 3*d* core level and valence band spectra of $KNbO_3$ bulk ceramic sample in the course of RuO_2 deposition. The black lines belong to the cleaned sample, whereas the green spectra are measured after depositing a few nanometers of RuO_2 on top. The bulk and surface components of the K 2*p* emission line are colored in green and grey in the clean XP-spectrum.

Figure A.16 shows that the K 2*p* emission line is overlapping with the higher binding energy side of the Ru 3*d* peak. This makes the evaluation of changes in the bulk and surface components more difficult. Hence, the spectra of the Ru 3*d* after depositing 68 nm RuO_2 is subtracted from all other K 2*p* peaks, which overlap with it, in the corresponding binding energy range. The resulting core levels are illustrated in Fig. A.17. The graph includes the fitted bulk and surface components for each emission line. With increasing RuO_2 layer thickness all K 2*p* components are getting lower in intensity.

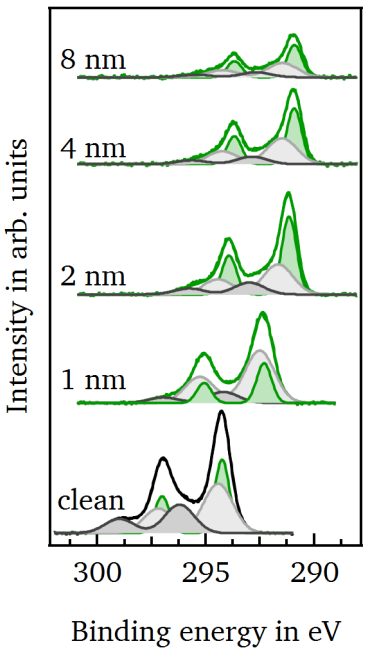

Figure A.17.: K 2*p* emission lines for an interface formation to a RuO_2. Bulk component (green), surface component I (dark gray) and surface component II (light gray) are fitted for each peak.

In addition, it is interesting to note that in Fig. A.14 and A.15 the Nb 3*d* peaks develop a shoulder at lower binding energies with increasing RuO_2 layer thickness, which is not observed at the interface with ITO. In contrast, this is not the case for $KNbO_3$ in Fig. A.16. For better comparison, the Nb 3*d* core levels of a $Na_{0.99}Ca_{0.01}NbO_3$ and a $KNbO_3$ sample are shown again in Fig. A.18 after cleaning and step-wise RuO_2 deposition. In order to identify differences in the peak shape, the Nb 3*d* peak after cleaning is plotted over the one after depositing 8 nm RuO_2. Here, the emission line of the clean sample is adjusted in intensity and binding energy that the maxima of both peaks are matching. A clear shoulder on the lower binding energy side can be identified for the $Na_{0.99}Ca_{0.01}NbO_3$ sample after the RuO_2 deposition, which is marked by an arrow in Fig. A.18. In contrast, no differences in the peak shape after cleaning and RuO_2 deposition are observed in case of $KNbO_3$. However, it is not clear what is causing the shoulder in the spectrum of the $NaNbO_3$-based samples. A very narrow space charge region resulting in higher band bending compared to the bulk could explain such a

peak broadening. This issue is further discussed in Section 6.4.2.

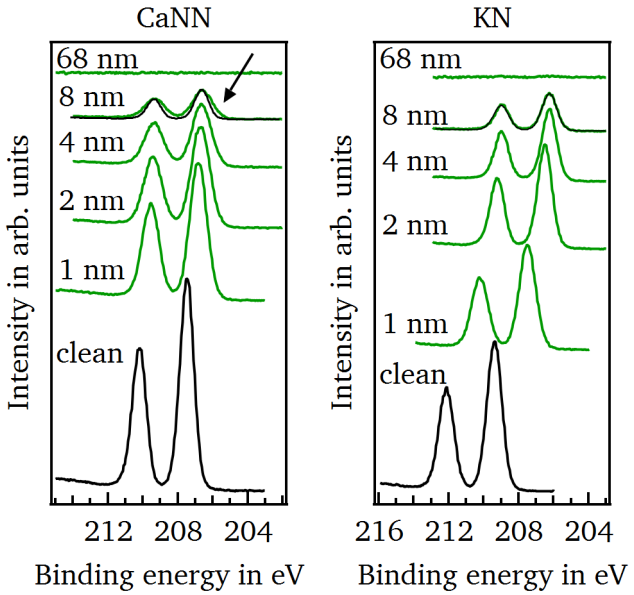

Figure A.18.: Nb 3*d* peak during RuO_2 deposition for a $Na_{0.99}Ca_{0.01}NbO_3$ (left) and a $KNbO_3$ ceramic sample (right). The respective spectra of the cleaned sample are plotted on top of the last but one spectrum for comparison. The asymmetry in the Nb 3*d* peak of the $Na_{0.99}Ca_{0.01}NbO_3$ sample is indicated by an arrow.

A.3. Transport properties and degradation

Impedance measurements were conducted as described in Section 4.12. The results including Nyquist plots and the extracted conductivity as function of temperature for all investigated samples are shown and discussed in Section 7.2. Figure A.19 illustrates the corresponding graphs of the complex impedance Z" and the complex modulus M" as a function of the frequency f at $250\,°C$, $425\,°C$, and $500\,°C$. The description and interpretation of these plots are outlined in Section 7.2 as well.

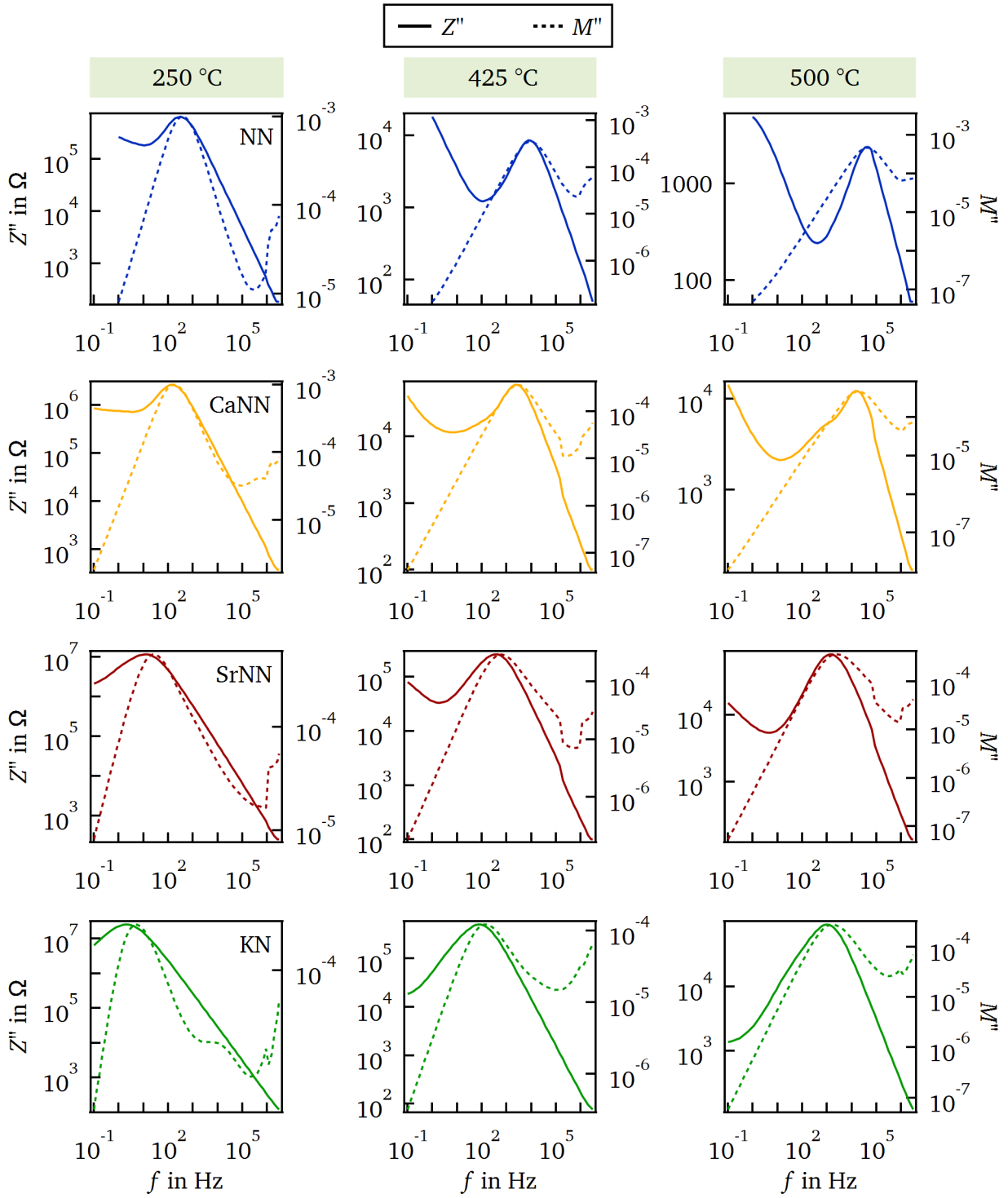

Figure A.19.: Z" and M" as a function of the frequency f for pure $NaNbO_3$ (blue) and $KNbO_3$ (green), $Na_{0.99}Ca_{0.01}NbO_3$ (yellow), and $Na_{0.99}Sr_{0.01}NbO_3$ (red) at $250\,°C$, $425\,°C$, and $500\,°C$.

A.3.1. Determination of diffusion coefficients

The basic idea of a relaxation experiment is illustrated in Section 3.9.1. Besides the identification of a n- or p-type behavior of the investigated sample, the chemical diffusion coefficient $\tilde{D}$ can be determined. In the following the derivation for this procedure is shortly described.

As the diameter of the samples analyzed in this work is much larger than the thickness of the samples, it is assumed that oxygen exchange only takes place on the samples' surfaces. Readers who are interested in taking radial diffusion into account are referred to [335, 336]. In general, the concentration C of a species in a material is a function of the place x and the time t, which can be separated into two functions, one in dependence of x and one of t.

$$C(x,t) = X(x) \cdot T(t) \tag{A.1}$$

Beginning with Fick's second law, following general solution for the concentration is obtained:

$$\begin{aligned} \frac{\partial C(x,t)}{\partial t} &= \tilde{D}\frac{\partial^2 C(x,t)}{\partial x}\frac{1}{T\tilde{D}}\frac{\partial T(t)}{\partial t} \\ &= \frac{1}{X}\frac{\partial^2 X(x)}{\partial x} \\ &= -\lambda^2 \\ \Rightarrow C(x,t) &= \sum_{n-1}^{\infty} \\ &\quad \left[A_n \sin(\lambda_n x) + B_n \cos(\lambda_n x)\right] \\ &\quad \cdot \exp\left(-\lambda_n^2 \tilde{D} t\right) \end{aligned} \tag{A.2}$$

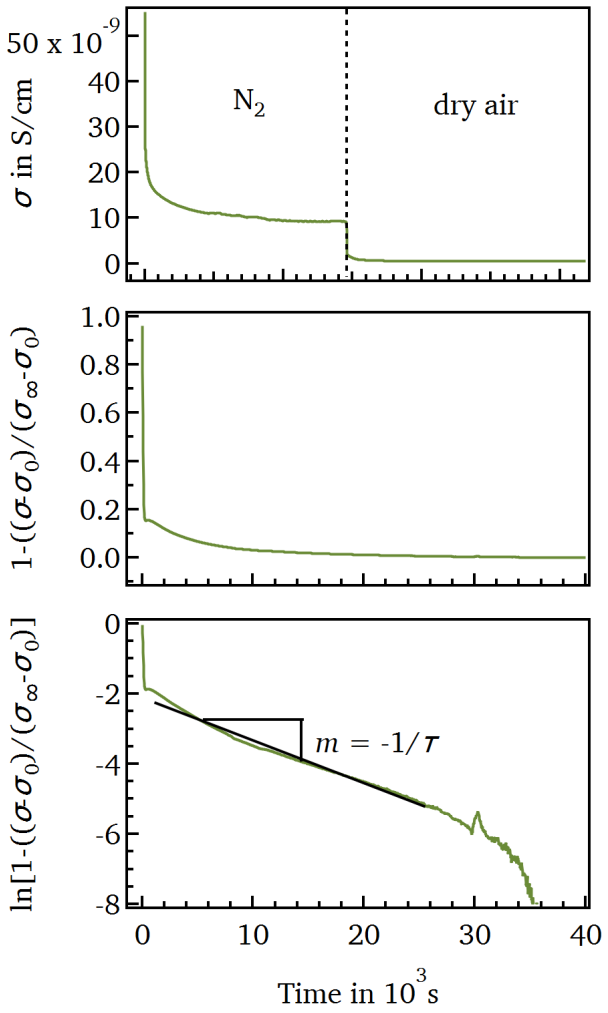

Figure A.20.: Conductivity (top), normalized conductivity (middle) and natural logarithm of it (bottom) as function of time. The slope m is given by the relaxation time τ.

With a sample thickness d, the assumptions made above lead to the following initial and boundary conditions:

$$C(x,0) = C_0 \qquad C\left(-\frac{d}{2},t\right) = 0 \qquad C\left(\frac{d}{2},t\right) = 0 \tag{A.3}$$

Including these conditions in the general solution results in the concentration term for a sheet:

$$C(x,t) = -\frac{4C_0}{\pi}\sum_{j=0}^{\infty}\frac{1}{2j+1}\cos\left(\frac{2j+1}{d}\pi x\right)\cdot\exp\left(-\frac{(2j+1)^2\pi^2\tilde{D}^2 t}{d^2}\right) \tag{A.4}$$

Next we need to consider the average concentration $\bar{C}(t)$ in the sheet:

$$\begin{aligned}\bar{C}(t) &= \frac{1}{d}\int_{-\frac{d}{2}}^{\frac{d}{2}} C(x,t)dx \\ &= \left[-\frac{4C_0}{\pi^2}\sum_{j=0}^{\infty}\frac{1}{(2j+1)^2}\left(-\sin\left(\frac{2j+1}{d}\pi x\right)\right)\cdot\exp\left(-\frac{(2j+1)^2\pi^2\tilde{D}^2 t}{d^2}\right)\right]_{-\frac{d}{2}}^{\frac{d}{2}} \\ &= \sum_{j=0}^{\infty}\frac{8C_0}{\pi^2(2j+1)^2}\cdot\exp\left(-\frac{(2j+1)^2\pi^2\tilde{D}^2 t}{d^2}\right)\end{aligned} \tag{A.5}$$

Finally, we can take the fractional change M_t/M_∞ into account, which is the ratio between total amount of diffused substance at time t and that at $t=\infty$. Assuming that the diffusing species under consideration are also responsible for the total charge transport in the material, following relation is obtained:

$$\begin{aligned}\frac{M_t}{M_\infty} &= \frac{\sigma(t)-\sigma_0}{\sigma_\infty-\sigma_0} = \frac{\bar{C}(t)-C_0}{C_\infty-C_0} \\ &= 1-\sum_{j=0}^{\infty}\frac{8}{\pi^2(2j+1)^2}\cdot\exp\left(-\frac{(2j+1)^2\pi^2\tilde{D}^2 t}{d^2}\right)\end{aligned} \tag{A.6}$$

The relaxation time τ is defined as $\tau = d^2/\pi^2\tilde{D}$. Expression A.6 can be further reduced by assuming $t \gg \tau$:

$$1-\frac{\sigma(t)-\sigma_0}{\sigma_\infty-\sigma_0} = \frac{8}{\pi^2}\cdot\exp\left(-\frac{t}{\tau}\right) \tag{A.7}$$

Figure A.20 shows the time dependent conductivity of a sample after changing the atmosphere from low to high oxygen partial pressure until an equilibrium state is reached. In the middle and at the

bottom of Fig. A.20 the normalized conductivity expressed by Equation A.7 and its natural logarithm are displayed. The natural logarithm of the normalized conductivity exhibits a linear behavior with time. Hence, the chemical diffusion coefficient $\tilde{D}$ can be determined by the slope [335–338].

Within this work it was only possible to measure one sample type since relaxation experiments take quite some time. Hence, Fig. A.21 shows the diffusion coefficients as function of temperature extracted from the relaxation measurements of $Na_{0.99}Ca_{0.01}NbO_3$ shown and discussed in Section 7.1.3. Here, relaxation experiments were conducted in dry air and in pure nitrogen. The extracted chemical diffusion coefficients $\tilde{D}$ in air and in nitrogen all follow the same trend with an activation energy ranging between $0.75\,\text{eV}$ to $1.00\,\text{eV}$. The reader should be reminded that these diffusion coefficients are representative for mechanism (2) illustrated in Fig. 7.5.

Besides DC-relaxation experiments, diffusion coefficients can be examined by the Nernst-Einstein-Equation (2.38). Under the assumption that with an AC-signal mainly the ionic conductivity is detected within the $NaNbO_3$- based samples, the impedance results described and analyzed in Section 7.2 can be used for this investigation. In case of the AC-measurements, the charge diffusion coefficient D^{σ}_{AC}, which is related to the tracer diffusion coefficient $D^{\star}_{\text{AC}}$ by the Haven ratio H (Equation A.8) is calculated instead of the chemical diffusion coefficient.

$$D^{\sigma}_{\text{AC}} = \frac{D^{\star}_{\text{AC}}}{H} \tag{A.8}$$

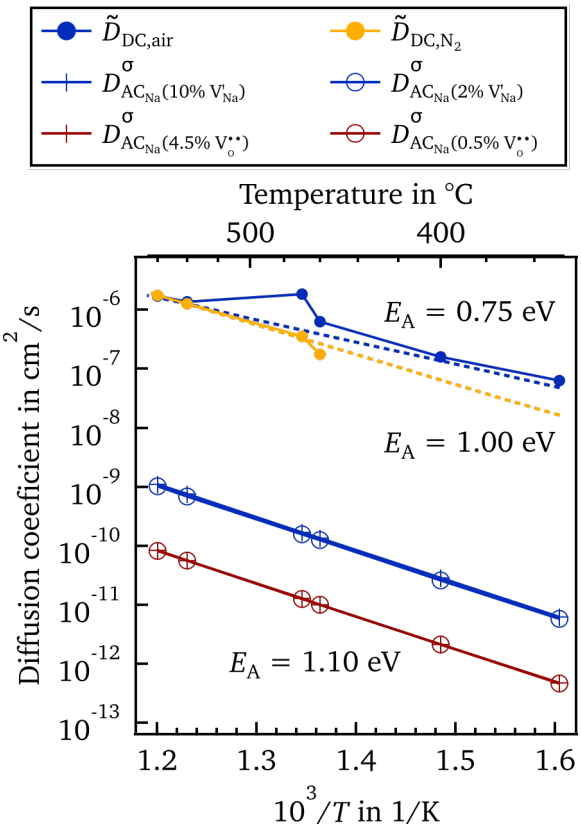

Figure A.21.: Chemical diffusion coefficient determined by relaxation experiments in air $\tilde{D}_{\text{DC,air}}$ and nitrogen $\tilde{D}_{\text{DC,N}_2}$, and charge diffusion coefficients for pure oxygen $D^{\sigma}_{\text{AC}_{\text{O}}}$ and pure sodium diffusion $D^{\sigma}_{\text{AC}_{\text{Na}}}$ for a low and a high defect concentration.

According to Equation 2.40, the charge diffusion coefficient must be multiplied by the thermodynamic factor in order to result in the chemical charge diffusion coefficient $\tilde{D}^{\sigma}$. In Section 2.4.2 it is explained that the chemical diffusion coefficient determined by relaxation experiments depends on ionic and electronic conductivity in order to maintain charge neutrality. The charge diffusion coefficient examined in the temperature dependent impedance measurements is only influenced by the ionic conductivity. Consequently, the charge diffusion coefficient is lower compared to the chemical diffusion coefficient, which can be seen in Fig. A.21. The relaxation experiments indicate that two

different diffusing species, most likely oxygen and sodium, are involved in the conduction process. It is not clear to which extend oxygen and sodium contribute to the total diffusion coefficient. Therefore, two different charge diffusion coefficients are calculated from the AC-experiments, one assuming only oxygen diffusion and a second one taking only sodium as diffusing species into account. Both values are defined for a low and a high vacancy concentration. There is no clear difference in the charge diffusion coefficient when changing the vacancy concentration because the concentration of the diffusing species is much higher compared to the vacancy concentrations. Furthermore, the charge diffusion coefficient is higher for sodium than for oxygen. In fact, a value in between these two limits is expected as probably both, sodium and oxygen, add to the measured conductivity. For all cases an activation energy of 1.1 eV is extracted from the calculated diffusion coefficients of the AC-measurements, which is comparable to the 0.75 eV to 1.00 eV of the relaxation experiments.

A.3.2. Degradation

Degradation experiments investigating the impact of simultaneous application of high temperatures and electric fields were performed as described in Section 4.11.4. The results are illustrated and analyzed in Section 7.4.
When the electric field is changed at a constant temperature, the sample is charged accordingly. A charging peak can be identified within the first few seconds, which is shown in Fig. A.22. Afterwards, a second exponential decaying process is dominating the conductivity behavior, which might be related to ion migration.

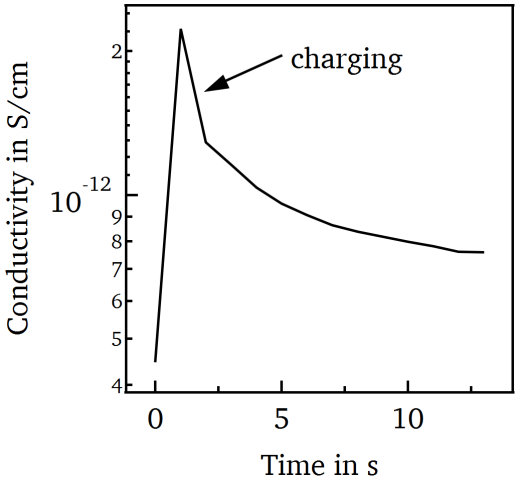

Figure A.22.: Charging of the ceramic capacitor after changing the electric field strength during the degradation experiments.

In addition, one undoped $NaNbO_3$ sample was examined after the degradation experiments with XPS. In Fig. A.23 the Nb $3d$ peak is shown. A clear shoulder located at around 206.4 eV can be identified,

which fits well with binding energies found in literature for Nb^{4+} [302]. This can be evidence for the formation of electron polarons on the niobium site in $NaNbO_3$-based materials. These electron polarons might play a role in the degradation process.

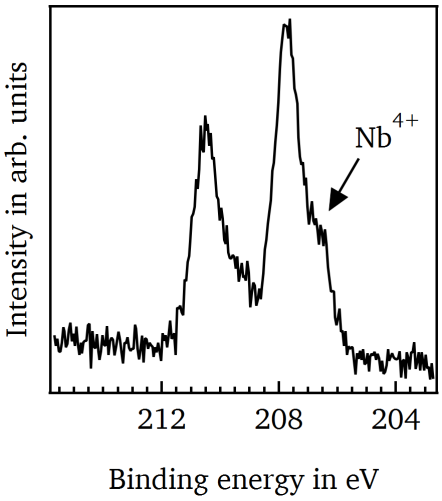

Figure A.23.: Nb^{4+} peak detected in the Nb 3*d* emission line with XPS after conduction the degradation experiments on an undoped $NaNbO_3$ sample.

A.3.3. Electrode degradation

In order to examine the electrode degradation, first Pt as back contact was sputtered and afterwards the ITO front contact was deposited as described in Section 4.13. As the sample has to be taken out of the ultra-high vacuum system and mounted on a special sample holder for the in situ degradation experiments, carbon adsorbents on the surface can be observed, which is shown in the XP-survey spectra in Fig. A.24. After heating for about 2 h to 3 h at 100 °C and 200 °C in the XPS-chamber, the intensity of the C 1*s* peak is significantly reduced due to evaporation of the carbon adsorbents. Both measurements were done at room temperature.

When measuring XP-spectra with applied electric field at 100 °C the surface of the sample is charging leading to a shift in the binding energy of the emission lines. Although ITO exhibits a high conductivity especially under reducing conditions, which is the case for ITO acting as cathode, the current during the degradation experiments is too high. Hence, the surface is charging during XPS measurements. When applying 30 V a fast increase in conductivity is followed by a slow decrease due to relaxation behavior of ion migration as shown in Fig. A.25. Therefore, the shift in binding energy of the core level emission lines compared to the room temperature measurement is decreasing with time because the current is lowering, hence, the surface charging is reduced. This relation is illustrated in Fig. A.25. Arrows indicate the time one elemental peak was recorded.

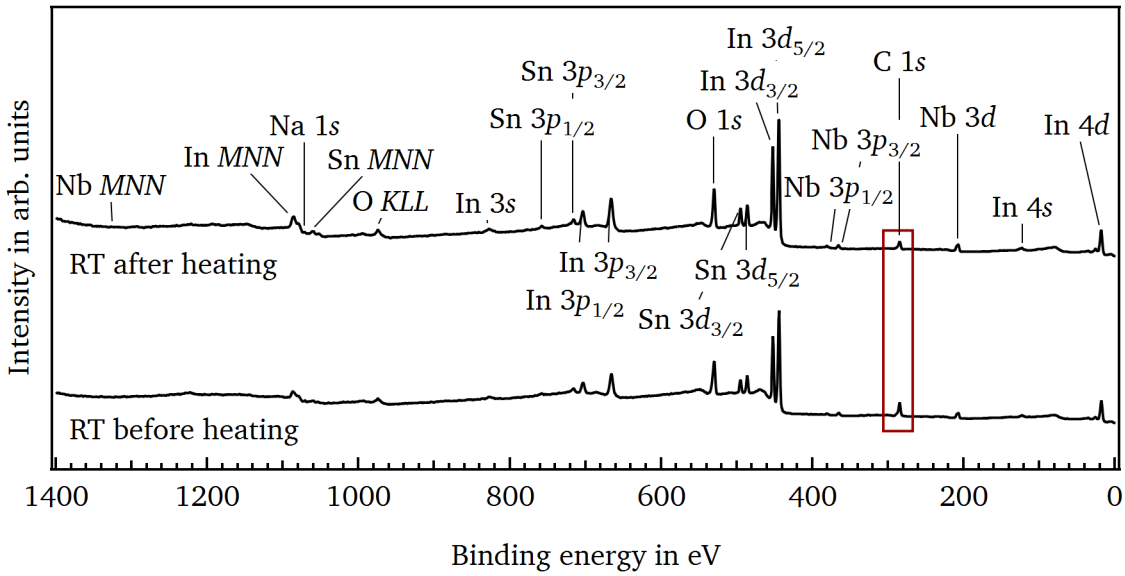

Figure A.24.: Survey XP-spectra of $Na_{0.99}Ca_{0.01}NbO_3$ with an ITO-electrode after mounting on the sample holder and after heating at 100 °C and 200 °C in the XPS-chamber. A clear reduction of the C 1s peak due to the evaporation of carbon adsorbents can be observed.

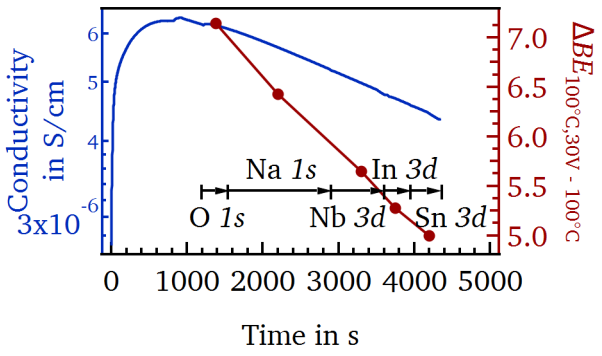

Figure A.25.: Conductivity on the left axis and binding energy difference of the core level lines between 100 °C with applied voltage and room temperature as a function of time for ITO as cathode. Arrows mark the time period of each examined peak.

A.3.4. Heating in oxidizing and reducing atmospheres with a thick ITO layer

Heating experiments with a thick ITO film on top of a $K_{0.5}Na_{0.5}NbO_3$ ceramic pellet were conducted and analyzed by Sabrina Kahse within her advanced research internship [312]. For convenience the Na 1*s*, O 1*s*, K 2*p*, and Nb 3*d* emission lines are plotted in Fig. A.26. After cleaning (black) all spectra can be identified while after the ITO deposition no emission lines related to the $K_{0.5}Na_{0.5}NbO_3$ sample can be observed anymore. Interestingly, after taking the sample out of the vacuum atmosphere, mounting it on the special sample holder, and transferring it back in the XP-chamber, a small K 2*p*

peak is detected. In addition, an expected C 1*s* line and a shoulder in the O 1*s* core level line due to the carbon absorbents is recorded. After heating at 100 °C, 200 °C, and 300 °C the intensity of the K 2*p* peak is increasing. With applied negative electric field the K 2*p* emission line is clearly visible. In addition, a small broad Na 1*s* peak can be observed. Hence, the alkaline ions within $K_{0.5}Na_{0.5}NbO_3$-based samples are mobile at elevated temperature and diffuse towards the surface. In contrast, no niobium can be detected after all heat treatments.

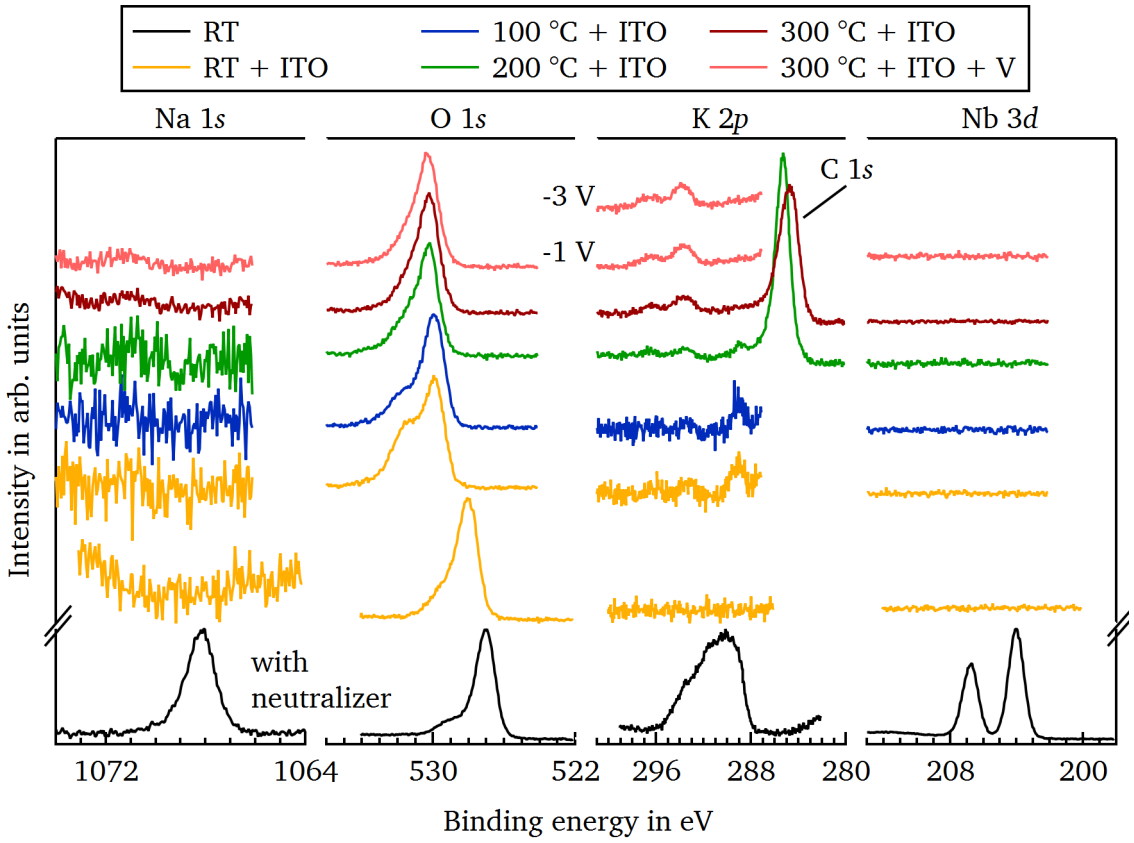

Figure A.26.: Na 1*s*, O 1*s*, K 2*p*, and Nb 3*d* emission lines for a $K_{0.5}Na_{0.5}NbO_3$ ceramic after cleaning (black), after depositing a thick ITO-layer (yellow), while heating at 100 °C (blue), 200 °C (green), and 300 °C (dark red), and while heating at 300 °C and applying a voltage (light red) adopted from [312].

A.4. Polaron model

The polaron model developed in Section 8.2 is applied to the temperature dependent conductivity curves measured in air and N_2 on a $Na_{0.99}Sr_{0.01}NbO_3$ sample. The corresponding plots are illustrated in Fig. A.27 on the left side while the related band diagrams are shown on the right side. It can be observed that the model does not fit as good as for the undoped and Ca-doped $NaNbO_3$ sample. Here, hole polaron hopping in the high temperature region and electron polaron hopping in the low temperature regime is assumed because it shows less deviation than electron hole polaron hopping in the high temperature part. However, the $Na_{0.99}Sr_{0.01}NbO_3$ samples are special. On the one hand, they have a higher conductivity in N_2 than in air suggesting n-type behavior above $300\,°C$. On the other hand, they exhibit a decreasing conductivity with cycle number in N_2 (see Fig.7.3 in Section 7.1.2), which hints more to a p-type behavior. Furthermore, the additional Ca-concentration in these samples could influence the electronic properties. Hence, $Na_{0.99}Sr_{0.01}NbO_3$ samples without any contamination from calcium or other elements need to be prepared in future for further investigations.

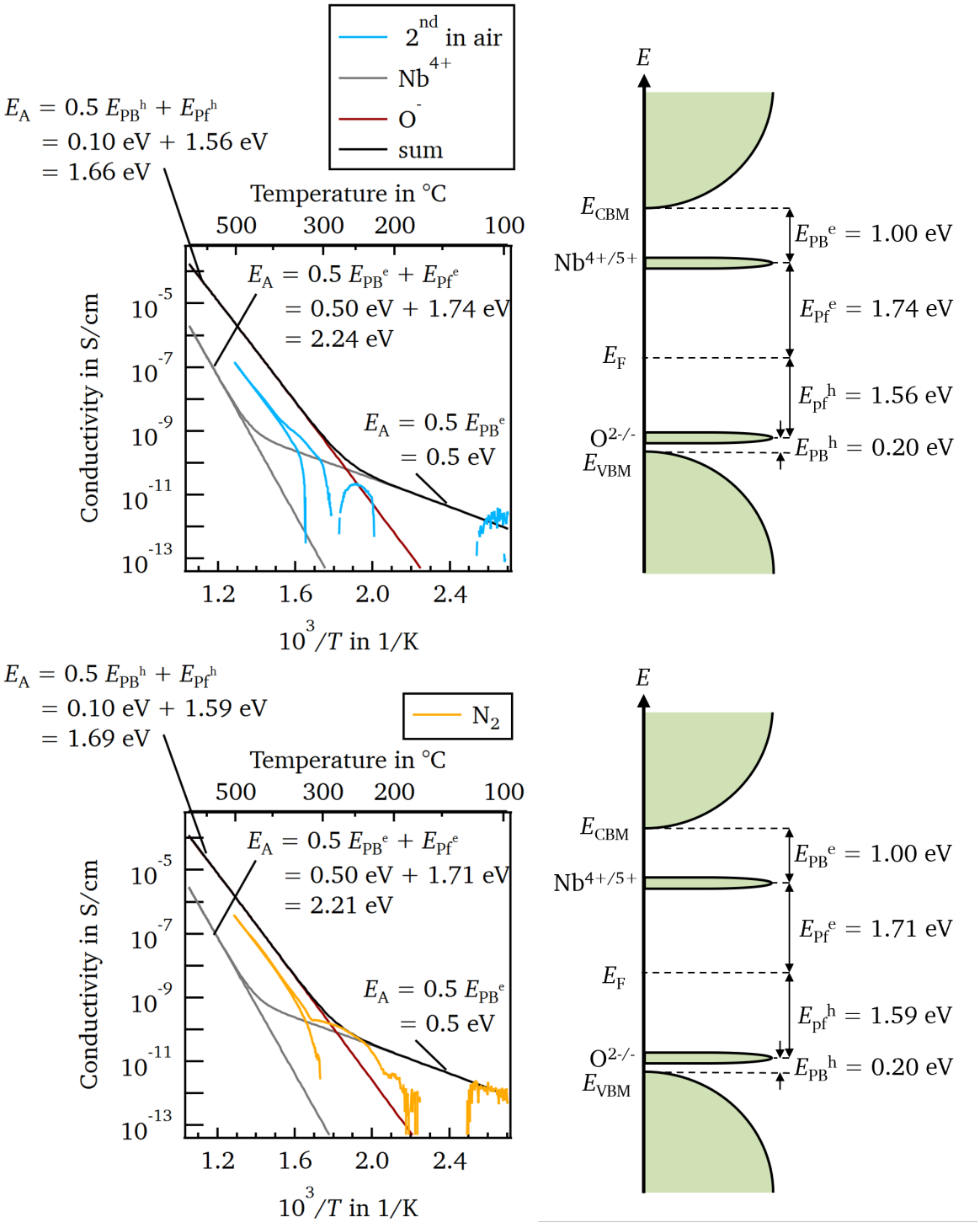

Figure A.27.: Measured and fitted conductivity of $Na_{0.99}Sr_{0.01}NbO_3$ in air (top) and nitrogen (bottom) including all relevant energies and the corresponding band diagrams.

Publications and Conferences

Publications

2023 A. Klein, K. Albe, N. Bein, O. Clemens, K. A. Creutz, P. Erhart, M. Frericks, E. Ghorbani, J. P. Hofmann, B. Huang, B. Kaiser, U. Kolb, J. Koruza, C. Kübel, K. N. S. Lohaus, J. Rödel, J. Rohrer, W. Rheinheimer, R. A. De Souza, V. Streibel, A. Weidenkaff, M. Widenmeyer, B.-X. Xu, and H. Zhang. "The Fermi energy as common parameter to describe charge compensation mechanisms: A path to Fermi level engineering of oxide electroceramics." In: *Journal of Electroceramics*.

2022 N. Bein, B. Kmet, T. Rojac, A. Benčan Golob, B. Malič, J. Moxter, T. Schneider, L. Fulanovic, M. Azadeh, T. Frömling, S. Egert, H. Wang, P. van Aken, J. Schwarzkopf, and A. Klein "Fermi energy, electrical conductivity, and the energy gap of $NaNbO_3$." In: *Physical review materials* 6, 08440

2019 N. Bein, P. Machado, M. Coll, F. Chen, M. Makarovic, T. Rojac, and A. Klein "Electrochemical Reduction of Undoped and Cobalt-Doped $BiFeO_3$ Induced by Water Exposure: Quantitative Determination of Reduction Potentials and Defect Energy Levels Using Photoelectron Spectroscopy" : In: *J. Phys. Chem. Lett.*, 10, 7071−7076

Attended Conferences and Summer Schools

2022 **FLAME Summer School (Annweiler-Bindersbach, Germany)**
Defect dipoles in $NaNbO_3$ and $KNbO_3$ - *oral presentation*

2020 **Materials Science and Engineering Congress (online)**
Interface analysis of KN and NN by XPS measurements - *oral presentation*

Electroceramics Conference XVII (online)
Interface analysis of KN and NN by XPS measurements - *oral presentation*

Electroceramics Conference XVII (online)
The Fermi Level in Bismuth Ferrite - *poster presentation*

2019 **International Conference on Microelectronics, Devices and Materials (Bled, Slovenia)**
The Fermi Level in Bismuth Ferrite - *oral presentation*

FLAME Summer School (La Clusaz, France)
Energy Band Alignment - *oral presentation*

European Meeting on Ferroelectricity (Lausanne, Switzerland)
The Fermi Level in Bismuth Ferrite - *oral presentation*

Supervised Theses

2022 **Sabrina Kahse**
Investigation of the Fermi Level of Rare-Earth Pyrochlore Ruthenates
Master's Thesis

2021 **Sabrina Kahse**
Investigation of the Stability of the BTO|ITO and KNN|ITO Interface
Advanced research lab

Yannick Stähling
Elektrische Eigenschaften von Nb_2O_5 und reduzierten Nb_2O_5 Dünnschichten
Bachelor's Thesis

2019 **Christoph Keinert**
Herstellung und Charakterisierung von Niob(V)-oxidschichten
Bachelor's Thesis

Acronyms

AFE antiferroelectric

ALD atomic layer deposition

ARXPS angle resolved x-ray photoelectron spectroscopy

CBM conduction band minimum

CVD chemical vapour deposition

DAISY-MAT **Da**rmstadt **I**ntegrated **Sy**stem for **Mat**erial Research

DC direct current

DFT density functional theory

DOS density of states

EELS electron energy loss spectroscopy

FE ferroelectric

FWHM full width at half maximum

GW Green's function G and dynamical screened interaction W

ITO Sn-doped In_2O_3

KNLNT $0.95(K_{0.49}Na_{0.49}Li_{0.02})(Nb_{0.8}Ta_{0.2})O_3$-$0.05CaZrO_3$ with $2\,wt\,\%$ MnO_2

LabVIEW Laboratory Virtual Instrumentation Engineering Workbench

RF radio frequency

SEM scanning electron microscopy

STEM scanning transmission electron microscopy

TEM transmission electron microscopy

V''''_{Ti} titanium vacancy

$\mathbf{V}''_{\mathrm{Ba}}$ barium vacancy

VBM valence band maximum

XPS x-ray photoelectron spectroscopy

XRD x-ray diffraction